

CRANFIELD INSTITUTE OF TECHNOLOGY

COLLEGE OF AERONAUTICS

Ph.D. Thesis

H S DEO

Numerical Techniques for Predicting  
Aerodynamic Characteristics of Bodies

Supervisor : Dr.P.A.T.Christopher

January 1986

ProQuest Number: 10820993

All rights reserved

INFORMATION TO ALL USERS

The quality of this reproduction is dependent upon the quality of the copy submitted.

In the unlikely event that the author did not send a complete manuscript and there are missing pages, these will be noted. Also, if material had to be removed, a note will indicate the deletion.



ProQuest 10820993

Published by ProQuest LLC (2019). Copyright of the Dissertation is held by Cranfield University.

All rights reserved.

This work is protected against unauthorized copying under Title 17, United States Code  
Microform Edition © ProQuest LLC.

ProQuest LLC.  
789 East Eisenhower Parkway  
P.O. Box 1346  
Ann Arbor, MI 48106 – 1346

## ACKNOWLEDGEMENTS

I would like to thank my supervisor, Peter Christopher, for his continual guidance and informative suggestions throughout the research programme. Also, my sincere thanks go to David Catherall, who was always able to offer so much knowledge and expertise, and without whom the research would have been more painstaking.

I would also like to extend my gratitude to my family and fellow colleagues at the Institute who have made the last three years so worthwhile.

Finally, the last couple of months have been especially enjoyable, and for that I would like to thank my wife.

## SUMMARY

Two methods are presented for predicting the aerodynamic characteristics of bodies in inviscid and irrotational flow. The first method is limited to incompressible flow and makes use of panels of ring sources to approximate the body surface. The technique is dedicated to single, axisymmetric body configurations in either uniform longitudinal or rectilinear motion. The versatility of the method is due to the use of sources as singularities placed on the body surface, allowing discontinuous body profiles to be analysed. The method has been compared for accuracy and efficiency with experimental and theoretical results.

Further investigation showed that at present there existed no numerical technique which could predict the aerodynamic behaviour of multiple bodies in compressible flow. Hence, a fully three-dimensional method was developed which made use of the Full Potential Equation (F.P.E.) in conservative form. A computational mesh is placed around the body configuration and at each mesh node the F.P.E. is satisfied in finite difference form. The method is able to give a complete description of the flow around the bodies at transonic mach numbers. Comparisons to test the accuracy and efficiency of the method are limited to either, purely subsonic flow for two body configurations or zero incidence for transonic flow around a single body.

## CONTENTS

CONTENTS	PAGE
ACKNOWLEDGEMENTS	
SUMMARY	
CONTENTS	
LIST OF FIGURES	
NOTATION	
1.0 INTRODUCTION	1
2.0 INTRODUCTION TO SINGULARITY METHODS	
2.1 Flow Assumptions	5
2.2 Historical Perspective	7
2.2.1 Axial Singularity Methods	7
2.2.2 Panel Methods	8
2.3 Present Study	9
3.0 METHOD OF SOLUTION	
3.1 Definition of Potential Flow	12
3.1.2 Boundary Conditions and Pressure Calculation	14
3.2 Reduction of the Problem to an Integral Equation for the Source Density Distribution on the Body Surface	
3.2.1 General	16
3.2.2 Setting up the Linear Equations	17
3.3 Defining the Body Shape	19

3.4	Matrices of Influence Coefficients	21
3.5	Influence Matrix for the Cross Flow	23
3.6	Computation of the Pressure Coefficient	25
4.0	INTEGRATING THE KERNEL TO OBTAIN THE VELOCITIES AT A CONTROL POINT	
4.1	Velocity Due to Axial Flow	28
4.2	Effect of an Element at it's own Control Point	31
4.3	Velocities due to Cross Flow	32
4.4	Axisymmetric Bodies in Curvilinear Flow	34
5.0	DISCUSSION AND RESULTS	
5.1	General	37
5.2	Axisymmetric Bodies with Varying Nose Shape in Uniform Flow	38
5.3	Prolate Ellipsoid at Incidence	38
5.4	Effects of Panel Distribution	39
5.5	Comparison with SPARV	40
5.6	Comparison with Experiment	41
5.7	Prolate Ellipsoid in Curvilinear Flow	42
5.8	Effects of Varying Nose Bluffness	42
APPENDIX.A DESCRIPTION OF THE SOURCE-RING PROGRAM		
A.1	Input of Flow Behaviour and Body Coordinates	45
A.2	Calculation of the Element	

Characteristics	45
A.3 Velocity Induced by an Element at it's own Control Point	46
A.4 Velocity Induced at Other Control Points	47
A.5 Source Strength and Tangential Velocity Calculation	47
A.6 Pressure and Load Calculations	48
6.0 INTRODUCTION TO COMPUTATIONAL FLUID DYNAMICS	49
7.0 OVERVIEW OF THE SOLUTION OF THE FULL POTENTIAL EQUATION	
7.1 Finite Difference Formulation	53
7.2 Grid Generation	54
7.3 Introduction of Artificial Viscosity	58
7.4 Solution Algorithm	60
7.5 The Non-Conservative Scheme	63
8.0 SPATIAL DIFFERENCING OF THE FULL POTENTIAL EQUATION IN CONSERVATION FORM	
8.1 Formulation of the Equations	65
8.2 Differencing Operators	68
8.3 Finite Difference Formulation	70
8.4 Far-Field Boundary Conditions	72
8.5 Body Specification	73
8.6 Effects of Decoupling	75
8.7 Pressure Distribution Calculation	76

9.0	GRID GENERATION AND COORDINATE STRETCHING	
9.0	General	79
9.1	Stretching Algorithm	80
10.0	INTRODUCTION OF ARTIFICIAL COMPRESSIBILITY IN TRANSONIC REGIONS	
10.0	General	87
10.1	Evolution of Supersonic Regions	88
11.0	AF2 FACTORISATION AND SOLUTION ALGORITHM	
11.0	General	91
11.1	Solution Algorithm	92
12.0	DISCUSSION OF RESULTS	
12.1	General	97
12.2	Transonic Comparison Errors	98
12.3	Ellipsoid of Ratio 1:1	100
12.4	Ellipsoid of Ratio 8:1 at 5 Degrees Incidence	101
12.5	Tangent Ogive Cylinder Results	101
12.6	Tangent Ogive cylinders in Transonic Flow	102
12.7	Double Ellipsoids of Fineness Ratio 4:1	104
12.8	Double Ogive-Cylinder Configurations	104
12.9	Double Ogive-Cylinders with Stagger	106
13.0	CONCLUSIONS	108
14.0	RECOMMENDATIONS FOR FURTHER WORK	



14.1 General	111
14.2 Axisymmetric Two Body Configuration	111
14.3 Multiple Body Configurations	113
14.4 Arbitrary Body Specification	114
14.5 The use of Surface Splines	115
14.6 Normal Force Calculation	115
14.7 Accurate Shock Capture	116

#### APPENDIX.A1 DESCRIPTION OF THE FINITE VOLUME PROGRAM

A1.1 General	117
A1.2 Initial Data Input	117
A1.2.1 Ellipsoid	117
A1.2.2 Missile	118
A1.3 Calculation of a Cell Face Area	118
A1.4 Three-Dimensional Cell Investigation	122

REFERENCES	123
------------	-----

#### FIGURES

## LIST OF FIGURES

1. A ring source at  $x$  of radius  $r$ , in axial and cross flow
2. Arbitrary point lying relative to a point source
3. Elemental surface source distribution, on an arbitrary surface  $S$ , inducing a velocity at some point  $P$
4. Defining an axisymmetric body using frustum elements
5. Nose and tail cones, with frusta make up the approximated shape of the axisymmetric body
6. A ring source of constant strength lying in plane  $x=b$
7. Integrations performed along a line segment (top) and around a circular ring at sections along the line segment
8. Treatment of a single sub-element
9. A ring source of strength  $\cos(\theta)$  lying in plane  $x=b$
10. A body at incidence and yaw in curvilinear motion, with  $R$  radius of curvature
11. A panel, either side of the centre of gravity of a body, experiencing an angular velocity  $V$
12. Point distribution over a nose or half body
13. The non-analytic profiles, missile shapes used
14. Pressure distribution on a tangent ogive cylinder

15. Pressure distribution on an ellipsoid cylinder
16. Pressure distribution on a hemisphere cylinder
17. Ellipsoid of fineness ratio 1/8 in uniform oncoming flow
18. Ellipsoid of fineness ratio 8/1 in uniform cross flow
19. Load distribution on an ellipsoid of fineness ratio 100/15 at 5 degrees
20. Ellipsoid cylinder of fineness ratio 6/1 at 5 degrees using different panel distributions
21. Ellipsoid cylinder of fineness ratio 6/1 at 5 degrees using 100 panels
22. Comparison of experimental and theoretical pressure distribution, Ogive cylinder body, angle of attack=0.14 degrees
23. Comparison of experimental and theoretical pressure distribution, Ogive cylinder body, angle of attack=8.14 degrees
24. Normal load distribution on an ellipsoid (4/1) in curvilinear motion
25. Load distribution on tangent ogive cylinders of various ratios at 5 degrees

26.  $dC_m/dx$  variation along a body at 5 degrees for varying bluntness
27. Variation of total  $C_m$  and peak value of  $dC_m/dx$  with nose length for missile at 5 degrees
28. Variation of  $X_{c.p}$  with nose length for missiles at 5 degrees
29. Sheared coordinates
30. Blunt body coordinate system
- 31a. Elliptic body in physical grid space
- 31b. Elliptic body in computational grid space
- 32a. Double missile configuration in physical space
- 32b. Double missile configuration in computational space
33. Flow in and out of a computational cell
34. Internal computational domain with dummy boundaries
35. Body conforming mesh and Cartesian non-conforming mesh
36. Cell cut by a body surface
37. Calculation of surface variation of  $C_p$  to predict the pressure distribution
38. Regions of varying grid line density

39. Varying grid line density regions for a missile
40. Y-direction Stretching for two bodies
41. Domain dependant differencing on shock formation
42. Direction of sweeping during one iteration step
43. Variation of  $\log(\text{residual})$  with iteration number
44. Velocity calculation errors due to shock formation
45. Surface  $C_p$  distribution over a sphere  $M=0.0$ ,  
Angle of Incidence= $0.0$
46. Surface  $C_p$  distribution for  $M=0.01$ , Ellipsoid 8:1,  
Angle of attack= $5.0$  degs.
47. Surface  $C_p$  distribution for  $M=0.01$ , Cylinder with  
Ogive nose 4:1, Angle of attack= $0.14$  degs.
48. Surface  $C_p$  distribution for  $M=0.01$ , Cylinder with  
Ogive nose 4:1, Angle of attack= $4.14$  degs.
49. Pressure distribution comparison for an ogive-cylinder  
 $M=0.5$  Incidence= $0.0$
50. Pressure distribution comparison for an ogive-cylinder  
 $M=0.7$  Incidence= $0.0$
51. Pressure distribution comparison for an ogive-cylinder  
 $M=0.9$  Incidence= $0.0$
- 52a. Pressure distribution for an ogive-cylinder  
 $M=0.5$  Incidence= $3.0$

- 52b. Pressure distribution for an ogive-cylinder  
M=0.5 Incidence=3.0
- 52c. Pressure distribution for an ogive-cylinder  
M=0.5 Incidence=5.0
53. Pressure distribution for an ogive-cylinder  
M=0.7 Incidence=3.0
54. Pressure distribution for an ogive-cylinder  
M=0.7 Incidence=5.0
55. Pressure distribution for an ogive-cylinder  
M=0.9 Incidence=3.0
56. Pressure distribution on bottom ellipsoid of  
configuration, M=0.0 Incidence=0.0 Spacing=0.025
57. Pressure distribution on bottom ellipsoid of  
configuration, M=0.5 Incidence=0.0 Spacing=0.025
58. Pressure distribution on bottom ellipsoid of  
configuration, M=0.5 Incidence=5.0 Spacing=0.025
59. Pressure distribution for double ogive-cylinder of  
configuration, M=0.0 Incidence=0.0 Spacing=0.025
60. Pressure distribution for bottom ogive-cylinder of  
configuration, M=0.0 Incidence=5.0 Spacing=0.025
61. Pressure distribution for top ogive-cylinder of  
configuration, M=0.0 Incidence=5.0 Spacing=0.025
62. Pressure distribution for bottom ogive-cylinder of

configuration, M=0.0 Incidence=5.0 Spacing=0.05

63. Pressure distribution for top ogive-cylinder of configuration, M=0.0 Incidence=5.0 Spacing=0.05
64. Pressure distribution for a double ogive-cylinder of configuration, M=0.5 Incidence=0.0 Spacing=0.025
65. Pressure distribution for a double ogive-cylinder of configuration, M=0.7 Incidence=0.0 Spacing=0.025
66. Pressure distribution for a double ogive-cylinder of configuration, M=0.8 Incidence=0.0 Spacing=0.025
67. Pressure distributions on both ogive-cylinders of configuration, M=0.5 Incidence=5.0 Spacing=0.025
68. Pressure distributions for both ogive-cylinders of configuration, M=0.6 Incidence=5.0 Spacing=0.025
69. Pressure distributions for both ogive-cylinders of configuration, M=0.7 Incidence=5.0 Spacing=0.025
70. Pressure distributions for both ogive-cylinders of configuration, M=0.8 Incidence=5.0 Spacing=0.025
71. Peak pressure Vs mach number for both ogive-cylinders of configuration, Incidence=5.0 Spacing=0.025
72. Pressure distribution for bottom ogive-cylinder of configuration, M=0.01 Incidence=0.0 Spacing=0.025 Stagger=0.1
73. Pressure distribution for top ogive-cylinder of

- configuration,  $M=0.01$  Incidence=0.0 Spacing=0.025  
Stagger=0.1
74. Pressure distribution for bottom ogive-cylinder of  
configuration,  $M=0.01$  Incidence=5.0 Spacing=0.025  
Stagger=0.1
75. Pressure distribution for top ogive-cylinder of  
configuration,  $M=0.01$  Incidence=5.0 Spacing=0.025  
Stagger=0.1
76. Pressure distribution for bottom ogive-cylinder of  
configuration,  $M=0.5$  Incidence=0.0 Spacing=0.025  
Stagger=0.1
77. Pressure distribution for top ogive-cylinder of  
configuration,  $M=0.5$  Incidence=0.0 Spacing=0.025  
Stagger=0.1
78. Pressure distribution for bottom ogive-cylinder of  
configuration,  $M=0.5$  Incidence=5.0 Spacing=0.025  
Stagger=0.1
79. Pressure distribution for top ogive-cylinder of  
configuration,  $M=0.5$  Incidence=5.0 Spacing=0.025  
Stagger=0.1
80. Two bodies in asymmetric configuration
81. New coordinate system for a body at incidence
82. Grid lines between three bodies
83. A missile shaped body with non-circular cross-



section

84. Body section in the x-direction
85. Accurate cell face area calculation using splines
86. Body points used for calculating the normal force
87. Form of a smeared shock over a few grid points
88. Bodies used as test cases for the C.F.D. work
89. Constant grid line distribution between two  
bodies
90. Cell face area prediction for the x-wise flow
- 91a. X-direction cell side calculation
- 91b. X-direction cell side calculation
92. Accurate determination of a cell face area
93. Body surfaces cutting a cell face
94. Determination of the area through which fluid  
flows
95. Cell face areas lying mid-way between control points
96. Ways a body surface can cut a cell face

## MAIN NOTATION

$x, y, z$	- Physical Cartesian Coordinates
$\underline{V}$	- Total Velocity Vector
$\infty$	- Indicates conditions at Infinity
$\underline{U}, \underline{V}, \underline{W}$	- Free-stream Velocity Vectors
$\rho$	- Density
$p$	- Pressure
$\nabla$	- Gradient Vector
$t$	- time
$\underline{n}, \underline{t}$	- Normal and Tangential Vectors
$\phi$	- Perturbation Potential
$C_p$	- Pressure Coefficient
$\alpha$	- Angle of Incidence (Fig.1)
$\beta$	- Angle of Yaw (Fig.1)

### Notation Specific to Sections.1 to 6

$\underline{F}$	- Prescribed Normal Velocity
$\underline{v}$	- Perturbation Velocity Vector
$\underline{V}_{abs}$	- Absolute Velocity Vector
$\underline{V}$	- Velocity Vector due to Source Distribution
$\underline{V}_{rel}$	- Relative Velocity Vector
$P_s$	- Static Pressure
$\Omega$	- Angular Velocity
$\underline{R}$	- Radial arm Vector
$R_s$	- Radius of Rotation of Surface Point
$r(P, q)$	- Distance between Points P and q
$x, y, z$	- Location of an Arbitrary Point

$xq, yq, zq$	- Location of a Point Source
$\sigma(q)$	- Source Distribution
$S$	- Surface
$\iint_S$	- Double Integral over a Surface $S$
$i, j$	- Vectors along Axis
$i, j$	- Location of Matrices
$\Sigma$	- Summation Sign
$Effect(i, j)$	- Velocities induced by the $j$ 'th element at the $i$ 'th control point
$A_{ij}, B_{ij}, \Theta_{ij}$	- Matrices of Influence Coefficients
$v_{ij}$	- Velocity Vector Matrix
$\theta, \psi$	- Circumferential Angles
$\beta$	- Element Slope in Section.4
$a$	- Radius of Source-Ring
$b$	- Location of Source-Ring
$V_x, V_y, V_\theta$	- Velocities in $x, y,$ and $\theta$ directions
$h, r$	- Distance Measurement
$V_c$	- Velocity due to Source-Ring
$V_{total}$	- Total Velocity due to a Cone Frusta
$\Delta S$	- Element Length
$y_0$	- Y-Coordinate of a Control Point
$d$	- Central Section of an Element
$R, \theta$	- Coordinates in Section.4
$x', y', z'$	- Body Coordinate System
$\Omega_x', \Omega_y', \Omega_z'$	- Rotations about Axes
$V_{\Omega_x}$	- Velocity due to a Rotation
$R_l$	- Nose Length for Bodies
$C_m$	- Moment Coefficient
$C_n$	- Load Coefficient

Xc.p. - Location of Centre of Pressure

Notation Specific to Sections.6 to 14

$\phi_t$  - Damping Term

$\phi_{st}, \phi^{xt}$  - Extra Damping Terms in Presence of Shock

$\gamma$  - Ratio of Specific Heats

$a$  - Speed of Sound

$q$  - Velocity Vector

$M_\infty$  - free-stream Mach Number

$\Phi$  - Velocity Potential

$V$  - Volume

$S$  - Surface

$u, v, w, q$  - Velocities

$x, y, z$  - Physical Space Coordinate System

$X, Y, Z$  - Computational Space Coordinate System

$\Delta x, \Delta y, \Delta z$  - Physical Space Grid Widths

$\Delta X, \Delta Y, \Delta Z$  - Computational Space Grid Widths

$i, j, k$  - Grid Point Node

$\overleftarrow{\delta}, \overrightarrow{\delta}$  - Backward and Forward Difference Operators

$f, g$  - Functions

$|_{ijk}$  - Denoting Evaluation at some Point

$S_{1..5}$  - Cell Face Areas

$s, S_1$  - Denote Lengths on Body Surface in Section.8.7

$w_x, w_y, w_z$  - Weights Associated with a Particular Face

$x_l, x_t$  - Leading and Trailing Edges

$\xi_x, \xi_z$  - Truncation Error Indicators

$a, a_0, a_1,$

$a_3, b, b_1,$

$b_2, c, c_0,$

$c_1, c_2, r$  - Constants Specific to Section.9  
 $\rho_c$  - Radius of Curvature of Leading or Trailing Edge  
 $\mu, \nu$  - Switching Terms  
 $\tilde{\rho}$  - Shifted Density Value  
 $\rho_s \Delta s$  - Amount of Density Shift  
 $\overline{\delta}$  - Forward or Backward Difference Operator  
 $\Delta$  - Correction of Perturbation Potential  
 $n$  - Number of Sweep  
 $\alpha_1, \alpha_2$  - Acceleration Parameters  
 $\sigma$  - Relaxation Parameter  
 $L$  - Residual Operator  
 $N, N_1, N_2$  - Operating Factors  
 $F$  - Dummy Matrix  
 $A, B, C, D, E$   
 $A', B', C', D', E'$  - Dummy Variables used in Section.11.1  
 $NX, NY, NZ$  - Grid Intervals  
 $L, M, N$  - Grid Intervals  
 $\alpha_{1k}, \alpha_{2k}$  - Initial Values for Acceleration Parameters  
 $K$  - Counter  
 $X_2, X_1$  - Distance Measurement  
 $N_k$  - Iteration Number for Acceleration Parameters

Notation Specific to Section.14

$\bar{x}, \bar{y}$  - Body Coordinate System  
 $h_1, h_2$  - Lengths  
 $r_x, r_y, r_z$  - Parameters Specifying a Body Point  
 $S_1, \dots, S_5$  - Area Values  $i$   
 $A, B, C, D,$   
 $P, Q$  - Arbitrary Points

jm,j,jb,jt,

k,kl,kr - Grid Point Indicators

Notation Specific to Appendix.A1

A1,A2,A4,

R - Geometric Variables

kl,nj,nk - Grid Point Indicators

Z1,Z2,

Y1,Y2 - Body Measurements in Physical Space

Z1T,Z2T,

Y1T,Y2T - Body Measurements in Computational Space

NY, NZ - Number of Grid Points in Y- and Z-directions

W,X,Y,Z,

G,H,I,J,R,

X1,X2,Y1 - Arbitrary Points

a,c,d - Length of Cell Face Sides

A1, A2 - Areas

S1, S2 - Surface Boundaries

CHAPTER 1

## INTRODUCTION

The importance of Aerodynamics has grown during the last century, and for many years the prediction methods available were confined to simple flow configurations, over body shapes such as ellipsoids. To study the behaviour of the flow around more complex shapes, such as wing-fuselage configurations, the wind tunnel had to be used. Models of the required shapes could be tested for accurate pressure distributions and flow visualisation techniques used to enhance the understanding of the flow behaviour. As the shapes of aircraft became more complex, the cost in producing a model which was efficient in it's design, increased. This increase was related to the length of time required to produce the model and test it through a sufficient set of conditions, such as a range of incidence. The flow around a model could be affected by the tunnel characteristics, such as blockage, turbulence and flow distortion, and results for the flow at high subsonic Mach numbers were not always readily available.

Although the development of prediction methods continued, the amount of mathematical effort required to produce results, such as loads for a particular shape, was considerable. With the advent of the computer, prediction methods became less costly in terms of human effort and started to be used in parallel to wind tunnel testing. This helped to produce a rational design of a particular body or shape in less time.

Two types of prediction methods developed; analytical methods, which require restrictive assumptions and can treat only simple configurations, and numerical methods, which entail fewer restrictions and can be used to treat more complex configurations. Numerical methods can be used to provide pressure distributions on the surface and around a body at low supersonic Mach numbers. However, a complete description of the flow-field can only be obtained from the full Navier-Stokes equations and many physical phenomena (for example buffetting and separated flow behaviour) cannot be properly modelled until methods are developed for the solution of these equations. For the present and near future it appears that computer codes based on the Navier Stokes equations do not offer the prospect of being low cost, routine methods for aerodynamic design purposes.

The desirability of numerical simulations is enhanced when it is considered that the cost of running a wind-tunnel is continually increasing, whilst the cost of computer power is rapidly decreasing.

The numerical methods available today allow many different body geometries and configurations to be computed, and their aerodynamic behaviour analysed. The first numerical techniques used singularities, such as sources and vortices, placed on the axis. Later they were distributed on surface panels. These methods assume the flow to be inviscid and neglect vorticity, and use the potential function to satisfy Laplace's equation, thus simulating only incompressible flow. The boundary layer



is assumed to be thin and so can be neglected, although displacement thickness models are sometimes used to simulate boundary layer effects. The centre-line singularity methods are limited to the amount of bluffness that can be created, although imaginary source techniques can handle any degree of bluffness. The panel methods distribute singularities on the body surface and are able to compute the flow for fully three-dimensional flows about bodies which may have discontinuities in their curvature. These require long computer codes and heavy use of storage. Bodies of revolution may also be approximated by the use of cone frusta, upon which source-rings are placed. The initial stage of the research investigates the versatility of the panel technique suggested by Hess and Smith (Ref.1) for axisymmetric bodies with the aim of introducing computationally more efficient procedures, and further, to adapt the method not only for a body in uniform flow at incidence and yaw, but also in curvilinear motion.

As the flow speed increases, compressibility effects cannot be ignored, and Laplace's equation can no longer be used. To compute flows up to low supersonic speeds, the full potential equation can be used in finite difference form. Finite difference methods involve the use of a computational grid or mesh, at the nodes of which (where the grid lines cross) the full potential equation is satisfied. The grid is set up either to conform with the body shape or to be rectangular everywhere. Stretching functions are used to map the infinite physical space, containing the whole flow field, into a simpler computational domain in which the calculations are performed.

The full potential formulation is valid for subsonic irrotational flows and may be used for low supersonic flows provided the shock waves that occur are weak. The finite volume formulation of Wedan and South (Ref.2) is used. The publication provides only a summary of the method and gives results for single two-dimensional and axisymmetric bodies. In the present work the method is developed from the basic mass flow equation to enable the calculation of transonic flow around single and double body configurations.

Thus the present research investigates two numerical methods to compute the flow past axisymmetric and three-dimensional bodies throughout the subsonic and transonic flight regime.

CHAPTER 2

## INTRODUCTION TO SINGULARITY METHODS

## 2.1 Flow Assumptions

As the flow around bodies under consideration becomes more complex, certain simplifications need to be introduced so that the resulting flow equations can be theoretically analysed. One major assumption commonly used is that the flow equations can be linearised, this enables the flow about a body to be transformed into a simpler problem. For example, due to the linearity of Laplace's equation, the flow problem for incidence may be decomposed into the superposition of the axial and normal (or lateral) flow solutions. If a flow is considered in which it is assumed that there is no separation, then viscosity can be neglected. Further, if it is assumed that there is no vorticity, the complete model can be approximated by the potential function, and thereby described by Laplace's equation (continuity) and Bernoulli's equation (velocity-pressure relation). See Goldstein Ref.3. Such a model may be used to determine the aerodynamic behaviour of a body at low incidence. To take into account the effects of the boundary layer, a displacement thickness model may be used, determined from the initial flow calculation. The calculation is then repeated for the modified body, consisting of the original shape plus the boundary layer, see Myring and Thompson, Refs.4 and 5.

For streamlined shapes at zero incidence, viscous effects,

other than skin friction will only be significant near the trailing edge, where the boundary layer is relatively thick. For all regions except near the tail, the boundary layer will be relatively thin, and so the potential flow solution outside this layer will closely model the real flow. When such a body is placed at moderately high incidence, flow separation will occur and the simple potential flow model will no longer be accurate, thereby limiting the theory to angles of attack where it is known that the results will have good accuracy.

It must be noted that unlike aerofoils, which produce circulation and lift, there is no Kutta condition to be satisfied at the trailing edge for bodies. Thus potential flow around a streamlined body predicts zero lift but not a zero moment. However, this is not a serious problem, since in practice most bodies are blunt at the base, either by design or, due to boundary layer thickening and separating. To allow for these effects, a wake closure is added to the body, to simulate the surface streamline continuity away from the body into the wake. This is usually done by making the aft body 'closure' similar in shape to the body nose. Although recently, Chow (Ref.6) has attempted to model a closure shape based on the knowledge of the pressure distribution on the body surface.

Due to the inaccurate modelling of the flow about the body base, the calculations are usually terminated after 75% of the chord or less.

## 2.2 Historical Perspective

### 2.2.1 Axial Singularity Methods

Through the years several potential methods have been developed to predict the aerodynamic forces on bodies in a flow field. Analytic solutions have been obtained for ellipsoids, Lamb (Ref.7), and Kaplan (Ref.8), giving exact results for both the longitudinal and lateral flows. Although these methods have been computed by Smith (Ref.9) and James (Ref.10), the amount of computational effort required is considerable. To enable complex configurations and different body shapes to be analysed, numerical techniques must be considered.

The first numerical method was developed by Rankine (Ref.11), this used the linearity of Laplace's equation to generate axisymmetric body shapes in uniform, inviscid and incompressible flow. A parallel uniform stream was superimposed onto an axial distribution of discrete real sources of zero total strength. The strengths of the source and sink at the nose and tail are such that, stagnation points are established and the stagnation streamlines generate a closed axisymmetric body. In 1911 Fuhrmann (Ref.12) extended this method to generate both sharp and blunt bodies by using a continuous distribution of sources along the axis. The afore-mentioned methods are simple to compute but are 'indirect' in that the body shape is calculated for a given distribution of sources. Acknowledging the simplicity of the method, Von Karman (Ref.13) applied it to the 'direct' problem

of determining the distribution of sources required to generate the flow over a prescribed body. The solution of the problem involves a Fredholm integral equation of the first kind, which can be solved approximately by reducing it to a set of linear simultaneous equations. The lateral flow has also been modelled by Von Karman using doublet distributions.

The axial singularity methods have been extended for use in interference problems such as store-store interaction, see Refs.14, 15 and 16. Adams and Sears (Ref.17) used a Fourier series to develop the cross-flow potential and included displacement effects, thereby generating bodies with non-circular cross-sections. The axial singularity methods are applicable to axisymmetric bodies and are not necessarily restricted to flows which are uniform in the cross-flow plane. The main disadvantages of these methods are that they are unable to model shapes which have discontinuities in their curvature and cannot generate more complex three-dimensional shapes. Much more general methods are the so called 'panel' methods where the body surface is approximated by panels of singularities.

### 2.2.2 Panel Methods

Green's theorem shows that any solution of Laplace's equation can be expressed as the integral of the potential induced by source and doublet singularities distributed on the surface of the body. The singularity strengths are determined by the boundary conditions, such as the free-stream conditions

at infinity, and the flow being tangential to the body surface. In 1932 Lamb (Ref.7) showed that any continuous acyclic, irrotational flow of an incompressible fluid could be regarded as being due to a distribution of simple sources over the flow boundary. Lotz, Weinstein and Van Tuyl (Refs.18, 19, and 20) developed methods employing sources or doublets distributed uniformly around a ring or over a disc having a radius equal to the body radius, and set normal to the stream direction. In this manner, any discontinuities in the body curvature are automatically dealt with. Such methods generate flows about very bluff axisymmetric bodies in subsonic flow, but involve the solution of complete elliptic integrals. Vandrey used a source-ring method (Ref.21) and obtained results for bluff nosed bodies. For more bluff shapes the vortex-ring method (Refs.22, 23 and 24) can be used. Such methods are invaluable for predicting the flow around bodies of revolution, but for three-dimensional shapes the surface panel method is used.

### 2.3 Present Study

Modern computing power has enabled Lamb's idea to be developed into the now classic methods detailed by Hess and Smith (Ref.1), for solving the incompressible flow around two-dimensional, axisymmetric and three-dimensional bodies. The integral equation for the potential at any point is discretised by approximating the body surface by a large number of flat quadrilateral panels. On the surface of each panel is placed a source distribution of constant strength. Curved panels can also be used, see Johnson (Ref.25). The velocity

induced at some control point by the source distribution on each panel is calculated, giving rise to a total perturbation velocity at that control point. By applying the boundary condition that there must be no flow normal to the body surface, leads to a set of linear equations for the source distribution on each panel. Velocities are then calculated at the control points knowing the constant source distributions and so the pressures obtained.

For fully three-dimensional bodies, a large number of panels is required to sufficiently approximate the body shape. For bodies of revolution, the panels that are used need not be surface quadrilaterals, but a set of cone frusta. These are then assumed to have source-ring distributions placed on their surface and their associated strengths calculated as above.

It was the aim of the initial research to develop the method proposed by Hess and Smith to deal with bluff and pointed bodies at incidence in uniform and curvilinear flow, with the hope of obtaining computationally more efficient procedures capable of giving accurate pressure distributions.

Source-rings are placed on the surface of the body (Fig.1), since arbitrary bodies with discontinuous profiles are to be considered, the distribution of the source-rings itself must be discontinuous. To simplify the analysis, the body is approximated by straight line segments (see later) upon which a constant distribution of source-rings is placed.



The formulations for axisymmetric bodies are described in sections 4.2 and 4.3 of Ref.1, wherein the velocity potential and velocity components are expressed in terms of complete elliptic integrals  $K(k)$  and  $E(k)$ , of the first and second kind respectively, with the argument  $k$ , being a geometric parameter. The subsequent longitudinal integration is performed numerically using the 'three eights' rule, with a special procedure for calculating the effect of a source at it's own control point. Although the expressions associated with the source-ring are exact, it was found to be simpler to perform both longitudinal and circumferential integrations by numerical means. Further by taking the symmetries of the flow over a body of revolution into account when defining the surface source distribution, two types of source-ring alone are required. These can be combined to give both the flows due to rectilinear motion and curved flight for an axisymmetric body. The results of this method are compared for accuracy and efficiency with numerical programs SPARV (Ref.26), Albone (Ref.23) and Jones (Ref.27), and experimental results (Ref.28).

CHAPTER 3

## METHOD OF SOLUTION

## 3.1 Definition of Potential Flow

Neglecting viscosity and assuming that density is constant, the Navier-Stokes equations generate the momentum equation,

$$\frac{\partial \underline{V}}{\partial t} + (\underline{V} \cdot \nabla) \underline{V} = -\frac{1}{\rho} \nabla P \quad 3.1.1$$

and the continuity equation becomes

$$\nabla(\underline{V}) = 0 \quad 3.1.2$$

Eqns.(3.1.1) and (3.1.2) hold for either exterior flow as around a body or interior flow as in the case of pipes. If there exists a region of fluid, then a body immersed in this fluid will experience pressure forces when put in motion. To solve the above equations, certain boundary conditions need to be supplied and these generally are that the normal velocity at a body surface is zero,

$$\underline{V} \cdot \underline{n} \Big|_{\text{Body Surface}} = 0 \quad 3.1.3$$

Where  $F$  denotes the presence of other prescribed normal velocities at the body boundary. Also that free-stream conditions exist at infinity. The velocity field existing on the surface of the body is the sum of two components

$$\underline{V} = \underline{V}_{\infty} + \underline{v} \quad 3.1.4$$

The velocity vector  $\underline{V}_{\infty}$  is the free-stream velocity and  $\underline{v}$  is the disturbance of the free-stream due to the presence of the body. If it is assumed that the flow is irrotational then  $\underline{v}$  may be expressed as the gradient of the perturbation potential function  $\phi$ ,

$$\underline{v} = \underline{\nabla} \cdot \phi \quad 3.1.5$$

Since  $\underline{V}_{\infty}$  satisfies the equation of continuity then  $\underline{v}$  must also,

$$\underline{\nabla} \cdot (\underline{v}) = 0 \quad 3.1.6$$

Combining Eqns.(3.1.5) and (3.1.6) generates Laplace's equation

$$\nabla^2 \phi = 0 \quad 3.1.7$$

The boundary conditions mentioned can now be written in terms of the potential function as

$$\nabla \phi \cdot \underline{n} \Big|_s = \frac{\partial \phi}{\partial n} \Big|_s = \underline{V}_\infty \cdot \underline{n} \Big|_s - F \quad 3.1.8$$

and the condition at infinity is

$$|\nabla \phi| \rightarrow 0 \quad 3.1.9$$

By specifying the conditions that exist at the body surface and at infinity, Eqn.(3.1.7) has an exact solution. Since there are no time-dependant terms in the equation the velocities on the body surface are those that would exist instantaneously as though the flow was well established and steady.

### 3.1.2 Boundary Conditions and Pressure Calculations

It is normally assumed, in rectilinear motion, that the flow over a moving body can be calculated by assuming the body to be stationary and moving the fluid. However, in curvilinear motion the flow must have a cross-flow static pressure gradient to sustain the motion. Vandrey (Ref.21) tackles the problem by putting the fluid at rest at infinity

and then moving the body itself. At any point the surface velocity is  $V_{abs}$  and the velocity due to the presence of singularities is  $V_0$ , giving a relative velocity

$$\underline{V}_{rel} = \underline{V}_0 - \underline{V}_{abs} \quad 3.1.10$$

To satisfy the condition that there is no net flow through the body surface, i.e. the transpiration velocity is zero, then the normal components of the free-stream and the singularity velocities normal to the surface must be equal. Vandrey calculates the pressure coefficient by considering the full steady Bernouilli equation, as

$$C_p = \frac{P_s - P_\infty}{\frac{1}{2} \rho |\underline{V}_\infty|^2} = \frac{1}{|\underline{V}_\infty|^2} (V_{abs}^2 - V_{rel}^2) \quad 3.1.11$$

If we assume uniform rectilinear flow then Eqn.(3.1.11) degenerates into the classic form of Bernouilli's equation

$$C_p = 1 - \frac{|\underline{V}_{rel}|^2}{|\underline{V}_\infty|^2} \quad 3.1.12$$

However, for curved flight the equation for the pressure coefficient is

$$C_p = \frac{1}{\Omega^2 |R|^2} \cdot (\Omega^2 R_s^2 - |V_0 - \Omega R_s|^2) \quad 3.1.13$$

where  $\Omega$  is the angular velocity,  $R_s$  the radius of rotation of a surface point, and  $R$  the radius of rotation of the reference position. The normal load at any point along the axis of the body can be found by integrating the pressure distribution around the circumference.

The method is applicable to ensembles of bodies moving relative to each other by specifying separate boundary conditions, but is restricted to the direct problem where the body surface is defined. The inverse problem of calculating a body shape by defining the pressure distribution is more difficult.

### 3.2 Reduction of the Problem to an Integral Equation for the Source Density Distribution on the Body Surface

#### 3.2.1 General

The basis of the method is to discretise a continuous source distribution on some body by approximating the body using surface panels. An unknown source distribution is placed on surface of each panel. The normal velocities induced at the control points of the panels are calculated and by applying a boundary condition that there is no component of velocity normal to the surface, the actual source distributions for the panels are determined. These can be used to calculate the tangential velocities at the control points and these in turn

used to determine the pressure.

### 3.2.2 Setting up the linear equations

For any body moving in some fluid the problem can be defined by Eqs.(3.1.7), (3.1.8) and (3.1.9). Consider, a unit point source located at a point  $q$  whose Cartesian coordinates are  $X_q, Y_q, Z_q$ , and a field point  $P$  located at  $X, Y, Z$ , see Fig.2, then the potential at  $P$  due to the source at  $q$  is

$$\phi_P = \frac{1}{r(p, q)}$$

3.2.2.1

$$r(p, q) = \left[ (x-x_q)^2 + (y-y_q)^2 + (z-z_q)^2 \right]^{1/2}$$

Such a point source satisfies Eqn.(3.1.7) and Eqn.(3.1.9) at all points except at  $q$  where the source is located. If a distribution,  $\sigma(q)$ , of such point sources is placed over a surface area  $dS$ , see Fig.3, then the potential at field point  $P$ , due to the distribution on the whole surface  $S$ , is

$$\phi_P = \iint_S \frac{\sigma(q)}{r(p, q)} dS$$

3.2.2.2

As shown in Fig.3.

The general form of  $\sigma(q)$  is arbitrary satisfying two of the three equations for the direct problem of potential flow. It must also satisfy Eqn.(3.1.8), which gives a boundary condition

for the body surface. If the point under consideration lies on the body surface  $S$ , then the integration of Eqn.(3.2.2.2) for a continuous source density distribution on  $S$  will cause the integrand to become singular. This is because the distance between  $q$  and  $P$  is zero, causing the integration to become infinite. Though by careful analysis, see Kellogg (Ref.29), it can be shown that the normal velocity induced at a point  $P$ , lying on the surface, is determined from the limiting process of approaching the surface,

$$2\pi\sigma(P) \qquad 3.2.2.3$$

Where  $\sigma(P)$  is the value of the source density distribution at  $P$ . The total normal perturbation velocity at  $P$ , together with the free-stream contribution must be equal to the prescribed normal velocity  $F$ . The integral equation for the source density  $\sigma(P)$  becomes

$$2\pi\sigma(P) - \oint_S \frac{\partial}{\partial n} \left[ \frac{1}{r(p,q)} \right] \sigma(q) \cdot dS = -\Omega(P) \cdot V_\infty + F \qquad 3.2.2.4$$

The integrand is called the 'kernel' of the equation. Eqn.(3.2.2.4) satisfies the third condition as given by Eqn.(3.1.8) and is solely dependant on the geometry of the problem since the differentiation is carried out with respect to the outward normal vector.



### 3.3 Defining the Body Shape

The body under consideration is prescribed by defining the coordinates for a set of points lying on the surface. The panels on which the unknown source distribution is to be placed are formed by joining the input points by straight-line segments, Fig.4. The surface elements formed by joining the points with straight-line segments must be of a small dimension to accurately approximate the given body shape. This reduces the problem of determining the continuous source density function  $\sigma(q)$  to that of determining a finite number of values  $\sigma_i$ , for each surface element,  $i$ . To achieve satisfactory results, the set of points must form a closed shape, implying that the first and last points must lie on the x-axis, corresponding to the nose and the tail. For axisymmetric bodies the profile curve is input with the x-axis as the line of symmetry, so that only the half plane above the axis need be defined by the coordinates. The circular panel formed by the straight-line segments is a frustum of a cone, Fig.5. A control point is chosen at which the normal velocity boundary condition is to be satisfied, and is, for simplicity, the point lying midway between two body points. Hence the number of control points is one less than the number of points defining the body shape.

It should be noted that the surface elements defining the body geometry are simply devices for effecting the numerical solution of the integral equation. The velocities obtained at these points are not the actual velocities that exist at the

x-coordinate of the input body. For a particular element the normal velocity will only be zero at the control point and non-zero at all other points on the element; that is the element 'leaks'. The computed flow has significance only at the control points themselves and at points off the body surface.

The accuracy of the method is dependant on the efficient distribution of the surface panels. Elements should be concentrated in regions on the body where the flow is expected to vary rapidly, for example, near body discontinuities or where body curvature is high, near leading and trailing edges. In regions where the flow is varying smoothly less points are required, but most importantly, a small element must not be placed next to a large one. This has the effect of causing the accuracy of the small element to be that associated with the large element, due to the interaction of leakage affects. The size of the panels must vary smoothly over the body to obtain continuous velocity distributions.

The unknown source density function on the body surface is taken to be a function of source-rings placed over the body. This is a natural choice for axisymmetric bodies, since the cross section itself is circular, and also the mathematics is greatly simplified. The source strength distribution associated with each surface element is assumed to be constant. The source-ring that is appropriate for use with axisymmetric flows gives rise to a potential and a velocity at a control point that can either be expressed in terms of complete

elliptic integrals or, obtained by numerically integrating around the source-ring. The second integration along the element length must be done numerically for each method.

### 3.4 Matrices of Influence coefficients

Having approximated the body surface with surface elements, these are then assumed to have associated source distributions  $\sigma_i$ , where  $i$  denotes the element number. If there are  $N$  elements, let us consider the second element. The normal velocity induced at the control point of the second element is the summation of the effects of all source distributions on elements 1,3...N, together with effect of second element at it's own control point. Using Eqn.(3.2.2.4) this can be written as

$$2\pi\sigma_2 - \iint_{S_1} \frac{\partial}{\partial n_1} \left[ \frac{1}{r_{(1,2)}} \right] \sigma_1 \cdot dS_1 - \iint_{S_3} \frac{\partial}{\partial n_3} \left[ \frac{1}{r_{(3,2)}} \right] \sigma_3 \cdot dS_3 - \dots$$

3.4.1

$$\dots - \iint_{S_N} \frac{\partial}{\partial n_N} \left[ \frac{1}{r_{(N,2)}} \right] \sigma_N \cdot dS_N = -\underline{n}_2 \cdot \underline{V}_\infty + F_2$$

Each of the terms involving double integrals represents the effect of that particular surface element upon the control point of the second element. The terms on the right side of Eqn.(3.4.1), are the contributions of the free-stream component normal to the body surface,  $-\underline{n}_2 \cdot \underline{V}_\infty$ , and any other prescribed normal velocities that maybe present,  $F_2$ .

To solve for the source density distribution associated with each element, equations similar to Eqn.(3.4.1) can be written in matrix form

$$\begin{aligned}
 E_{\text{fect}(1,1)} - E_{\text{fect}(1,2)} - \dots - E_{\text{fect}(1,N)} &= -\underline{\eta}_1 \cdot \underline{V}_\infty + F_1 \\
 E_{\text{fect}(2,1)} - E_{\text{fect}(2,2)} - \dots - E_{\text{fect}(2,N)} &= -\underline{\eta}_2 \cdot \underline{V}_\infty + F_2 \\
 \vdots & \\
 E_{\text{fect}(N,1)} - E_{\text{fect}(N,2)} - \dots - E_{\text{fect}(N,N)} &= -\underline{\eta}_N \cdot \underline{V}_\infty + F_N
 \end{aligned}
 \tag{3.4.2}$$

or

$$\sum_{j=1}^N A_{ij} \cdot \sigma_j = -\underline{\eta}_i \cdot \underline{V}_\infty + F_i
 \tag{3.4.3}$$

$i = 1, 2, \dots, N$

Eqn.(3.4.3) satisfies the normal flow boundary condition and the matrix  $A_{ij}$  is called the matrix of influence coefficients for the normal velocity. Diagonal terms of the form  $A_{ii}$  are usually of greater magnitude than off-diagonal terms since they represent the integration of the source distribution on element  $i$  for the velocity induced at control point  $i$ . Eqn.(3.4.2) is a set of linear algebraic equations for the values of the source density on the surface panels and the desired approximation to the integral Eqn.(3.2.2.4). To obtain the entries for the terms  $A_{ij}$ , the source strengths  $\sigma_j$  are set to be of unit value. This is because the elements of  $A_{ij}$  are only dependant on the body geometry, and are independant of the source distribution and onset flow conditions. Matrix

inversion techniques can be applied to Eqn.(3.4.3) to determine the true values of the source distributions,  $\sigma_j$ . To obtain the actual normal velocities, the entries of  $A_{ij}$  are multiplied by the proper values of the source density  $\sigma_j$ , as determined by the inversion. The velocity at any control point is made up of a normal component and a tangential component. The velocity vector,  $\underline{v}_{ij}$ , due to the source distributions for any panel can be decomposed into these two components,

$$\underline{v}_i = \underline{v}_{ni} + \underline{v}_{ti}$$

$$\underline{v}_{ni} = \sum_{j=1}^N A_{ij} \cdot \sigma_j$$

$$\underline{v}_{ti} = \sum_{j=1}^N B_{ij} \cdot \sigma_j$$

3.4.4

$$i = 1, 2, \dots, N$$

assuming  $\sigma_j$  are the actual source distributions on each panel. The matrix  $A_{ij}$  has already been defined, matrix  $B_{ij}$  is similar to  $A_{ij}$  but represents the influence coefficients for the tangential velocities.

### 3.5 Influence Matrix for the Cross Flow

A body immersed in a uniform stream at incidence can, within the assumptions of linear theory, be considered to experience the combination of axial flow together with a cross flow component in a direction perpendicular to the x-axis. For the case of axial flow, influence matrices  $A_{ij}$  and  $B_{ij}$  can be formed. It is reasonable to assume that for the cross flow

there must also be such matrices. For an axi-symmetric body in an onset flow parallel to the x-axis, the flow along the surface of any meridian plane at any angle  $\Theta$  will be the same as in any other meridian plane. Thereby, the source strength at the surface will not vary with circumferential angle for any x-station. For uniform cross flow, consider a body surface source-ring formed in the y-z-plane, subject to a cross-flow  $V_\infty$ . The total velocity due to the cross flow must be killed at  $\Theta=180$  degrees, pulled in at  $\Theta=0$  degrees, and the normal velocity must be unaffected at  $\Theta=90$  and 270 degrees. To achieve this the source-ring density distribution must be proportional to the cosine of the circumferential angle, see Ref.1. The source density distribution can be written as

$$\sigma(\Theta) = \cos(\Theta) \quad 3.5.1$$

$\Theta$  is measured positive as shown in (Fig.9). Similar expressions can be arranged for this case as in the axisymmetric flow problem to obtain the tangential and normal velocity components. For the cross flow, there also exists a circumferential velocity component which does not contribute to the normal velocity calculation. The matrix  $\Theta_{ij}$  can be formed, corresponding to the circumferential velocity component at a point obtained by circumferentially rotating a control point onto the x-z-plane. For pure cross flow, a total of three influence matrices exist, one for the normal velocity, one for the tangential velocity, and one for the

circumferential velocity.

The combination of the tangential velocity components for both the axial and cross flow cases enables the surface pressure coefficients at the control points to be calculated.

### 3.6 Computation of the Pressure Coefficient

Eqn.(3.4.3) allows the determination of the actual source density distribution for each surface element. The entries of matrix  $B_{ij}$  are the tangential velocities induced by the elements at other control points. To obtain the actual tangential velocities these entries must be multiplied by the source densities  $\sigma_j$  as obtained from

$$\sigma_j = [A_{ij}]^{-1} \cdot [-\eta_j \cdot V_\infty + F_j] \quad 3.6.1$$

$$j = 1, 2, \dots, N$$

$$i = 1, 2, \dots, N$$

The tangential velocities are then determined by

$$T_i = \sum_{j=1}^N B_{ij} \cdot \sigma_j + \xi_i \cdot V_\infty \quad 3.6.2$$

$$i = 1, 2, \dots, N$$

$T_i$  is the total velocity in a direction tangential to the profile curve and is measured positive in the increasing x-direction. Similarly for the uniform cross flow case the tangential velocity is

$$T_{2i} = \sum_{j=1}^N B_{2ij} \sigma_{2ij} + \underline{t}_i \cdot \underline{V}_{\infty} \quad 3.6.3$$

$i=1, 2, \dots, N$

The subscript 2 for Eqn.(3.6.3) denotes the equivalence in the method used to determine the required quantities for both axial and cross flow. Assuming that the source density varies as the cosine of the circumferential angle, the tangential velocity at any circumferential location  $\theta$ , is  $T_{2i} \cdot \cos(\theta)$ . The circumferential component of velocity at a control point for the cross flow case, is obtained by circumferentially rotating a control point 90 degrees into the x-z-plane,

$$T_{3i} = \sum_{j=1}^N \theta_{ij} \cdot \sigma_j + \underline{j}_i \cdot \underline{V}'_{\infty} \quad 3.6.4$$

$i=1, 2, \dots, N$

where  $\underline{j}_i$  is the unit vector parallel to the y-axis and  $\underline{V}'_{\infty}$  is the onset-flow velocity evaluated at the rotated location of the control point. Circumferential velocity components at other values of  $\theta$  are  $T_{3i} \cdot \sin(\theta)$ . For the flow due to a uniform stream at incidence  $\alpha$  to the x-axis, the velocity component tangential to a meridian curve at a circumferential angle  $\theta$  is

$$T_i \cos(\alpha) + T_{2i} \sin(\alpha) \cdot \cos(\theta) \quad 3.6.5$$

and the circumferential velocity component is



$$T_{3i} \sin(\alpha) \cdot \sin(\theta)$$

3.6.6

If the onset flow is assumed to have a unit magnitude, the surface pressure coefficient is

$$C_{pi} = 1 - \left[ T_{1i} \cos(\alpha) + T_{2i} \sin(\alpha) \cdot \cos(\theta) \right]^2$$

3.6.7

$$- \left[ T_{3i} \sin(\alpha) \cdot \sin(\theta) \right]^2$$

These formulae give velocity and pressure at any  $\alpha$  and  $\theta$  in terms of the basic flow solutions. The quantity  $dC_N/dx$  is determined by integrating the pressure distribution around the body at a particular  $x$ -station, and  $dC_M/dx$  by taking the moment of  $dC_N/dx$  about the nose.

CHAPTER 4

INTEGRATING THE KERNEL TO OBTAIN THE VELOCITIES  
AT A CONTROL POINT

#### 4.1 Velocity due to Axial Flow

Source-rings are placed on the surface of each element, Fig.4, and the total velocity induced at a control point is the integration of the ring source distribution over the line-segment elements that approximate the profile curve of the body. Consider a unit source-ring located at  $x=b$  and of radius  $a$ , see Fig.6, then the potential at a control point P due to small element of length  $d\psi$ , is given by

$$\phi = \int_{-\pi}^{\pi} \frac{a}{r} \cdot d\psi \quad 4.1.1$$

The control point lies in the  $x$ - $y$ -plane on the meridian surface, the distance  $r$  can be replaced by

$$r = \left[ (x-b)^2 + y^2 + a^2 - 2ay \cos(\psi) \right]^{1/2} \quad 4.1.2$$

where  $\psi$  is the circumferential angle around the source-ring measured from the positive  $y$ -axis. On differentiating the potential with respect to  $x$  and  $y$ , the corresponding velocity

components are

$$V_x = - \frac{\partial \phi}{\partial x} = 2a \int_0^{\pi} \frac{(x-b)}{r} d\psi$$

4.1.3

$$V_y = - \frac{\partial \phi}{\partial y} = 2a \int_0^{\pi} \frac{(y-a \cos(\psi))}{r} d\psi$$

Elliptic integrals can be used to integrate the above expressions in the circumferential direction or, as in present method, the integration can be carried out numerically using the 'three-eighths' rule. The source-ring is subdivided into  $N_c$  points and the integrand determined at each of these points. The total velocity induced by a source-ring is the sum of the integrated values of Eqn.(4.1.3)

$$V_c = \frac{3h}{8} \left[ \int(\cdot) \Big|_1 + 3 \int(\cdot) \Big|_2 + \dots \int(\cdot) \Big|_{N_c} \right]$$

4.1.4

$$\int(\cdot) \Big|_x = 2a \int_0^{\pi} \frac{(x-b)}{r} d\psi, \quad \int(\cdot) \Big|_y = 2a \int_0^{\pi} \frac{[y-a \cos(\psi)]}{r} d\psi$$

where  $h$  is  $\pi/(N_c-1)$ . The second integral involves integrating the source-ring distribution along the length of the line-segment element, from  $x_1, y_1$  to  $x_2, y_2$ , Fig.7. The length is divided into  $N_A$  points, and at each of these points the source-ring is integrated circumferentially. Hence, the total velocity at a control point is the sum of the numerical integration in the circumferential direction at each of the points along the surface element,  $1, 2, \dots, N_A$ , using the

'three-eighths' rule. The resulting expression for the total velocity in the x-direction say, is

$$V_{\text{total}} = \frac{3 \cdot h_t}{8} \left[ V_{c_1} + 3V_{c_2} + \dots + V_{c_{N_L}} \right] \quad 4.1.5$$

where  $h_t = \Delta S / (N_L - 1)$  and  $\Delta S$  is the element length. For each new  $V_{c_i}$  the radius and location of the source-ring is determined using

$$\begin{aligned} a &= y_1 + S \cdot \sin(\beta) \\ b &= x_1 + S \cdot \cos(\beta) \end{aligned} \quad 4.1.6$$

where  $\beta$  is the slope of the line-segment element,  $x_1, y_1$  are the coordinates of the beginning of the element, and  $S$  denotes distance along the element length. The number of points,  $N_L$ , placed upon the line-segment is determined by the minimum of the two distances, see Fig.7,

$$R_{\text{MIN}} = \text{MIN} \left[ (x_1, y_1 - x, y), (x_2, y_2 - x, y) \right] \quad 4.1.7$$

$$N_L = 16 \cdot \Delta S / R_{\text{MIN}}$$

Thus the further the point in question is from the element, the fewer sub-elements are required in the calculation. The minimum number is three.

#### 4.2 The Effect of an Element at it's own Control Point

To calculate the terms  $A_{ii}$  for the coefficient matrix, a refined procedure is adopted because Eqn.(4.1.3) is singular when  $x=b$ , and  $y=a$ . On integrating along the line-segment  $\bar{c}$ , to obtain the velocity at the control point  $P_i$ , the following method is used. See Hess and Smith (Ref.1, Section.4.2). The element is subdivided into three regions, Fig.8. The outer ends are treated as normal elements using the procedure outlined in Section.4.1, but the central section of length  $2d$ , has a series expression for the velocity components derived from the elliptic integration of Eqn.(4.1.3),

$$V_x' = -\sin 2\beta \left( \frac{d}{y_0} \right) \left\{ 1 + \frac{1}{144} \left( \frac{d}{y_0} \right)^2 \left[ 13 + 6 \sin^2 \beta + 6 \ln \left( \frac{d}{8y_0} \right) \right] + \dots \right\}$$

$$V_y' = -2 \left( \frac{d}{y_0} \right) \left\{ \sin^2 \beta + \ln \left( \frac{d}{8y_0} \right) - \frac{1}{48} \left( \frac{d}{y_0} \right)^2 \left[ 3 \cos^2 \beta - 2 \sin^4 \beta + 3 \ln \left( \frac{d}{8y_0} \right) \right] + \dots \right\} \quad 4.2.1$$

The value of  $d$  is determined by the length of the panel  $\Delta S$ , and the distance,  $y_0$ , of the control point from the x-axis,

$$d = 0.08 y_0 \quad \text{if} \quad 0.08 y_0 < \Delta S / 2$$

$$d = \Delta S / 2 \quad \text{if} \quad 0.08 y_0 > \Delta S / 2 \quad 4.2.2$$

Such a formulation allows  $d$  to be as small as possible to reduce the truncation errors in the series, and as large as

possible to reduce errors arising from the use of the numerical integration near a singularity. Finally, the limiting effect of approaching the singularity control point, as deduced by Kellogg (Ref.29), induces a velocity normal to the element of magnitude  $2\pi$ . The components are

$$V_x'' = -2\pi \cdot \sin(\beta)$$

4.2.3

$$V_y'' = +2\pi \cdot \cos(\beta)$$

The total velocity at a control point  $P_i$  is the sum of four contributions, the velocities given by Eqns.(4.1.3), (4.2.1), (4.2.3) and the contribution from the ends of the element on which the point under consideration lies.

#### 4.3 Velocities due to Cross Flow

A source-density distribution that varies as the cosine of the circumferential angle produces a potential with a similar variation. Consider a source-ring (Fig.9) with strength  $\cos(\psi)$ , by introducing cylindrical coordinates  $R$  and  $\theta$ , the potential at point  $P$  can be written,

$$\phi = 2a \int_0^{\pi} \frac{\cos(\psi)}{r} d\psi$$

4.3.1

$$r = \left[ (x-b)^2 + R^2 + a^2 - 2aR \cos(\theta - \psi) \right]^{1/2}$$

and by a change of variable this becomes

$$\phi = 2a \cdot \cos(\theta) \int_0^{\pi} \frac{\cos(\psi)}{r} d\psi, \text{ and}$$

4.3.2  
(cont)

$$r = \left[ (x-b)^2 + R^2 + a^2 - 2aR \cos(\psi) \right]^{1/2} \quad 4.3.2 \text{ (cont)}$$

The axial, radial and circumferential velocity components at the point  $(x, R, \Theta)$  due to the source-ring are

$$V_x = 2a \cdot \cos(\Theta) \int_0^\pi \left[ (x-b) \cdot \cos(\psi) / r^3 \right] \cdot d\psi$$

$$V_y = 2a \cdot \cos(\Theta) \int_0^\pi \left[ (R - a \cdot \cos(\psi)) \cdot \cos(\psi) / r^3 \right] \cdot d\psi \quad 4.3.3$$

$$V_\theta = \frac{2a}{R} \cdot \sin(\Theta) \int_0^\pi \left[ \cos(\psi) / r \right] \cdot d\psi$$

The terms in the integrand are independent of  $\Theta$ . By replacing  $R$  by  $y$ , which becomes in a sense a radial direction, the factors  $\cos(\Theta)$  and  $\sin(\Theta)$  are ignored, but are used when considering the flow at a particular circumferential location. The velocity components become

$$V_x = 2a \cdot \int_0^\pi \left[ (x-b) \cdot \cos(\psi) / r^3 \right] \cdot d\psi$$

$$V_y = 2a \int_0^\pi \left[ (y - a \cdot \cos(\psi)) \cdot \cos(\psi) / r^3 \right] \cdot d\psi \quad 4.3.4$$

$$V_\theta = \frac{2a}{y} \int_0^\pi \left[ \cos(\psi) / r \right] \cdot d\psi$$

To obtain the velocity for an element at its own control point, similar expressions to Eqn.(4.2.1) and Eqn.(4.2.3) are derived and the series become

$$V_x' = -\sin 2\beta \cdot \left( \frac{d}{y_0} \right) \left\{ 1 - \frac{1}{48} \left( \frac{d}{y_0} \right)^2 \left[ 9 - 2 \sin^2 \beta + 6 \ln \left( \frac{d}{8y_0} \right) \right] + \dots \right\} \dots \quad 4.3.5 \text{ (cont)}$$

$$V_{y'} = -2 \left( \frac{d}{y_0} \right) \left\{ 2 + \sin^2 \beta + \ln \left( \frac{d}{8y_0} \right) + \frac{1}{144} \left( \frac{d}{y_0} \right)^2 \left[ 9 - 43 \sin^2 \beta + 6 \sin^4 \beta \right. \right. \\ \left. \left. + (27 - 24 \sin^2 \beta) \cdot \ln \left( \frac{d}{8y_0} \right) \right] + \dots \right\} \quad 4.3.5 \quad (\text{Cont})$$

$$V_{\theta'} = 4 \left( \frac{d}{y_0} \right) \left\{ \left[ 1 + \ln \left( \frac{d}{8y_0} \right) - \frac{1}{144} \left( \frac{d}{y_0} \right)^2 \left[ 10 \sin^2 \beta \right. \right. \right. \\ \left. \left. \left. + (6 \sin^2 \beta - 9) \cdot \ln \left( \frac{d}{8y_0} \right) \right] \right] + \dots \right\}$$

The matrices  $A_{ij}$  and  $B_{ij}$  for axial flow, and the matrices  $A_{ij}$ ,  $B_{ij}$  and  $i_j$ , for cross flow, can now be determined. The normal velocity condition is satisfied for both types of flow by assuming the oncoming free-stream to be uniform and of unit magnitude.

#### 4.4 Axisymmetric Bodies in Curvilinear Flow

Having presented the theory for a body at incidence, this section develops the theory to calculate the flow around an axisymmetric body moving in curved flight at incidence and yaw, see Fig.10.

From Ref.24, the body movement may be considered to be the superposition of the following elementary movements,

- a) Translation in  $x'$ -direction

$$V_{x'} = \underline{R} R \cdot \cos \alpha' \cdot \cos \beta'$$

- b) Translation in  $y'$ -direction

$$V_{y'} = -\underline{R} R \cdot \sin \alpha' \cdot \cos \beta'$$

4.4.1.

- c) Translation in  $z'$ -direction

$$V_{z'} = \underline{R} R \cdot \sin \beta'$$



d) Rotation about the  $x'$ -axis

$$\Omega_{x'} = \Omega \cdot \sin \alpha'$$

4.4.1 (Cont)

e) Rotation about the  $y'$ -axis

$$\Omega_{y'} = \Omega \cdot \cos \alpha'$$

Where  $\alpha'$  and  $\beta'$  are shown in Fig.10. For the present method it is assumed that the body is stationary and the fluid is in motion, thus if the flow is at incidence  $\alpha$  and yaw  $\beta$ , (Fig.1), the flow equations can be written as,

a) Fluid motion in x-direction

$$V_x = \Omega R \cdot \cos \alpha \cdot \cos \beta$$

b) Fluid motion in y-direction

$$V_y = \Omega R \cdot \sin \alpha$$

c) Fluid motion in z-direction

$$V_z = \Omega R \cdot \cos \alpha \cdot \sin \beta$$

d) Rotation about the z-axis

$$\Omega_z = \Omega$$

Motion in the x-direction is simply a longitudinal flow problem, whilst the components of the flow in the y- and z-directions can be treated as lateral flows. Hence the translations a), b), and c) are calculated using the previous analysis.

Using the principle that a body moving in a perfect fluid is analogous to a stationary body with the fluid moving around it,  $V_{\Omega_z}$  can be determined. Taking the origin of the coordinate system at the centre of gravity of the body (Fig.11), a control point P will experience a velocity

$$V = \Omega_z \sqrt{(r^2 + z^2)} \quad 4.4.3$$

This velocity is normal to the radial arm, OP. If the rotating arm is at an angle  $\theta$  to the body axis of symmetry, then the velocity components in the x- and y-directions are

$$V_x = V \cdot \sin \theta$$

$$V_y = V \cdot \cos \theta \quad 4.4.4$$

The Eqn.(4.4.4) is applicable only to the left side of the body origin, on the right side,

$$V_x = V \cdot \sin \theta$$

$$V_y = -V \cdot \cos \theta \quad 4.4.5$$

The rotation about the z-axis is equivalent to body experiencing pure cross flow of magnitude  $\Omega_z$ .

CHAPTER 5

## DISCUSSION AND RESULTS

## 5.1 General

The type of body which can be analysed by the present method must be closed and axisymmetric, such as ellipsoids and ogive cylinders. The present comparisons are made with experimental results (Ref.28) and numerical methods, SPARV (Ref.26), Albone (Ref.23), and Jones (Ref.27). The point distribution must be carefully chosen such that the regions which expect to generate the highest flow accelerations have the largest number of points. The following equation is used for all the cases to distribute points on the body nose, see Fig.12,

$$\alpha_i = R1 \cdot \sin^{-1}(h \cdot i) / \pi$$

5.1.1

$i = 1, 2, \dots$  no. of nose points

where  $h$  is a constant equal to  $1/n$ .  $R1$  is the length of the half body in the case of ellipsoids, and the nose length in the case of the nosed-cylinders. For ellipsoids the point distribution is symmetric about the mid-section. For the nosed-cylinders, the aft cylinder point distribution is chosen by intuition to achieve a gradual increase in panel length towards the trailing edge. To avoid a large panel being placed adjacent to a small panel, the first panel of the aft cylinder

is of the same length as the last panel on the nose. The closure for such bodies is usually similar to the nose shape or is an ellipsoid.

All the results are obtained either on the VAX 11/750 or the VAX 11/782 machines.

## 5.2 Axisymmetric Bodies With Varying Nose Shapes in Uniform Flow

For comparison the Integral Equation method developed by Albone (Ref.23) is used for the various bodies shown in Fig.13. The disadvantage of the Albone technique is that only zero incidence cases can be compared, and SPARV has to be used for non-zero incidence flow. For the bodies in Fig.13, 80 longitudinal panels with 18 circumferential integral points are used, and the total body length is 1. The results shown in Figs.14 to 16 are symmetric about the mid-section of the body because the closure is the same shape as the nose.

## 5.3 Prolate Ellipsoid at Incidence

The exact analytic method of Jones (Ref.27), can predict the flow around ellipsoids of various bluntness. A comparison with this method should show the accuracy of the present method for bodies with continuous slope and curvature at all incidences. The surface panel distribution for an ellipsoid of ratio 1:8 in uniform axial flow is determined by Eqn.(5.1.1), this clusters points around the leading edge and the maximum

thickness of the body. For such an extreme bluff case, the number of points required is large, of the order of 100, and requires more circumferential integration points, of the order of 30, to obtain accurate flow resolution. A slender ellipsoid of ratio 8:1 in uniform cross flow requires less points. The results obtained by the present method are compared with those obtained by Jones, Figs.17 to 18.

Due to the linearity of Laplace's equation, the solution for various flow problems can be combined, in particular, the flow around a body at incidence in uniform flow can be obtained by the superposition of the axial flow and cross flow solutions. The results for the two cases may be combined to obtain the loads experienced by the body at incidence. Fig.19 shows the results for a prolate ellipsoid of ratio 100:15 at an angle of 5 degrees, compared with those predicted by Jones.

#### 5.4 Effects of Panel Distribution

To obtain accurate results, panels must be clustered in regions where the body curvature changes rapidly, and where large flow changes are expected. As in the case of the ellipsoid cylinder (Fig.13), the panel density is increased at the leading edge and maximum thickness of the body. This alone is not sufficient to accurately predict the flow characteristics, since the error associated with placing a large panel adjacent to a small panel can produce inconsistencies in the results. Hence it is advisable to have a smooth variation of panel dimension along the whole length of

the body. Such a distribution is automatically produced by Eqn.(5.1.1). If the panel length is not varied smoothly the flow curve can be dramatically effected. This can be shown by changing the length of adjacent panels at a nose cylinder junction, Fig.20, for an cylinder having an elliptic shaped nose of fineness ratio 6:1.

To investigate this behaviour more closely the hemisphere cylinder of Fig.13, is used as test case. The large panel is the first panel after the nose-cylinder junction, and the smaller panel is the last panel on the nose section. There is a gradual increase in panel length over the aft cylinder. The large panel is successively reduced in length until the pressure coefficient curve becomes smooth. It was concluded that the large panel must be no greater than approximately six times the small panel length. This observation varies for the type of body being considered, since a smoother body, such as a tangent-ogive cylinder, induces a less erratic behaviour at the nose-cylinder junction. The effect of the error due to the abnormal lengths of the two panels is smeared over three to four panel lengths.

#### 5.5 Comparison with SPARV

SPARV is a widely used method which can be applied to 2-D bodies, 3-D bodies, multiple bodies with wing systems, such as complete aircraft. The intention is to compare program run times, in terms of C.P.U., for the present method against those for SPARV, to validate using the source-ring method when

considering axisymmetric bodies. A cylinder with an elliptic nose of ratio 6:1 at 5 degrees incidence is compared using the two methods, Fig.21.

The Source-Ring used 100 longitudinal panels and 30 integral points and SPARV used 80 longitudinally and 14 circumferentially. These were such that sufficient convergence in the results had been achieved. On average the Source-Ring method has a saving of almost 45% in C.P.U. time over SPARV, and a considerable reduction in storage requirement.

Although the present method is not as versatile as SPARV, in that it is unable to predict fully three-dimensional flow characteristics, it offers considerable advantages when determining the flow past axisymmetric bodies at incidence and yaw.

## 5.6 Comparison with Experiment

The method is compared for general accuracy against experimental results (Ref.28) using a tangent ogive cylinder, (Fig.13), at various incidences. The results, Figs.22 to 23, show that the method is accurate and agrees well with experimental observations. The results are not in exact agreement due to the development of a boundary layer and effects of separation in the real flow. The irregularities in the experimental results were due to local disturbances caused by surface discontinuities.

## 5.7 Prolate Ellipsoid in Curvilinear Flow

The original theory presented by Hess and Smith has been extended to axisymmetric bodies moving in curvilinear motion at incidence and yaw. The only case for comparison are the results obtained by Jones for ellipsoids. The method of superposition is used to treat curvilinear motion as the combination of flow problems (Section.4.4). The test case is an ellipsoid of ratio 4:1 at zero incidence and yaw, the theoretical results by Jones are in good agreement with the Source-Ring method, see Fig.24.

To obtain the flow past an axisymmetric body in uniform flow and curvilinear flow, at incidence and yaw, the problems can be treated separately. The solutions are then 'added'.

## 5.8 Effects of Varying Nose Bluffness

In this section an axisymmetric body with a tangent-ogive nose is used as a test case to observe the variation of normal loading at incidence as the nose length is progressively reduced.

Most bodies have a flat base, which if accurately modelled, would cause infinite flow accelerations around the corner where the body surface becomes discontinuous. To prevent instabilities occurring in the program, the wake from the base flow is modelled by adding a closure to the body being tested. Due to the results being valid only for the initial 75% of the



body length, a conical closure is used for simplicity. For the examples considered in the present work, all the bodies are very slender, with the length of the trailing cylinder being almost three times the length of the nose.

The ratios of body radius to nose length (the fineness ratio) used are  $5/30$ ,  $5/20$ ,  $5/10$ ,  $5/5$  and  $5/3$ , the nose shape varying from an ogive to an oblate ellipse. Each body is placed at an incidence of 5 degrees, using 100 axial panels and 18 circumferential integral points. The results are presented on Figs.25 to 28.

As the bluntness is increased, or the nose length decreased, the point along the body at which the peak in  $dC_n/dX$  occurs, moves progressively toward the nose, see Fig.25. Also, the region of the body which experiences load decreases with the trailing cylinder contributing little to the overall lift. It would appear that in the limit a flat cylinder, the nose length being zero, at incidence would produce a lift of infinite peak value acting over an very small region.

Because  $dC_m/dX$  varies directly with  $dC_n/dX$ , the results for this quantity along the body length should be similar to Fig.26, but of differing magnitude, as shown on Fig.25.

Fig.27, shows the variation of peak  $dC_m/dX$  and total  $C_m$ , about the nose point, with nose length. A flat cylinder, of infinite fineness ratio, would produce a finite moment which can be obtained by extrapolating the  $C_m/\text{Nose length}$  curve until it

intersects the vertical axis, point F. This implies that since the moment is non-zero, the flat cylinder is producing lift.

From the results of  $C_n$  and  $C_m$ , the centre of pressure, X.c.p. (about the nose,  $X=0$ ), can be calculated and its variation with nose length observed, Fig.28. If the nose length is zero, the X.c.p. position is still positive, verifying the above results, that there must be a moment acting at the nose due to the presence of lift produced by the aft cylinder, at incidence.

APPENDIX A

## DESCRIPTION OF THE SOURCE-RING PROGRAM

## A.1 Input of Flow Behaviour and Body Coordinates

The body is approximated by a set of x,y coordinates lying on the profile curve of the body. The set of points are input in the increasing x-direction. Points should be concentrated in regions where large flow fluctuations are expected and sparsely in regions where they are not. These regions must be linked by a gradual change in point concentration if an accurate solution is to be obtained. The body coordinates, the body length, the maximum thickness of the body, and the moment reference center are input. Finally the flow properties are entered by specifying magnitude of the oncoming stream, and if there is curvilinear flow, the radius of curvature. The angles of attack and yaw are input when the coefficient of pressure calculating routine is called.

## A.2 Calculation of the Element Characteristics

The four main element properties required for uniform axial and cross flow are, the coordinates of the control point, assumed to lie midway along the element length, the angle of the element relative to the horizontal axis, the total length of the element, and the value  $d$ , required in the series approximation as the integration along the element length nears the element control point. These are calculated after the body

has been approximated by a set of points which are joined by straight line segments.

For curvilinear flow, the angle of the radial arm, joining the moment reference center and each control point, with the horizontal axis is required, (Fig.11). These are used to determine the velocity at each element control point due to the body rotating about point O.

The vectors on the right side of the equations in Section.3.6 are required, these are usually components of the free-stream flow resolved into directions normal and tangential to the element. For curvilinear flow, the tangential velocity component is only due to the body rotation, there is no normal component. Hence the constant values of the element properties and the vectors required for the solution of the flow problem can be obtained.

### A.3 Velocity Induced by an Element at it's Control Point

As discussed earlier in Section.4, the velocity induced by a element at it's own control point comprises three terms, a series solution about the control point, integration over a sub-element and the value  $2\pi$  due to the limiting process of approaching the surface. The series is usually terminated after three terms. The integration over the sub-element is done by treating it as a separate element, inducing a velocity at the control point. There are two sub-element integrations, one for each 'end' of the element. The velocities due to each

term are summed and resolved into normal and tangential components, and stored in locations  $(i,i)$  of the coefficient matrices. There exist five such matrices, normal and tangential velocities for uniform axial flow, and normal, tangential, and circumferential velocities for uniform cross flow.

#### A.4 Velocity Induced at Other Control Points

The velocity induced at a control point due to a distribution of source rings on an element is calculated as described in Section.4. The element in question is split into a number of integration points which is a function of the distance between the control point and the nearest end of the element. The induced velocity involves a two phase integration, one circumferentially and the other longitudinally along the element length. The velocity induced by the  $j$ 'th element at a control point on the  $i$ 'th element is resolved into the normal and tangential components and stored in locations  $(i,j)$  of the coefficient matrices.

The coefficient matrices for each flow are now fully calculated and the remaining problem of determining the source strength distribution on each element becomes trivial.

#### A.5 Source Strength and Tangential Velocity Calculation

The source strengths required on each panel are obtained by inverting the coefficient matrices containing the normal

velocity components, Eqn.(3.6.1), and multiplying by the normal vectors due to the free-stream. The inversion is done for each of the three flows, uniform axial flow, uniform cross flow and curvilinear flow. The NAG routine F04FAF, (Ref.30) automatically performs the inversion and multiplication, and outputs the source strength values for each element in vector form. The total tangential velocities for each flow are calculated by multiplying the source strength vectors by the coefficient matrices containing the tangential velocity components, and adding the free-stream tangential values, Eqns.(3.6.2), (3.6.3) and (3.6.4).

#### A.6 Pressure and Load Calculations

The values for the angles of incidence and yaw, together with the meridian angle at which the pressure distribution is required are input. The pressure and load distributions are determined as described in Section.3. The process can be repeated for any combination of incidence, yaw and meridian plane angle. If only the meridian angle is altered, the load distribution remains unchanged

CHAPTER 6

## INTRODUCTION TO COMPUTATIONAL FLUID

## DYNAMICS

Transonic aerodynamics is the focus of strong interest at the present time because it is known to encompass one of the most efficient regimes of flight. Methods need to be developed to calculate such flows over two- and three-dimensional shapes thereby eliminating the need to rely on extensive, large scale wind-tunnel testing to produce rational designs.

The mathematical difficulties of the problem are associated with the analysis of the mixed hyperbolic and elliptic type of equations, and the presence of flow discontinuities. The computational method should be capable of predicting the location and strength of shock waves, and in three-dimensional application, should be efficient and economical in its use of the computer. In meeting these objectives the primary choices to be made concern first the most suitable formulation of the equations, second the construction of a favourable coordinate system and thirdly the development of a finite difference scheme which is stable, convergent and also capable of accommodating the proper discontinuities. Since we are concerned with the flow at fairly low supercritical mach numbers over efficient aerodynamic shapes, we may assume that the shock waves are quite weak. A strong shock wave would cause boundary layer separation and buffeting, invalidating the

analysis. The error in ignoring changes in entropy through shock waves, and the resulting vorticity should therefore be small, and we can expect to obtain a satisfactory approximation by using the transonic full potential equation for irrotational flow instead of the full Euler equations. In particular, for three-dimensional calculations, the replacement of five dependant variables (three velocity, pressure and energy), for the Euler equations, by a single velocity potential, in the full potential formulation, leads to important savings in machine time and memory.

In the present work the conservative form of the full potential will be used in favour of a non-conservative approach, thereby ensuring at least one property, namely mass, is always conserved, even in the presence of any shocks that occur. In the conservation form of the full potential equation the scheme is usually made stable in the presence of shocks, by the use of artificial viscosity, which is introduced as a damping term. The strength of the shock determines the amount of damping that must be introduced, but at very high Mach numbers the scheme will become unstable. This is due to separation and the assumption of constant entropy no longer being valid. Having approximated the full potential equation in finite difference form, it must be satisfied at a certain number of points. A grid or mesh is set up encompassing the flow-field and the body. The choice of the type of grid to be used is dictated by the complexity of the configuration considered, although Cartesian meshes are favoured over conforming grids, the ability to satisfy the body boundary condition is more



difficult. In computational fluid dynamics the field of grid generation is vast and to cover it thoroughly would take a long time. It is sufficient to say that the two types of grid, conforming and Cartesian, and the advantages in adopting one over the other is dictated by the problem under consideration. As with panel methods, the position of the grid points determines the accuracy of the solution, and the speed of convergence of the algorithm. Grid points are located in regions where the changes in the flow are more pronounced and sparsely in regions where the accelerations are small. The discrete form of the full potential equation is solved at all the grid points, and if there are many such points, the iteration procedure can take a long time to arrive at a converged solution. To increase the rate of convergence an efficient algorithm must be used. Many such algorithms exist; at present the most efficient is the multi-grid method though close behind are the Approximate Factorisation (AF) schemes.

The aim of the present method is to develop a full three-dimensional finite difference program that can predict transonic flow around single and multi-body configurations, and to compare the method for efficiency and accuracy with existing programs, such as SPARV (Ref.26) and the ARA transonic program, (Ref.31). The method is an extension of the work done by Wedan and South (Ref.2), which gave accurate results for two-dimensional and axi-symmetric shapes considering that the equations were only first-order accurate at the body surface. The field of Computational Fluid Dynamics (C.F.D.) covers a wide range of topics, the following sections will be introduced

by a brief historical review before the approaches adopted by the present method are discussed.

CHAPTER 7

## OVERVIEW OF THE SOLUTION OF THE FULL POTENTIAL EQUATION

## 7.1 Finite Difference Formulation

The first practical numerical technique for solving two-dimensional steady transonic flow was developed by Murman and Cole (Ref.32). The method used retarded differences in regions of supersonic flow encompassing a hyperbolic system and central differences in subsonic flow which mimics an elliptic system. To represent this domain dependence the equations were written using one sided differences. From this initial work two different schools of thought emerged as to the form the difference equations must take. They may either be conservative which ensures conservation of mass but not momentum, such as the present method, or non-conservative. It is accepted that the Euler equations provide an adequate model of the inviscid flow in which mass, momentum and energy are conserved, and it is usual to use the conservation form for their solution. The situation with the full potential equation is rather different, in this case the flow is required to be isentropic; an assumption that is not valid when shocks are present. It is then not possible to conserve both mass and momentum and the choice of adopting the conservation scheme has the appeal of being consistent in the sense that at least one property is always conserved. However this is still an incomplete model of the inviscid flow. It is therefore arguable whether a conservative scheme that conserves mass but

not momentum is necessarily better than a scheme that makes no attempt to conserve either. For the non-conservative scheme, mass continuity, in the vicinity of a shock, is ensured by the introduction of extra mass. This is due to the flow conditions on either side of the shock being different, resulting in flow deceleration. Baker (Ref.33) carried out transonic flow calculations using the non-conservative potential equation and the results obtained compared well with those of Holst (Ref.34), who used a conservative method.

## 7.2 Grid Generation

It has been discussed that there exist various techniques for solving the full potential equation, either in conservative or non-conservative form. Both types of equation require the solution of a discretised form which approximates the exact equation. This is then solved at a finite number of grid points. To get an accurate solution, the grid points must be properly distributed in the region disturbed by the body. This section will consider the ways a computational grid can be generated to contain the flow-field and the body about which the flow is being calculated. During the past decade the area of grid generation has received considerable attention and a good summary of this subject is given by Carr and Forsey (Ref.35) and Thompson (Ref.44).

The full potential equation defining the flow field cannot be solved in closed form and requires an iterative solution. Hence, it is necessary to discretise the problem so that one

satisfies a numerical approximation to the partial differential equations at a finite number of points. The adequacy of the solution of this numerical analogue depends not only on the finite difference approximation, but also on the position of the points at which the equation is satisfied. This is because the solution depends not only on the potential at the specific point, but also on the effects of neighbouring points. The first and perhaps best known transonic code for solving the full potential equation is the aerofoil analysis program of Garbedian, Korn and Bauer (Ref.36) using a circle mapping method.

It is usual to map an infinite physical plane around the body to a finite rectangular computing space. The advantages of this are that firstly the complete flow-field is mapped to a finite space, and secondly the density of grid points can be made to vary smoothly. A sparse distribution of points is used at large distances from the body where flow accelerations can be expected to be small and a finer distribution on the body surface, particularly at the leading and trailing edges, where the flow changes more rapidly.

Shearing transformations work well for slender pointed bodies (Fig.29), but for blunted bodies the slope at the nose becomes infinite and such methods are inapplicable. To overcome this difficulty, South and Jameson (Ref.37) used a combination of normal and shearing transformations. This produced a grid aligned with the body, but with grid lines normal to the body surface at the nose (Fig.30). Both the conformal mappings and

the shearing transformations can be combined to produce stretched grids for aerofoils (Cauchy (Ref.38)) and for nacelles (Jameson and Cauchy (Ref.39)).

It has been assumed that the transformations produce grids aligned with the body surface, this requirement has been relaxed by Carlson (Ref.40) for solving the flow about aerofoils, and later by Rehner (Refs.41, 42, 43) for the nacelle problem. The grid is allowed to extend into the body and stretching functions are used to pack grid points where large flow accelerations are expected. Having decreased the problem of grid generation, the application of the flow tangency condition on the body surface is markedly more difficult than with conforming grids. In the non-aligned grid approach a grid point does not necessarily lie on the body surface and complicated difference formulae, involving several of the surrounding points, are used to determine the potential at the body boundary. The aligned-mesh methods have been extensively used for simple single body shapes and it is only for complicated shapes, such as double body configurations, that the non-aligned method is useful.

Another method widely used is that of Thompson (Refs.44, 45) using a numerical generation technique. In its simplest form this amounts to a numerical determination of the lines of equi-potential and equi-stream function for incompressible flow. This method can be applied to arbitrary shapes in both two- and three-dimensions. In its original form this can be used for simple configurations such as wing-body problems, but

is too complex to use in more extreme cases such as when nacelles are included.

Thompson's method has been extended to three-dimensional configurations, see Ref.46 and Ref.47, by separating the flow-field into blocks and applying a Thompson mapping for each block. This has its disadvantages in that there is no logical way of dividing the flow region into blocks and there is also the problem of treating the block interfaces. It is reasonable to expect that the distribution of grid points, in effect the coordinate stretching, can change abruptly on passing across such interfaces. Also at interface boundaries, the multi-block can generate a grid node where five rather than four grid lines meet. It is these difficulties that decided the use of the rectangular grid in the present work.

Hence, it seems that the separation of the grid space into blocks using a Thompson mapping, together with a finite volume analysis, would be the most promising combination of techniques for complex three-dimensional geometry (Ref.48). Such mappings have allowed complex grids to be placed over whole aeroplane shapes with nacelles and pylons, (Ref.49).

It is worth mentioning a Solution Adaptive Grid technique (SAG), developed by Holst and Brown (Ref.50). Generally the SAG method used some aspect of the flow-field solution to re-cluster or redistribute grid points, to reduce the solution truncation error. Their work was primarily on aerofoils. The results showed an accuracy which was equivalent to the use of a

standard grid with two or three times as many grid points. The shock capture was much sharper, in that there was less smearing, because the redistribution of points was determined by the position of the shock.

### 7.3 Introduction of Artificial Viscosity

When the boundaries are prescribed, the non-existence of smooth transonic solutions of the potential equation requires consideration of weak solutions. The appropriate solution admits discontinuities across which mass is conserved but momentum is not, so that a drag force appears. If however, we do not impose a restriction on the type of jumps to be allowed, corresponding to the entropy inequality, weak solutions of the potential equation are in general non-unique (Ref.51). The equation is invariant under reversal of the flow direction, so that a body with fore and aft symmetry, for example, admits both a solution with a compression shock, and a corresponding reversed flow solution with an expansion shock. To obtain uniqueness we must exclude discontinuous expansions. We ought, therefore, to restore in the numerical scheme the directional property which was removed by the exclusion of the entropy from the equation. This indicates the need to ensure that the dominant terms of the truncation error represent artificial viscosity.

It was first shown by Murman and Cole (Ref.32), for the case of the small disturbance equations, where the flow is almost aligned with the x-axis, that the required artificial viscosity



can be introduced in an effective and simple manner by using upwind differences to represent derivatives in the stream-wise direction at all points in the hyperbolic region. Moreover, when the dominant truncation error is included, the resulting finite difference formula resembles the viscous transonic equation which can admit solutions with the approximate structure of a shock wave. The difference equations exhibit similar behaviour and shock waves emerge in the course of the calculation as compression layers spread over a few mesh widths in which the artificial viscosity becomes the dominant term. In the case where the flow is not necessarily aligned with the x-axis, in the case of bodies having large diameters, the artificial viscosity can have a destabilising effect on the numerical scheme as well as imparting an incorrect zone of dependence to the finite difference equations.

To overcome this limitation, Jameson (Refs.48, 52, 53) extended the use of upwind differencing, in the hyperbolic region, to the exact potential equation, for the non-conservative rotated difference and conservative schemes. The grids used were aligned with the aerofoil surface in order to accurately represent the surface flow tangency condition. In Jameson's work, an artificial viscosity term in the supersonic region is added to the governing equations implicitly via upwind differencing as in the rotated difference method, or explicitly as in the conservation scheme. The second feature is that the iterative procedure, based on line relaxation (see next section), is constructed such that, in the supersonic region the artificial time-dependant equation describing the

development of the solution through iteration is essentially hyperbolic with the flow direction (Ref.53), with the addition of the artificial viscosity, this equation becomes parabolic. Based on Von Neumann stability analysis, Jameson concluded that no damping term in the artificial time  $t$  (namely  $\phi_t$ ) is allowed in the supersonic region; hence the relaxation factor is kept at one in supersonic flow and greater than one (and less than two) in the subsonic region. For stability augmentation, in particular near the sonic line, extra time-dependant terms ( $\phi_{st}$ ) are sometimes needed and are added to the scheme.

#### 7.4 Solution Algorithm

In this section the various schemes available for solving the discretised finite difference equation are mentioned. All methods first appeared as methods for solving the elliptic equations, the first method was called Successive Line Over Relaxation (SLOR) and was used by Murman and Cole (Ref.32). For many years SLOR has been the standard method for solving the non-linear equations in steady transonic flow problems, and although it is easy and reliable to use, it's convergence rate is slow, mainly because of the slowness with which information can be transmitted in the direction opposite to that in which the calculation proceeds, the transmission rate being one step length per iterative cycle (iteration). Several thousand iterations are often needed to obtain a converged solution, although there are ways of reducing this to several hundred iterations, for example, by adding a vortex flow in lifting

problems, to speed up the transmission of information to the far-field, or by performing a preliminary calculation on a coarse mesh. Each successive vertical grid line is updated (relaxed) in a single matrix inversion step requiring less time than solving point by point. The grid lines are relaxed by sweeping in the downwind direction.

Other methods have been developed more recently. Rapid elliptic solvers were used by Martin and Lomax (Ref.54) to calculate subcritical and mildly super-critical flows. After linearising the flow equations by using the approximate solution obtained from the previous iteration the resulting linear equation is solved exactly over the complete flow-field. Although the method converges in much fewer iterations than SLOR, the computation time for each iteration is greater than other methods, and it becomes unstable when a region of super-critical flow is present. It is also limited to fairly simple computational domains, in particular, coordinate stretching can be used in only one of the two directions.

Horizontal Line Over Relaxation can also be used and was attempted by Wedan and South (Ref.2), but was found to be no better than SLOR. The Alternate Direction Implicit (ADI) or the Approximate Factorisation (AF) schemes were originally developed for equations of parabolic and elliptic type. Their use was extended to transonic flow problems by Ballhaus and Steger (Ref.55) who used these techniques to remove the time step limitation in a relaxation solution of the unsteady Transonic Small Perturbation equation (TSP). The extension to

steady TSP came quickly, and Ballhaus, Jameson and Albert (Ref.56) proposed two factorisations, AF1 and AF2, aimed at solving the exact potential equation. Holst (Ref.57) has applied a variation of AF2 to the full potential equation. Baker (Ref.58) also applied both AF1 and AF2 to the full potential equation, and using a circle plane mapping, introduced a further factorisation, AF3, which was found to be faster than the other two, although the reason for this was not at the time evident. Other workers have had mixed success with AF schemes, sometimes finding particular schemes to be fast in particular domains and sometimes finding them disappointing, for example on stretched Cartesian meshes, with optimal sets of acceleration parameters difficult to determine (Refs.57,59).

Another fast iterative method which is currently receiving great interest, is the multi-grid method originally proposed by Federenko (Ref.60), and developed further by Brandt (Ref.61) to be applicable to a variety of flow problems. This method has been applied to the transonic flow problem by South and Brandt (Ref.62) and by Jameson (Ref.63). In this method, a calculation is performed over a range of successively coarser grids, then over successively finer grids. It is easy to see how information can be spread rapidly over the whole flow-field by the use of coarser meshes, whilst the finer meshes are used for the local flow details. Put another way, if one imagines the error to be made up of Fourier components, see Ref.67, then the coarser meshes are used to reduce the low frequency error (global discrepancies) while the finer meshes reduce the high frequency errors (localised deviations from the converged

solution). Transfer of data from coarse to fine mesh is achieved by interpolation. After carrying out a small number of fine grid iterations, the high frequency modes will be much reduced, although the low frequency end of the error spectrum will be largely unaffected. If we now go to the coarser grid with half the number of grid points the opposite occurs. We thus see that on each grid the iterative cycle is used as a routine for reducing or smoothing out the error modes at both extremes of the frequency band. The sequence of smoothing operations aimed at covering the entire spectrum can be compared with the cycle of acceleration parameters used in AF schemes. The goal is the same but the multi-grid method is more efficient due to the coarse grid iteration taking less time than fine grid iteration. The main disadvantage is the organisational complexity of the computer code.

For a more complete review of the C.F.D. to present see Kutler (Ref.64).

### 7.5 The Non-Conservative Scheme

Before the method presented by Wedan and South (Ref.2) was undertaken, the author attempted to program the non-conservative, non-aligned mesh approach adopted by Carlson (Ref.40). The method is second-order accurate though much more complex than that used in Ref.2. It was found that the method forced the iterative scheme to march around the body and not through the whole grid. This implied that the mesh above the body-axis and that below had to be updated separately. In

addition complex difference formulae had to be used to satisfy the body boundary condition. Each vertical grid line which intersected the body had to be updated twice. Firstly, to get an accurate value of  $\phi$  for the point inside the body boundary, and secondly, using this value to update the same vertical grid line for a more accurate solution. The overall method proved to be slow and cumbersome due to the above complexities and the use of SLOR as an iterative solution scheme. The solution required hundreds of iteration steps to converge for blunt bodies, such as ellipsoids and an even greater number for a sphere. This led the author to favour the Finite Volume method discussed in Ref.2.

CHAPTER 8

## SPATIAL DIFFERENCING OF THE FULL POTENTIAL EQUATION IN

## CONSERVATION FORM

## 8.1 Formulation of the Equations

In the isentropic flow of a perfect gas the equation of state

$$\frac{p}{\rho^\gamma} = \text{Constant} \quad 8.1.1$$

is assumed to hold, where  $p$  is the pressure,  $\rho$  is the density and  $\gamma$  is the ratio of specific heats. If the density is normalized by the value unity at infinity and  $M_\infty$  is the Mach number at infinity, the speed of sound  $a$  is given by

$$a^2 = \frac{dp}{d\rho} = \frac{\rho^{\gamma-1}}{M_\infty^2} \quad 8.1.2$$

The equation of mass conservation in a steady flow can be written in the following divergence form

$$\nabla \cdot (\rho \mathbf{q}) = 0 \quad 8.1.3$$

$\underline{q}$  being the velocity vector. We assume the existence of a velocity potential  $\Phi$  so that the velocity can be represented as

$$\underline{q} = \nabla \Phi \quad 8.1.4$$

Since the flow has been assumed irrotational and isentropic (these conditions are necessary for the existence of a potential function) we can integrate the momentum equation to obtain Bernouilli's equation

$$\frac{q^2}{2} + \frac{a^2}{\gamma-1} = \text{Constant} \quad 8.1.5$$

After normalising the velocities and speed of sound by the free-stream velocity, the governing Eqn.(8.1.3), may be expressed in non-dimensional form

$$\nabla \cdot (\rho \cdot \nabla \Phi) = 0 \quad 8.1.6$$

Since the flow is isentropic, the non-dimensional density  $\rho$  can be written uniquely in terms of the velocity



$$\rho = 1 + \frac{\gamma-1}{2} \cdot M_\infty^2 (1-q^2)^{\frac{1}{\gamma-1}} \quad 8.1.7$$

and the speed of sound becomes

$$a^2 = \frac{1}{M_\infty^2} + \frac{\gamma-1}{2} (1-q^2) \quad 8.1.8$$

The pressure coefficient at any point in the flow field is given by

$$C_p = \frac{p-p_\infty}{\frac{1}{2} \rho_\infty u_\infty^2} = \frac{2}{\gamma M_\infty^2} \left\{ \left[ 1 + \frac{\gamma-1}{2} \cdot M_\infty^2 (1-q^2) \right]^{\frac{\gamma}{\gamma-1}} - 1 \right\} \quad 8.1.9$$

In a Cartesian coordinate system the 'full potential equation' for two-dimensional flow becomes

$$\left( \rho \Phi_x \right)_x + \left( \rho \Phi_y \right)_y = 0 \quad 8.1.10$$

Applying the divergence theorem to the integral form of the governing Eqn.(8.1.6), and integrating over an arbitrary volume  $V$ , gives

$$\iiint_V \left[ \nabla \cdot (\rho \underline{q}) \right] \cdot dV = \int_S (\rho \underline{q} \cdot \underline{n}) \cdot dS = 0 \quad 8.1.11$$

where  $S$  is the surface enclosing  $V$  and  $\underline{n}$  is the unit outward normal on  $S$ . Eqn.(8.1.11) thus gives the continuity equation expressed in surface flux form. The numerical solution of this equation is discussed in the following sections.

## 8.2 Differencing Operators

With the assumption of irrotationality, a non-dimensional perturbation potential  $\phi$  may be introduced, and the velocities expressed as discrete derivatives of this function.

Consider a uniform grid with increment  $\Delta x$  between grid lines in the  $x$ -direction and  $\Delta y$  in the  $y$ -direction. The continuous function  $\phi(x,y)$  can be approximated at a number of grid points  $i,j$  in such a way that the discrete solution  $\phi_{i,j}$  will approximate the continuous potential  $\phi(x,y)$  as the grid increments  $\Delta x$  and  $\Delta y$  tend to zero. The continuous potential at a point  $i$  can be expanded as a Taylor series

$$\phi_{i+1} = \phi_i + \Delta x \cdot \phi'_i + \frac{\Delta x^2}{2} \cdot \phi''_i + \dots$$

$$\phi_{i-1} = \phi_i - \Delta x \cdot \phi'_i + \frac{\Delta x^2}{2} \cdot \phi''_i - \dots$$

8.2.1

Assuming the velocity can be expressed as

$$V_x = \frac{\partial \phi}{\partial x} + u_\infty,$$

8.2.2

$$V_y = \frac{\partial \phi}{\partial y} + v_\infty$$

then a second order backward difference formula for the velocity in the x-direction is

$$U_x \approx \frac{\phi_i - \phi_{i-1}}{\Delta x} + U_\infty \equiv \overleftarrow{\delta}_x \phi_x + U_\infty \quad 8.2.3$$

with similar expressions for the y- and z-directions. Similarly a forward difference becomes

$$U_x \approx \frac{\phi_{i+1} - \phi_i}{\Delta x} + U_\infty \equiv \overrightarrow{\delta}_x \phi_x + U_\infty \quad 8.2.4$$

In practice a stretching function, discussed later, is introduced to map the infinite physical domain, see Figs.31a and 32a, into a finite computational interval  $(-1,1)$ , (Figs.31b and 32b). Equal intervals  $\Delta X$  and  $\Delta Y$  are then taken in the computation space to define a grid that is non-uniform in the physical space. Under this transformation the difference formulae become

$$x = f(X), \quad X_x = dX/dx$$

$$U_x \approx X_x|_{i-\frac{1}{2}} \cdot \frac{\phi_i - \phi_{i-1}}{\Delta X} + U_\infty, \quad 8.2.5$$

$$U_x \approx X_x|_{i+\frac{1}{2}} \cdot \frac{\phi_{i+1} - \phi_i}{\Delta X} + U_\infty$$

This notation will be used in approximating the mass conservation equation.

### 8.3 Finite Difference Formulation

To discretise the mass conservation equation, Eqn.(8.1.11), for numerical solution, the computational domain is sub-divided with constant rectangular 'cells' with faces  $S_1, S_2, S_3, S_4, S_5$ , and  $S_6$  as shown in Fig.33. At each point  $i, j, k$  lying inside the computational cell the mass flow Eqn.(8.1.11), is satisfied. Since the cell sides are parallel to the  $x$ -,  $y$ - and  $z$ -axis, Eqn.(8.1.11) may be rewritten as

$$\int_{S_2} (\rho u) dS_2 - \int_{S_1} (\rho u) dS_1 + \int_{S_4} (\rho w) dS_4 - \int_{S_3} (\rho w) dS_3 + \int_{S_6} (\rho v) dS_6 - \int_{S_5} (\rho v) dS_5 = 0 \quad 8.3.1$$

where velocities  $u, v$  and  $w$  are non-dimensionalised by the free-stream velocity. Eqn.(8.3.1) simply states that the mass flow into the cell is balanced by the mass flow out, ensuring mass conservation. If average values of the flux quantities at the cell faces are taken, then Eqn.(8.3.1) is simply

$$(\rho u S)_2 - (\rho u S)_1 + (\rho v S)_6 - (\rho v S)_5 + (\rho w S)_4 - (\rho w S)_3 = 0 \quad 8.3.2$$

The mass flowing into a cell in any of the three directions,  $x$ ,  $y$  or  $z$ , is measured by the mass flowing across a face, lying

normal to that direction. The values of  $\rho_u$ ,  $\rho_v$ , and  $\rho_w$  are now the averaged values lying on the cell sides and not the cell centre. The finite difference equations for the velocity components, Eqn.(8.2.5), can be rewritten as

$$\begin{aligned} u &= X_x \cdot \phi_x + \cos\alpha \cdot \cos\beta \\ v &= Y_y \cdot \phi_y + \sin\alpha \\ w &= Z_z \cdot \phi_z + \cos\alpha \cdot \sin\beta \end{aligned} \quad 8.3.3a$$

where

$$X_x = \frac{dX}{dx}, \quad Y_y = \frac{dY}{dy}, \quad Z_z = \frac{dZ}{dz} \quad 8.3.3b$$

introducing free-stream incidence  $\alpha$  and yaw  $\beta$  (Fig.1), in the computational coordinate system. Eqn.(8.3.2) then becomes

$$\begin{aligned} & \left[ \rho \cdot (X_x \cdot \phi_x + \cos\alpha \cdot \cos\beta) \cdot S \right]_2 - \left[ \rho \cdot (X_x \cdot \phi_x + \cos\alpha \cdot \cos\beta) \cdot S \right]_1 \\ & + \left[ \rho \cdot (Y_y \cdot \phi_y + \sin\alpha) \cdot S \right]_6 - \left[ \rho \cdot (Y_y \cdot \phi_y + \sin\alpha) \cdot S \right]_5 \\ & + \left[ \rho \cdot (Z_z \cdot \phi_z + \cos\alpha \cdot \sin\beta) \cdot S \right]_4 - \left[ \rho \cdot (Z_z \cdot \phi_z + \cos\alpha \cdot \sin\beta) \cdot S \right]_3 = 0 \end{aligned} \quad 8.3.4$$

The densities at the cell sides are computed by averaging the cell-centred values. If Eqn.(8.3.4) is written using difference operators, then it becomes

$$\rho_{i+\frac{1}{2}} S_2 \left[ X_x \Big|_{i+\frac{1}{2}} \cdot \vec{\delta}_x \cdot \phi_{ijk} + \cos\alpha \cdot \cos\beta \right] - \rho_{i-\frac{1}{2}} S_1 \left[ X_x \Big|_{i-\frac{1}{2}} \cdot \vec{\delta}_x \cdot \phi_{ijk} + \cos\alpha \cdot \cos\beta \right] + \dots$$

8.3.5  
(Cont)

$$\rho_{j+\frac{1}{2}} S_6 \left[ Y_y \Big|_{j+\frac{1}{2}} \cdot \overrightarrow{\delta Y} \phi_{ijk} + \sin \alpha \right] - \rho_{j-\frac{1}{2}} S_5 \left[ Y_y \Big|_{j-\frac{1}{2}} \cdot \overleftarrow{\delta Y} \phi_{ijk} + \sin \alpha \right] \quad 8.3.5$$

(Cont)

$$+ \rho_{k+\frac{1}{2}} S_4 \left[ Z_z \Big|_{k+\frac{1}{2}} \cdot \overrightarrow{\delta Z} \phi_{ijk} + \cos \alpha \cdot \sin \beta \right] - \rho_{k-\frac{1}{2}} S_3 \left[ Z_z \Big|_{k-\frac{1}{2}} \cdot \overleftarrow{\delta Z} \phi_{ijk} + \cos \alpha \cdot \sin \beta \right] = 0$$

This is again second-order accurate for constant cell side. The density at the cell center is computed from the potential using the isentropic relation, Eqn.(8.1.7), where the cell-centered velocity is

$$q_{ijk}^2 = u_{ijk}^2 + v_{ijk}^2 + w_{ijk}^2 \quad 8.3.6$$

with

$$u_{ijk} = X_x \Big|_i \cdot 0.5 \cdot \left[ \overrightarrow{\delta X} + \overleftarrow{\delta X} \right] \cdot \phi_{ijk} + \cos \alpha \cdot \cos \beta$$

$$v_{ijk} = Y_y \Big|_j \cdot 0.5 \cdot \left[ \overrightarrow{\delta Y} + \overleftarrow{\delta Y} \right] \cdot \phi_{ijk} + \sin \alpha \quad 8.3.7$$

$$w_{ijk} = Z_z \Big|_k \cdot 0.5 \cdot \left[ \overrightarrow{\delta Z} + \overleftarrow{\delta Z} \right] \cdot \phi_{ijk} + \cos \alpha \cdot \sin \beta$$

The flow equation has been formulated for all grid points in the flow, and as yet no body has been placed in the computational space.

#### 8.4 Far Field Boundary Conditions

The grid stretching routine maps boundaries at infinity to a finite distance in the computational space. This domain extends from -1 to +1 in all directions and is rectangular. At infinity the perturbation potential is zero and free-stream

conditions exist, i.e. a Dirichlet boundary. The computation proceeds from 2 to  $L$ , 2 to  $M$ , and 2 to  $N$  in the  $x$ -,  $y$ -, and  $z$ -directions, where  $L$ ,  $M$  and  $N$  denote the number of grid intervals in each direction, see Fig.34. All points

$$(1, j, k), (L+1, j, k) \quad \text{for } j=1, 2, \dots, M+1, k=1, 2, \dots, N+1$$

$$(i, 1, k), (i, M+1, k) \quad \text{for } i=1, 2, \dots, L+1, k=1, 2, \dots, N+1$$

$$(i, j, 1), (i, j, N+1) \quad \text{for } i=1, 2, \dots, L+1, j=1, 2, \dots, M+1$$

lying on the dummy boundaries have a perturbation potential value of zero. This implies that the total perturbation velocity is zero.

### 8.5 Body Specification

Most methods for solving the full potential equation use body conforming grids and satisfying the body boundary condition is fairly simple, due to grid points lying on the body surface, (Fig.35). Methods that use non-aligned grids experience difficulty at the body surface. To obtain an accurate solution for such methods, all grid points are updated by sweeping around the body and grid points lying inside the body are neglected. This introduces more computational complexity, furthermore, the potential at point  $P$ , lying just inside the body, (Fig.35b), is required to enable all other points on the same vertical grid line to be updated, see Carlson (Ref.40). This point is usually updated by satisfying the condition that the flow must be tangential to the body surface and complex difference formulae are introduced, using a collection of surrounding points lying outside the body. This

implies that the four quadrants of a circle, say, require four difference formulae for update of the internal points. The present method overcomes this difficulty by a simple treatment of the surface boundary, and is in an integral sense exact.

Consider a cell cut by the body surface as shown in Fig.36, at which the boundary condition of no flow normal to the surface,  $q \cdot \eta = 0$ , is to be applied. Since this requires that there be no flow through surface  $S_5$ , The corresponding mass flow Eqn.(8.3.2), can be written

$$(\rho u s)_2 - (\rho u s)_1 + (\rho v s)_6 + (\rho w s)_4 - (\rho w s)_3 = 0 \quad 8.5.1$$

Eqn.(8.5.1) is equivalent to Eqn.(8.3.2) if

$$S_5 = 0 \quad 8.5.2$$

Hence, the body boundary condition is easily implemented by redefining the face areas of the computational cell. For all cells lying completely outside the body boundary, the cell side areas are of unit value, those lying completely inside have a value of zero, and those cut by the surface are recalculated. In three-dimensions, this area calculation is achieved by approximating the body surface by straight lines, (Fig.36). The type of cell face and the calculation of it's area is discussed in Appendix.A1.



There is an added advantage in using this formulation for the body boundary condition. For cells lying inside and outside, the intermediate cell cut by the body surface effectively decouples the mass flow equation predicting the potentials on either side of the boundary. For a closed body this leads to regions interior and exterior to the body which are decoupled through existence of zero-flux surfaces. As a result the finite difference Eqn.(8.3.5) requires no further structuring and the solution algorithm can effectively sweep through the whole grid in complete neglect of the presence of the body. The solution of the internal region gives zero flux everywhere, except for a point lying inside the body boundary, since there is no flux into or out of this region.

#### 8.6 Effects of Decoupling

Decoupling allows the iteration procedure to proceed, unaltered through the body. Although this greatly simplifies the algorithm, the values of the velocity obtained by the differencing of the potentials on either side of the zero cell area may be erroneous due to the decoupling effect. To prevent this, the velocity is written in terms of switching functions which guarantee that at a point  $i,j,k$ , the velocity will be calculated as either a completely backward or completely forward difference in the presence of zero cell face areas.

When a cell has one or more zero cell face areas, an inaccurate cell-centered density may be computed since the density is obtained from the average of the velocities at the cell faces.

To correct this, a weighting function, in addition to the switching function, is introduced which shifts the evaluation of the cell-centered velocity components towards the values at the non-zero areas. Consider the x-direction

$$u = \frac{W_x|_{i+1/2} \cdot X_x|_{i+1/2} (\phi_{i+1} - \phi_i) + W_x|_{i-1/2} \cdot X_x|_{i-1/2} (\phi_i - \phi_{i-1})}{(W_x|_{i+1/2} + W_x|_{i-1/2}) \Delta X} + \cos \alpha \cdot \cos \beta \quad 8.6.1$$

$W_x$  is the weight.

If either of the weights are zero then the velocity calculation shifts towards the non-zero value. If both the weights are zero, the cell effectively lies within the body and the velocity becomes zero. This eliminates the possibility of the density in a supersonic body cell being biased toward an unrelated value across a zero cell face area.

### 8.7 Pressure Distribution Calculation

Computational methods solving the full potential equation solve a discretised form at a finite number of grid points. At these points the potential value,  $\phi$ , is known and stored. This enables all flow quantities of interest, such as velocity components, pressure, and Mach number to be calculated. The quantity of most interest is the pressure distribution upon the surface of the body, from which the load acting on the body can be determined. The pressure distribution can be calculated wherever grid lines intersect the body surface. The potential

at the body surface is obtained by extrapolating the values along the vertical grid lines onto the surface. The NAG routine E01AAF is used, (Ref.30).

Consider points I-1, I, I+1 where the vertical grid lines meet the body surface, (Fig.37). The points are separated by body distances S1 and S2, then the tangential component of velocity at the point I, is given as the derivative of the potential

$$V_t = \frac{\partial \phi}{\partial s} + V_{fs} \quad 8.7.1$$

where  $V_{fs}$  is the free-stream tangential component. Expressing the potential in finite difference form, then

$$\begin{aligned} \phi_{i+1} &= \phi_i + S_2 \cdot \phi_i' + \frac{S_2^2}{2} \cdot \phi_i'' + \dots \\ \phi_{i-1} &= \phi_i - S_1 \cdot \phi_i' + \frac{S_1^2}{2} \cdot \phi_i'' - \dots \end{aligned} \quad 8.7.2$$

Using the above equations, the tangential velocity becomes

$$\begin{aligned} V_t &= V_{fs} + \frac{1}{S_1 S_2} \left[ \frac{S_1^2 \phi_{i+1} - S_2^2 \phi_{i-1}}{S_1 + S_2} \right] \\ &+ \frac{1}{S_1 S_2} \cdot \phi_i (S_2 - S_1) \end{aligned} \quad 8.7.3$$

This form is second order accurate. Eqn.(8.7.3) has to be modified when the I'th point is the first or the last point on the body surface. Referring to (Fig.37), to calculate the velocity at points  $I_n$  and  $I_t$ , the potential at points A and B is required. These points do not lie on vertical grid lines

and so the horizontal line J is used. Field potential values on this line are extrapolated onto the nose and tail to be used in Eqn.(8.7.3). We still need to obtain the free-stream component of the tangential velocity  $V_{fs}$ . If the free-stream velocity vector of magnitude,  $q$ , is at an angle  $\alpha$  to the horizontal, and the body slope at point I is  $\gamma$ , then the tangential free-stream component is

$$V_{fs} = q \cdot \cos(\alpha - \gamma) \quad 8.7.4$$

This involves knowing the body slope, explicitly, at all body points. Hence the total tangential velocity is

$$V_t = \frac{\partial \phi}{\partial S} + q \cdot \cos(\alpha - \gamma) \quad 8.7.5$$

Since, by definition the normal component of velocity at the surface is zero then only the tangential component is considered and the pressure coefficient at these points can be determined from Eqn(8.1.9).

CHAPTER 9

## GRID GENERATION AND COORDINATE STRETCHING

## 9.0 General

All methods available for solving the full potential equation in discretised form require the generation and use of a grid. Two types of grid are normally used, those that conform to the body shape, and those that are rectangular and non-conforming, each have their disadvantages and advantages. Both require some form of mapping to translate the stretched physical grid to a uniform computational grid with constant spacing between grid lines in each of the X-, Y-, and Z-directions. For the present method, a rectangular grid is used which generates grid points in regions where the flow behaviour is changing rapidly, this is done by the use of stretching algorithms. The body is placed in the physical grid with the required concentration of grid lines in the relevant flow regions. Under the stretching transformations the whole grid space including the body is stretched such that the distance between grid lines, in the computational space, is constant. For simple body shapes, such as ellipsoids and regular missile bodies, this type of rectangular grid is sufficient and there has been no need implement complex algorithms to generate grids which follow the shape of the body.

The rectangular grids can easily be extended to three

dimensions and the stretching functions do not have to be drastically altered in the presence of more complex configurations, such as two bodies. If conforming grids had been used, routines for generating the grid would have to be changed for each different configuration of body or bodies. On the other hand, the calculation of the cell face areas required for the solution of the finite volume method would be greatly simplified, since the cells would be of two types, those that lie completely inside the body boundary and those that lie completely outside. The body boundary condition is easy to satisfy for each method without the need to use complicated difference formulae to update points lying on either side of the body boundary. Although conforming grids produce more accurate results, in the present research it is found to be less complicated in terms of computer code, to generate a rectangular non-conforming grid. The present stretching algorithms are used from Ref.66.

### 9.1 Stretching Algorithm

In the present work a Cartesian mesh is used, if no stretching function is present the results can prove to be in error and the speed of convergence of the solution can be very slow. This is due to the slow rate at which the flow information can be transmitted throughout the whole grid. Stretching functions are used to place points in the mesh and on the body such that these disadvantages are reduced. The functions are required to map the infinite physical domain to a finite computational space. One of the most useful stretching

functions is the tangent function, this can be made to produce an infinite value for  $\alpha$  when  $\Theta = 90$  degrees say,

$$\alpha = \tan(\Theta) \quad 9.1.1$$

If  $\Theta$  is replaced by  $\pi \cdot X/2$ , the physical plane coordinates  $\alpha$ , are mapped to computational plane coordinates  $X$ ,

$$\alpha = \tan\left(\frac{\pi}{2} \cdot X\right) \quad 9.1.2$$

The above equation implies that when  $X = \pm 1$  then  $\alpha = \infty$ , or  $\alpha = -\infty$ , this stretching can be further adapted to cluster points in particular regions of the flow, for example near leading and trailing edges. Consider the function

$$X = a \cdot \tan^{-1}[c \cdot (\alpha - b)] \quad 9.1.3$$

This has the following advantages

- a) it tends to a constant value as  $\alpha \rightarrow \pm \infty$ ,
- b) for large  $\text{abs}(\alpha)$ , it forces  $X$  to behave in a similar manner to  $\phi$ , so that  $\phi_\alpha$  is well behaved near  $X = \pm 1$ ,
- c) it allows easy control of the nature of the stretching;  $\alpha = b$  is the position at which the stretching is centred, the product  $a \cdot c$  controls it's strength, and the quotient  $a/c$  controls it's extent of influence (the speed at which it tends to a constant).

The form used in the single body case for the  $x$ -direction is taken from Ref.66,

$$\begin{aligned}
 X = \bar{a} \cdot & \left\{ a_0 \cdot \tan^{-1} [c_0(x-x_l)] + a_1 \cdot \tan^{-1} [c_1(x-x_t)] \right. \\
 & + a_2 \cdot \left[ (x-x_l) \cdot \tan^{-1} [c(x-x_l)] - (x-x_t) \cdot \tan^{-1} [c(x-x_t)] \right. \\
 & \left. \left. + \frac{1}{2c} \ln \left[ \frac{1+c^2(x-x_t)^2}{1+c^2(x-x_l)^2} \right] \right] \right\}
 \end{aligned}
 \tag{9.1.4}$$

where

$$\bar{a} = \frac{2}{\pi \cdot (a_0 + a_2 + a_1)}
 \tag{9.1.5}$$

$x_l$  is the leading edge and  $x_t$  is the trailing edge. The first two arctangents in Eqn.(9.1.4) are centred near the leading and trailing edges of the shape;

$$\begin{aligned}
 x_l &= -0.5 \\
 x_t &= -x_l
 \end{aligned}
 \tag{9.1.6}$$

The leading edge is chosen to be near to  $x=0.5$ , but such that it lies midway (in the computational plane) between two grid points. It should be noted that the solution is not sensitive to the precise positioning of the leading edge, but numerical stability (and hence speed of convergence) in the vicinity of the leading edge may occasionally be enhanced through control of it's position. The remaining three terms control the density of grid lines between the leading and



trailing edges. Without these terms there would be a high concentration of grid lines at either location ( $C_0$  or  $C_1$  large) and very little between. To alleviate this more arctangents could be used to pull grid lines away from the leading and trailing edges requiring high  $C$  values. Again this would lead to regions around the point at which they were placed containing a high concentration and more arctangent terms would be required to alleviate this. The solution is to have a constant distribution of arctangents at all points between  $\chi_l$  and  $\chi_t$ , with equal strength,  $C$ , and equal but vanishingly small weight  $\alpha$ ; this process yields a fairly linear behaviour of the stretching function  $F(x)$  between  $\chi = \chi_l$  and  $\chi = \chi_t$ . Values for some parameters in Eqn.(9.1.4), which have given good grid-line distributions in all the cases attempted are, see Figs.31a, and 31b,

$$\alpha_0 = \alpha_1 = 1, \alpha_2 = 4, C = 6 \quad 9.1.7$$

It now remains to determine values for the parameters  $C_0$  and  $C_1$  in the first two arctangents. The areas in which high concentrations of grid lines are needed are leading and trailing edges where the surface curvature can be high, causing the flow to change direction abruptly. It therefore seems logical that the spacing in these regions be made proportional to the radius of curvature of the leading and trailing edges. The parameters  $C_0$  and  $C_1$  are chosen such that

$$X_x = \text{MAX} \left[ \frac{1}{\Delta x \cdot \rho \cdot \epsilon_x}, 1 \right] \quad 9.1.8$$

where

$\epsilon_x$  and  $\epsilon_z$  (see later) are truncation errors 9.1.9

and  $\rho_c$  is the radius of curvature of the body at the leading and trailing edges. This results in three regions which have differing grid line concentrations, Fig.38, and the density of grid lines varies smoothly between each region. In this case the stretching is symmetrical about  $\chi=0$ . Regions II have a high concentration of grid lines whilst I and III are more sparse. For a missile shaped body such as an ogive nosed cylinder, the stretching produces six different regions (Fig.39). Again the result is a high concentration of grid lines around the nose and tail. Such a stretching is achieved in two steps. Firstly, the stretching for the nose is produced by using a body having an aft section which is a mirror image of the nose. This results in regions I, II and III. Secondly, the stretching for the aft section of the missile is produced by using a body having a nose which is the mirror image of the original missile tail section. This results in regions IV, V and VI.

The stretching for the y- and z-direction are both the same for single body configurations. The function used in the present method is again taken from Ref.66,

$$Z = \bar{a} \left\{ a_0 \tan^{-1}(C_0 z) + a_1 \left[ (z-b_1) \tan^{-1} [c(z-b_1)] \right] \dots \right. \quad 9.1.10$$

(cont)

$$\begin{aligned}
 & - (z-b_2) \cdot \tan^{-1} [c \cdot (z-b_2)] + \frac{1}{2c} \cdot \ln \left[ \frac{1+c^2 \cdot (z-b_2)^2}{1+c^2 \cdot (z-b_1)^2} \right] \\
 & + a_2 \cdot \tan^{-1} [c_1 \cdot (z-b_1)] + a_3 \cdot \tan^{-1} [c_2 \cdot (z-b_2)]
 \end{aligned}
 \tag{9.1.10 (cont)}$$

where

$$\bar{a} = \frac{2}{\pi \cdot a_0 + a_1 \cdot (b_1 + b_2) + a_2 + a_3}
 \tag{9.1.11}$$

and

$$b_1 = \Gamma, \quad b_2 = -\Gamma
 \tag{9.1.12}$$

Here, one arctangent, usually the strongest, is centred at  $Z=0$ , with the other two at  $Z=-\Gamma$  and  $Z=\Gamma$  where  $\Gamma$  is the maximum radius of the body. The values chosen are

$$a_0 = 1, \quad c = 2, \quad c_1 = c_2 = 4/\Gamma^2, \quad a_1 = 1/(2\Gamma)
 \tag{9.1.13}$$

Parameters  $a_2$  and  $a_3$  are chosen such that  $a_2 + a_3 = 1$  and  $Z=0$  when  $z=0$ ;  $c_0$  is chosen such that

$$Z_2|_{z=0} = \text{MAX} \left[ \frac{1}{\Delta Z \cdot \rho_c \cdot \epsilon_z}, \quad \frac{\Delta Z}{\Delta X} \right]
 \tag{9.1.14}$$

These choices are for similar reasons as the x-stretching. For a double body configuration, Fig.40, the only stretching that has been changed is the y-direction. The assumption that the bodies are of a high fineness ratio dictated that a simple

stretching of the arctangent form should be used. For the region bounded by B and  $+\infty$ , and the region bounded by A and  $-\infty$ , the function used is

$$y = a \cdot \tan(b \cdot \gamma) + c \quad 9.1.15$$

The parameter  $\alpha$  controls the concentration of grid lines near the axis of symmetry of each body. For the region lying between the lines A and B, a simple stretching of the following form is used

$$y = a_1 \left( \frac{\gamma}{b_1} \right)^n \quad 9.1.16$$

the parameter  $n$  is a user defined constant usually close to 1. For a high flow resolution a large number of grid lines are required in this region when the bodies are close together. As the distance AB is increased, the parameter  $n$  should be made larger, thereby placing more points near the axis of the body and less in the region between the two body surfaces, see Figs.32a and 32b.

For a two-body configuration with stagger, the stretching for all directions is unaltered.

CHAPTER 10INTRODUCTION OF ARTIFICIAL COMPRESSIBILITY IN TRANSONIC  
REGIONS

## 10.0 General

In transonic flows the introduction of some form of artificial viscosity (either implicitly or explicitly) is necessary in order to stabilise a shock-capturing numerical method. In the present work the scheme is made stable by the explicit introduction of an artificial viscosity. In subsonic regions there is no need for the introduction of artificial viscosity and an elliptic system of equations applies. In the supersonic regions, where a hyperbolic system of equations applies, upwind differences must be taken in order to correctly model the physics of the flow. Since no disturbance can propagate in a direction opposite to the flow, the solution at a particular station depends only on up-stream (or upwind) conditions, (Fig.41). Hence, a switching term is used which introduces artificial viscosity in the supersonic regions. By using a particular solution algorithm the whole grid can be updated using central difference formulae. In the present work, the artificial viscosity is introduced by modifying the density. On expanding the factors in the AF2 scheme (see Chapter.11), a term of the form  $\phi_{xt}$  is automatically generated. This extra term is dependant on time, and as the solution converges it tends to zero, so that at convergence,

the original flow equation is satisfied as closely as possible.

### 10.1 Evolution of Supersonic Regions

Eqn.(8.3.4), is a suitable finite difference scheme for subsonic flow. However, for supersonic regions a properly chosen artificial damping term must be added to prevent physically unrealistic expansions occurring. For Cartesian coordinate systems, to ensure that the shocks that occur are of the correct form, Jameson (Ref.53), adds the following artificial viscosity term explicitly to the non-conservative form of the full potential equation,

$$-\Delta x.(\mu.\phi_{xx})_x \quad 10.1.1$$

where

$$\mu = \text{MIN} \left[ 0, \epsilon. \left( 1 - \frac{\phi_x^2}{a^2} \right) \right] \quad 10.1.2$$

This is analogous to the switching used in the Murman mixed-difference procedure (Ref.65), and is equivalent to retarding the density by an amount

$$-\Delta x.(\nu.\rho_x.\phi_x)_x \quad 10.1.3$$

where

$$\nu = \text{MAX} \left[ 0, \left( 1 - \left[ \frac{a}{\phi_x} \right]^2 \right) \right] \quad 10.1.4$$

For flows containing strong shocks, oscillations in the solution can appear ahead of the shock. These arise because of insufficient artificial viscosity and can quickly lead to numerical instability. To damp down the pre-shock oscillations, the amount of artificial viscosity can be increased by using a different definition of the switching function. Holst, Ref.34, uses the following

$$\nu = \text{MAX} \left[ 0, c \cdot M^n \cdot (1 - M^{-2}) \right] \quad 10.1.5$$

where  $n$  and  $c$  are user defined constants.  $n$  is usually set to 2 and  $c$  is usually set between 1.5 and 2.0. The use of Eqn.(10.1.5) instead of the standard definition for  $\nu$ , increases the amount of upwinding. The present method employs Holst's fully conservative scheme involving an upwind density shift of

$$\tilde{\rho}_{ijk} = \rho_{ijk} - \mu_{ijk} \cdot (\rho_s \Delta s)_{ijk} \quad 10.1.6$$

$$\mu_{ijk} = \text{MAX} \left[ 0, c \cdot \left( 1 - \frac{a_{ijk}}{q_{ijk}} \right) \right]$$

where

$$\begin{aligned} (\rho_s \Delta s)_{ijk} &= \left( \frac{u}{q} \right)_{ijk} \overline{\delta x} \cdot \rho \cdot \Delta X + \left( \frac{v}{q} \right)_{ijk} \overline{\delta y} \cdot \rho \cdot \Delta Y \\ &+ \left( \frac{w}{q} \right)_{ijk} \overline{\delta z} \cdot \rho \cdot \Delta Z \end{aligned} \quad 10.1.7$$

and

if  $u_{ijk} > 0$  then

$$\overleftarrow{\delta x} \cdot \rho \cdot \Delta x = [\rho_{ijk} - \rho_{i-1jk}] \cdot X_x \Big|_{i-1/2}, \quad 10.1.8a$$

if  $u_{ijk} < 0$  then

$$\overrightarrow{\delta x} \cdot \rho \cdot \Delta x = [\rho_{i+1jk} - \rho_{ijk}] \cdot X_x \Big|_{i+1/2} \quad 10.1.8b$$

$\overrightarrow{\delta x}$  and  $\overleftarrow{\delta x}$  are forward and backward differencing operators with similar expressions for the Y- and Z-directions. Eqn.(10.1.8) ensures the correct differencing to be used dependant on the sign of the velocity components U, V or W. One major advantage of this form for the artificial viscosity is that the extension to three dimensions is simple. The scheme is centrally differenced and second order accurate in subsonic regions. In supersonic regions the differencing is a combination of the second order accurate central differencing used in subsonic flow and first order accurate upwind differencing resulting from the addition of artificial viscosity. As the flow becomes increasingly supersonic, the increase of the factor  $C$ , makes the scheme increasingly retarded in the upwind direction. The present approach allows a complex elliptic-hyperbolic problem to be solved by a purely elliptic relaxation scheme.



CHAPTER 11

## AF2 FACTORISATION AND SOLUTION ALGORITHM

## 11.0 General

At the present time two main solution algorithms for the full potential equation are in use, the AF2 scheme and the multi-grid method. The latter makes successive use of coarse and fine meshes to reduce the errors associated with the low and high frequencies of the error spectrum. Similarly the AF2 scheme uses acceleration parameters in a cyclic fashion. It must be noted that the multi-grid method must use some form of relaxation scheme, SLOR or AF2, to update grid points during each grid sweep. This suggests that the effective complexity of the computer code is doubled if a multi-grid strategy is used as compared to the use of an AF2 scheme alone.

The primary reason for not using the multi-grid method is that, for points lying inside the body there is no definable way to transfer information from the coarse mesh to the fine mesh. Another reason for adopting the AF2 scheme is that in the multi-grid method the implication of switching from coarse to fine meshes is to require extra computer storage. This is because of the nature of the present method. All the cell face areas for the grid points have to be stored. Hence, if two grids are continually in use then, two sets of cell face areas must be stored. This is not viable due to the limited store available. In addition, it may not allow for the presence of

more than one body in the flow field. Such unnecessary complications do not arise when the AF2 scheme is used.

### 11.1 Solution Algorithm

The collection of finite difference equations which result from the mass flow equation, applied to all cells in the computational domain, are solved by an AF2 factorisation scheme. The disturbance potential is updated by solving, simultaneously, for the correction in pseudo-time

$$\Delta \phi_{ijk} = \phi_{ijk}^{n+1} - \phi_{ijk}^n \quad 11.1.1$$

where the index  $n$  indicates the number of the sweep or equivalently a unit time step. Several guidelines for the construction of AF schemes can be formulated by considering the following general form for a two-level iteration procedure:

$$[N] \Delta = \sigma \cdot \alpha_1 \cdot \alpha_2 \cdot L(\phi^n) \quad 11.1.2$$

where  $\Delta$  is given by Eqn.(11.1.1),  $L(\phi^n)$  is the residual, which is a measure of how well the finite difference equation is satisfied by the  $n^{\text{th}}$  level,  $\alpha_1$  and  $\alpha_2$  are acceleration parameters, and  $\sigma$  is the relaxation parameter. The operator  $[N]$  determines the type of iterative procedure and, therefore,

determines the rate at which the solution procedure converges. In the approximate factorisation approach,  $[N]$  is chosen as a product of two or more factors indicated by

$$[N] = N_1 \cdot N_2 \quad 11.1.3$$

The factors  $N_1$  and  $N_2$  are chosen so that: (1) their product is an approximation to  $L$  and resembles  $L$  as closely as possible; (2) only simple matrix operations are required; (3) the overall scheme is stable. In the present case the operator  $L$  is given by Eqn.(8.3.5). Rewriting Eqn.(11.1.2) as

$$[N_1] \cdot [N_2] \Delta = \sigma \cdot \alpha_1 \cdot \alpha_2 \cdot L(\phi^n) \quad 11.1.4$$

implies that the iteration procedure is achieved in two steps, firstly

$$F = [N_1]^{-1} \cdot \sigma \cdot \alpha_1 \cdot \alpha_2 \cdot L(\phi^n) \quad 11.1.5$$

and secondly

$$\Delta = [N_2]^{-1} \cdot F \quad 11.1.6$$

The matrices formed for  $F$  and  $\Delta$  are tri-diagonal and hence can easily be inverted. Because the factors  $N_1$  and  $N_2$  can be chosen to ensure that sweeping occurs in alternate directions for each inversion step, information is quickly transmitted in

all directions. The whole grid is updated twice during one complete time-step, hence the method is potentially fast. It does, however, require careful choice of factors. In the present method, based on the scheme of Catherall (Ref.67), the three-dimensional factors are

$$\left[ \alpha_1 \alpha_2 \frac{z_2|_k}{\Delta z} \rho_{ijk} - \alpha_2 \frac{x_2|_i}{\Delta x} W_{x_{i+1/2}k}^{\frac{1}{2}} \vec{\delta x} \rho_{i-1/2jk} - \frac{y_2|_j}{\Delta y} \left( \vec{\delta y} \rho_{ij-1/2k} W_{y_{ij+1/2}k} \vec{\delta y} \right) \right] F_{ijk} \\ = \alpha_1 \alpha_2 \sigma \cdot L(\phi)_{ijk} \quad 11.1.7$$

$$\left[ \alpha_1 \alpha_2 \frac{y_2|_j}{\Delta y} + \alpha_1 W_{x_{ij+1/2}k}^{\frac{1}{2}} \frac{x_2|_i}{\Delta x} \vec{\delta x} - \vec{\delta z} \left( W_{z_{ijk}} \frac{z_2|_{k-1}}{\Delta z} \vec{\delta z} \right) \right] \Delta_{ijk} = F_{ijk}$$

Inherent in the scheme is the direction of sweeping of the grid. On expansion of the two factors, the right side of the equation does not match the left side. This apparent anomaly is not a handicap since at convergence the difference tends to zero and the factors multiplying  $\Delta$  become irrelevant. The parameters  $\alpha_1$  and  $\alpha_2$  are called 'acceleration parameters', and as the name suggests they must be carefully chosen so as to achieve the fastest convergence rate. The stability of this type of factorisation in two-dimensions is discussed in Ref.68. The first factor demands that the grid be swept in the upstream direction since the factor can be expanded as

$$A.F_{ijk} + B.F_{ijk} - C.[D.(F_{ij+1jk} - F_{ijk}) - E.(F_{ijk} - F_{ij-1jk})] \quad 11.1.8 \\ = \alpha_1 \alpha_2 \sigma \cdot L(\phi)_{ijk} + B.F_{i+1jk}$$

Where A, B, C, D and E are functions of quantities evaluated at the previous iteration level. The terms  $F_{i,j+1,k}$ ,  $F_{i,j,k}$ , and  $F_{i,j-1,k}$  are the unknowns. Their solution is dependant upon the right side of Eqn.(11.1.8) which contains  $F_{i+1,j,k}$ . The dummy plane at  $I=NX+1$  where  $NX+1$  is the number of points in the X-direction is set as

$$F(NX+1,J,K)=0 \text{ for } J=1,NY+1, K=1,NZ+1$$

Fig.42 shows the direction of sweep for the first step. On each Y-Z-plane the vertical grid lines are updated line by line. The grid is swept by constant X-planes. The second factor when expanded becomes

$$A' \Delta_{ijk} + B' \Delta_{ijk} - C' [D' (\Delta_{ijk+1} - \Delta_{ijk})$$

11.1.9

$$- E' (\Delta_{ijk} - \Delta_{ijk-1})] = F_{ijk} + B' \Delta_{i-1,jk}$$

Where A', B', C', D' and E' are evaluated from the previous iteration level. The term on the right side implies that the sweep be performed in the downstream direction on constant X-planes. The combination of both sweeps is equivalent to one time step or one complete iteration. Catherall (Ref.67) recommends that the acceleration parameters,  $\alpha_1$  and  $\alpha_2$  be chosen for each iteration from the series

$$\alpha_1 = \alpha_{1k} \left( \frac{\alpha_{1k}}{\alpha_{1k}} \right)^{\frac{k-1}{N\alpha-1}}$$

11.1.10

$$\alpha_2 = \alpha_{2k} \left( \frac{\alpha_{2k}}{\alpha_{2k}} \right)^{\frac{k-1}{N\alpha-1}}, \quad k = 1, 2, \dots, N\alpha$$

and theory gives

$$\alpha_{1h} = \alpha_{2h} = 2$$

$$\alpha_{1\lambda} = \bar{\alpha}_1 \cdot \Delta Z, \alpha_{2\lambda} = \bar{\alpha}_2 \cdot \Delta Y$$

11.1.11

$$\sigma = 2$$

and experiment suggests

$$\bar{\alpha}_1 = \bar{\alpha}_2 = 1$$

$$N_\alpha = 6$$

11.1.12

For difficult cases such as thick bodies and double body configurations the above values are changed, usually  $\alpha_{1\lambda}$  and  $\alpha_{2\lambda}$  are increased, and  $\sigma$  decreased.

It can be seen from Fig.43 how the effective residual varies with number of iterations. The AF2 scheme is usually of a magnitude faster than SLOR. The overall speed and hence iteration requirement is dependant on the flow geometry, such as the free-stream Mach number and angle of incidence. The rate of convergence is dependant on the number of bodies present and their configuration.

CHAPTER 12

## DISCUSSION AND RESULTS

## 12.1 General

From the basic mass flow equation a computer code was developed to reproduce the results for bodies described by Wedan and South. New and efficient algorithms were developed for calculating cell-surface areas, weighting functions, and a new AF2 scheme developed for three-dimensional geometry. The method was then further developed to compute transonic flow over double store configurations at incidence, and stagger. Comparisons for subsonic flow are made with SPARV (Ref.26) and with the ARA transonic, zero incidence program for single bodies at higher Mach numbers, (Ref.31). The method is also compared for accuracy with subsonic single body experimental tests carried out in the 8' by 6' wind-tunnel at Cranfield, (Ref.28).

The present method allows the flow about any body to be calculated, but only two types are considered. The ellipsoid, because the body surface has continuous slope and can be defined in all three dimensions, and the ogive-nose cylinder, because experimental results are readily available.

The ARA program can only be used for single axisymmetric bodies at zero angle of attack, and SPARV for subsonic single and multiple bodies in three-dimensional or axisymmetric form.

For subsonic flows around ellipsoids, the method is compared with SPARV. The results for the tangent ogive cylinder, with a nose length to maximum radius ratio of 4:1, are compared with SPARV and experimental results. For the high subsonic Mach numbers, the ARA program is used.

The double body case is compared with SPARV and finally, results for the double body case at transonic speeds at various angles of attack are presented. The latter are not compared with either experimental or theoretical results because none are available to the author.

All results are allowed to converge so that the residual is reduced by four orders of magnitude, and the acceleration and relaxation parameters altered such that the solution is stable.

## 12.2 Transonic Comparisons

When comparing the results obtained for axisymmetric bodies, by the ARA transonic program, a number of factors must be taken into consideration. The ARA method is based on Jameson's rotated difference scheme in non-conservative form, using an aligned mesh (Ref.52), whilst the present method is conservative and uses a non-aligned Cartesian grid. Although the ARA method is more complex, the use of rotated coordinates ensures that the calculation of  $\phi$  is always based on the correct difference whether in subsonic regions or supersonic regions. The use of an aligned mesh ensures that grid points lie on the body surface and the flow tangency condition at the



surface is easily satisfied. In the present approach, a grid point does not necessarily lie on the body boundary and all quantities that are required at the body surface are obtained by extrapolation. In the presence of shock waves, this will automatically introduce errors into the calculation. Referring to Fig.44, the potential at A is obtained from

$$\phi_A = \phi_2 + (\phi_2 - \phi_1) \cdot \frac{x_2}{x_1} \quad 12.2.1$$

Such a formula predicts the potential,  $\phi_A$  at A to be in the same domain as the potentials  $\phi_2$  and  $\phi_1$ . This is seriously in error because  $\phi_2$  and  $\phi_1$  lie outside the shock wave influence, whilst  $\phi_A$  lies inside. For the present method there is no apparent way to overcome this difficulty. Similarly, the potential at B is again incorrect but to a lesser extent, the potential at C is correctly predicted by Eqn.(12.2.1) To ensure accurate pressure calculations at the body surface, the number of grid points used in the y-direction would have to be increased. This is not a viable solution, since the storage requirements for the present three-dimensional program would exceed the allocation.

It is hoped that although the pressure distribution, obtained from the present method, will not agree exactly with the ARA results, the location of the shock wave will be the same.

### 12.3 Ellipsoid of Ratio 1:1

For a finite difference method using a non-aligned mesh and SLOR as the solution algorithm (Ref.40), the sphere proves to be a difficult case because information cannot readily be transmitted in the upstream direction. Although AF2 schemes alleviate this problem, the flow tangency condition is difficult to satisfy, and special finite difference formulae have to be used to obtain the potential value for a point lying just inside the body boundary.

For the present method, although the number of iterations required to produce a converged result is large, of the order of 60, there is no difficulty in satisfying the flow tangency condition. In general, for bodies having a high radius of curvature at the leading and trailing edges, the method requires more iterations to converge than for more slender bodies, such as ellipsoids of ratio 8:1. For the sphere, the values of the acceleration parameters,  $\alpha_{1A}$  and  $\alpha_{2A}$ , and the value for the relaxation parameter,  $\sigma$ , had to be varied until the solution became stable and converged. In addition, the position of the grid lines produced by the stretching functions had to be carefully monitored to reduce the risk of instability, although this latter effect is more prominent in the presence of shock waves. The results for the subsonic case, Fig.45, uses a mesh with 64 grid points in the x-direction and 40 in each of the y- and z-directions. There is good agreement with SPARV which used 64 longitudinal points and 32 circumferential points.

#### 12.4 Ellipsoid of Ratio 8:1 at 5 Degree Incidence

The present study is being undertaken to analyse the flow around missile shaped bodies. To generate a body having a fineness ratio more typical of a guided weapon, the major axis to minor axis of the ellipsoid is increased to 8:1 and placed at an incidence of 5 degrees to the horizontal axis. Due to the body being slender, the solution converged much more rapidly and produced results which agreed very well with those obtained by SPARV, see Fig.46, using 60 longitudinal panels and 14 semi-circumferential panels.

It must be mentioned that the C.P.U. requirement for the present method is of a magnitude greater than that required by SPARV. This is due to SPARV utilising the symmetry of the problem whilst the present method computes the flow around the ellipsoid in a fully three-dimensional sense. Also, the present method calculates quantities in the whole flow-field, whereas SPARV only calculates quantities on the body surface. To achieve a better comparison of C.P.U. time it would be more realistic to input the body shape in terms of x-, y-, and z-coordinates, for the SPARV results.

#### 12.5 Tangent Ogive Cylinder Results

It can be concluded from the previous results that the present method is in good agreement as compared with the numerical method, SPARV. The present method is compared for accuracy against experimental results for tangent ogive cylinder, having nose fineness ratio of 4:1, at subsonic flow for various incidences.

The experimental results carried out by Davies (Ref.28) for the 0.14 and 4.14 degrees incidence are compared in Figs.47 and 48. The closure used for the numerical calculation is an oblate ellipsoid. There are discrepancies between the numerical and the experimental results due to the exclusion of viscous effects in the numerical scheme.

## 12.6 Tangent Ogive Cylinders in Transonic Flow

The present method compares well with results produced by SPARV for the single body at low subsonic mach numbers. It was decided to test the method for transonic flow at zero incidence and compare the results with the ARA program. Figs.49 to 51, show the results for various mach numbers at zero incidence. All the results other than  $M=0.9$  show good agreement. The  $M=0.9$  case is not as accurate due to insufficient grid points in the shock region. It is apparent that the ARA program, although more accurate than the present method, cannot be used to observe the pressure distribution over the aft section of the missile. Such data is useful to have when comparing the effects of using differing closures. Also, there is no ability to place the body at incidence throughout the subsonic to low transonic flow region.

The angle of incidence is increased for various Mach numbers and the variation in position and value of the main suction peak observed. The Mach number is varied from 0.5 to 0.9 and the incidence kept at zero. From the results on Figs.49 to 51, it can be seen that as the mach number is increased, the

suction peak becomes larger. The position of the shock does not seem to move, though there is a small move towards the nose-cylinder junction, and the shock becomes more defined. If the mach number is fixed and the angle of incidence is increased, there is a little variation in position and magnitude of the suction peak, Figs.52 to 55. For the upper surface there is movement of the location towards the nose. There are differences in the pressure distributions between Fig.52a and Fig.52b, the former used a grid of  $100 \times 30 \times 30$  and the latter a grid of  $60 \times 44 \times 44$ . The distribution in Fig.52b is much smoother. It seems that the solution is dependant on the number of grid points placed in the y- and z-directions.

During the evaluation of the above results, the author was confined to using a fairly coarse mesh, also the effects of increasing the mach number resulted in the program needing to use a smaller value of relaxation parameter. This resulted in an increase in C.P.U requirement and increase in the number of iterations needed for the result to converge. Such observations apply only to the higher mach number and incidence cases. The results for the incidence cases have 'peaks' in the pressure distributions, the causes of which are discussed later.

The next section deals primarily with the double body case, with varying distances between the two bodies. SPARV is used to verify the subsonic results for both the ellipsoids and the tangent ogive bodies. For all the double body cases presented the number of grid points used in the x-direction was 60, the

number in the y-, and z-direction was 44. There are 15 points in the y-direction below the lower body and above the upper body, with 17 points between the centre-lines of the two bodies. The bodies are located above each other in the y-direction. The spacing refers to the distance between the line mid-way between the body centre-lines and the nearest body surface. This has been non-dimensionalised with respect to the body length.

### 12.7 Double Ellipsoids of Fineness Ratio 4:1

Having presented the results for a single body, the initial two body comparison is for ellipsoids. The subsonic comparison uses a spacing of 0.025 and zero incidence.

The subsonic zero incidence case was compared with SPARV, Fig.56. The results agree well showing the suction peak occurring at the point of maximum thickness. Varying the mach number and angle of incidence causes an increase in the suction peak value and little change in it's position, see Figs.57 and 58.

### 12.8 Double Ogive-Cylinder Configurations

Figs.59 to 63 depict the behaviour of the pressure distribution on double ogive-cylinder bodies for separations of 0.05 and 0.025. The subsonic results agree well with SPARV up to the closure region. Aft of the junction between the cylinder and the closure, the results disagree due to the

present method using far fewer grid points than SPARV. Such discrepancies cannot be overcome due to limited computer storage available to the user. Nevertheless, it can be concluded that the two methods would be in better agreement if the present method could deploy more grid points on the aft section of the body.

The remaining results, shown in Figs.64 to 70, are presented to observe the effects of increasing the free-stream mach number until the flow becomes critical.

If the incidence is fixed and the free-stream mach number varied, the location of the main suction peak moves towards the nose and the magnitude increases. If the bodies are brought closer the absolute value of the peak increases. The top body produces less lift than the bottom body due to the upper surface of the bottom body experiencing accelerated flow between the two bodies. The flow accelerating between the two bodies causes the suction peak on the lower surface of the top body to be greater than the suction peak on the lower surface of the bottom body. Fig.71, shows the variation of the suction peak value with mach number for 5 degrees incidence. The upper surface of the bottom body and the upper surface of the top body have almost the same values of peak pressure, whilst the other two surfaces vary significantly. The general shape of the curves are similar for all surfaces. At zero incidence the top surface of the top body has the same pressure distribution as the bottom surface of the bottom body. Similarly, the bottom and top surfaces of the top and bottom bodies respectively, have the same distribution.

If the mach number is fixed and the angle of incidence of the configuration is increased, then the location of the suction peaks for both bodies, move towards the nose. Also the top surfaces generate increasing lift and the bottom surfaces generate decreasing lift.

### 12.9 Double Ogive-Cylinders with Stagger

The remaining results concentrate on the effects of staggering the bodies by moving the top body forward. The subsonic cases for 0 and 5 degrees incidence are compared with SPARV. The free-stream mach number is then increased to 0.5 for 0 and 5 degrees incidence. From Figs.72 to 75, it can be seen that the results agree fairly well with SPARV for the initial 75% of the body. The aft closure is in error, this is due to insufficient number of points available for accurate flow resolution.

The pressure distributions for the surfaces of the bottom body are different as compared to those of the top body. The flow accelerating over the trailing edge of the top body causes the pressure distribution on the top surface of the bottom body to become more negative. Away from the the trailing edge of the top body, the flow decelerates and there is some pressure recovery, until the flow accelerates over the trailing edge of the bottom body. The bottom surface of the top body experiences the effects of the flow accelerating over the nose of the bottom body, causing the peak suction pressure to be less pronounced. The top surface of the top body has the expected pressure distribution.



From Figs.76 to 79, increasing the free-stream mach number to 0.5, and varying the incidence between 0 and 5 degrees, does not effect the form of the pressure distribution. The values of the peak suction pressure are increased and there is a movement of the location of the peak towards the nose.

There are irregularities in the pressure distributions for the double ogive-cylinder configurations due to a lack of points that can be placed on each body. Effectively, if there are a total of 44 points in the y-direction, then each half of the computational space containing the bodies has 22 points. This is not sufficient for accurate flow resolution. It has been shown in Figs.52a and 52b, for a single body, that the pressure distribution becomes smoother by increasing the number of points in the y-direction. Due to limited computer storage, an increase in points in the y- and z-directions meant reducing the number in the x-direction. This caused a reduction in the flow resolution and accuracy of the pressure distributions. Similarly, the double-body configurations are also affected. It seems likely that a total increase in points in all directions will result in smoother and more accurate pressure distributions.

CHAPTER 13

## CONCLUSIONS

The research program has been concerned with developing existing numerical methods and producing programs which are economical in the use of the computer, whilst being as accurate as possible. The applicability of the methods has been extended to a variety of flow problems ranging from a single axisymmetric body moving in curvilinear motion to the effects of transonic flow on a staggered double body configuration.

The initial research programme dealt with approximating an axisymmetric body using surface source panels. Satisfying Laplace's equation resulted in integral equations which could be solved for the required source distribution on each panel. The method proved to be computationally more efficient than existing methods and required less computer storage. Although the method is applicable to both blunt and pointed body shapes, the placement of the surface panels requires careful consideration. To avoid discrepancies in the surface pressure distribution, and hence the normal loads, the longitudinal dimension of the panels must vary smoothly over the length of the body. Applying the method to curvilinear motion was not difficult and gave good results for an ellipsoid of ratio 4:1.

The latter part of the research was aimed towards developing a transonic flow method which could predict the aerodynamic characteristics of fully three-dimensional bodies. The method made use of the full potential equation in conservative form

and was approximated using finite differences. The space enclosing the body configuration is divided into rectangular cells for which mass continuity is satisfied. Transformation or stretching functions are used to map the infinite physical space to a bounded computational domain. The algorithm involves updating the solution, by marching in both upstream and downstream directions, to ensure rapid transfer of data throughout the whole flow-field. In the present approach, the artificial viscosity required, to ensure stability in supersonic regions, is introduced by retarding the density. This simplifies the method and allows an elliptic solution procedure to be used on a mixed elliptic-hyperbolic problem. The resulting algorithm requires only simple tri-diagonal matrix operations. Pressure coefficient distributions show good agreement with other methods. It can be concluded that it is not necessary to match the computational grid to the body surface, and first order cell face area and potential extrapolation on to the body surface are sufficient.

The relative stability and speed of convergence is dependant on the acceleration and relaxation parameters. In many single and double body configurations, at high subsonic Mach numbers, these parameters are altered to stabilise the solution. Varying the input value of the radius of curvature, at the body nose and tail, affects the grid-line spacing at the leading the trailing edges. This in turn affects the accuracy of results. Other parameters, such as those which determine the amount of artificial viscosity used for the high subsonic Mach numbers are not fully tested, but kept fixed to maximise the amount of

damping used. For both single and double body configurations the accuracy of the method was much reduced due to the limitation on the amount of computer storage available. Comparisons for high subsonic flow at zero incidence can be improved by re-clustering the grid points around the location of the shock. The accuracy of the results, at the trailing edge, for the two body cases could be enhanced by using a greater number of grid points in that region.

The present full potential method is able to produce a complete description of the whole flow field containing the body. The total velocity at the cell centres can be used to gain an understanding of the flow patterns around the body or bodies under consideration. It is however, limited to flows having no or weak shocks, the Mach number being 0.95 or less for single bodies and less than 0.9 for double body configurations. These limits vary with the amount of incidence input to the body.

The present method can be effectively used to observe body-body interference effects at mach numbers close to one for various values of incidence and yaw.

CHAPTER 14

## RECOMMENDATIONS FOR FURTHER WORK

## 14.1 General

From the previous results and discussions it is apparent that the present method provides a useful tool for predicting the aerodynamic characteristics of single and multiple bodies in subsonic and transonic flow. The present work has been applied to various body shapes, the method can be made more versatile with the following extensions and modifications.

## 14.2 Axisymmetric Two Body Configuration

The present work has dealt with the two body case in a limited sense, concentrating on bodies which have their axis parallel to the x-axis. Here, the whole configuration can be put at incidence, yaw, and one body staggered with respect to the other. The asymmetric case would involve one or both of the bodies at incidence to the horizontal axis, and maybe, experiencing a flow also at incidence, see Fig.80. This type of asymmetric configuration is computed by defining the rotated body surface in terms of the normal Cartesian coordinate system. Consider a body at incidence,  $\alpha_2$ , to the horizontal axis, Fig.81. Then, the coordinates of the body can be expressed in terms of the x,y coordinate system, as

$$\begin{aligned}x &= \cos\alpha_2 \cdot \bar{x} + \sin\alpha_2 \cdot \bar{y} \\y &= \cos\alpha_2 \cdot \bar{y} - \sin\alpha_2 \cdot \bar{x}\end{aligned}\tag{14.2.1}$$

Assuming that the top and bottom surfaces of the body are described by a continuous function, the equation for the top surface is

$$\bar{y} = f(\bar{x})\tag{14.2.2}$$

The body is placed in a pre-determined grid and a  $x$ -grid line passes through its nose. To enable the cell face areas to be determined, we need to calculate the distances of the top and bottom surfaces from the horizontal axis. Assume an initial guess  $y_0$ , which yields a value  $g_0$ , where

$$g_0 = g(x, y_0)$$

$$g_0 = f(x \cdot \cos\alpha_2 - y_0 \cdot \sin\alpha_2) - y_0 \cdot \cos\alpha_2 - x \cdot \sin\alpha_2\tag{14.2.3}$$

Then another value  $y_1$ , yielding  $g_1$ , is used to supply another approximation to the actual value  $y$ , (Fig.81). A better approximation is then

$$y_2 = y_1 - g_1 \cdot \left( \frac{y_1 - y_0}{g_1 - g_0} \right)\tag{14.2.4}$$

This implies that the value of  $y_2$  can be determined iteratively by

$$y_n = y_{n-1} - g_{n-1} \cdot \left( \frac{y_{n-1} - y_0}{g_{n-1} - g_0} \right) \quad 14.2.5$$

This will yield the upper and lower values for the body surfaces at all the x values which lie between the nose and tail of the body. To obtain the cell face areas, a similar procedure as outlined in Appendix.A1 can be used. The values obtained for the areas will only be approximate due to the above approximation together with the use of straight line segments as discussed in Appendix.A1.

If it is assumed that the angles of attack are small, the stretching functions used in the double body case can be applied.

To input an asymmetric yaw configuration, in addition to incidence, the above procedure can be repeated to calculate the x-, y-, and z-coordinates of the body. For the yaw case the stretching function in the x-direction is unaltered, but the z-direction stretching has to be redefined to achieve the required clustering of grid-lines.

### 14.3 Multiple Body Configurations

Although a maximum of two bodies was tested in the present work, the method is able to handle other configurations, such as three bodies lying either symmetrically or asymmetrically, see Fig.82. Each body is treated separately and the new surfaces obtained (section.4.2). There will be interaction

between the bodies, especially in the region enclosed by ABCD. The stretching must be altered to pack points in this region, and can be done by using a stretching similar to that used for the two body case, in both the y-, and z-directions. The x-direction stretching remains unaltered.

#### 14.4 Arbitrary Body Specification

In the present work, the body surfaces could be defined using algebraic expressions, allowing comparatively easy calculation of the cell face areas. This condition can be relaxed and an arbitrary body shape input. For a simple tangent-ogive body, the three parameters  $r_x$ ,  $r_y$ , and  $r_z$  must be specified, see Fig.83, to enable the stretchings to be produced and the physical mesh set up. For non-analytically defined bodies, the program can be designed to proceed in the following way, refer to Fig.84 in the proceeding analysis:

Fig.84 shows the cross section of a body at a particular location,  $x_1$ , along it's length. The face showing lies in the y-z-plane. It is assumed that the body coordinate axis are centered at the point O. The cross section surface can be defined by stating the coordinates of all points  $I=I_1....I_n$ . The body surface points can be joined using straight-line segments and the cell face areas for each cell calculated as described in Appendix.A1. These coordinates are then input for all x-sections. The whole body has now been described.



#### 14.5 The Use of Surface Splines

The calculation of the cell face areas and the pressure distribution on the surface of the body makes use of straight line segments to approximate the body shape. Consider the calculation of a cell face area, then if the body shape changes rapidly, the situation shown in Fig.85, requires the need for a better body approximation. The area under the straight line-segment joining points BC (Fig.85) is  $S_2$ , and the area of the cell lying outside the body given by

$$S_1 = \Delta Y \cdot \Delta X - S_2 \quad 14.5.1$$

By the use of splines the body surface can be approximated much more accurately and the area lying outside becomes

$$S_1 = \Delta Y \cdot \Delta X - S_2 - S_3 \quad 14.5.2$$

where  $S_2+S_3$  is the new area under the points BC which are joined by some curve. The accuracy in the use of straight line segments is increased by increasing the number of points in the grid. This results in a decrease in the speed of convergence and it becomes necessary to allocate more computer storage, making the method less efficient.

#### 14.6 Normal Force Calculation

All results presented depict the variation of pressure along the x-axis of the meridian profile curve of the body. Velocity components and density at all grid points in the field is known enabling the pressure at all points to be determined. The pressure at the points formed by the intersection of the body surface and any grid line can be calculated. For example,

consider a body cross-section at some x-station, Fig.86. The pressure at point P is determined by a horizontal extrapolation along line J. Similarly, the pressure at point Q is determined by a vertical extrapolation along line K. This is done for all such intersecting grid lines. The results can then be integrated around the circumference of the body at that x-station to obtain the normal force. This involves the calculation of the distance along the surface between each surface point, S1, S2 etc.

#### 14.7 Accurate Shock Capture

Comparisons with the ARA program show that the present method smears the shock over a few grid widths (Fig.87) due to insufficient number of points around the x-station at which the shock occurs. To provide the method with a higher concentration of vertical grid lines, the stretching algorithm must be altered such that the required x-station becomes a parameter which controls the overall distribution of points in the x-direction. Once the position of the shock becomes known the stretching can be altered to cluster more grid lines around this point. This is similar to the SAG method used by Holst and Brown, (Ref.50).

APPENDIX A1

## DESCRIPTION OF THE FINITE VOLUME PROGRAM

## A1.1 General

The present program has been primarily designed for axisymmetric bodies although it has the capability to predict the flow about three-dimensional shapes, such as ellipsoids and missile shaped bodies with non-circular cross-sections. The program is able to give results for the flow about single or double body configurations at incidence and yaw. The two bodies tested in the present research are the ellipsoid and the ogive-nosed circular cylinder, with an elliptic closure, (Fig.88)

## A1.2 Initial Data Input

The program requests the number of bodies to be used in the calculation, either one or two, and enters the appropriate routine depending on the number chosen. The type of body is then selected, ellipsoid or missile. For either case the body dimensions are required, and input as follows.

## A1.2.1 Ellipsoid

The only dimensions required are the fineness ratio of the ellipsoid and this is input by specifying the lengths of the major and minor axis, (Fig.88). The lengths input are

scaled such that the overall length of the major axis becomes unity.

### A1.2.2 Missile

The type of missile that is most commonly used is shown in Fig.88, the values of the variables shown are input. In the present research, the nose is an ogive, a circular arc, and becomes tangent to the aft body at a distance  $A_1$  from the nose. The closure is added, usually elliptic, of fineness ratio  $A_3:R_1$ .

After obtaining the body parameters, the flow characteristics are input, such as the angles of attack and yaw and the free-stream Mach number. If a two body case is being tested, the program requires the amount of stagger and the distance between the centre line of the configuration and the nearest surface of either body. Lastly, the number of points required in the x-, y- and z-directions of the grid are input. In the two body configuration the number of points in the y-direction is calculated as the sum of the number of points between the centre-lines of the two bodies, the number lying below the bottom body, and the number above the top body, see Fig.89. They must all have odd values.

### A1.3 Calculation of a Cell Face Area

The proceeding section describes the method used to obtain the areas of the cell faces, which lie perpendicular to the x-,

y-, and z-directions. The procedure can also be used for the double body case.

Consider a body cross-section at some point  $X_1$ , see Fig.90, in the computing plane. The area associated with point  $J,K$  is  $ABCD$ . The distance between the full and broken grid lines is  $\Delta z/2$  in the z-direction and  $\Delta y/2$  in the y-direction. It can be seen from Fig.90 that a cell face can lie completely outside the body, as for point  $J_2, K_2$ , lie completely inside the body as for point  $J_1, K_1$ , or lie on the body boundary as for point  $J, K$ . All faces lying completely outside the body, such as  $A'B'C'D'$ , have an area  $\Delta z \cdot \Delta y/4$ , all faces lying inside the body have zero area, and the remaining type have to be determined as follows.

Consider the same section as in Fig.91a, the origin of the body axis system is assumed to lie at a point  $O$ , and the broken grid lines lie midway between the full grid lines. Each grid point, formed by the intersection of either set of lines, has associated horizontal and vertical distances. Consider point  $J, K$ , then the vertical distance for this point is  $a$  and the horizontal distance is  $b$ . Both distances for point  $J+1, K-1/2$  are zero, whilst the vertical distance for  $J-1/2, K-1/2$  is  $c$  and the horizontal distance is  $d$ . For point  $J+7/2, K$  the vertical distance is zero and the horizontal distance is  $h$ .

The lengths  $Z_r$  and  $Z_l$  are known for all horizontal grid lines, if the horizontal grid line does not cross the body boundary the two lengths are zero. Hence, for the point  $J, K$ , the

horizontal distance would be

$$b = (j+2-j) \cdot \Delta z - z_{\lambda} \quad \text{A1.3.1}$$

This is true only if  $(j+2-j) \cdot \Delta z$  is greater than  $z_{\lambda}$ . If it is less than  $z_{\lambda}$  the grid point lies within the body, and the associated horizontal distance is zero. If it is greater than  $z_{\lambda} + \Delta z/2$  then the horizontal distance is  $\Delta z/2$ . For the right half of the section, the horizontal distance for point  $J+7/2, K$  is given by

$$h = (j+4-j+2) \cdot \Delta z - z_r \quad \text{A1.3.2}$$

With similar conditions as the left half of the section.

The vertical distance associated with each grid point is determined in a similar fashion, as follows. Consider a new point  $J, K-5/2$ , Fig.91b. The lengths  $Y_b$  and  $Y_t$  are known for all vertical grid lines, if the grid line does not cross the body boundary, the two lengths are zero. Hence for the point  $J, K-5/2$  the vertical distance would be

$$c = [(k-1) - (k-5/2)] \cdot \Delta y - y_b \quad \text{A1.3.3}$$

This is true only if  $[(k-1) - (k-5/2)] \Delta y$  is greater than  $y_b$ . If it is less than  $y_b$ , then the grid point lies within the body and the associated horizontal distance is zero. If it is greater than  $y_b + \Delta y/2$  then the horizontal distance is  $\Delta y/2$ . The vertical distances for points lying above the

horizontal axis can be calculated in a similar fashion, for example, the vertical distance for point J,K is

$$a = [(k + 1/2) - (k - 1)] \cdot \Delta Y - Y_t \quad \text{A1.3.4}$$

Hence, the vertical and horizontal distances for all points, lying either on the full or broken grid lines, are known. Referring to Fig.92, the cell face area for the point J,K consists of four contributions, as shown by the shaded areas. This is true for all grid points formed by the intersection of the full grid lines, representing the actual computing grid. The four areas shown in Fig.92 can be easily determined since all the required lengths are known, from the preceding discussion. As an example, consider the point J-1/2, K-1/2, as in Fig.93. If the surface is S1, the area required is enclosed by the points W,X,Y, and Z. If the body surface is S2, then the area is enclosed by points W, X1, X2, Y1, and Z. For both cases the points X and Y, and X2 and Y1, are joined by straight line segments. The areas are given by, (see Fig.94),

$$\text{Area}|_{S_1} = (a+c) \cdot d, \quad d = \Delta z/2$$

A1.3.5

$$\text{Area}|_{S_2} = \frac{\Delta Y \cdot \Delta Z}{4} - 0.5 \left[ \left( \frac{\Delta Z}{2} - b \right) \cdot \left( \frac{\Delta Y}{2} - d \right) \right]$$

All the shaded areas in Fig.92, can be calculated in a similar fashion. Hence the total cell face area for the grid point J,K, shown in Fig.92, can be determined by adding the four values of the shaded areas.

The cell face areas formed by Y-plane and Z-plane body cuts can similarly be obtained. Hence for a particular cell point,  $I, J, K$ , all the cell face areas are known, see Fig.95. All the cell faces lie midway between computational grid points, for example, the face  $S_1$  lies midway between points  $I-1, J, K$  and  $I, J, K$  and  $S_4$  lies midway between points  $I, J, K$  and  $I, J+1, k$ . The number of possible ways the surface of a body can intersect a cell is discussed in the next section.

#### A1.4 Three-Dimensional Cell Investigation

There are sixteen possible ways a body surface can cut a particular cell face, Fig.96. To define and differentiate the possibilities, each of the grid points in the mesh is assigned a value of 1 or 0 depending on whether or not the grid point lies inside the body boundary. Analysing the face ABCD, the area lying outside the body boundary is calculated by connecting the points A and C by a straight-line segment. The area enclosed by points A, A', C', C, and D, is calculated as described in the previous section. If rotational similarity is used, then only four different equations need to be developed to calculate the areas for the sixteen possibilities.



REFERENCES

- (1) HESS, J.L., SMITH, A.M.O., "Calculation of Potential Flow about Arbitrary Bodies", Progress in Aerospace Science, Vol.8, 1967.
- (2) WEDAN, B., SOUTH, J.C., "A Method for Solving the Transonic Full-Potential Equation for General Configurations", Sixth AIAA C.F.D. Conference, Danvers, Macts, AIAA paper 83-1889-CP, July 1983.
- (3) GOLDSTEIN, S., Modern Developments in Fluid Dynamics, Dover, Vols.1 and 2, 1965
- (4) MYRING, D.F., "The Profile Drag of Bodies of Revolution in Subsonic Axisymmetric Flow", R.A.E. TR 72234, 1972.
- (5) THOMPSON, K.D., "Calculation of the Subsonic Normal force and Centre of Pressure Position of bodies of Revolution using Slender-Body Theory-Boundary Layer Method", Aeronautical Quarterly, Feb. 1980, pp.1-25.
- (6) CHOW, W.L., "Base Pressure of a Projectile within the Transonic Flight Regime", AIAA Jnl, Vol.23, No.3, March 1985.
- (7) LAMB, H., Hydrodynamics, Cambridge University Press, Sixth Edition, 1932.
- (8) KAPLAN, C., "Potential Flow about Elongated Bodies of

Revolution", NACA Report 516, 1935.

(9) SMITH, R.H., "Longitudinal Potential Flow about an Arbitrary Body of Revolution with Application to the Airship 'AKRON'", Jnl Aero Sci, Vol.3, Sept 1935, pp.26-31.

(10) JAMES, R.M., "A General Analytical Method for Axisymmetric Potential Flow about Bodies of Revolution", Computer Methods in Applied Mechanics and Engineering, 12, 1977, pp.47-67.

(11) RANKINE, W.J.M., "On the Mathematical Theory of Streamlines, Especially those with Four Foci and Upwards", Phil Trans. 161, 267, 1871.

(12) FUHRMANN, G., "Theoretische und Experimentelle Untersuchungen an Ballonmodellen", Zeitschrift fur Flugtechnik und Motorluftschiffart, Vol.11, 1911.

(13) KARMAN, TH. VON, "Calculation of Pressure Distribution on Airship Hulls", NACA TM 574, 1930.

(14) GOODWIN, F.K., DILLENIUS, M.F.E., NIELSEN, J.N., "Prediction of Six Degree of Freedom Store Separation Trajectories at speeds up to the Critical Speed", AFFDL-TR-72-83, Vols.1 and 2, Oct 1974.

(15) DYER, C.L., HEATH, C.B., "A Source-Doublet Approach to Modelling Triple Ejector Rack Store Configurations and Force Calculations", AFWAL-TR-81-3059, July 1981.

- (16) MARTIN, F.W., SAUNDERS, G.H., SMITH, C.J., "Image System Solution for Store Aerodynamics with Interference PT.1", Jnl Aircraft, 12, 3, March 1975, pp.151-155.
- (17) ADAMS, Mac C., SEARS, W.R., "Slender-Body Theory-Review and Extension", Jnl of Aero Sci, 20, 2, Feb 1953, pp.85-98.
- (18) LOTZ, J., "The Calculation of Potential Flow Past Airship Bodies in Yaw", NACA TM 675, 1931.
- (19) WEINSTEIN, A., "On Axially Symmetric Flows", Quart of App Maths, 5, 1948, p.379.
- (20) TUYL, A. Van, "Axially Symmetric Flow around a new Family of Half-Bodies", Quart of App Maths, 7, 1950, p399.
- (21) VANDREY, F., "A Method for Calculating the Pressure Distribution of a Body of Revolution Moving in a Circular path Through a Perfect Incompressible Fluid", ARC R-M 3139, 1953.
- (22) LANDWEBER, L., "The Axially Symmetric Potential Flow past Elongated Bodies of Revolution", David W.Taylor Model Basin Report 761, 1931.
- (23) ALBONE, C.M., "FORTRAN Programmes for Axisymmetric Potential Flow about Closed and Semi-Infinite Bodies", ARC CP 1216, 1972.
- (24) MOHAMMED, A., "An Integral Equation Technique for

Evaluating the Aerodynamic Characteristics of Bodies of Revolution in Curved Flight", M.Sc. Thesis, Cranfield Institute of Technology, 1982.

(25) JOHNSON, F.J., "A General Panel Method for the Analysis and Design of Arbitrary Configurations in Incompressible Flow", NASA CR 3079, May 1980.

(26) PETRIE, J.A.H., "Development of an Efficient and Versatile Panel Method for Aerodynamic Problems", Ph.D Thesis, University of Leeds, March 1979.

(27) JONES, R., "The Distribution of Pressures on a Prolate Spheroid", ARC R-M 1061, 1925.

(28) DAVIES, D.L., Wind Tunnel Test on Ogive-Cylinders in 8 by 6 Wind Tunnel at Cranfield Institute of Technology, 1985.

(29) KELLOGG, O.D., "Foundations of Potential Theory", Dover, 1953.

(30) NAG, Numerical Algorithms Library on the VAX 11/750.

(31) BAKER, T.J., "A Computer Program to Compute Transonic Flow over a Axisymmetric Solid Body", ARA Memo No.197.

(32) MURMAN, E.M., COLE, J.D., "Calculation of Plane Steady Transonic Flows", AIAA Jnl, Vol.9, pp.114-121, 1971.

(33) BAKER, T.J., "The Computation of Transonic Flow", ARA Memo 233, May 1981.

(34) HOLST, T.L., "A Fast Conservative Algorithm for Solving the Transonic Full Potential Equation", Prcs of AIAA Fourth C.F.D. Conference, Williamsburg, Va., AIAA Paper 79-1456, July 1979.

(35) CARR, M.P., FORSEY, C.R., " Developments in Coordinate Systems for Flow Field Problems", Prcs of Num Methods in Aero Fluid Dynamics Conference, Reading University, March 1981.

(36) GARBEDIAN, P., KORN, D., BAUER, F., "Supercritical Wing Sections 1", Lecture Notes in Economics and Mathematical Systems, Vol.66, pub. Springer 1972.

(37) SOUTH, F.C., JAMESON, A., "Relaxation Solutions for Inviscid Axisymmetric Transonic Flow over Blunt or Pointed Bodies", Prcs of AIAA C.F.D. Conference, Palm Springs, pp.8-17, 1973.

(38) CAUGHEY, D.A., "A Systematic Procedure for Generating Useful Conformal Mappings", Int Jnl Num Meth Eng, Vol.12, pp.1651-1657, 1978.

(39) JAMESON, A., CAUGHEY, D.A., "A Finite Volume Method for Transonic Potential Flow Calculations", AIAA Third C.F.D. Conference, Albq, N.M., June 1977.

(40) CARLSON, L.A., "Transonic Airfoil Analysis and Design Using Cartesian Coordinates", Prcs of AIAA Second C.F.D. Conference, Hartford, pp.175-183, June 1975.

(41) REYHNER, T.A., "Cartesian Mesh Solution for Axisymmetric Transonic Potential Flow around Inlets", AIAA Nineth Fluid and Plasma Dynamics Conference, San Diego, Calif, AIAA paper 76-421, July 1976.

(42) REYHNER, T.A., "Transonic Potential Flow around Axisymmetric Inlets and Bodies at Angle of Attack", AIAA, Vol.15, No.9, Sept 1977.

(43) REYHNER, T.A., "Transonic Potential Flow Computation about Three-Dimensional Inlets, Ducts and Bodies", AIAA Thirteenth Fluid and Plasma Dynamics Conference, Snowmass, Colorado, AIAA paper 80-1364, July 1980.

(44) THOMPSON, J.F., ed., "Numerical Grid Generation", North Holland Publishing co., New York 1982.

(45) THOMPSON, J.F., THOMAS, F.C., MARTIN, C.W., "Automatic Numerical Generation of Body Fitted Curvilinear Coordinate System for Field Containing any Number of Arbitrary Two-Dimensional Bodies", Jnl Comp Physics, Vol.15, pp.299-319, 1974.

(46) LEE, K.D., HUANG, M., YU, N.J., RUBBERT, P.E., "Grid Generation for General Three-Dimensional Configurations", Prcs

of the NASA Langley Workshop, Oct 1980.

(47) WEATHERHILL, N.P., FORSEY, C.R., "Grid Generation and Flow Calculations for Complex Aircraft Geometries using a Multi-Block Scheme", AIAA Paper 84-1665

(48) JAMESON, A., CAUGHEY, D.A., "Recent Progress in Finite Volume Calculations for Wing-Fuselage Combinations", AIAA Twelfth Fluid and Plasma Dynamics Conference, Williamsburg, Va., AIAA paper 79-1513, July 1979.

(49) WEATHERHILL, N.P., SHAW, J.A., FORSEY, C.R., "Grid Generation and Flow Calculations for Complex Aerodynamic Shapes", ARA Private Communication.

(50) HOLST, T.L., BROWN, B., "Transonic Airfoil Calculation Using Solution Adaptive Grids", Prcs AIAA Fifth C.F.D. Conference, pp.136-148, June 1981.

(51) SALAS, M.D. and GUMBERT, C.R., "Nonunique Solutions to the Transonic Potential Flow Equation", AIAA Jnl, Vol.22, No.1, Jan.1984.

(52) JAMESON, A., "Iterative Solution of Transonic Flows over Airfoils and Wings", Comms Pure and App Maths, Vol.27, 1974, pp.283-309.

(53) JAMESON, A., "Transonic Potential Flow Calculation Using Conservative Form", Prcs of AIAA Second C.F.D. Conference,

Hartford, Conn, June 1975, pp.148-161.

(54) MARTIN, E.D., LOMAX, H., "Rapid Finite Difference Computation of Subsonic and Transonic Aerodynamic Flows", AIAA paper 74-11, 1974.

(55) BALLHAUS, W.F., STEGER, J.L., "Implicit Approximate Factorisation Schemes for the Low Frequency Transonic Equation", NASA TM X-73082, Nov 1975.

(56) BALLHAUS, W.F., JAMESON, A., ALBERT, J., "Implicit Approximate Factorisation Schemes for the Efficient Solution of Steady Transonic Flow Problems", AIAA paper 77-634, June 1977.

(57) HOLST, T.L., "An Implicit Algorithm for the Conservative Transonic Full Potential Equation Using an Arbitrary Mesh", AIAA paper 78-1113, July 1978.

(58) BAKER, T.J., "A Fast Implicit Algorithm for the Conservative Potential Equation", Open Forum Presentation at AIAA Fourth C.F.D. Conference, Williamsburg, Va., July 1979.

(59) HAFEZ, M.M., SOUTH, J.C., MURMAN, E.M., "Artificial Compresibility Methods for Numerical Solution of Transonic Full Potential Equation", AIAA paper 78-1148, Seattle, Wash., July 1978.

(60) FEDERENKO, R.P., "The Speed of Convergence of one Interative Process", USSR Computational Mathematics and



Mathematical Physics, Vol.4, 1964, pp.227-235.

(61) BRANDT, A., "Multilevel Adaptive Technique (MLAT) for Fast Numerical Solution of Boundary Value Problems", Prcs of Third Int Conference on Num Meth in Fluid Mechanics, Vol.1, Springer-Verlag, New York, 1973, pp.82-89.

(62) SOUTH, J.C., BRANDT, A., "The Multi-Grid Method: Fast Relaxation for Transonic Flows", Advances in Engineering Science, NASA CP-2001, Vol.4, 1976, pp.1359-1369.

(63) JAMESON, A., "Acceleration of Transonic Potential Flow Calculation on Arbitrary Meshes by the Multiple Grid Method", AIAA paper 79-1458, July 1979.

(64) KUTLER, P. "A Perspective of Theoretical and Applied Computational Fluid Dynamics", AIAA Annual Conference, Reno, Jan 1983.

(65) MURMAN, E.M., "Analysis of Embedded Shock Waves Calculated by Relaxation Methods", Prcs of AIAA C.F.D. Conference, Palm Springs, Calif, July 1973.

(66) CATHERALL, D. and JOHNSON, M., "A Fast Method for Computing Transonic Two-Dimensional Potential Flows using a Non-Aligned Mesh", RAE Technical Report (to be published).

(67) CATHERALL, D., "The Optimization of Approximate-Factorisation Schemes for Solving Elliptic Partial

Differential Equations in Three Dimensions, featuring a new Two-Factor Scheme", RAE Technical Report (to be published).

(68) CATHERALL, D., "Optimum Approximate-Factorisation Schemes for Two Dimensional steady Potential Flow", AIAA Jnl, Vol.20, No.8, Aug 1982.

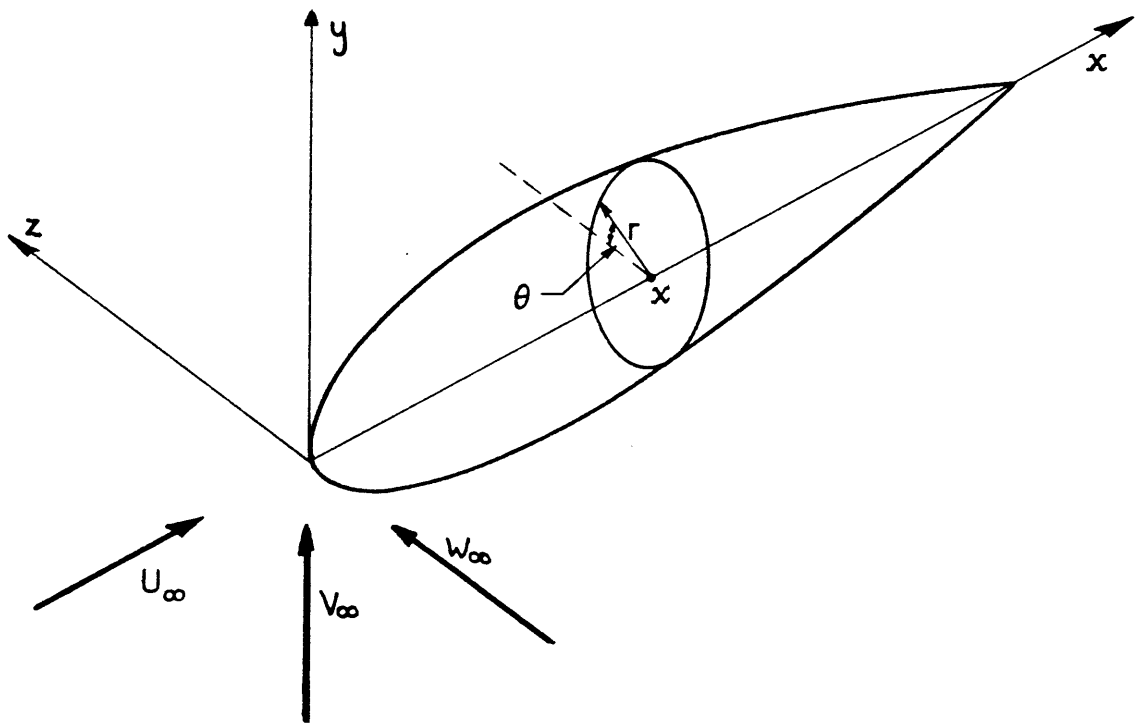
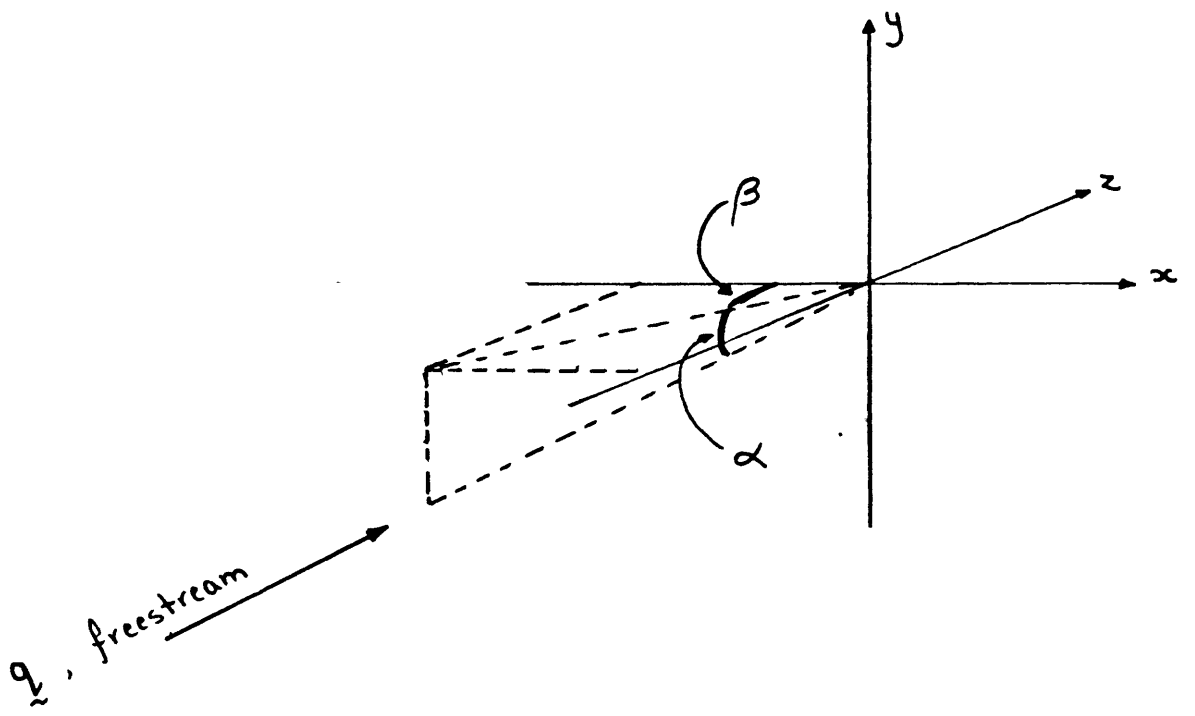
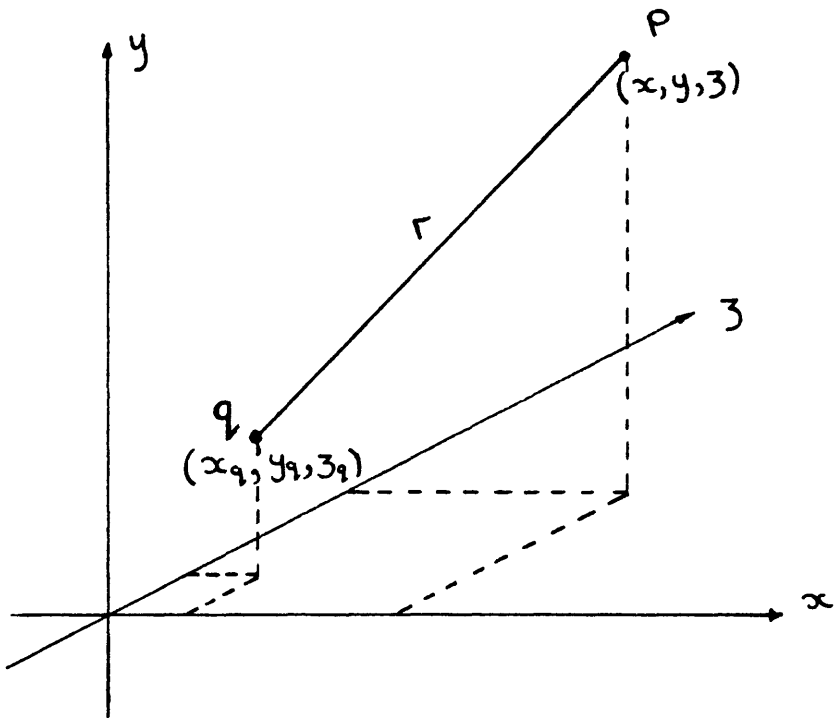


Figure 1 A ring source at  $x$  of radius  $r$ , in axial and cross flow.



$$r = [(x-x_q)^2 + (y-y_q)^2 + (z-z_q)^2]^{1/2}$$

Figure.2 Arbitrary point lying relative to a point-source

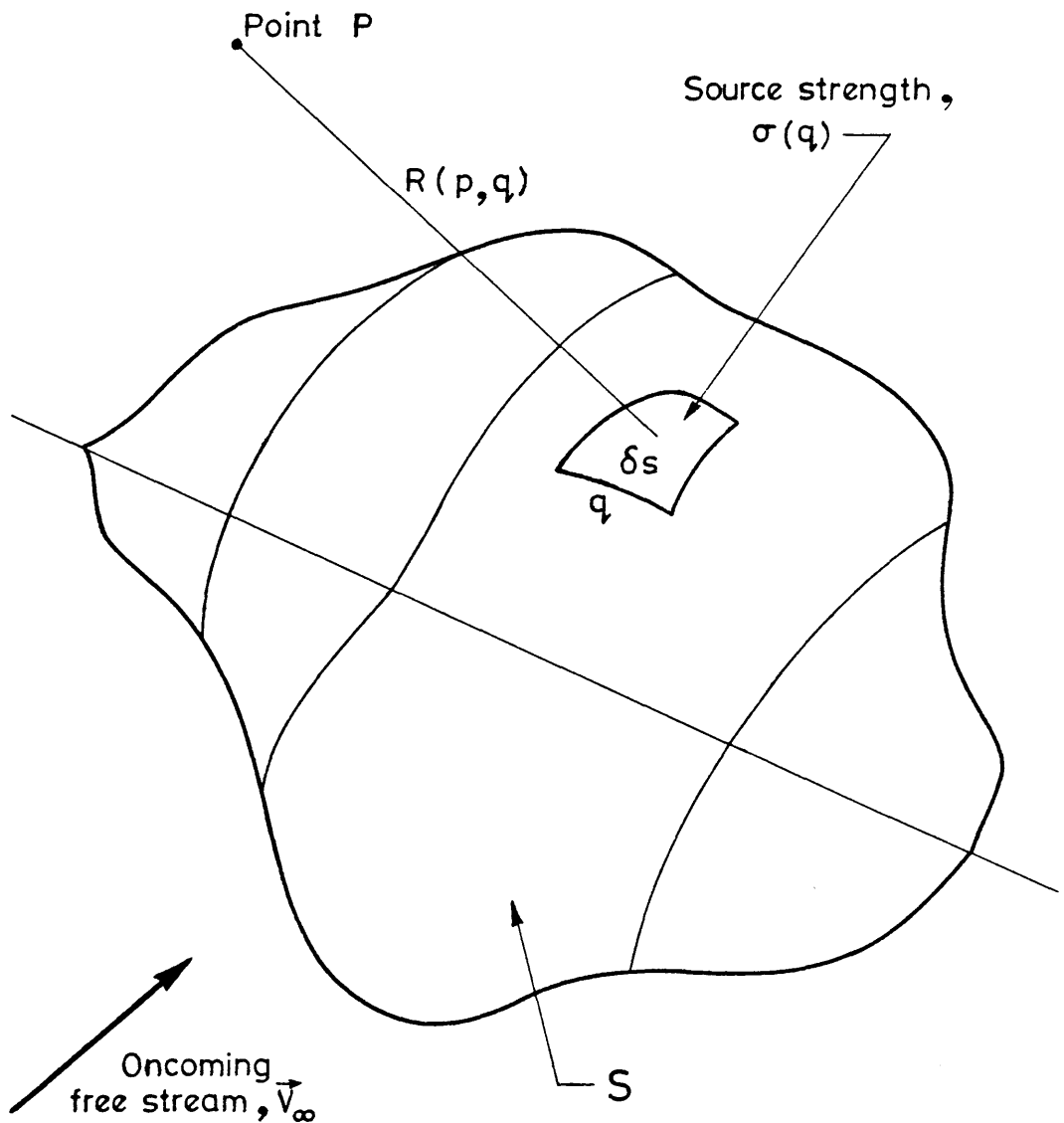


Figure.3 Elemental surface source distribution, on an arbitrary surface  $S$ , inducing a velocity at some point  $P$ .

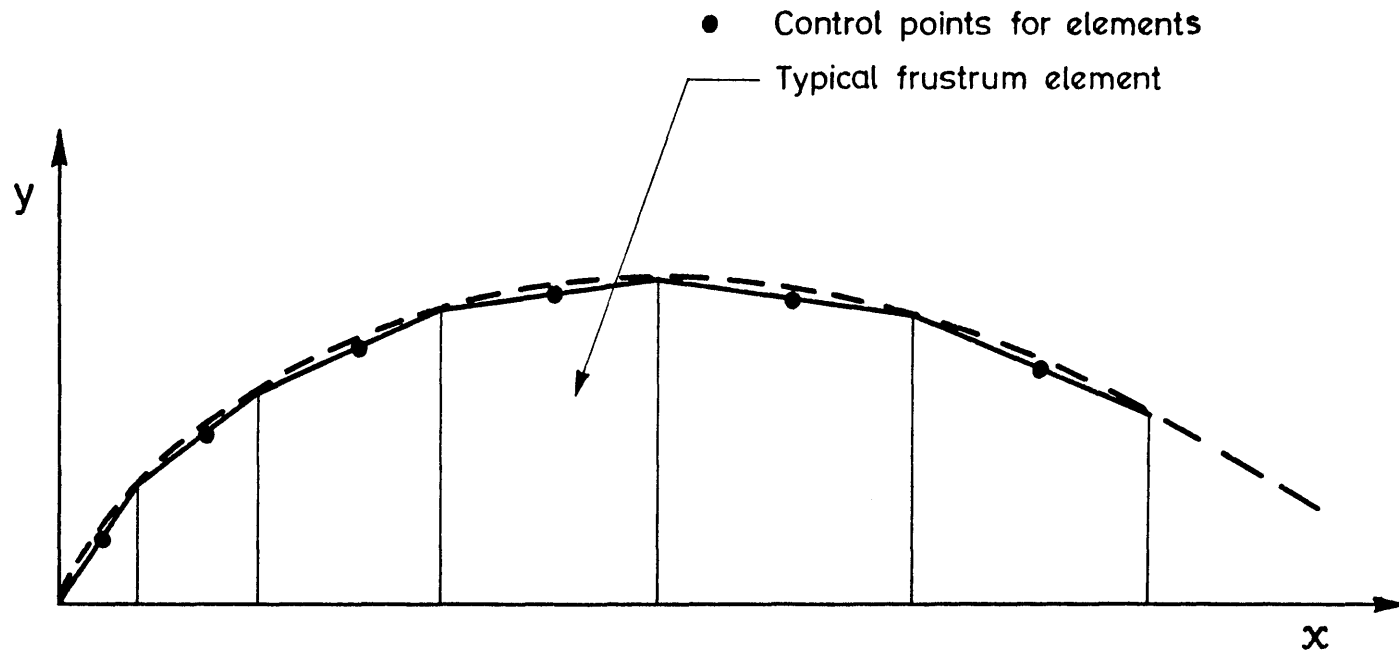


Figure 4 Defining an axisymmetric body using frustum elements.

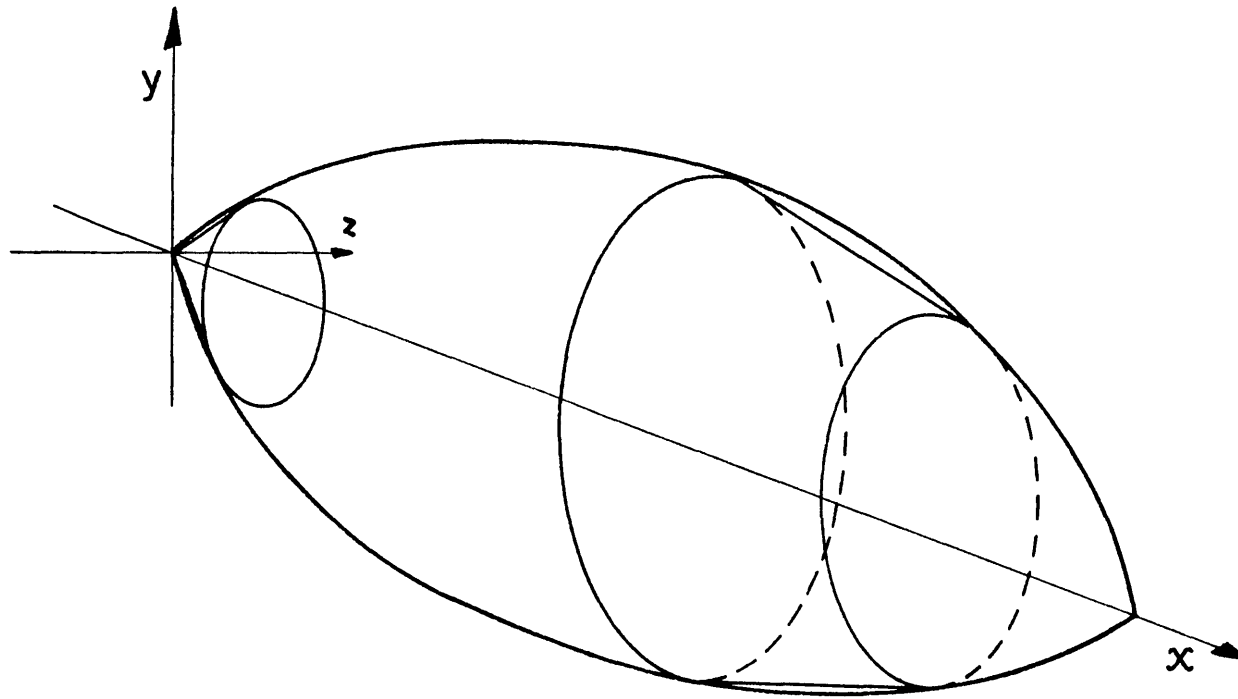


Figure 5 Nose and tail cones, with frustra make up the approximated shape of the axisymmetric body.

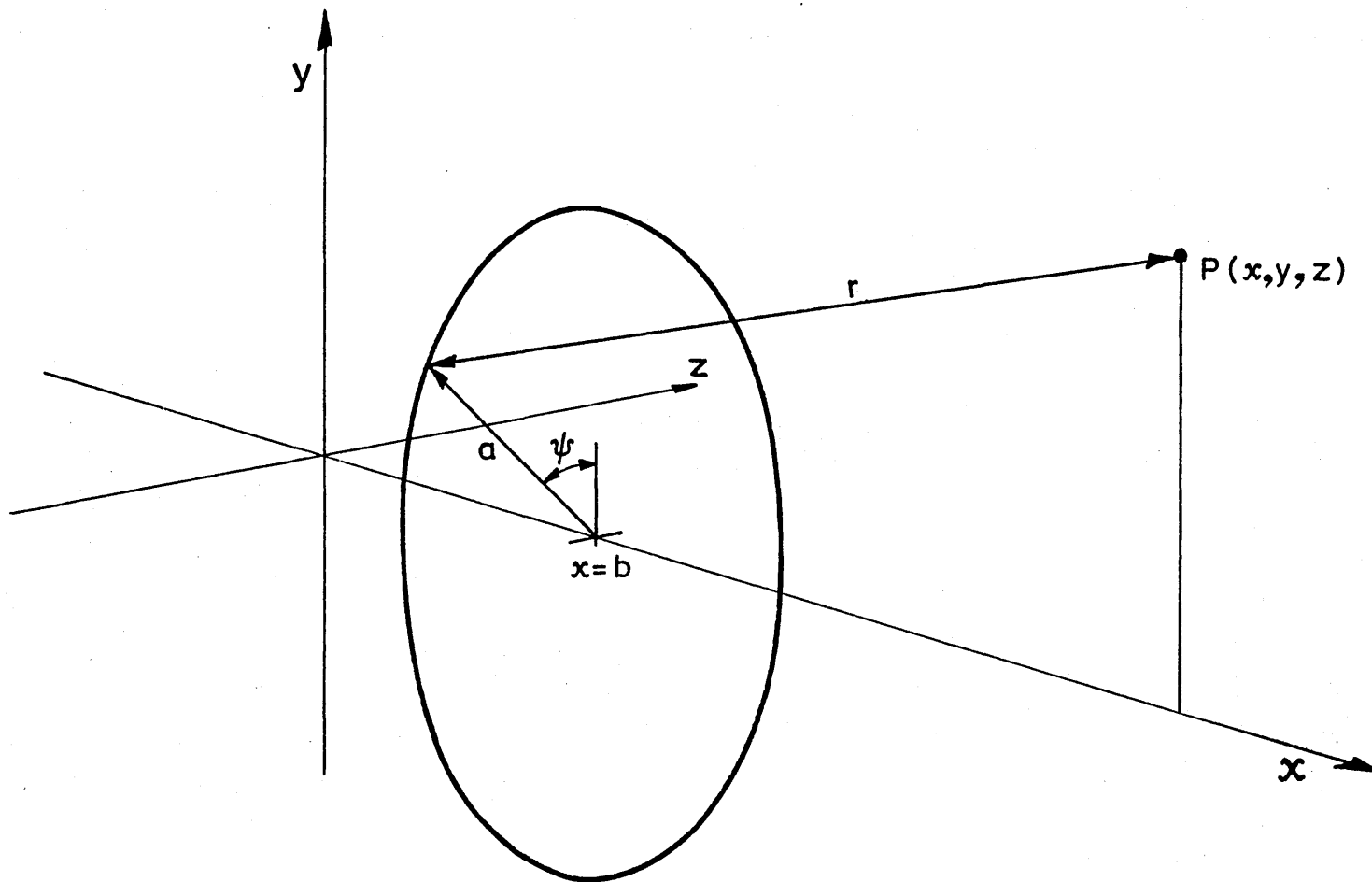


Figure 6 A ring source of constant strength lying in plane  $x=b$ .



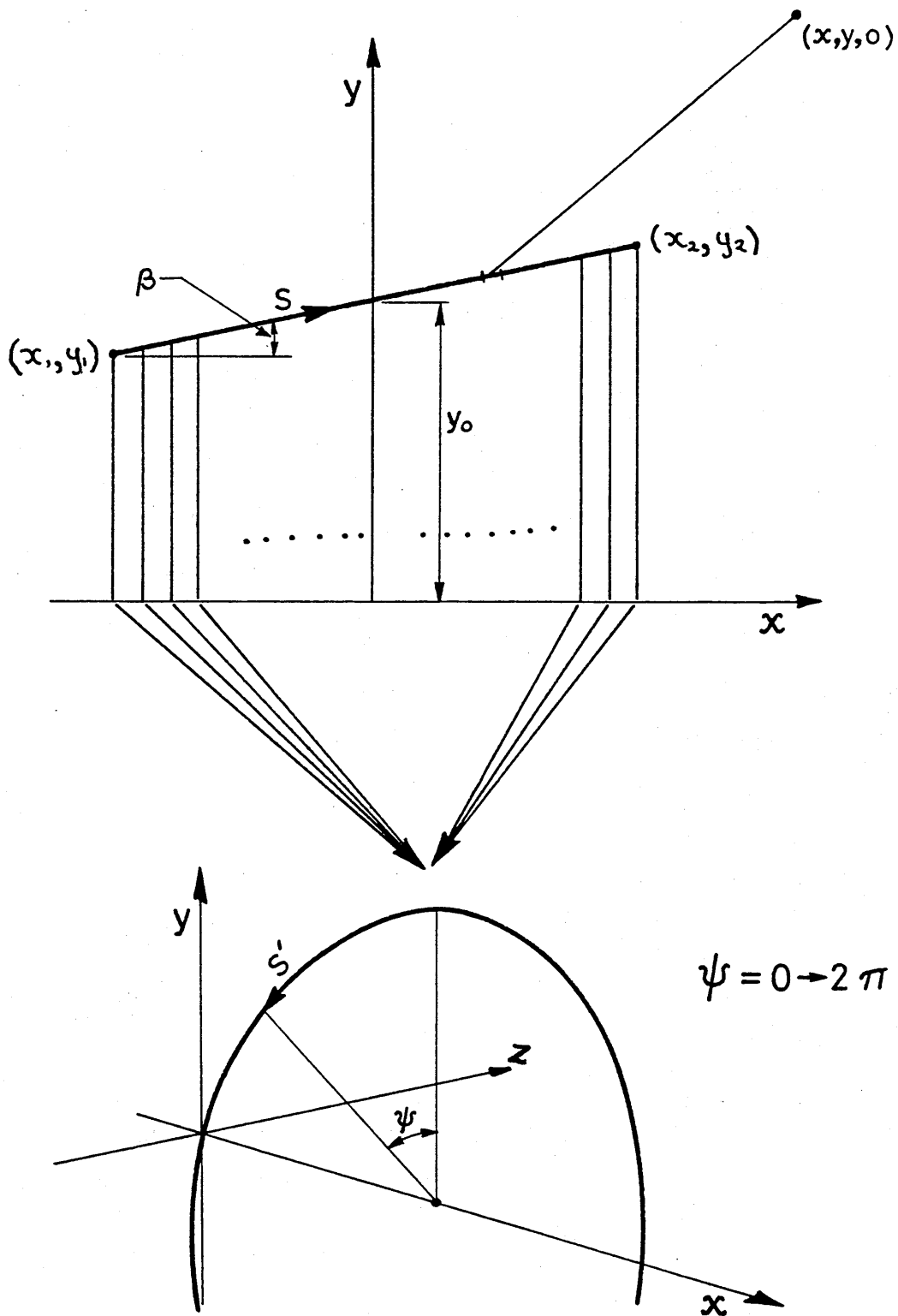


Figure 7 Integrations performed along a line segment (top) and around a circular ring at sections along the line segment.

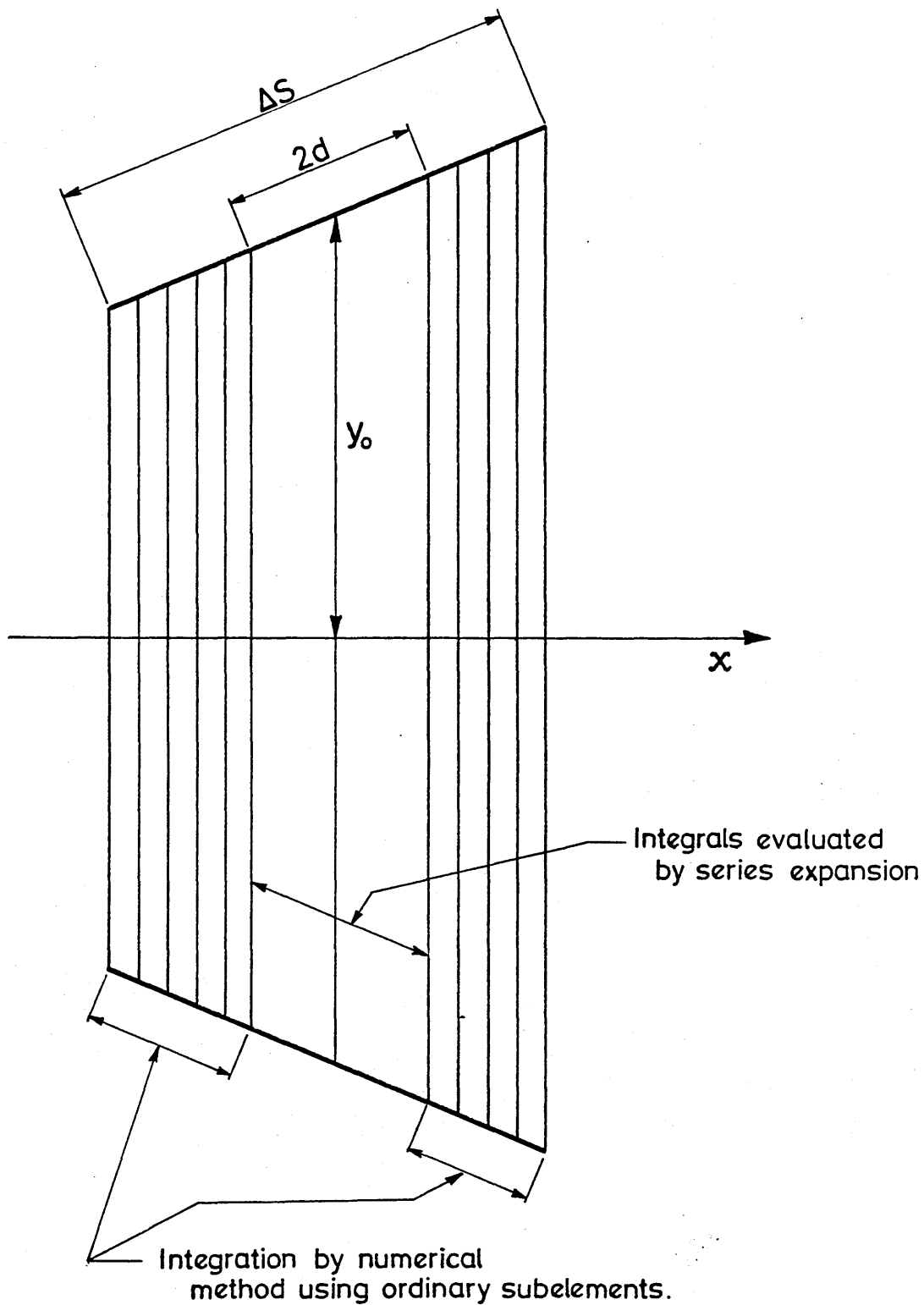


Figure 8 Treatment of a single subelement.

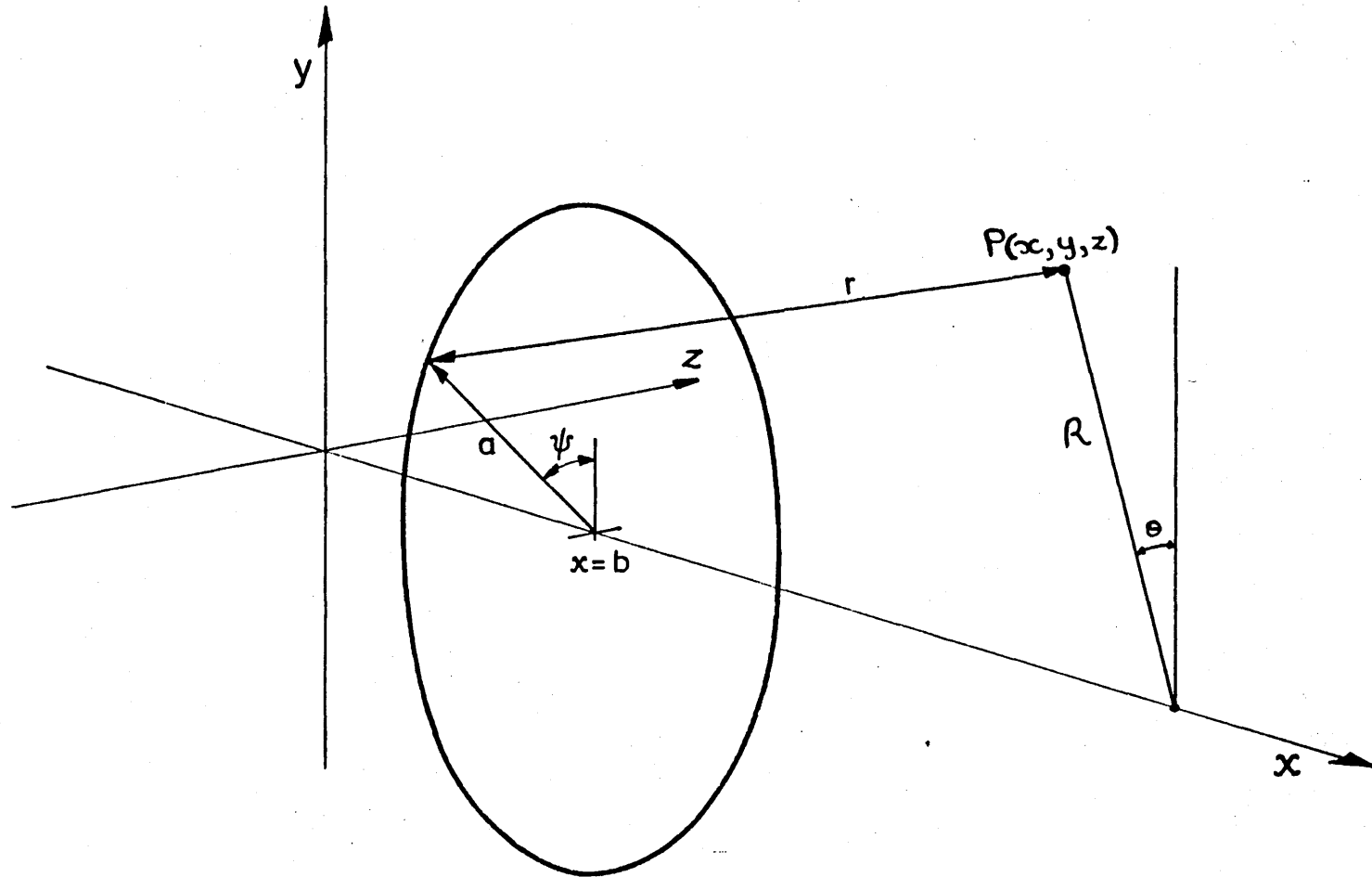


Figure.9 A ring source of strength  $\cos \psi$  lying in plane  $x=b$ .

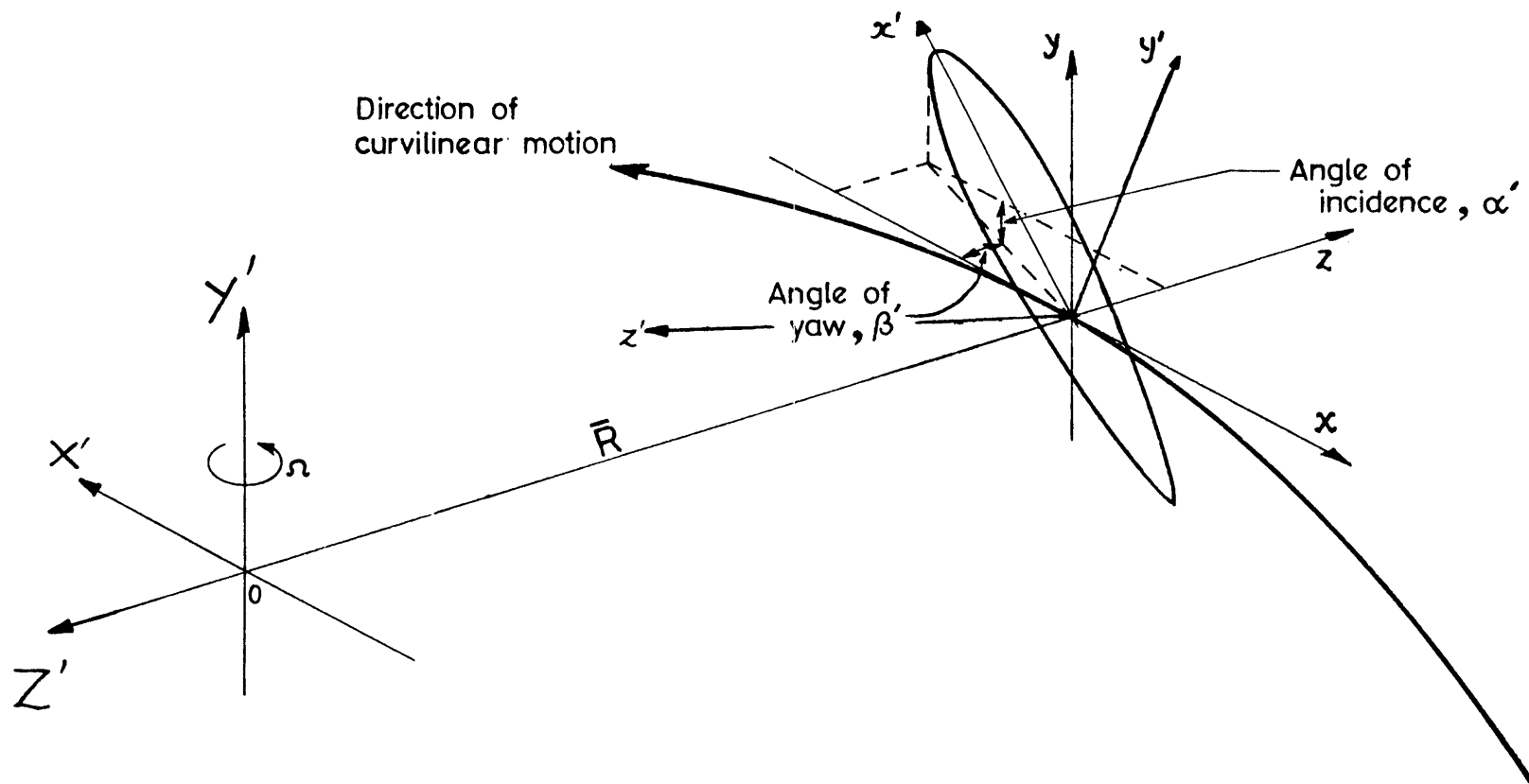


Figure 10 A body at incidence and yaw in curvilinear motion, with  $\bar{R}$  radius of curvature.

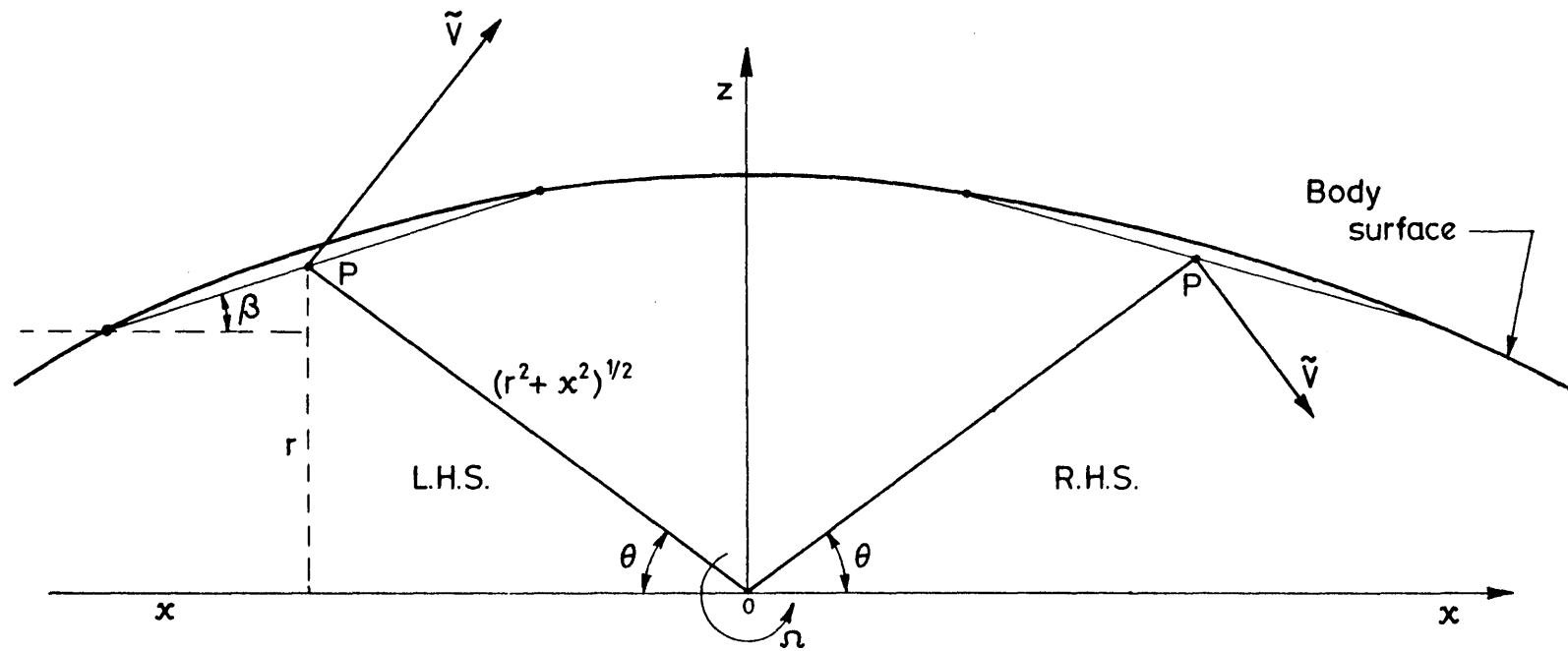
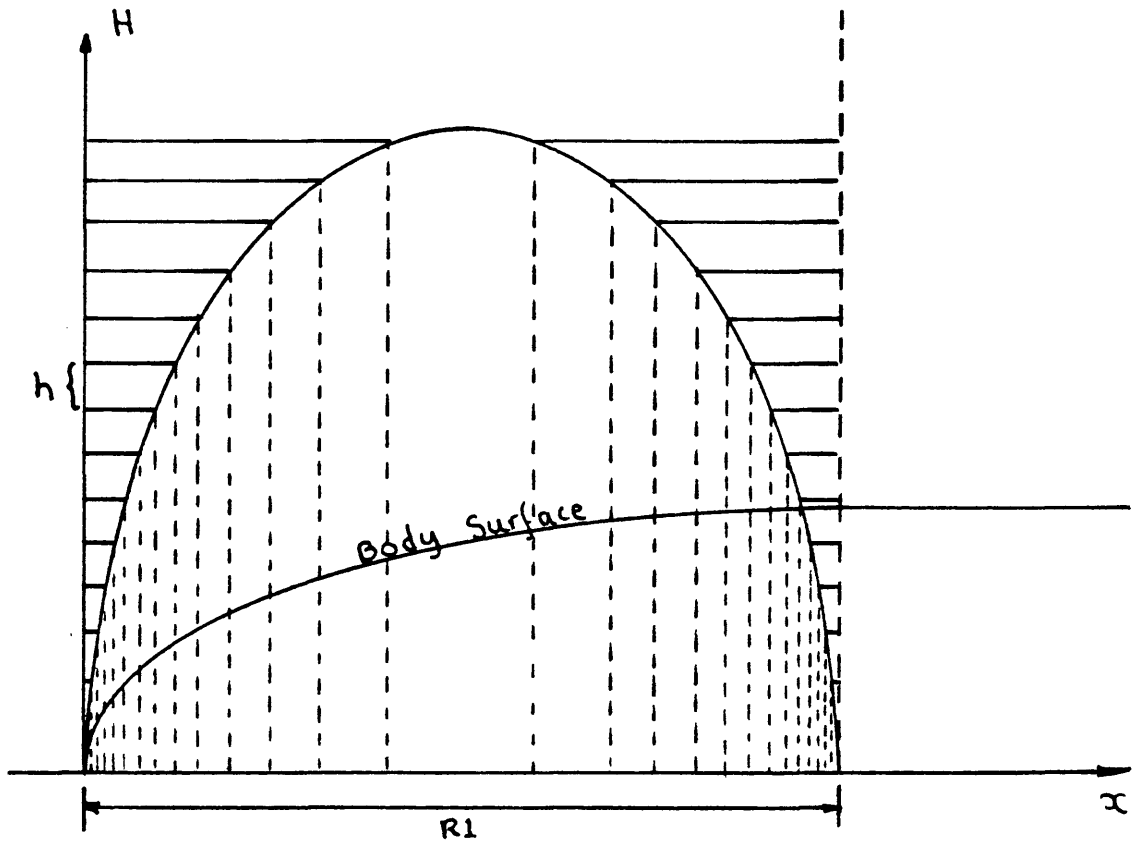


Figure 11 A panel, either side of the centre of gravity of the body, experiencing an angular velocity  $\tilde{v}$ .



$$i = 1, 2, \dots, n$$

$n$  = number of points on nose section.

$$h = 1/n$$

Figure 12 Point distribution over a nose or half body

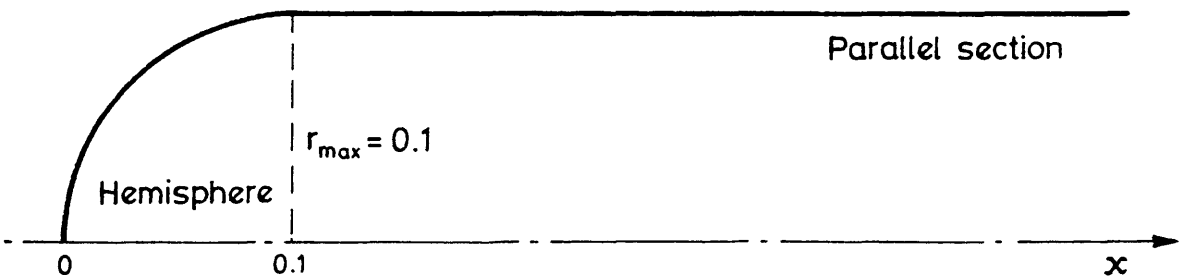
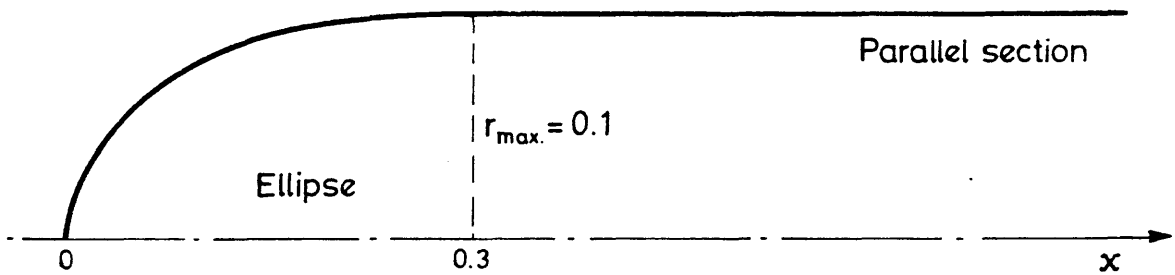
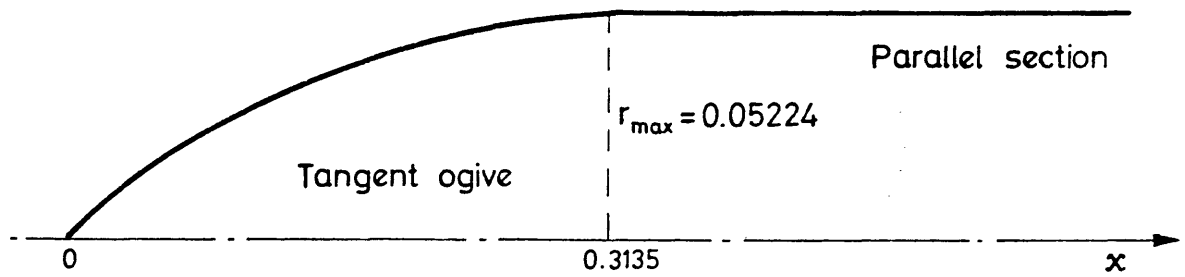


Figure 13 The non-analytic profiles, missile shapes used.

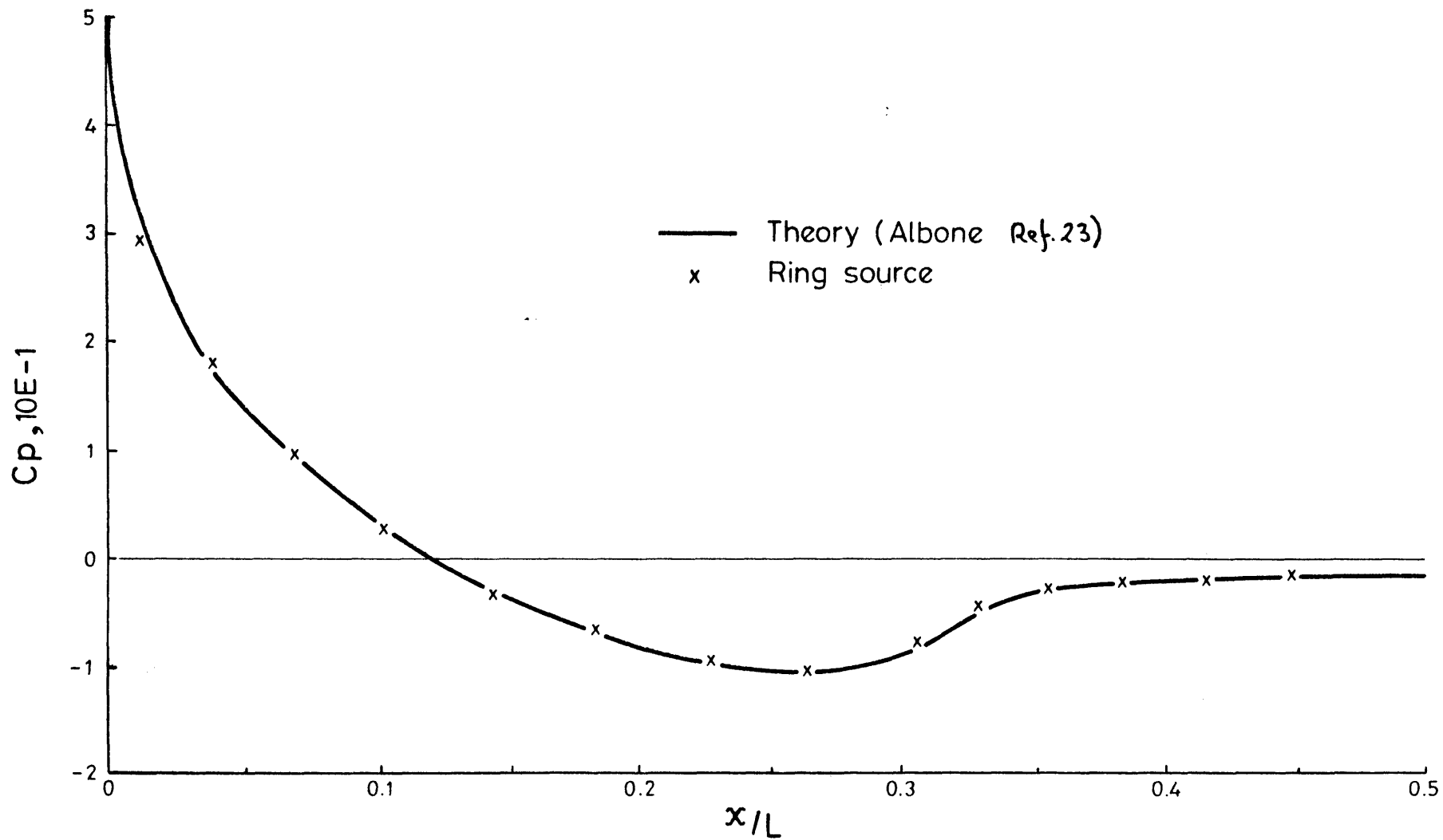


Figure 14 Pressure distribution on a tangent ogive cylinder.



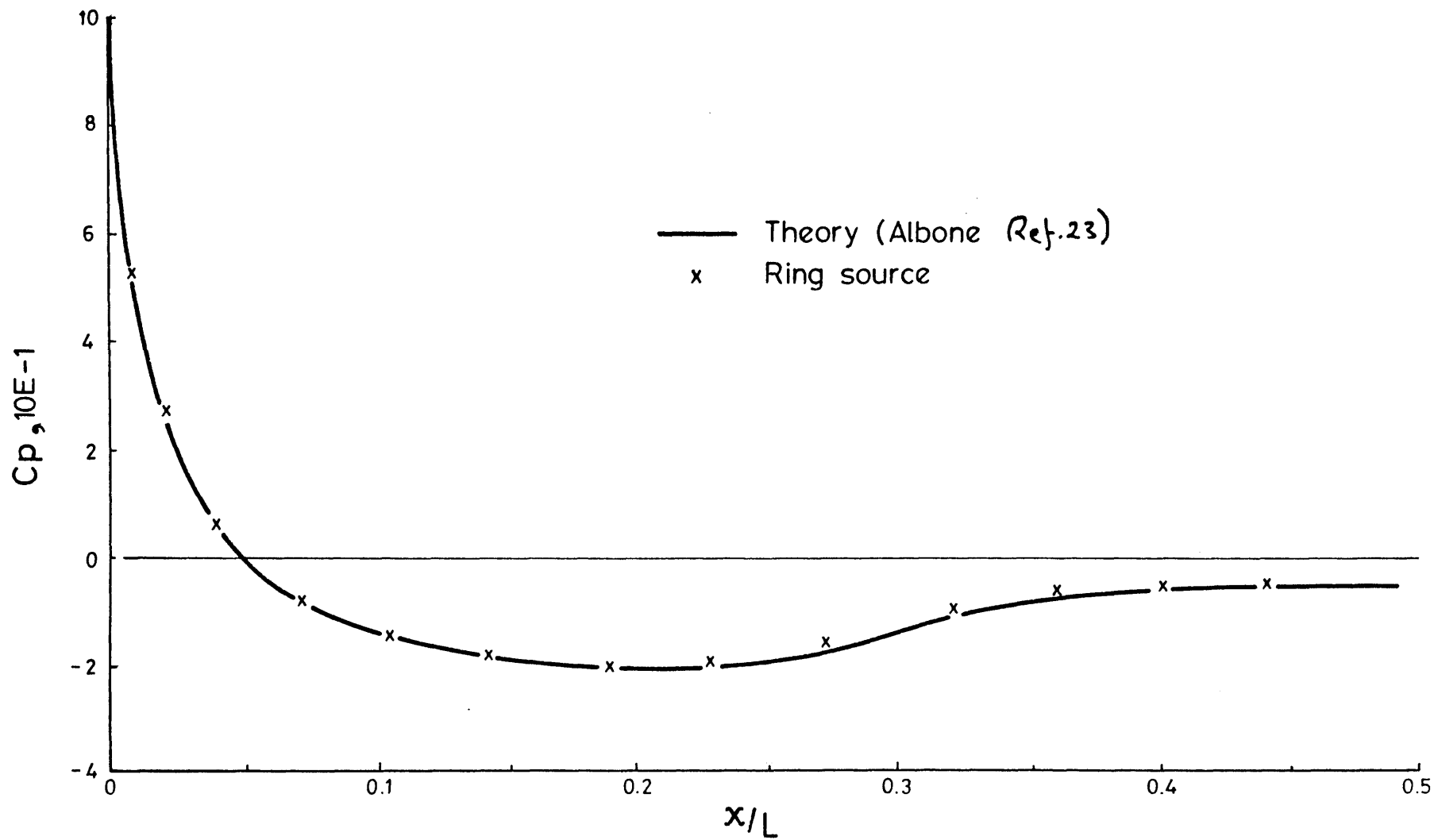


Figure 15 Pressure distribution on an ellipsoid cylinder.

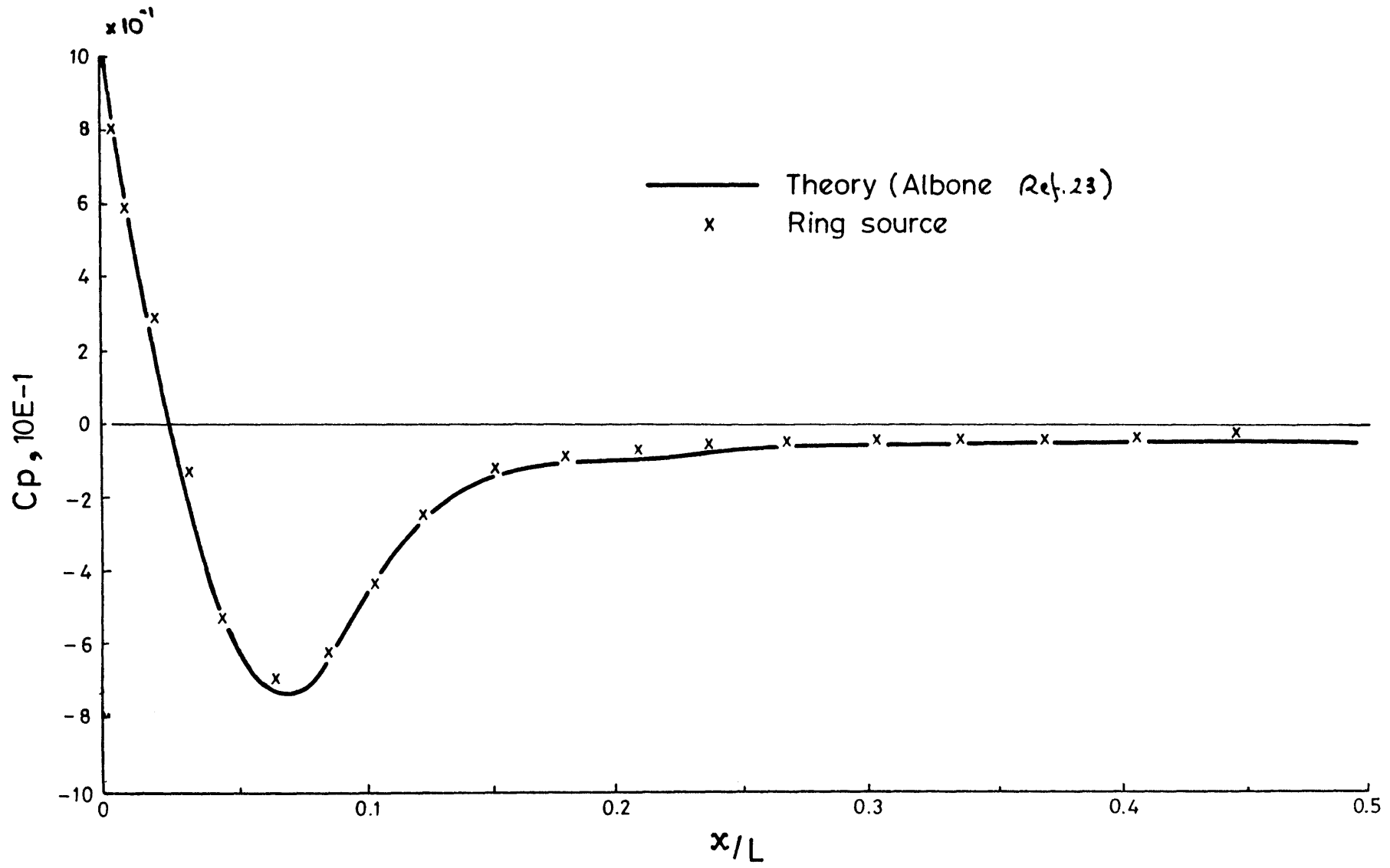


Figure 16 Pressure distribution on a hemisphere cylinder.

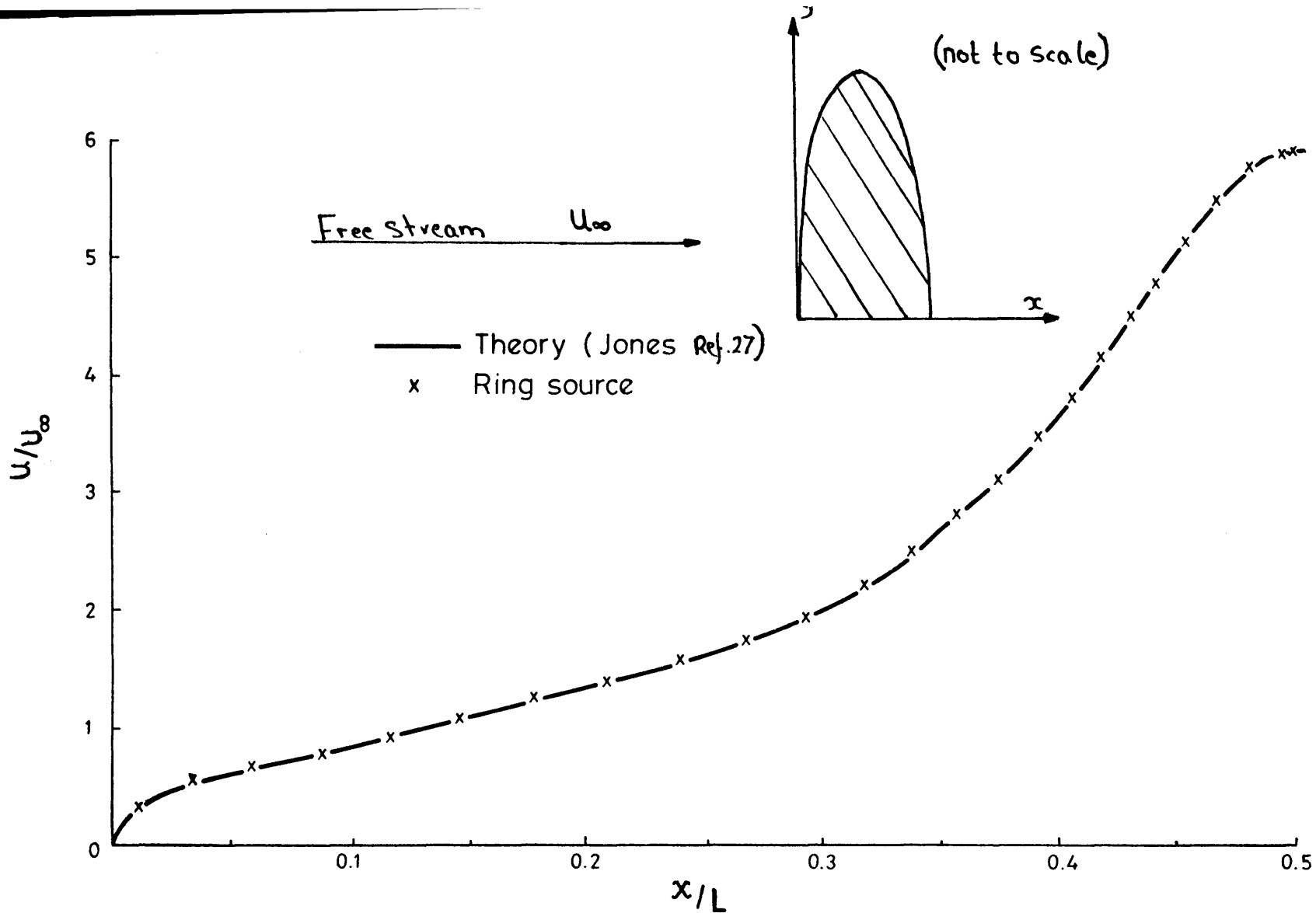


Figure 17 Ellipsoid of fineness ratio 1/8 in uniform oncoming flow.

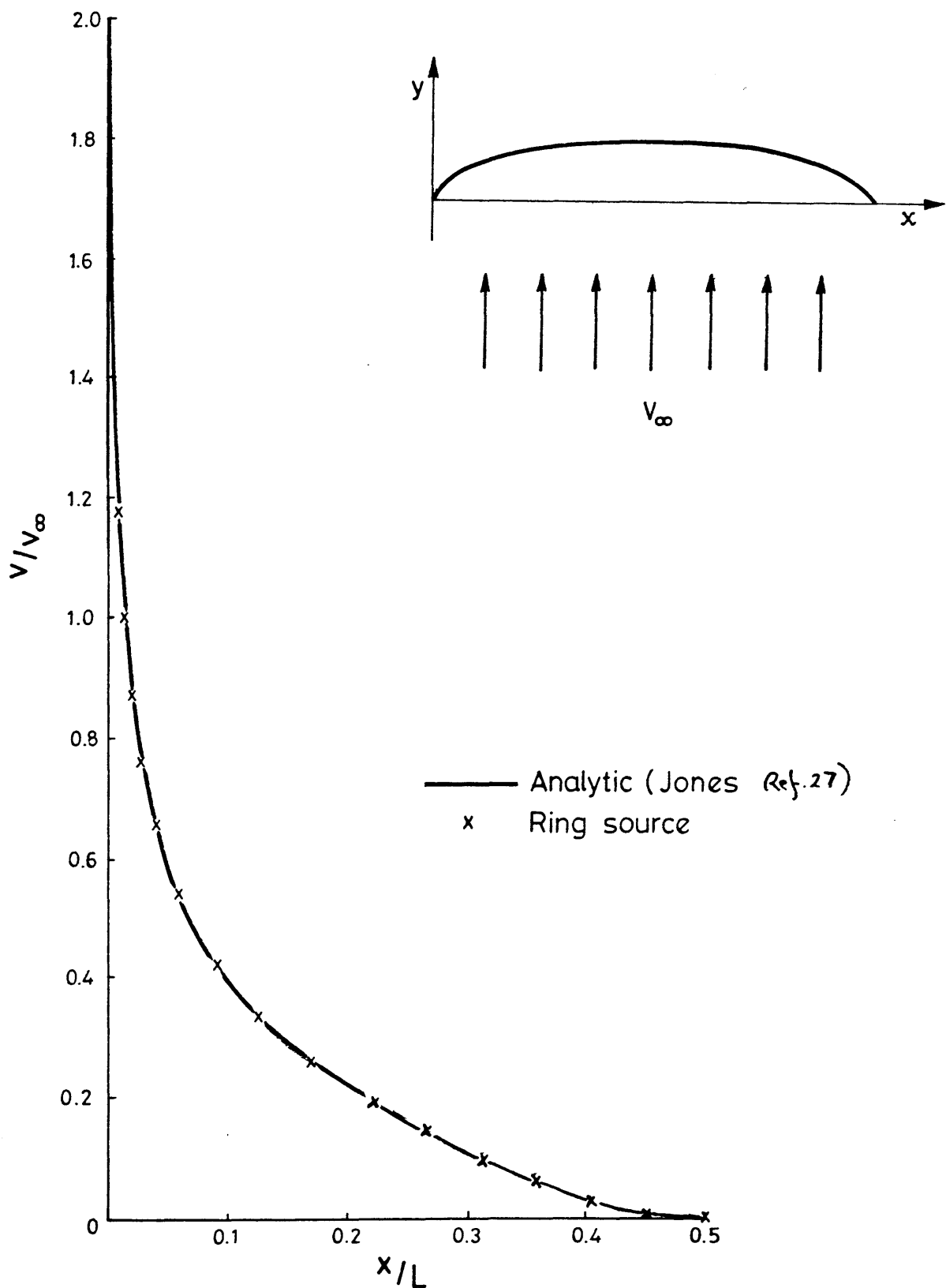


Figure 18 Ellipsoid of fineness ratio 8/1 in uniform cross flow.

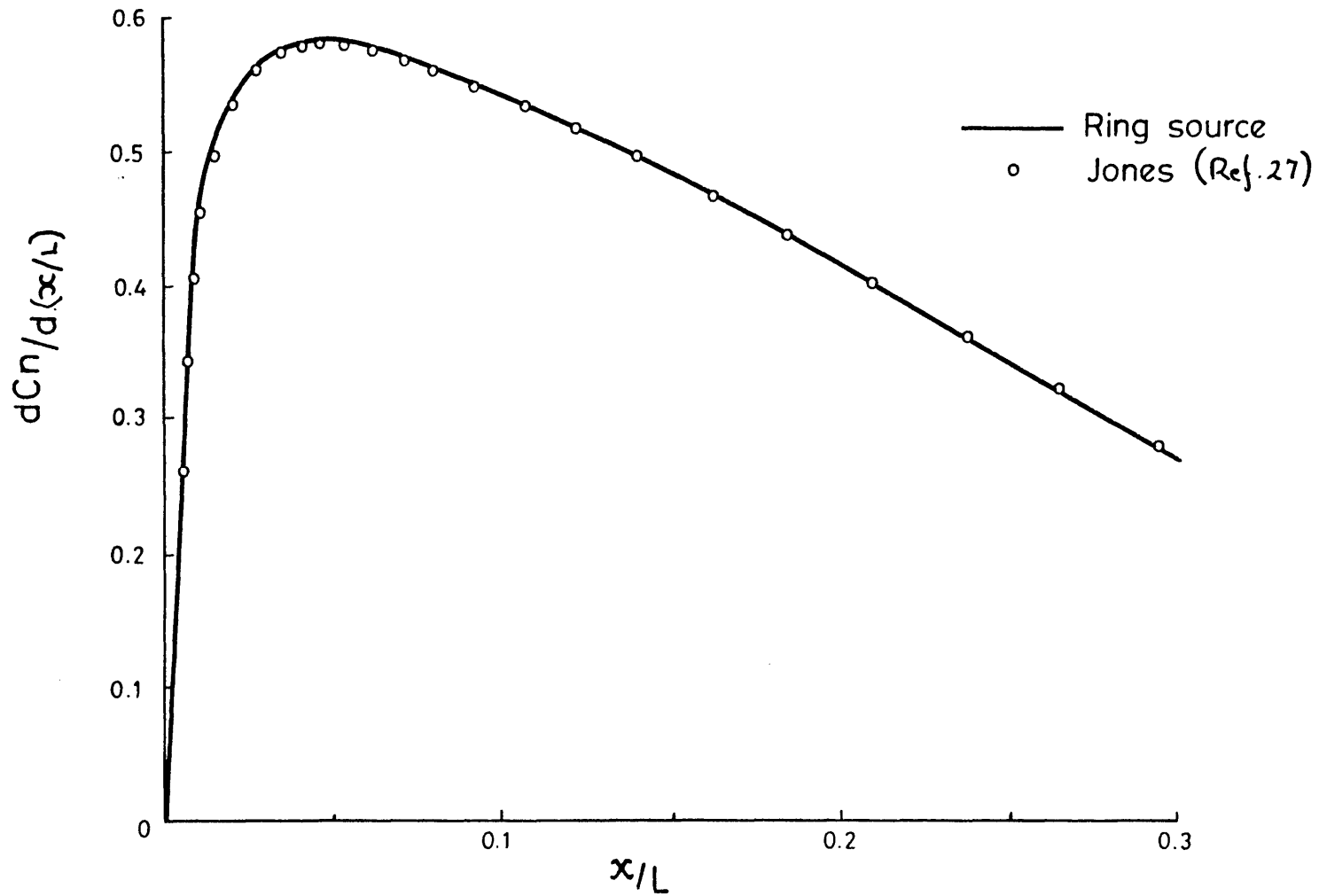


Figure 19 Load distribution on an ellipsoid of fineness ratio 100/15 at 5°.

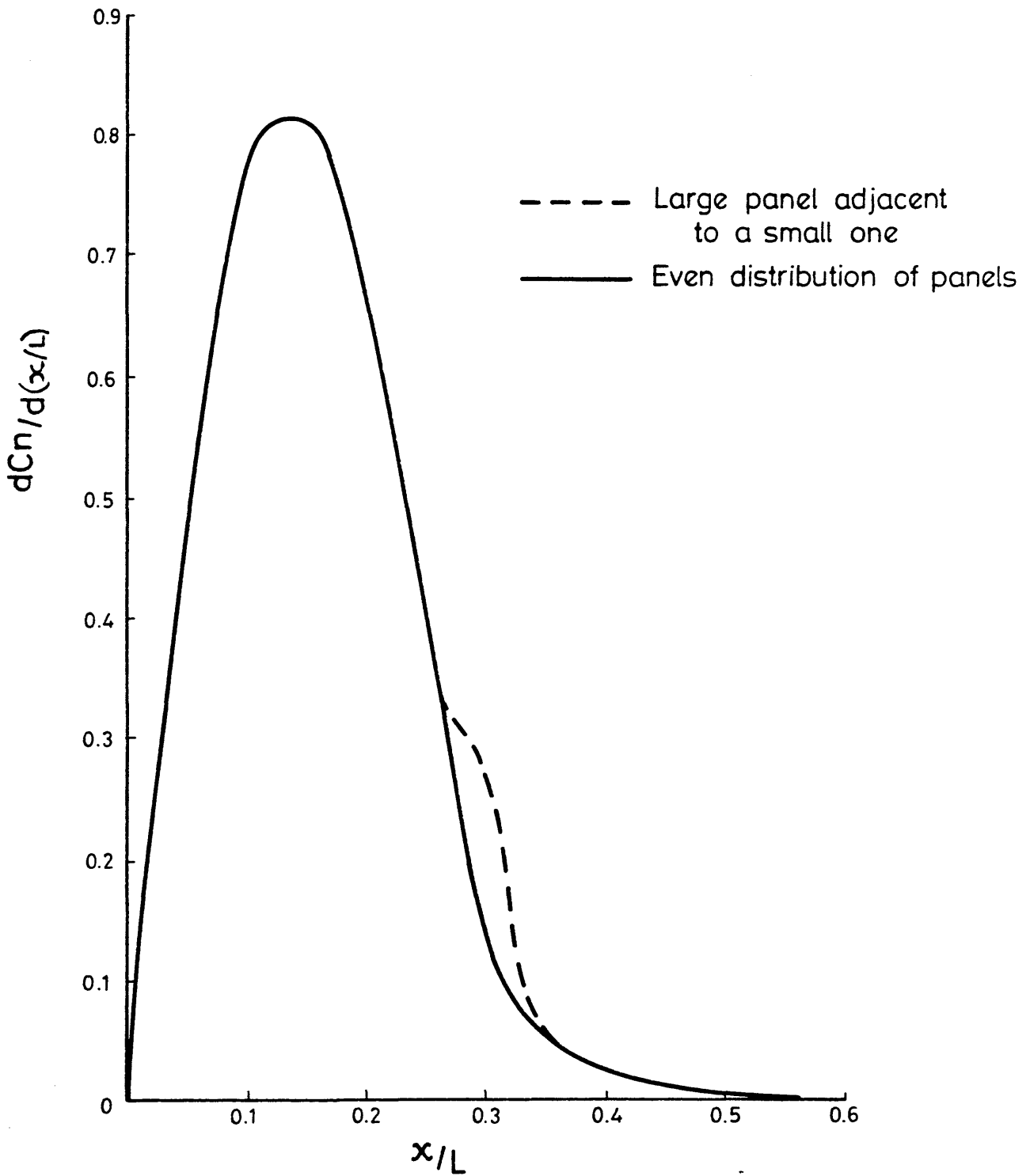


Figure 20 Ellipsoid cylinder of nose ratio 6/1 at  $\alpha = 5^\circ$  using different panel distributions.

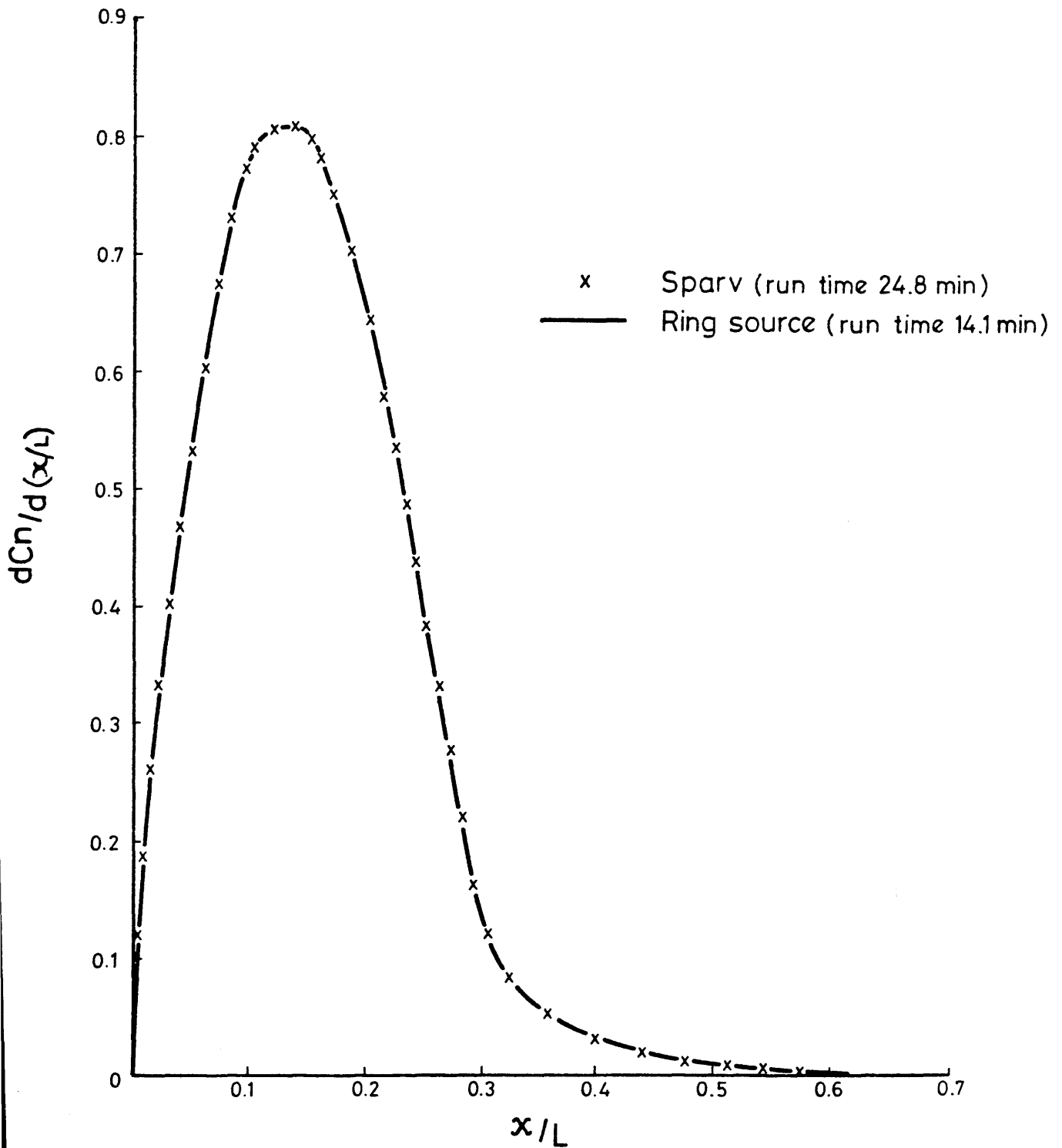


Figure 21 Ellipsoid cylinder of nose ratio 6/1 at  $\alpha = 5^\circ$ , using 100 panels.

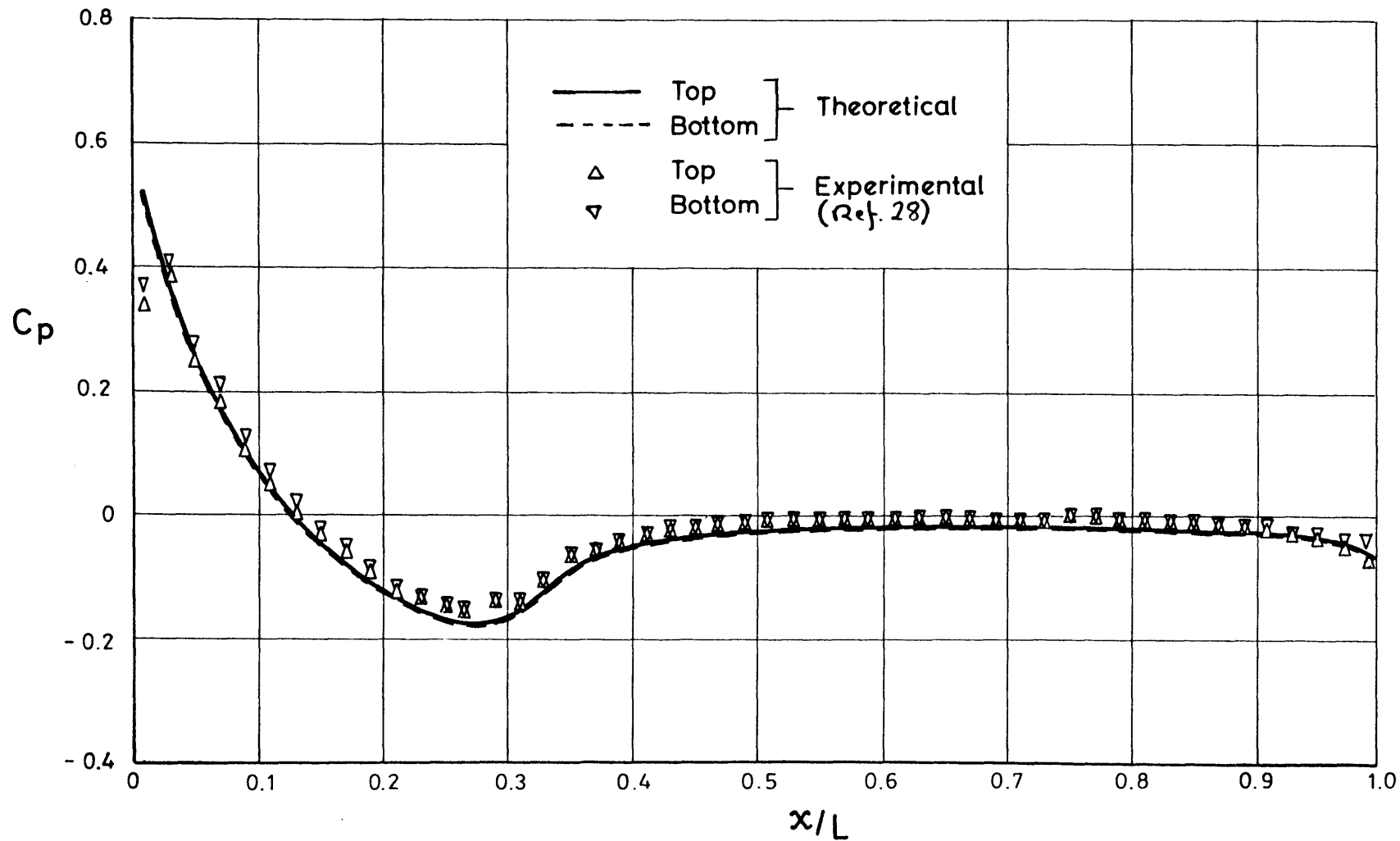


Figure 22 Comparison of experimental and theoretical pressure distribution. Ogive cylinder body, Angle of attack = 0.14 deg.



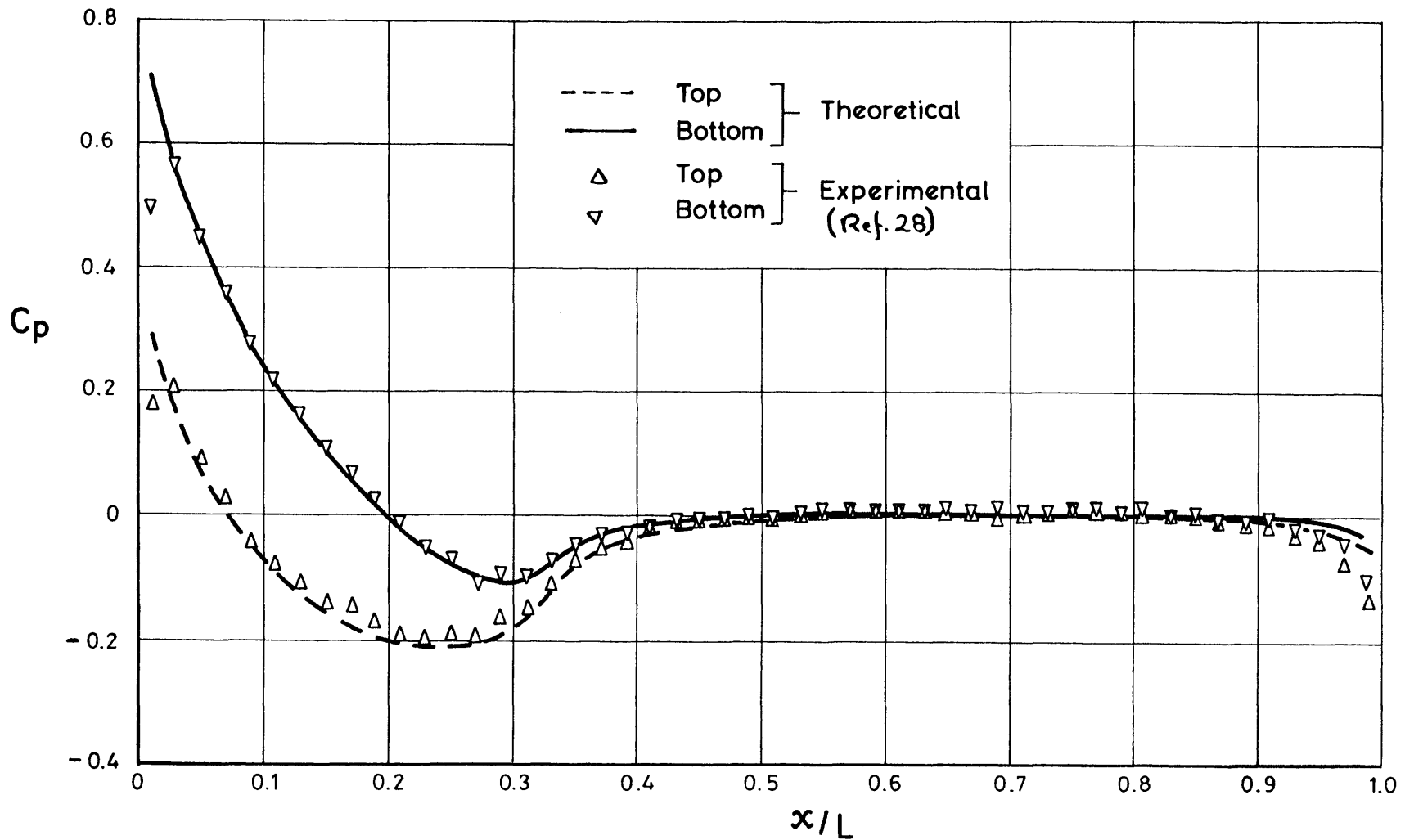


Figure.23 Comparison of experimental and theoretical pressure distribution.  
 Ogive cylinder body , Angle of attack = 8.14 deg.

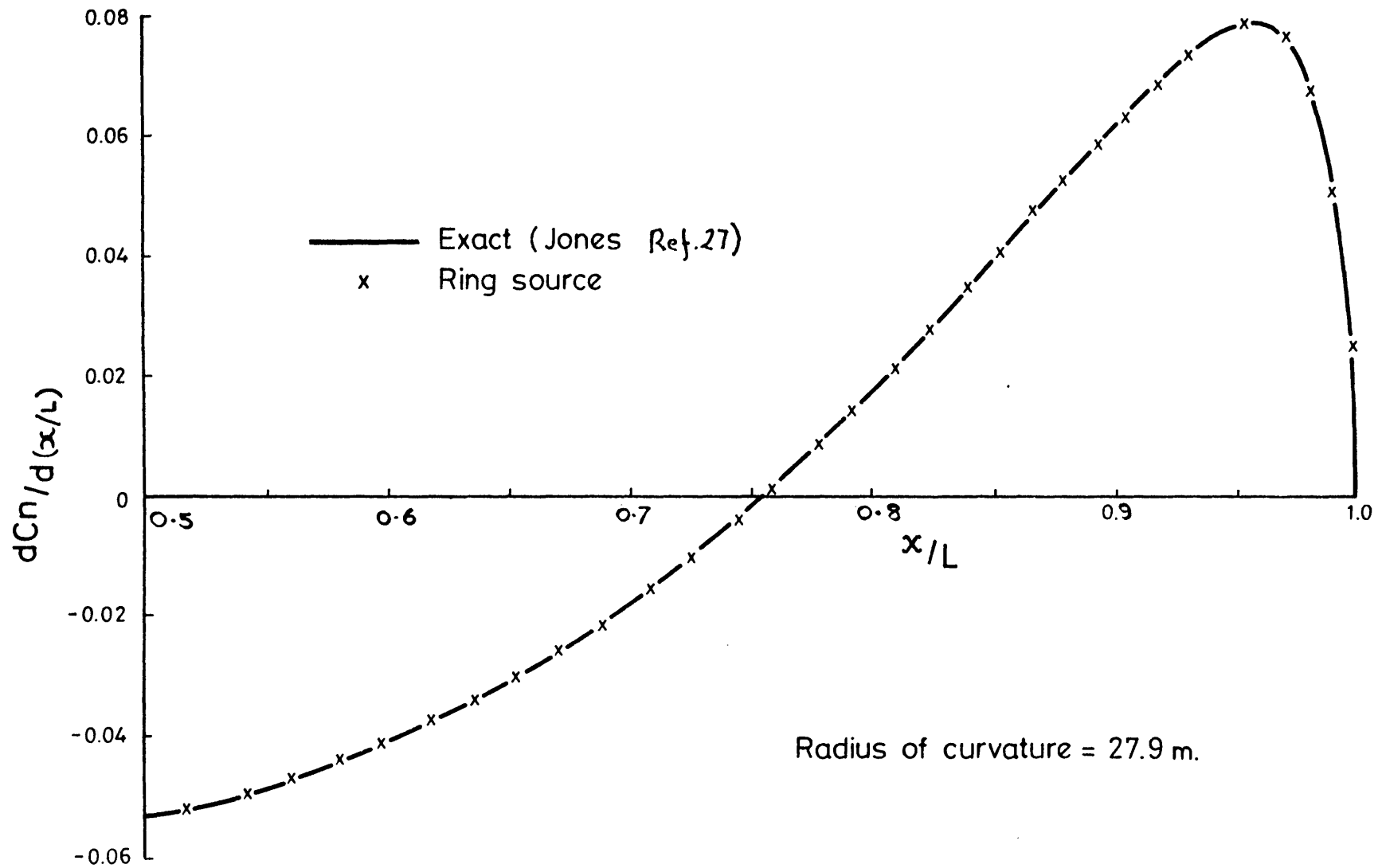


Figure 24 Normal load distribution on an ellipsoid (4/1) in curvilinear motion.

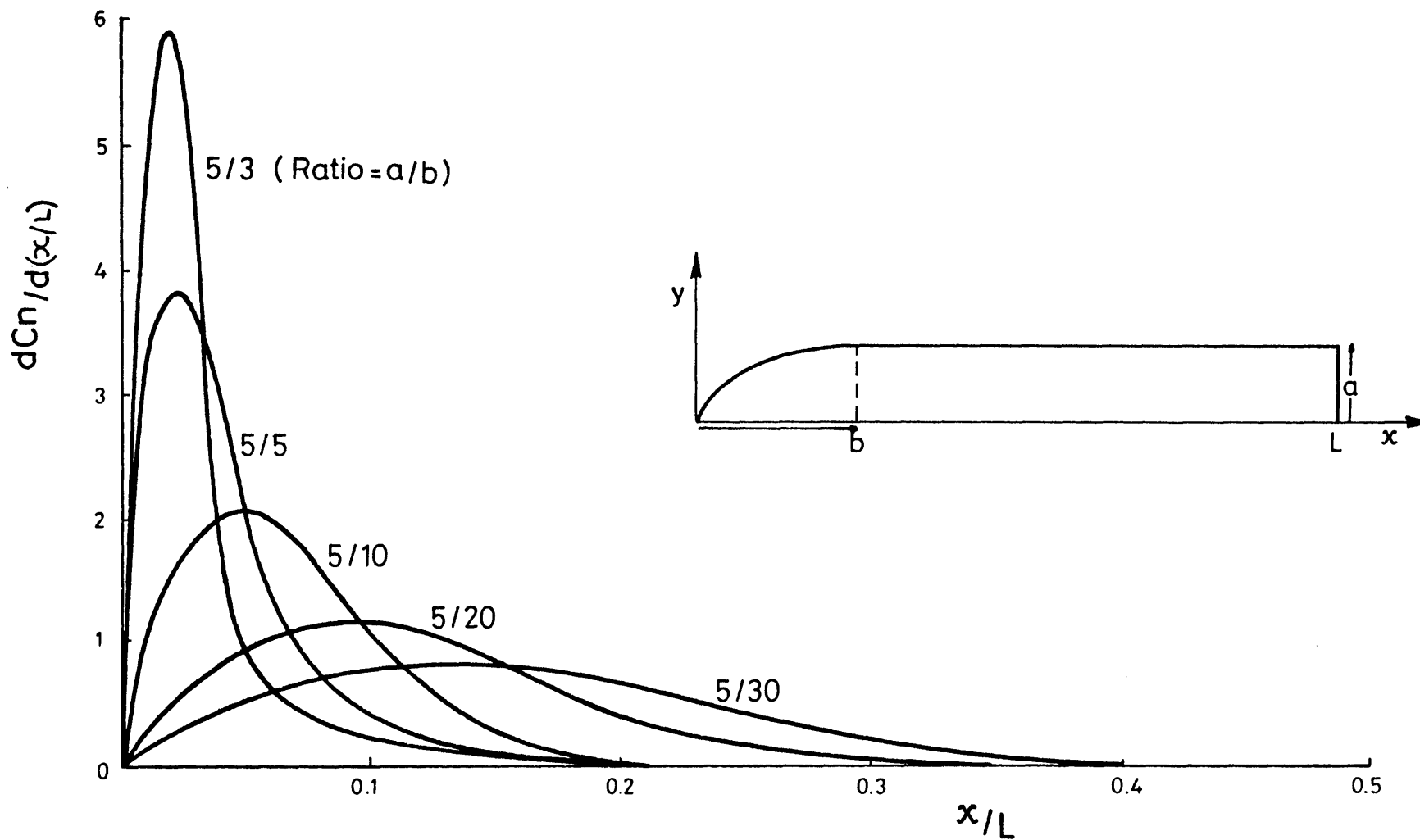


Figure 25 Load distribution on tangent ogive cylinders of various ratios at  $5^\circ$ .

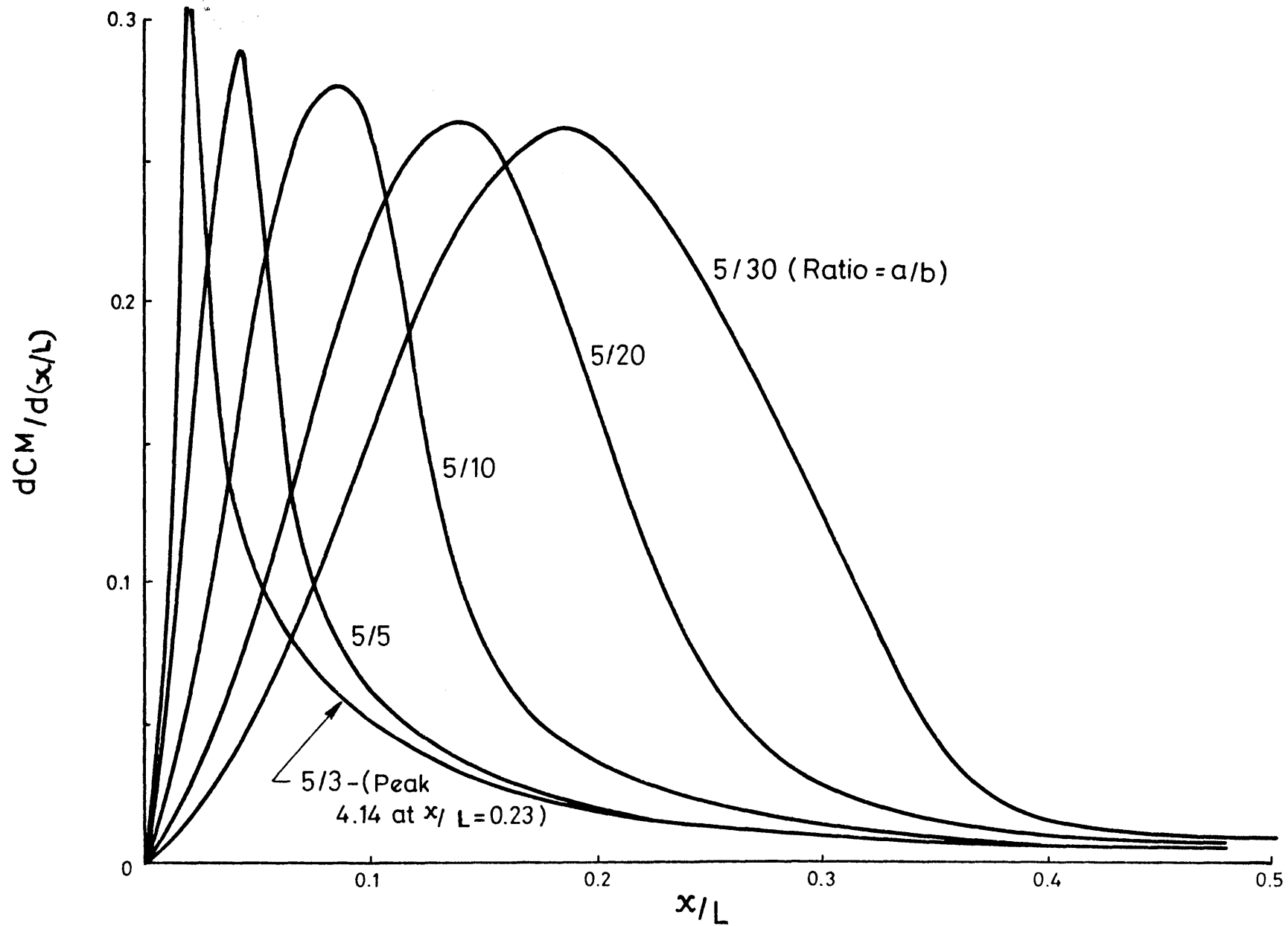


Figure 26  $dCM/dx$  variation along a body at  $5^\circ$  for varying bluntness.

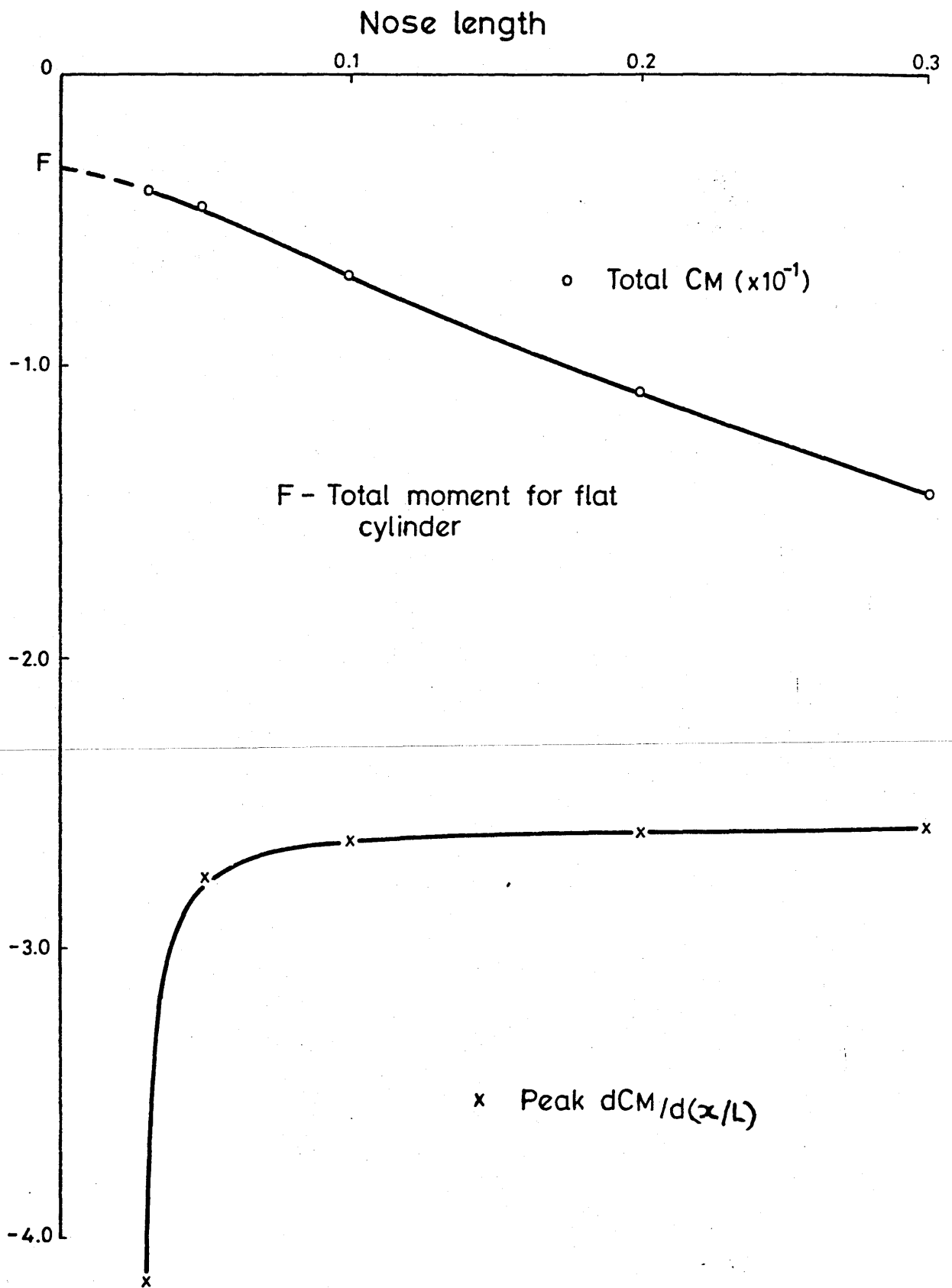


Figure 27 Variation of total CM and peak value of  $dCM/dx$  with nose length for missile at  $5^\circ$

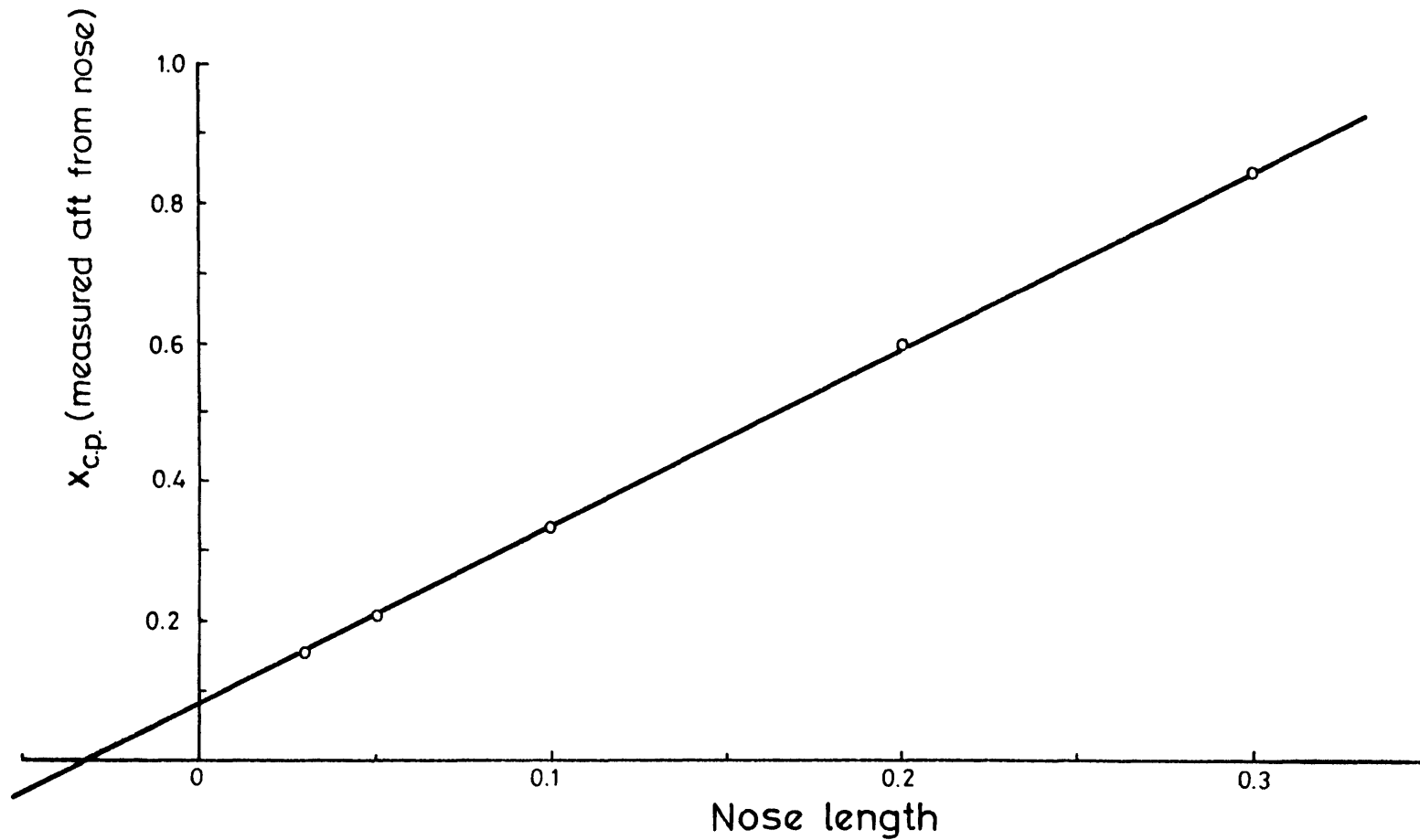


Figure 28 Variation of  $x_{c.p.}$  with nose length for missiles at  $5^\circ$

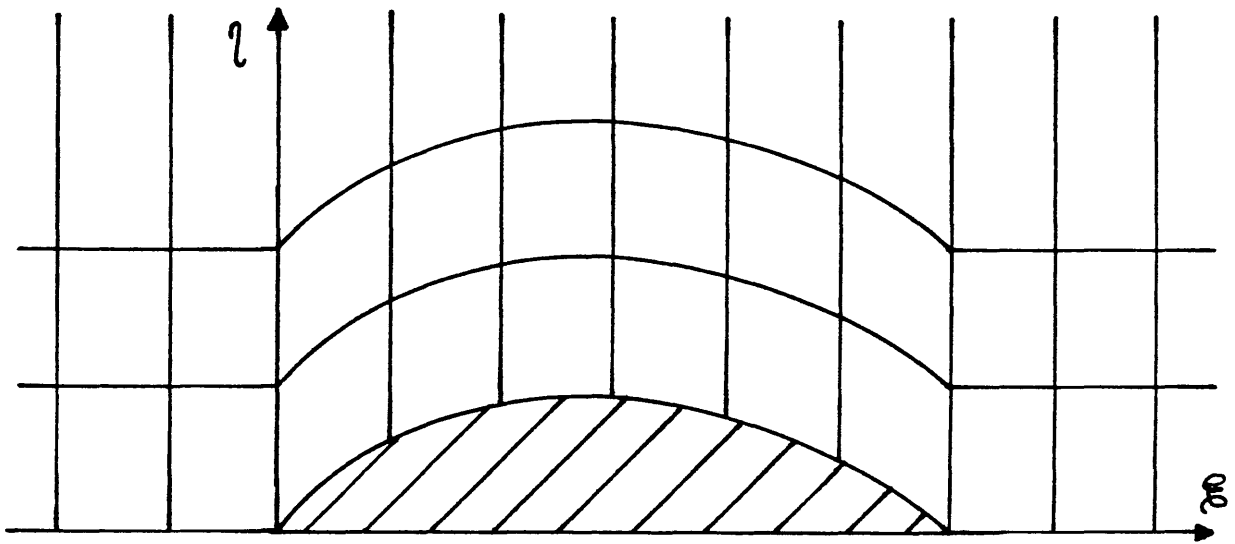


Fig.29 Sheared coordinates

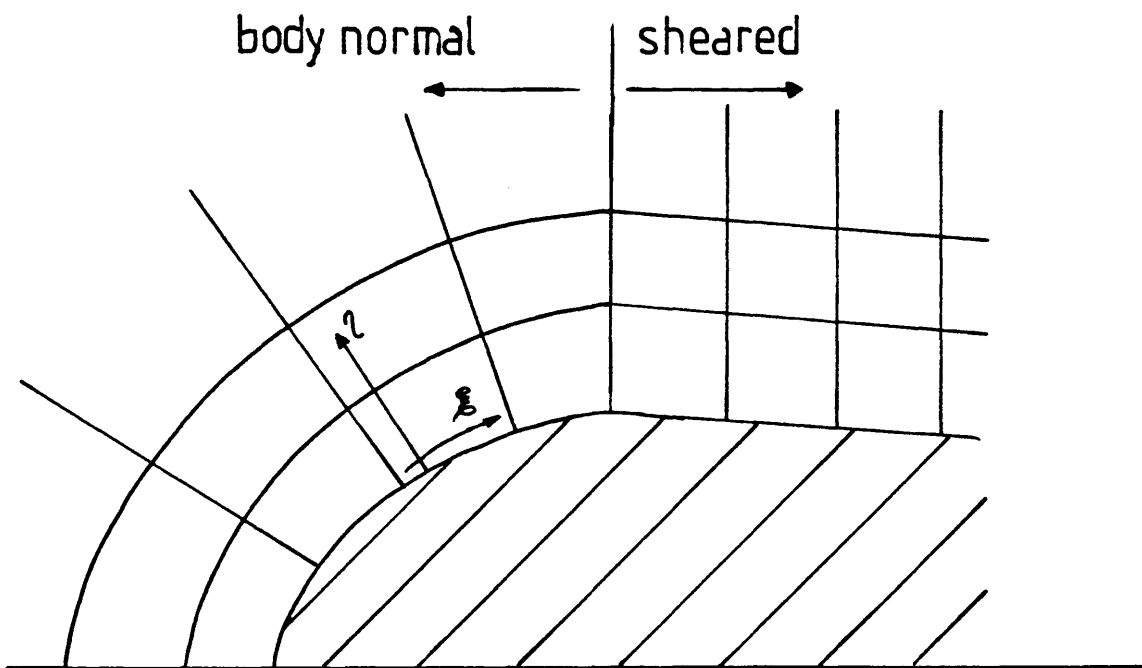


Fig.30 Blunt body coordinate system

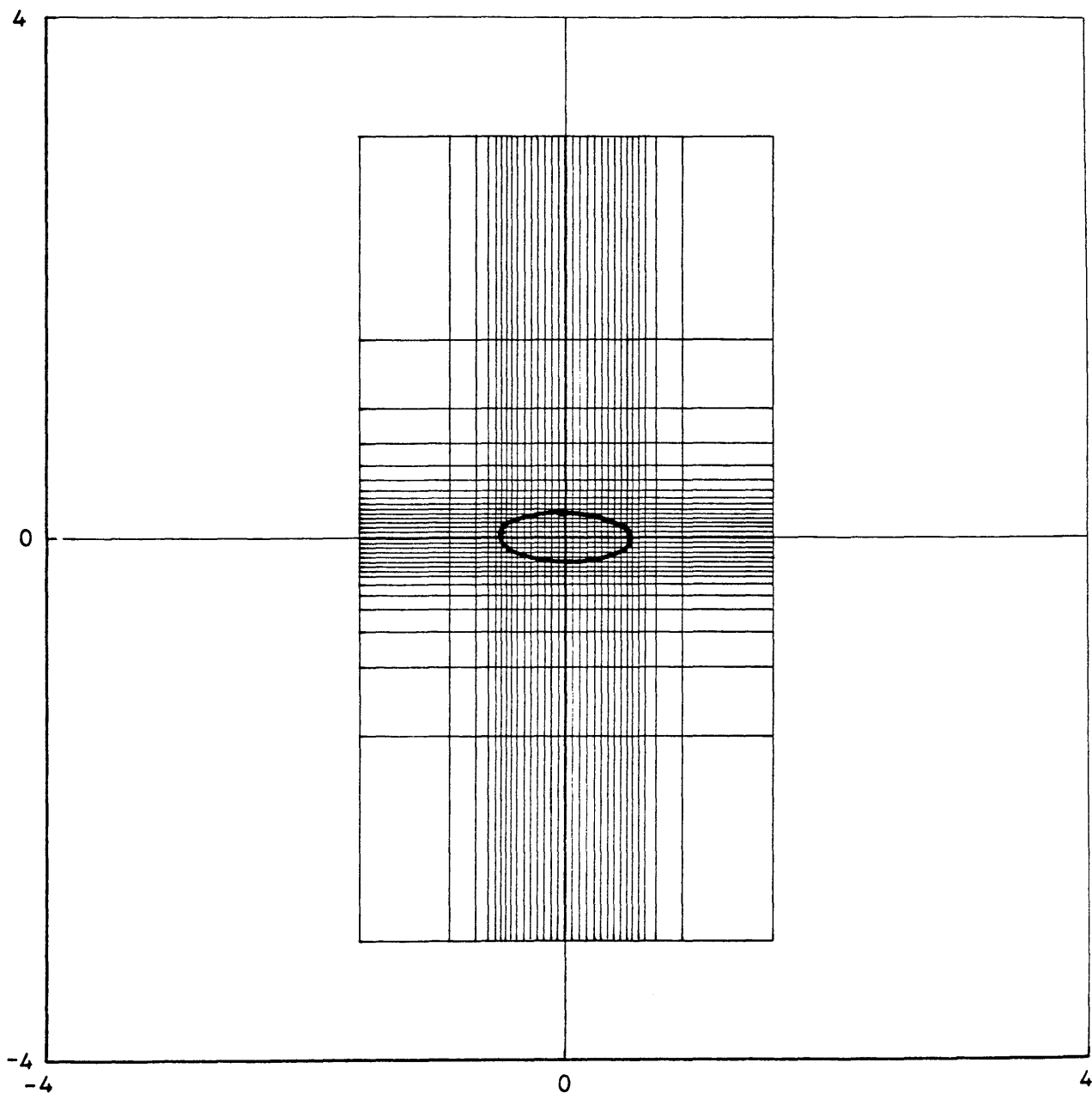


Figure 31<sub>a</sub> Elliptic body in physical grid space.



--- Increased clustering near nose.  
—— Continuous clustering over body.

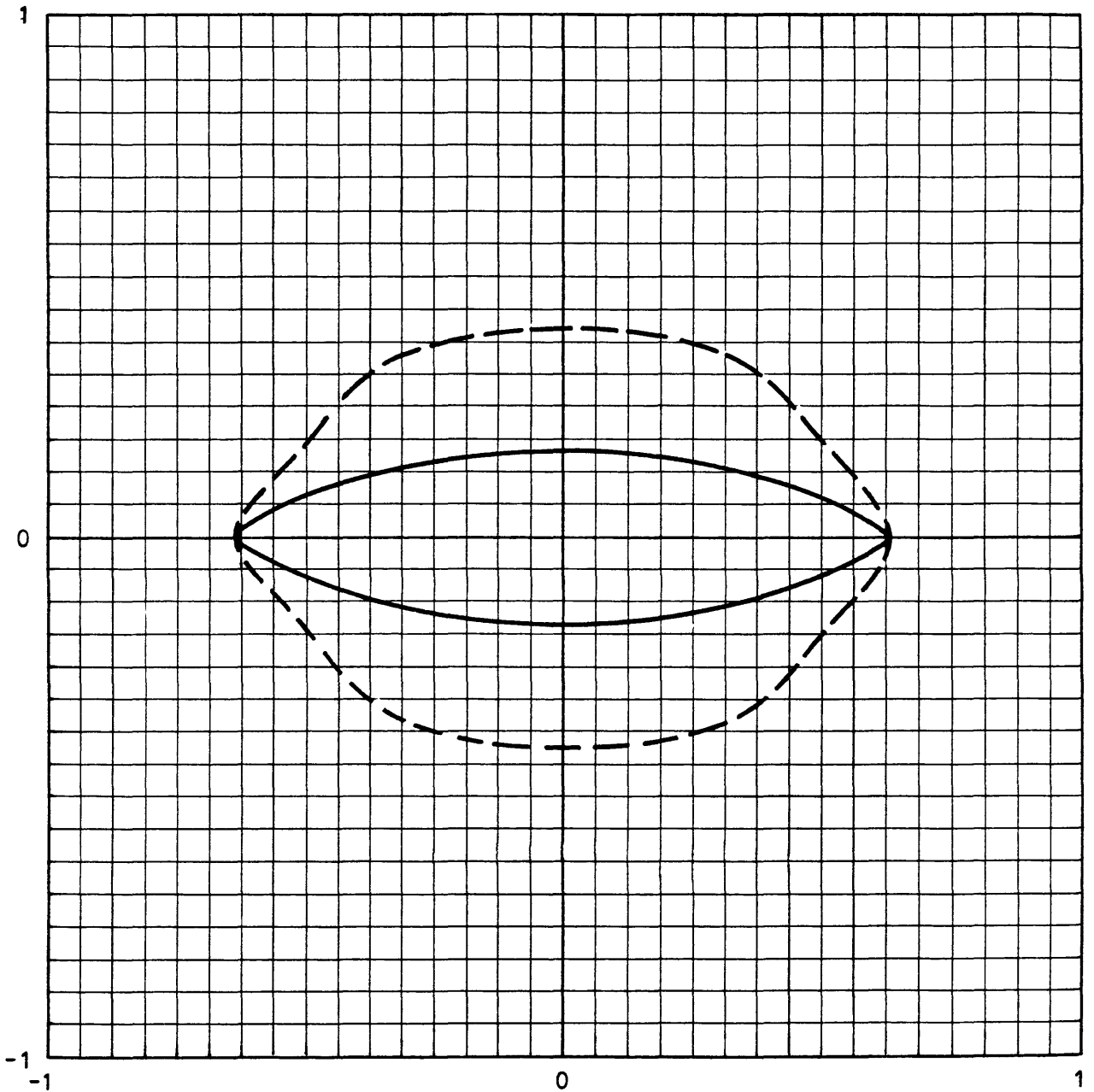


Figure 31b Elliptic body in computation grid space.

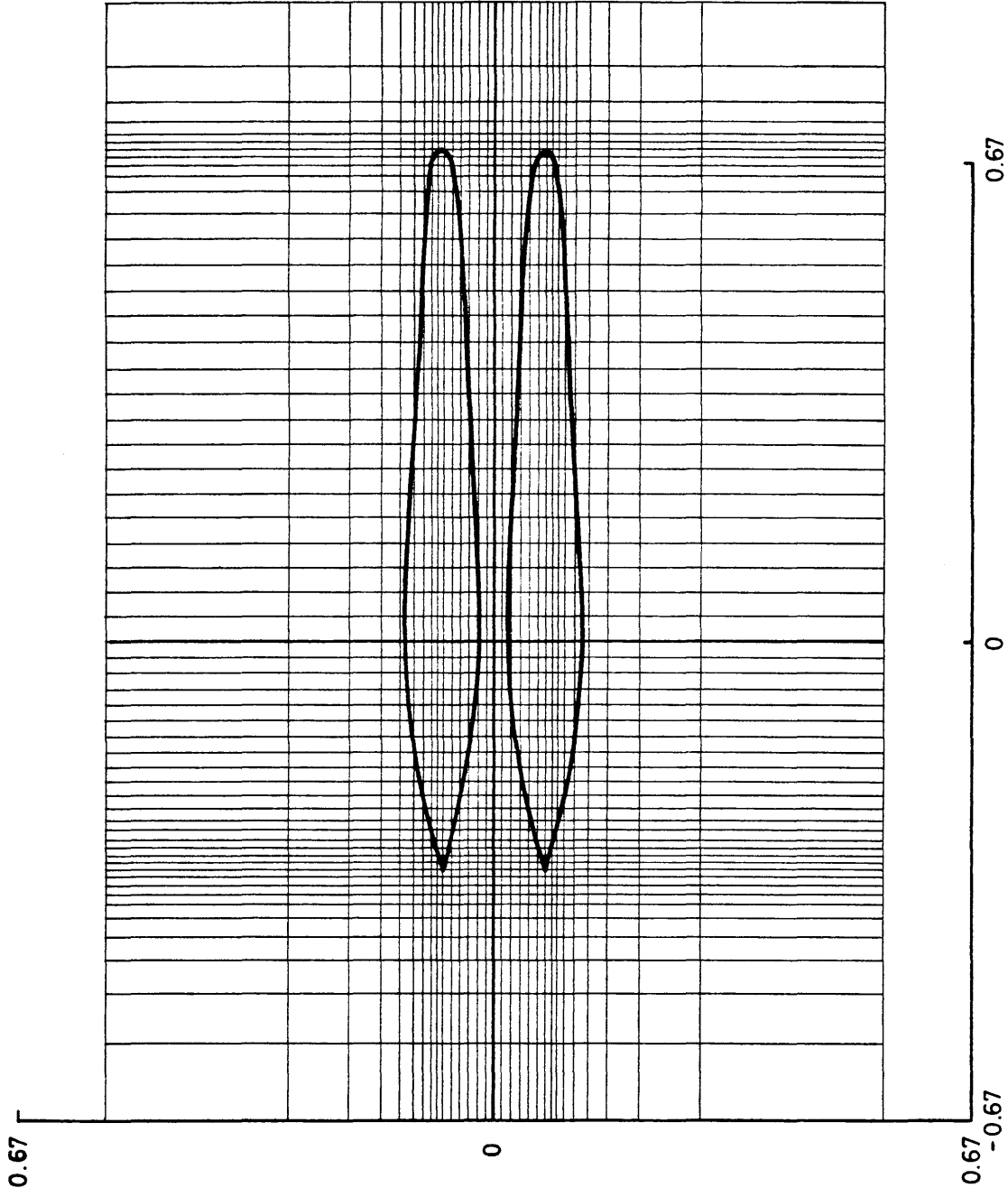


Figure 32a Double missile configuration in  $\alpha$  physical space.

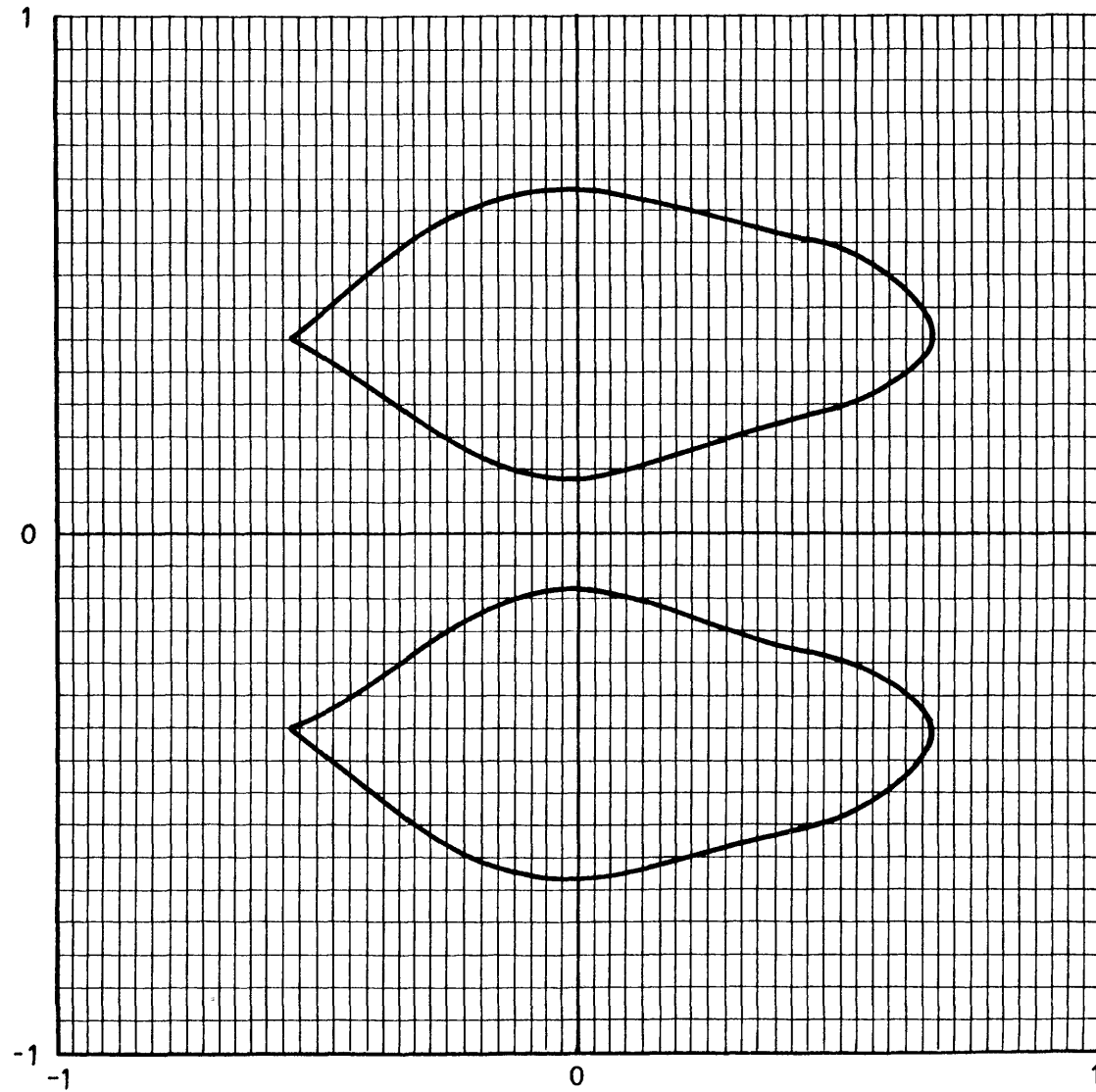


Figure 32b Double missile configuration in computational space.

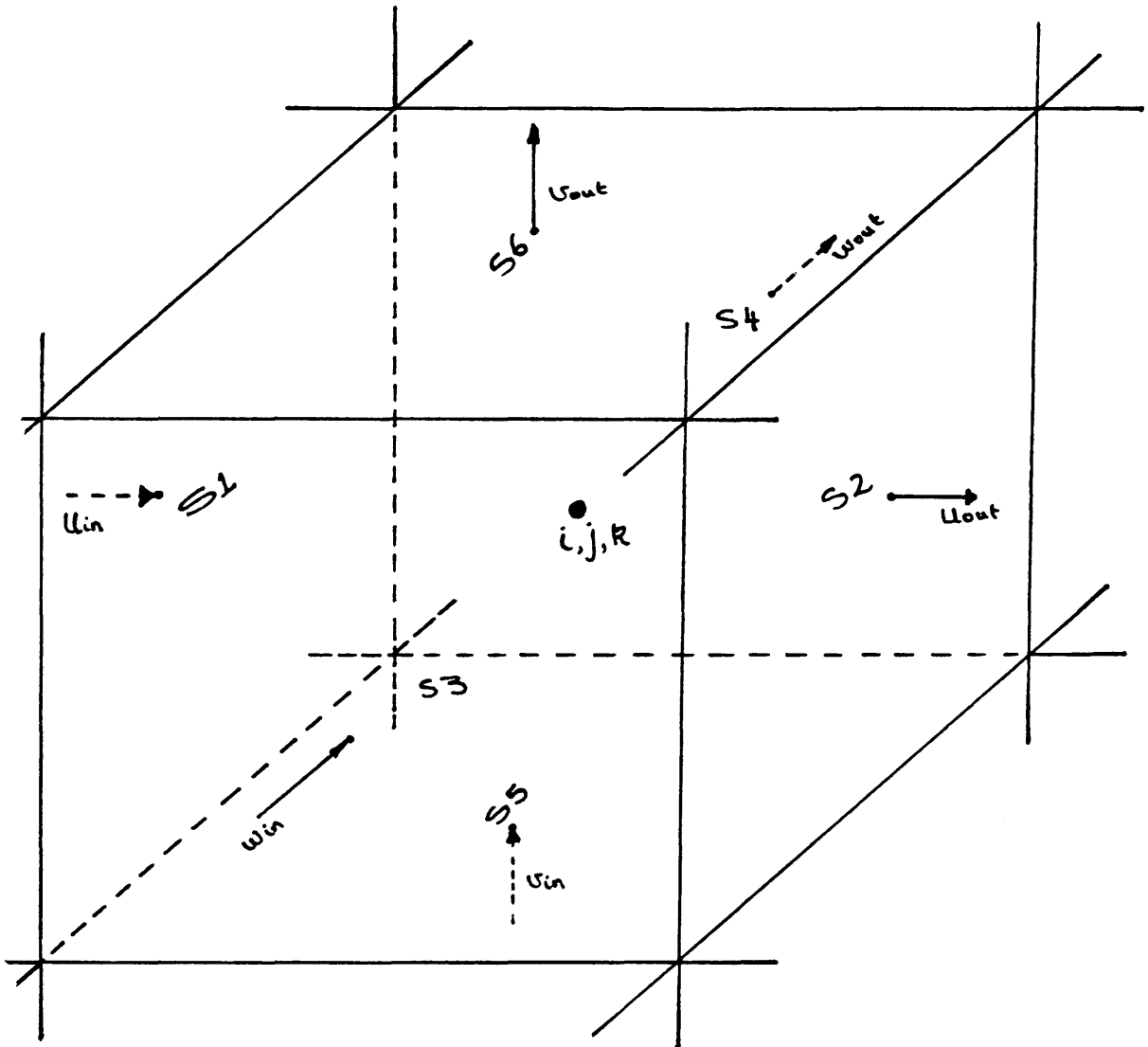


Fig.33 Flow in and out of a computational cell

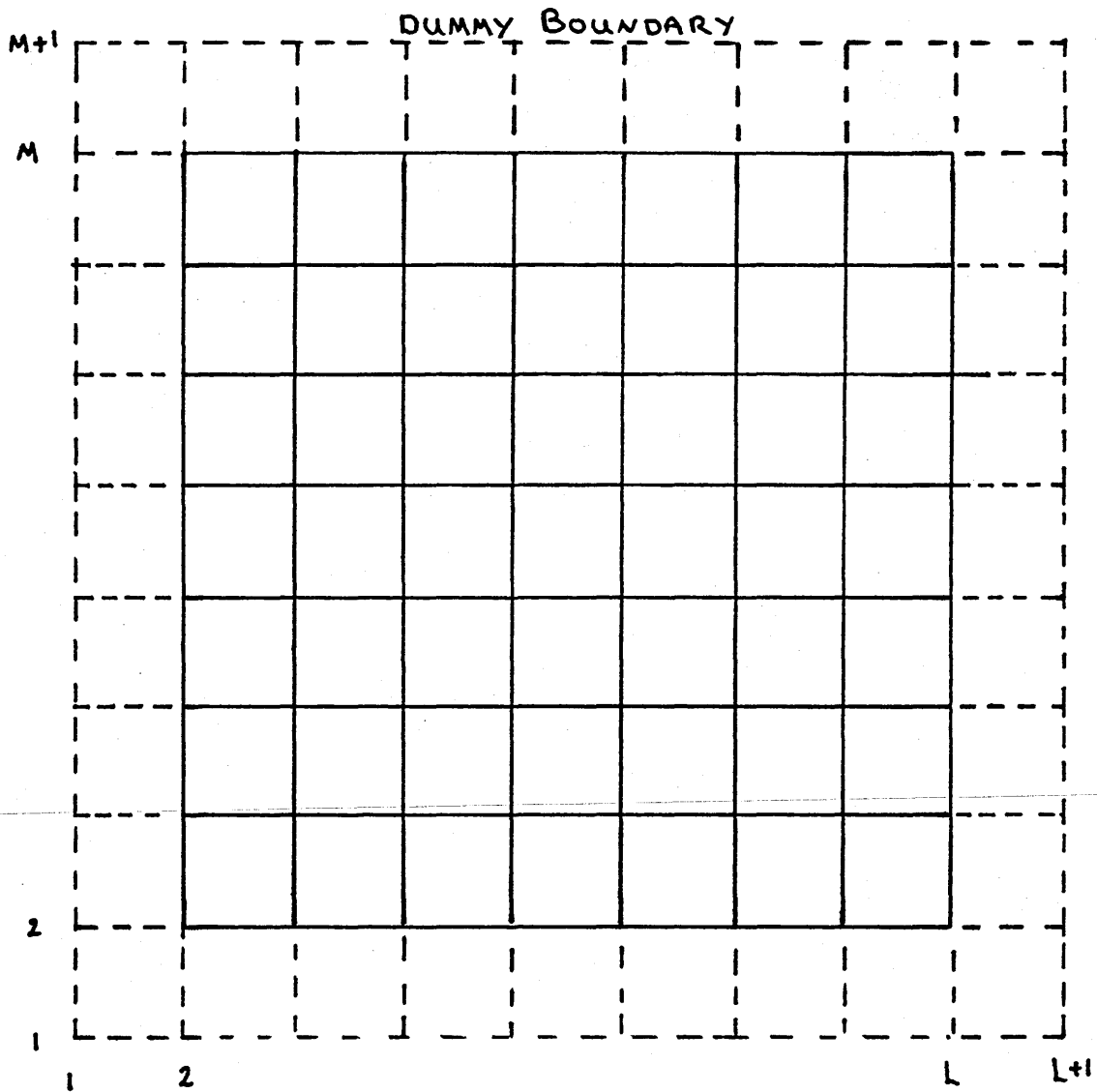
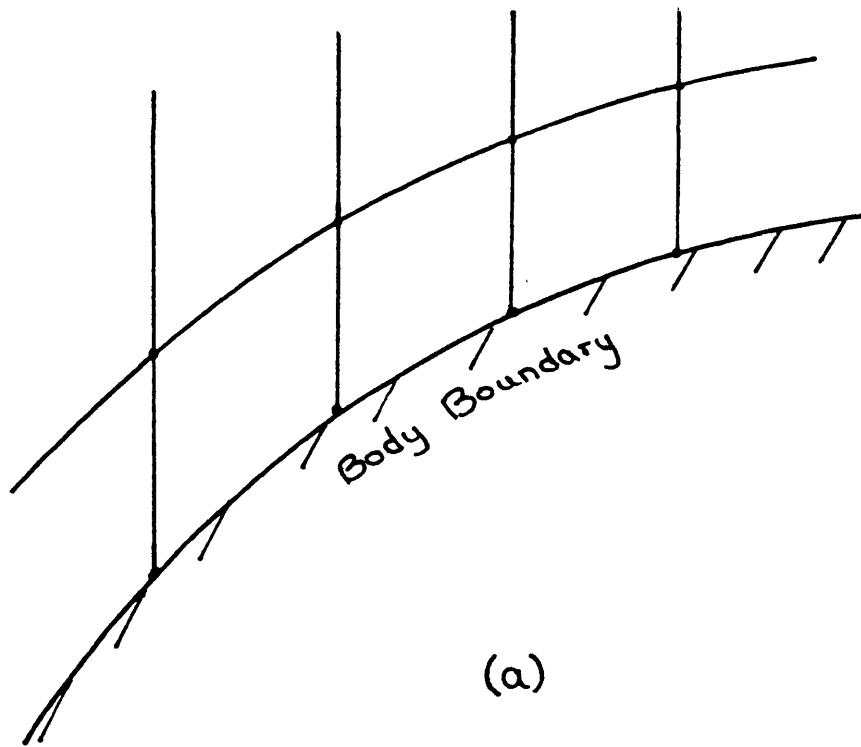
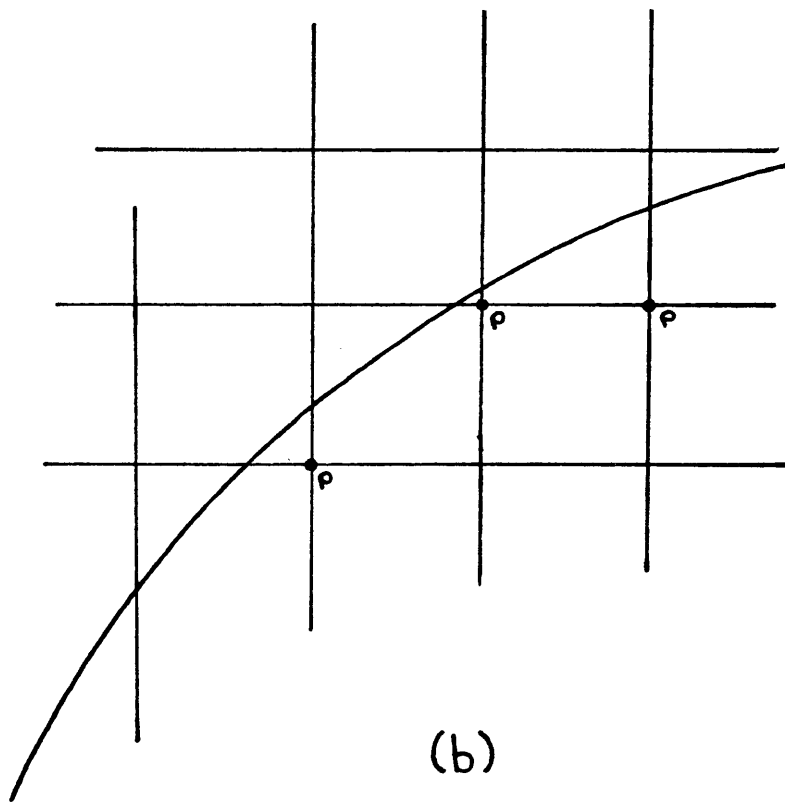


Fig.34 Internal computational domain with dummy boundaries



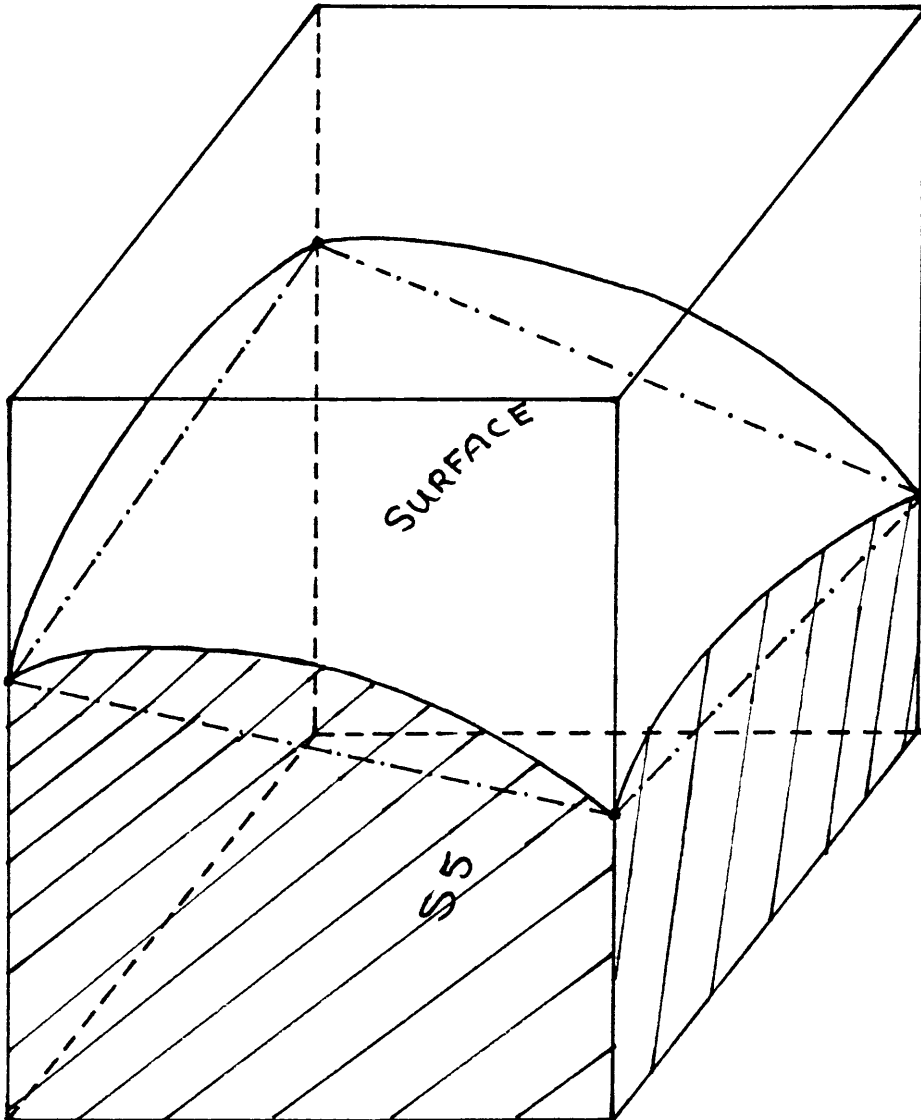
(a)



(b)

Fig.35 (a) Body conforming mesh

(b) Cartesian non-conforming mesh




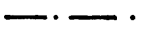
-  actual surface
-  approximated surface

Fig.36 Cell cut by a surface

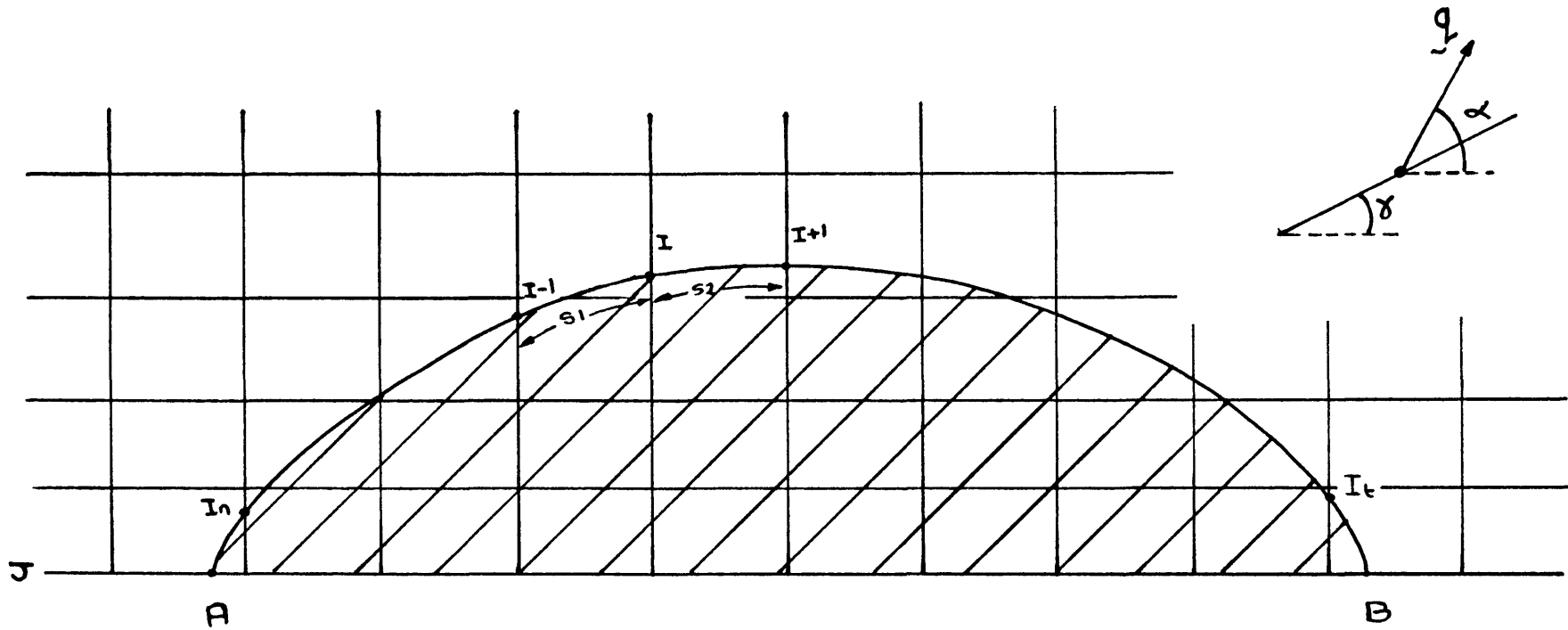


Fig.37 Calculation of surface variation of  $\phi$  to predict the pressure distribution



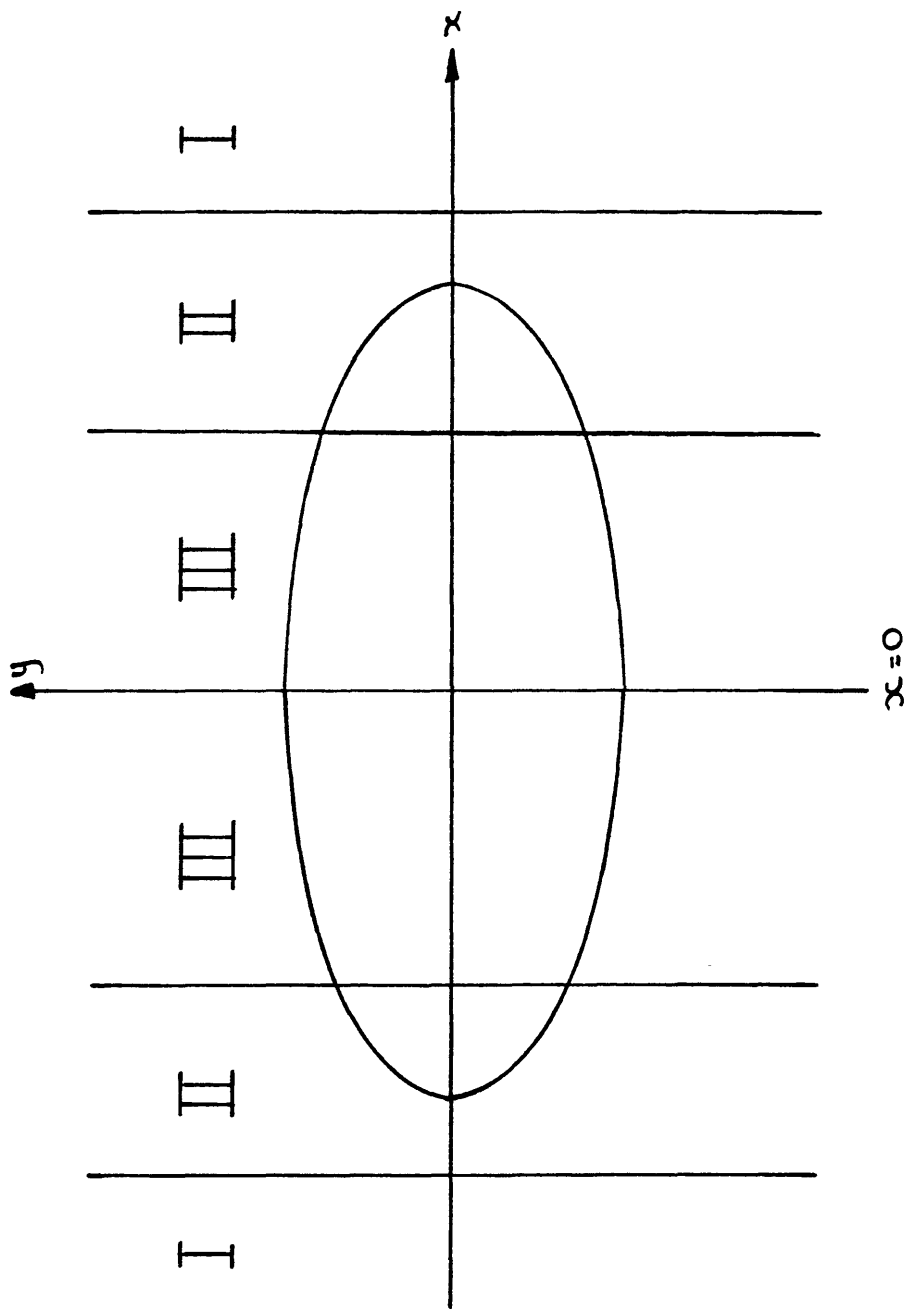


Fig.38 Regions of varying grid line density

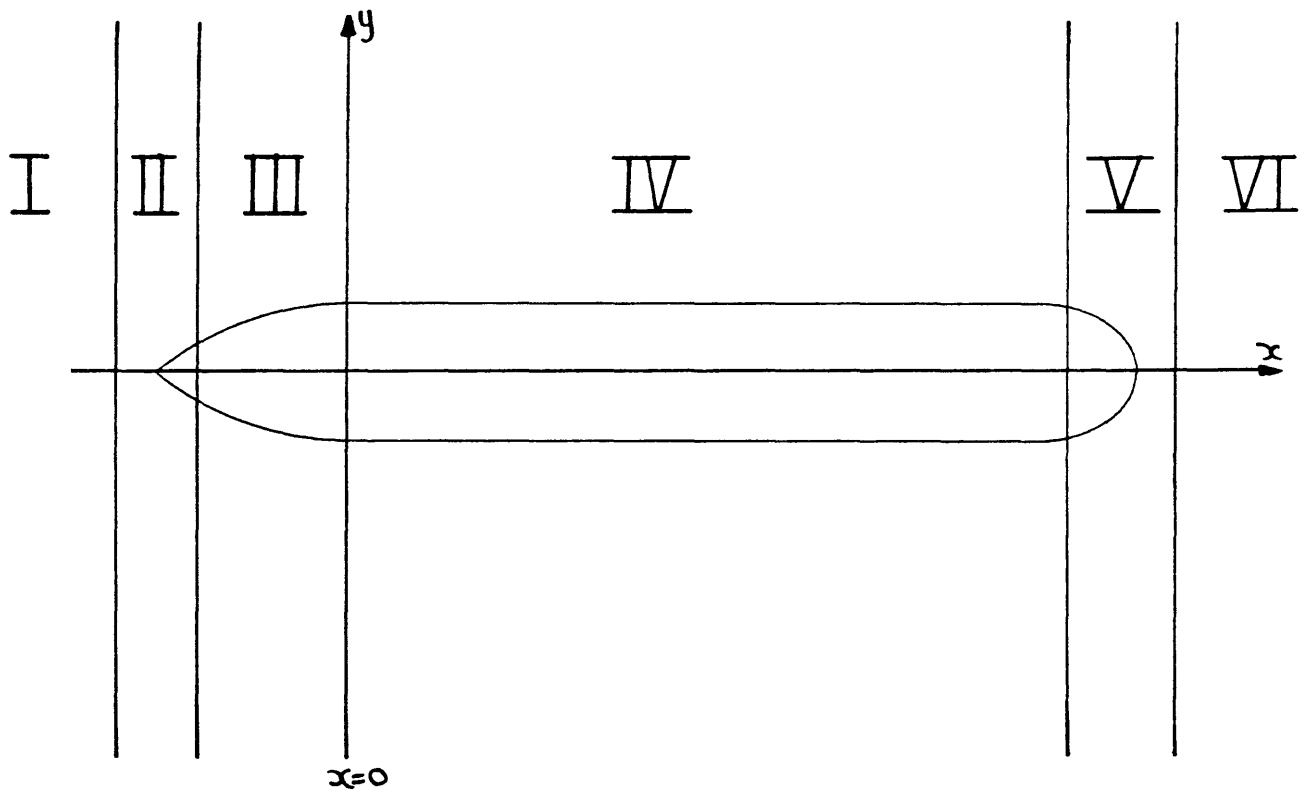


Fig. 39 Varying grid line density regions for a missile

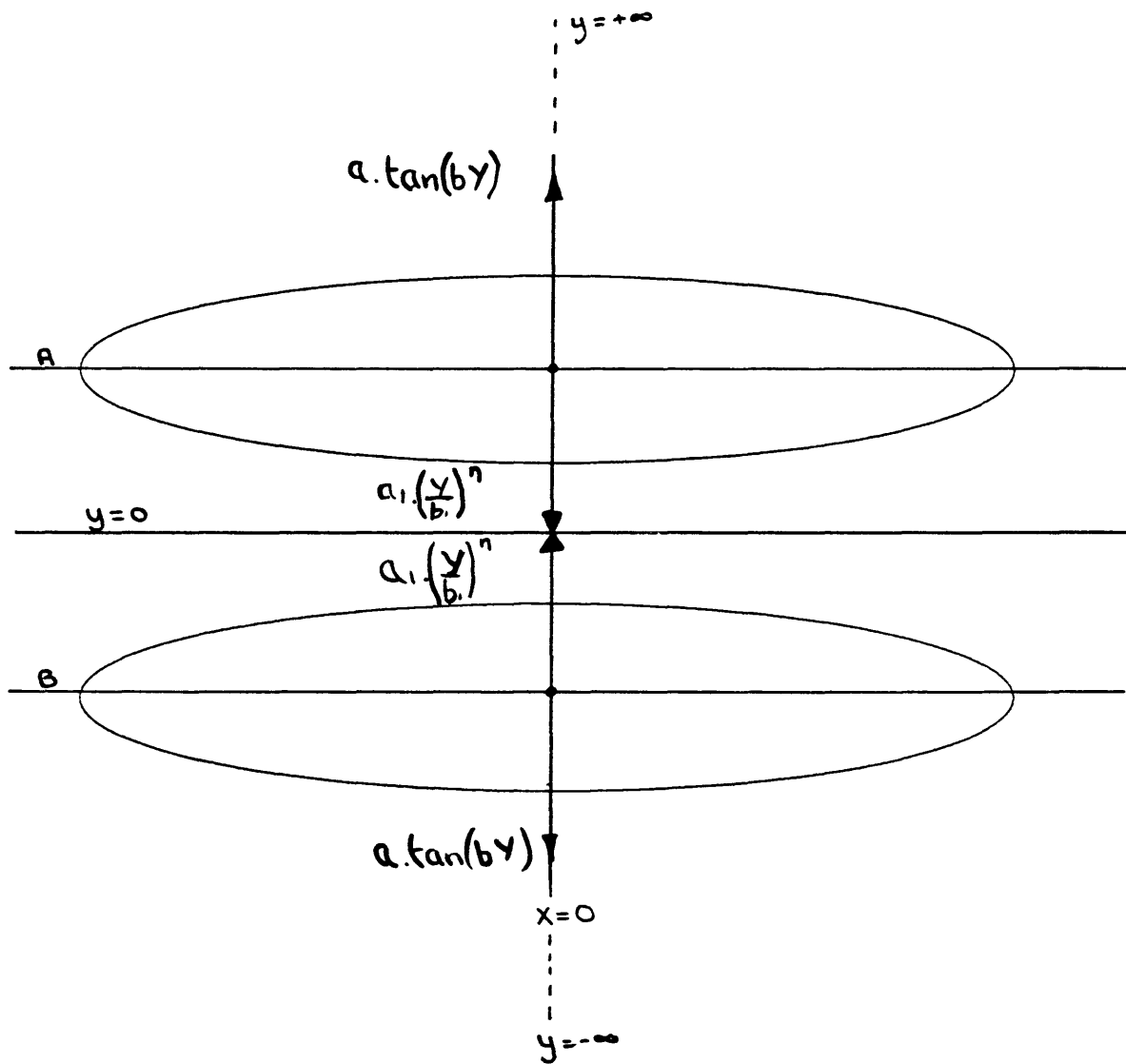


Fig.40 Y-direction stretching for two bodies

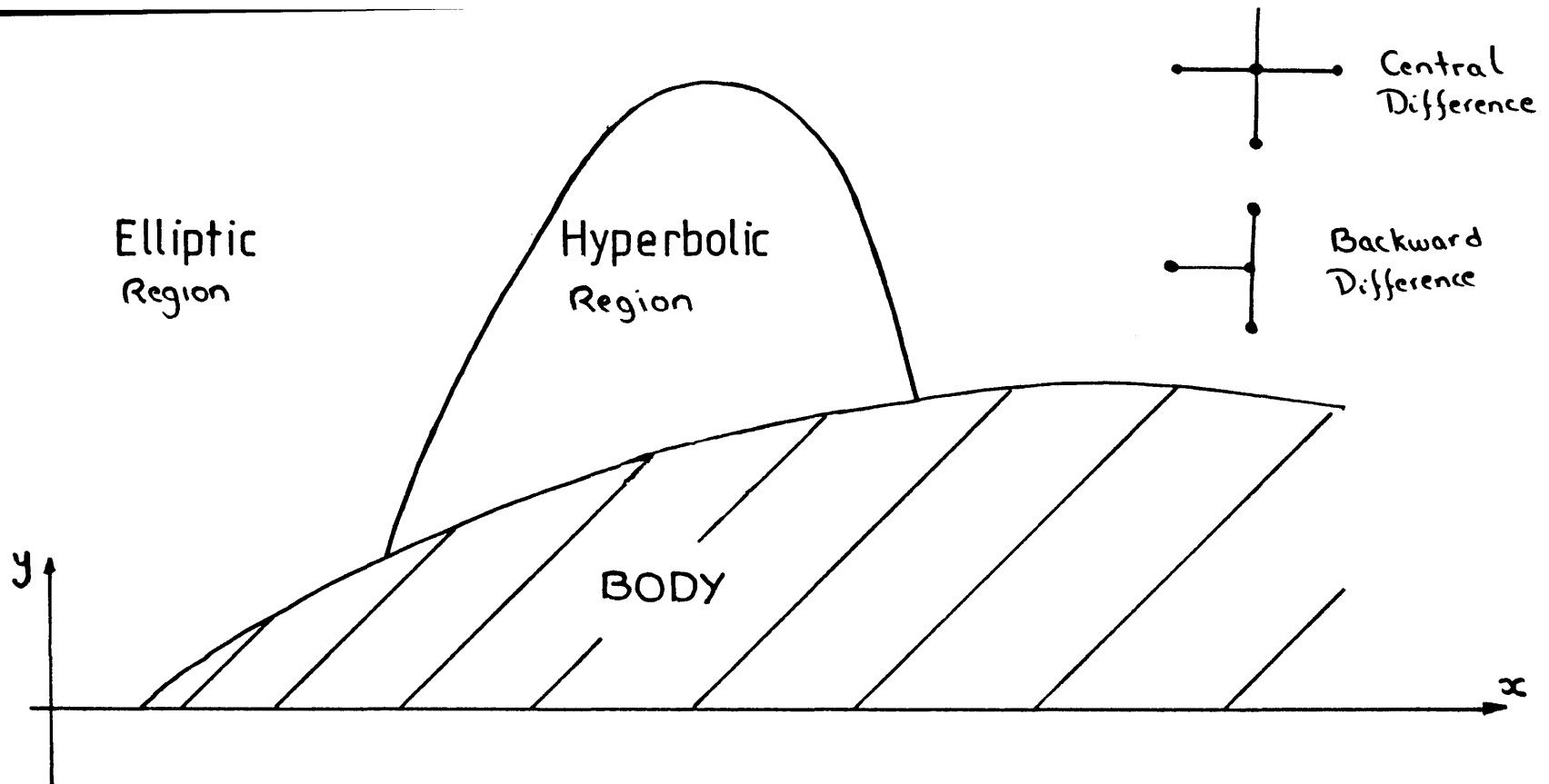
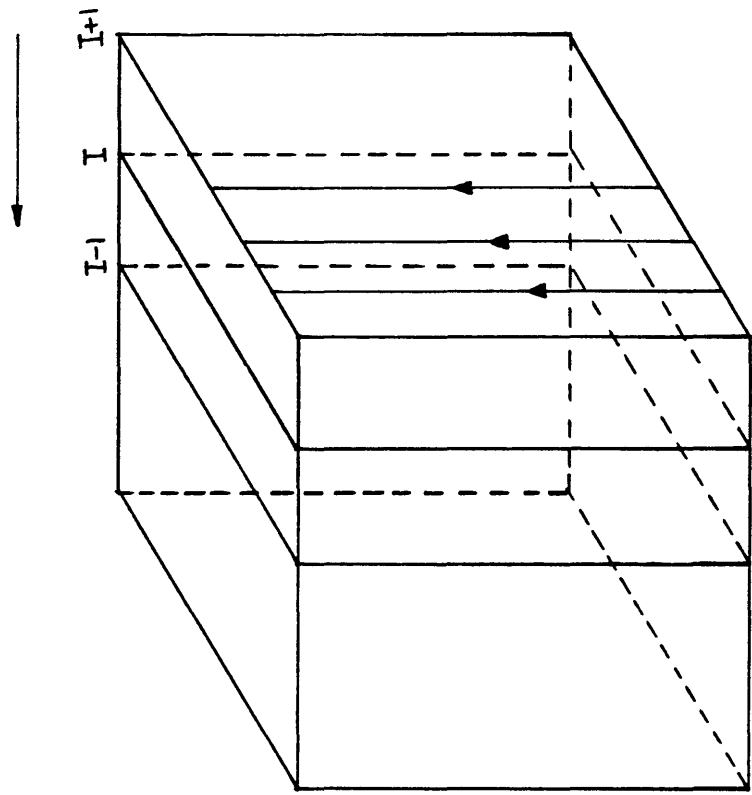
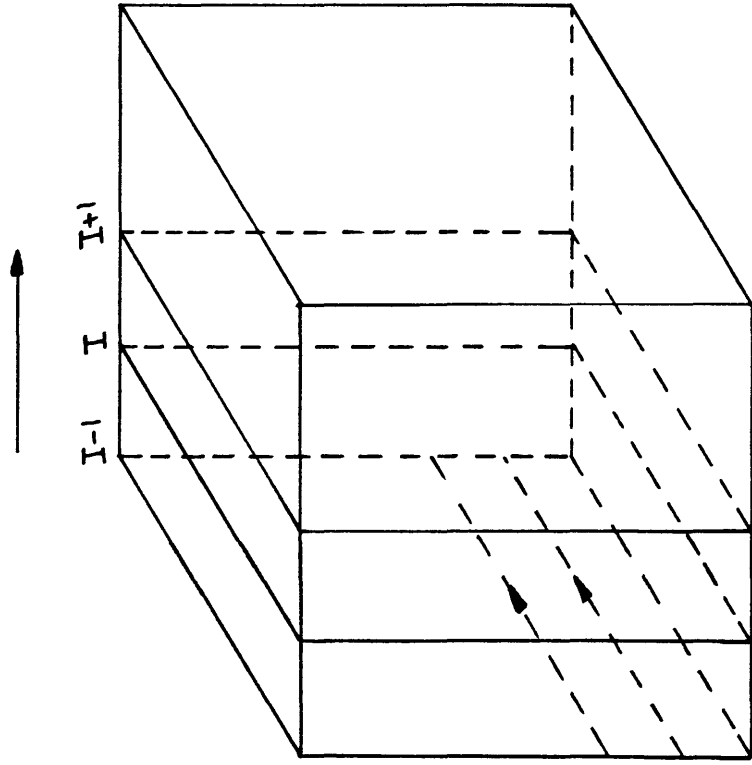


Fig.4\ Domain dependant differencing on shock formation



Step1



Step 2

Fig.42 Direction of sweeping during one iteration step

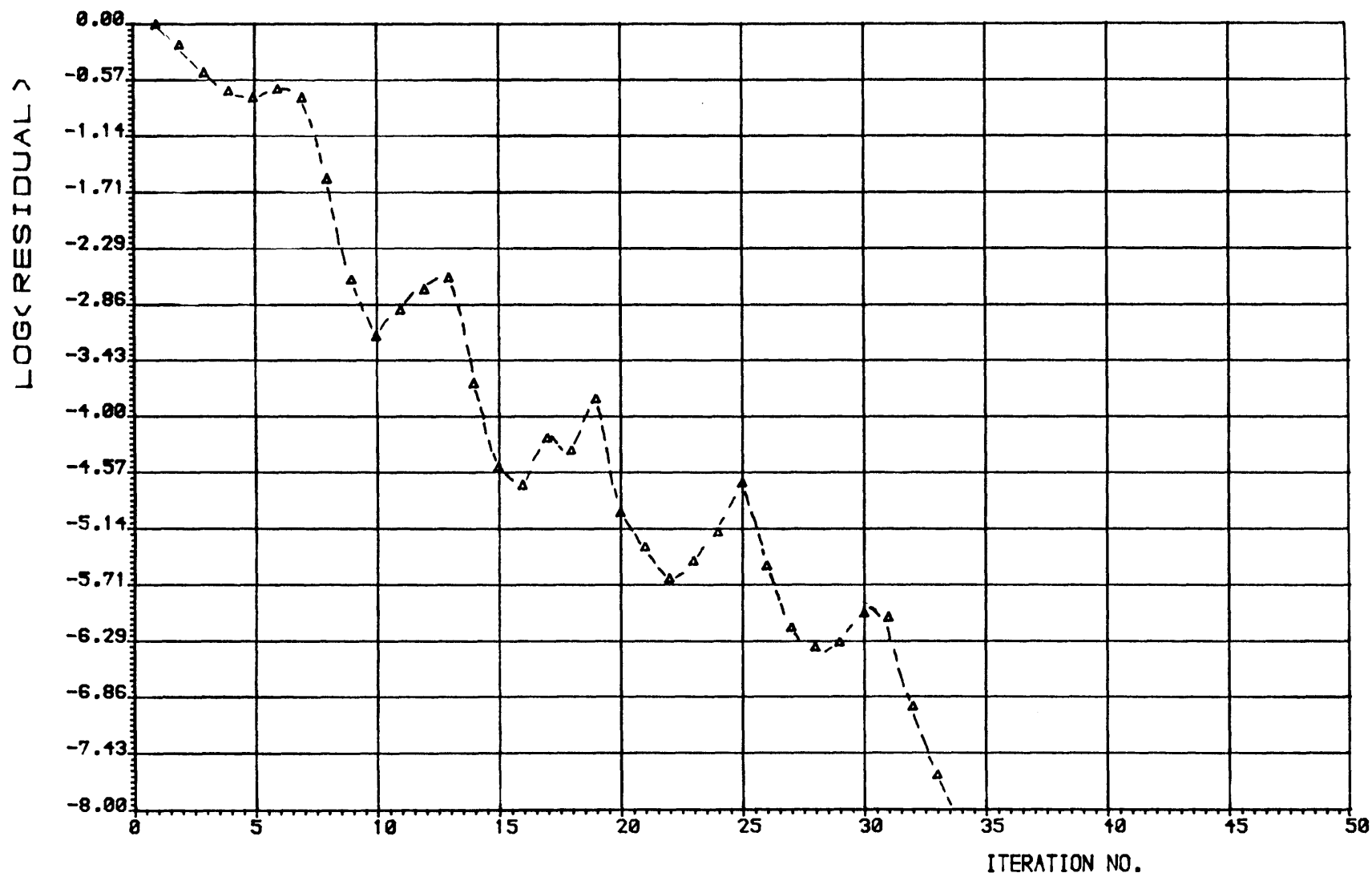


Fig.43. Variation of log(residual) with iteration number

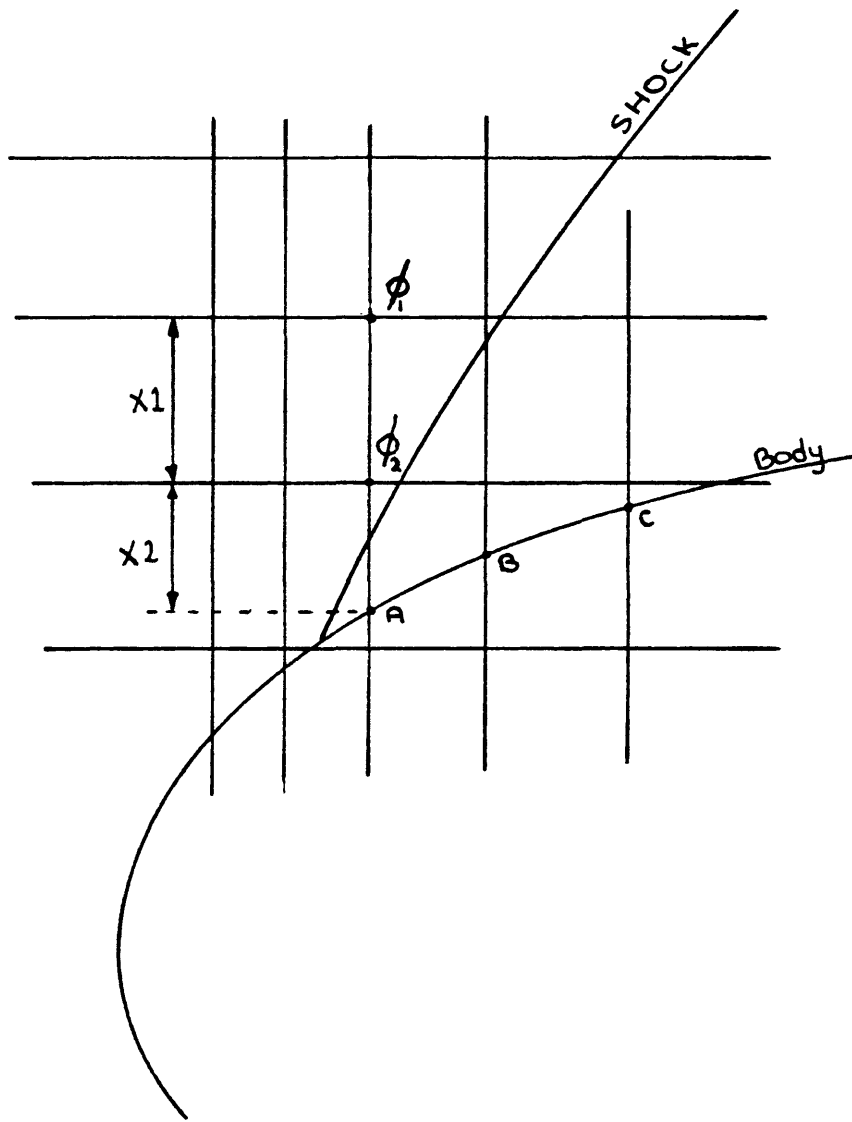


Fig.44. Velocity calculation errors due to shock formation

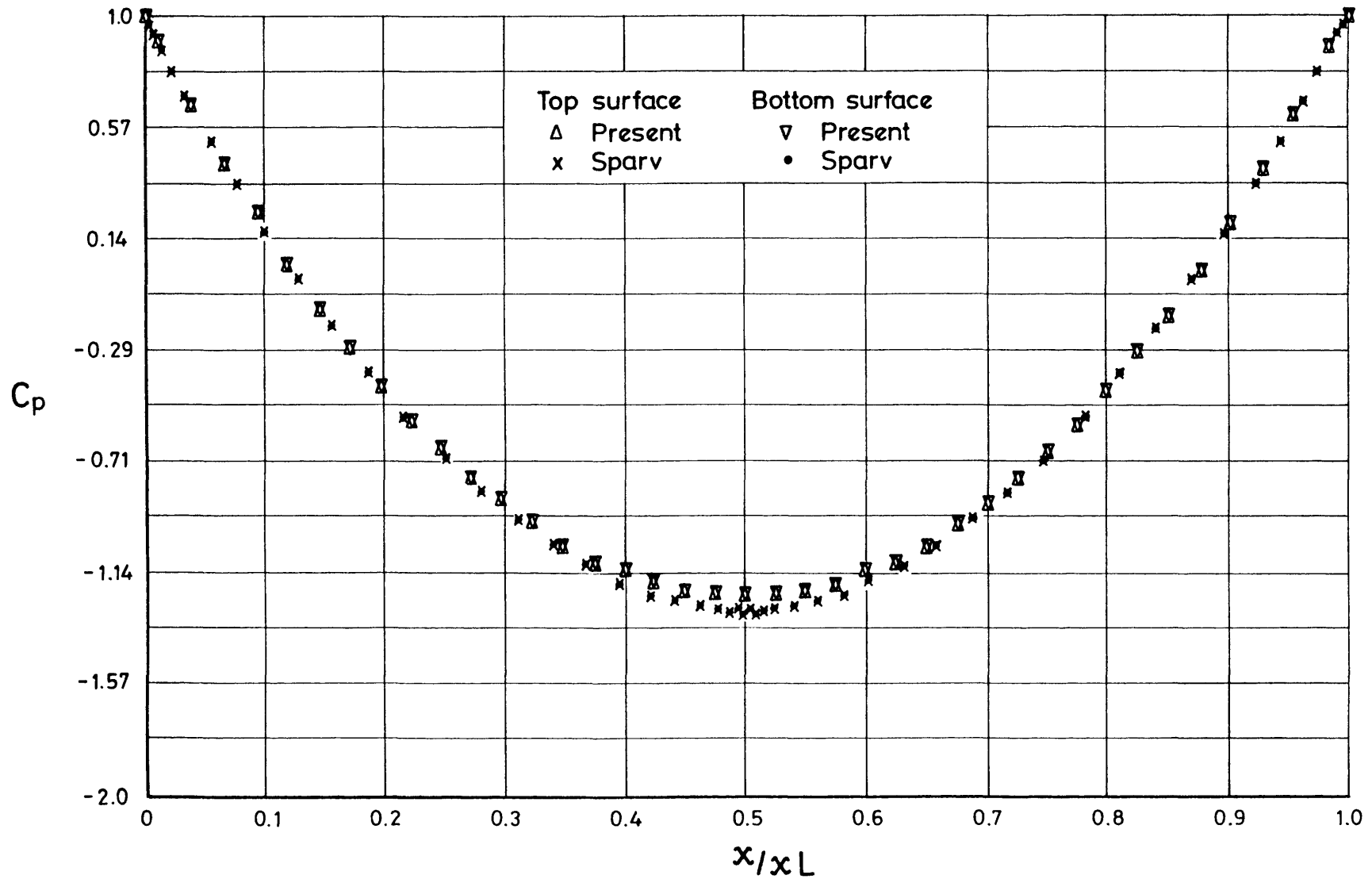


Figure 45 Surface  $C_p$  distribution over a sphere ,  $M = 0$  ,  
 Angle of attack = 0 deg.



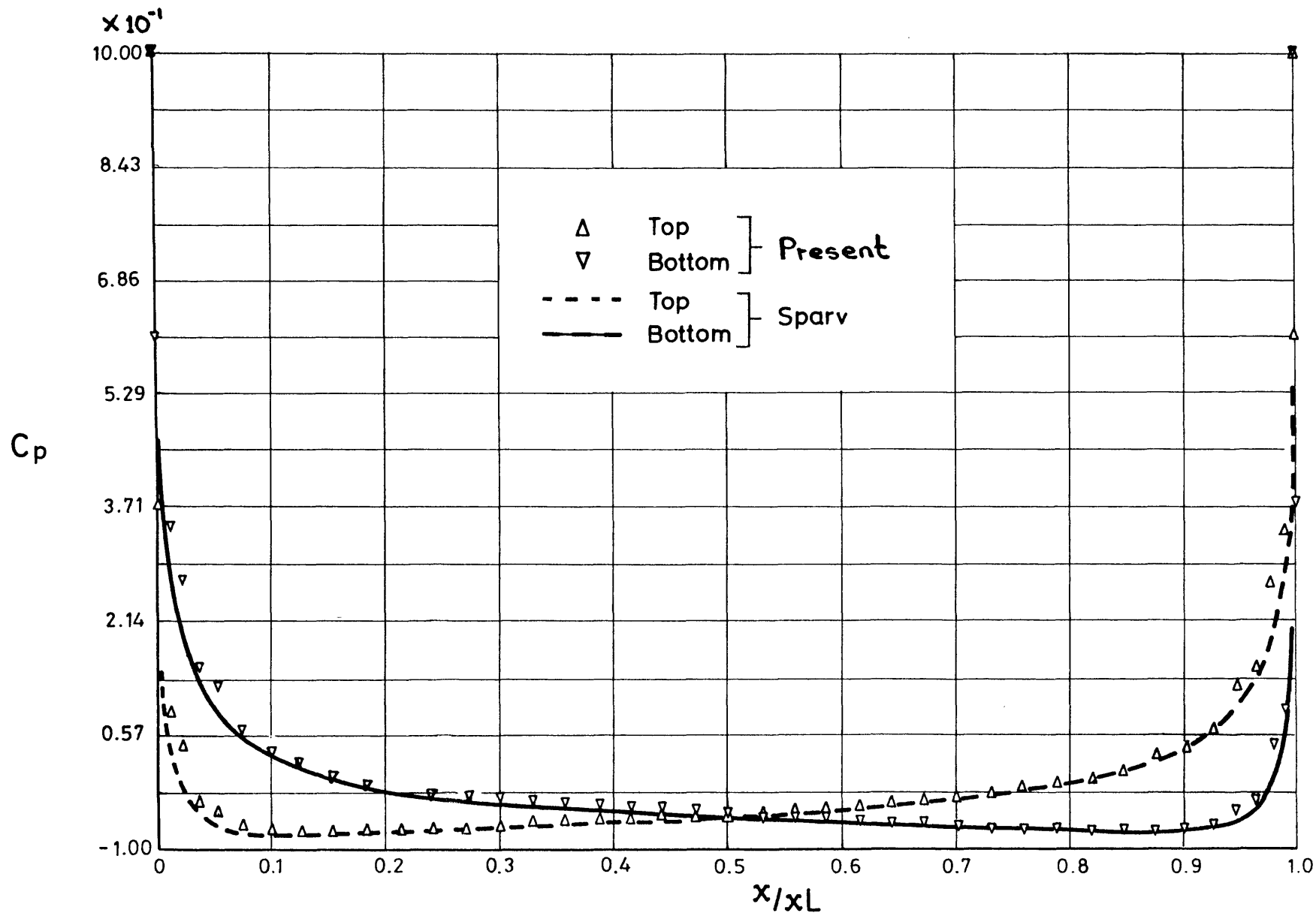


Figure 46 Surface  $C_p$  distribution for  $M = 0.01$  , Ellipsoid 8:1 , Angle of attack = 5.0 deg.

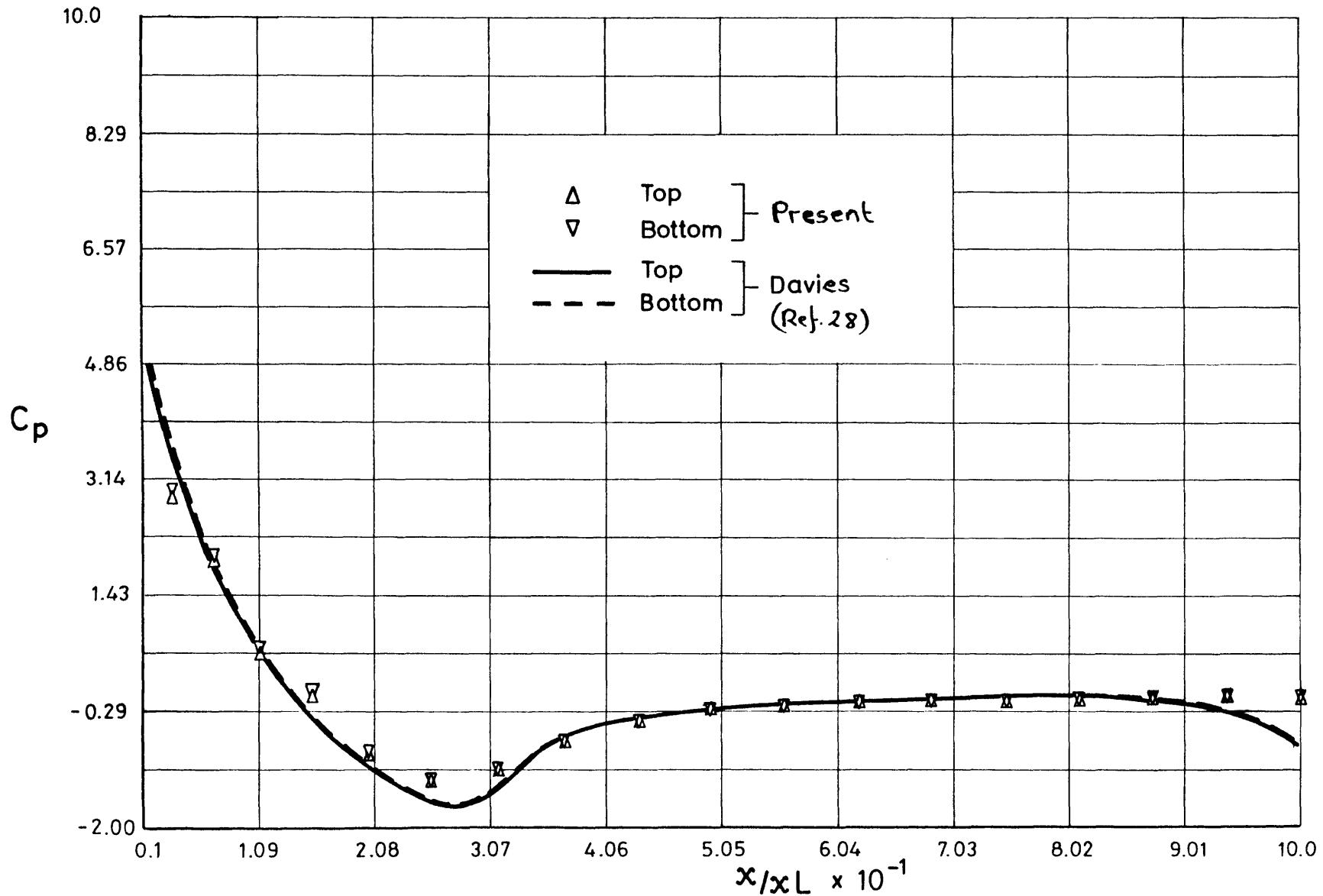


Figure 47 Surface  $C_p$  distribution for  $M = 0.01$  Cylinder with Ogive nose 4:1, Angle of attack =  $0.14^\circ$

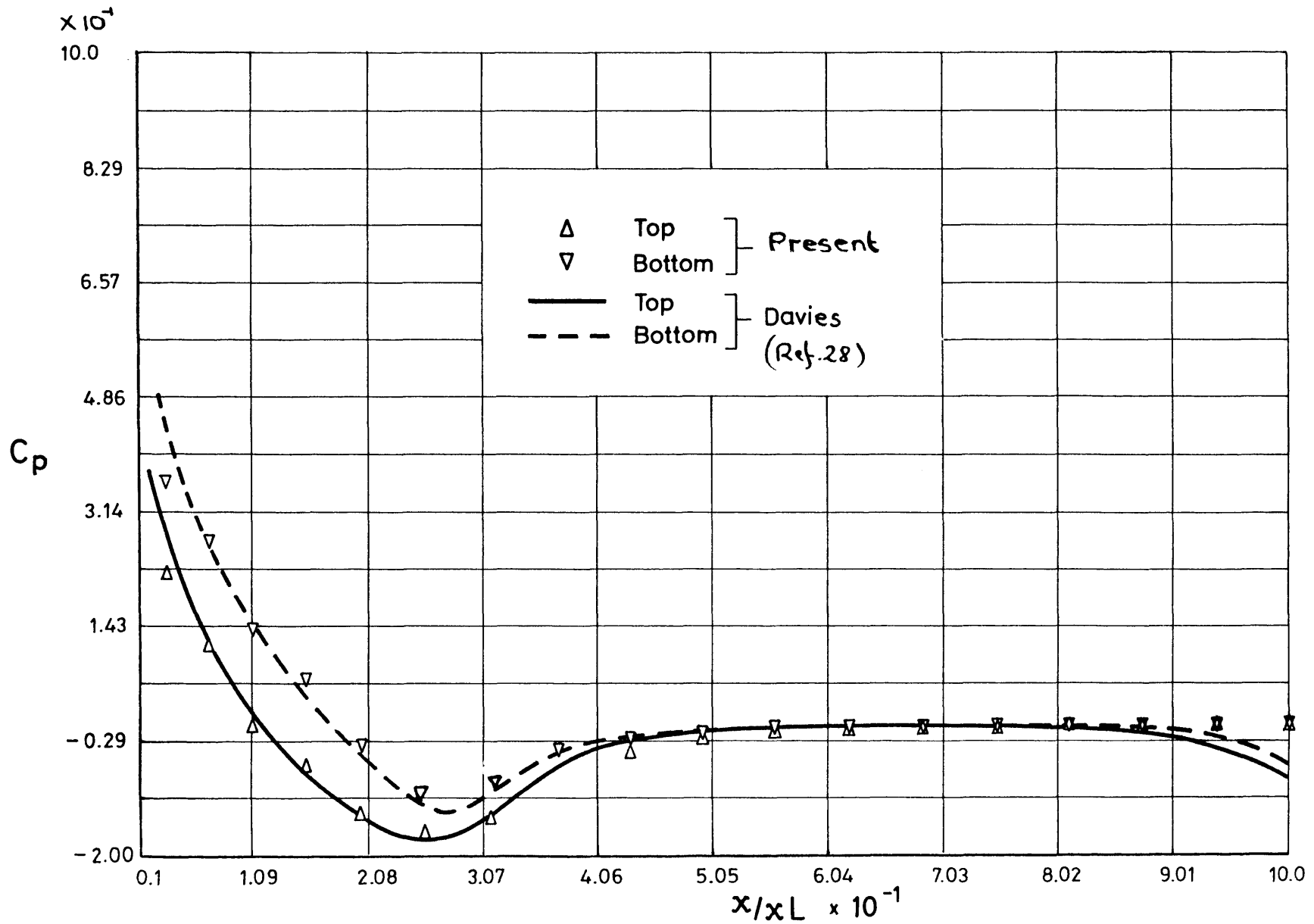


Figure 48 Surface  $C_p$  distribution for  $M = 0.01$ , Cylinder with Ogive nose 4:1, Angle of attack =  $4.14^\circ$

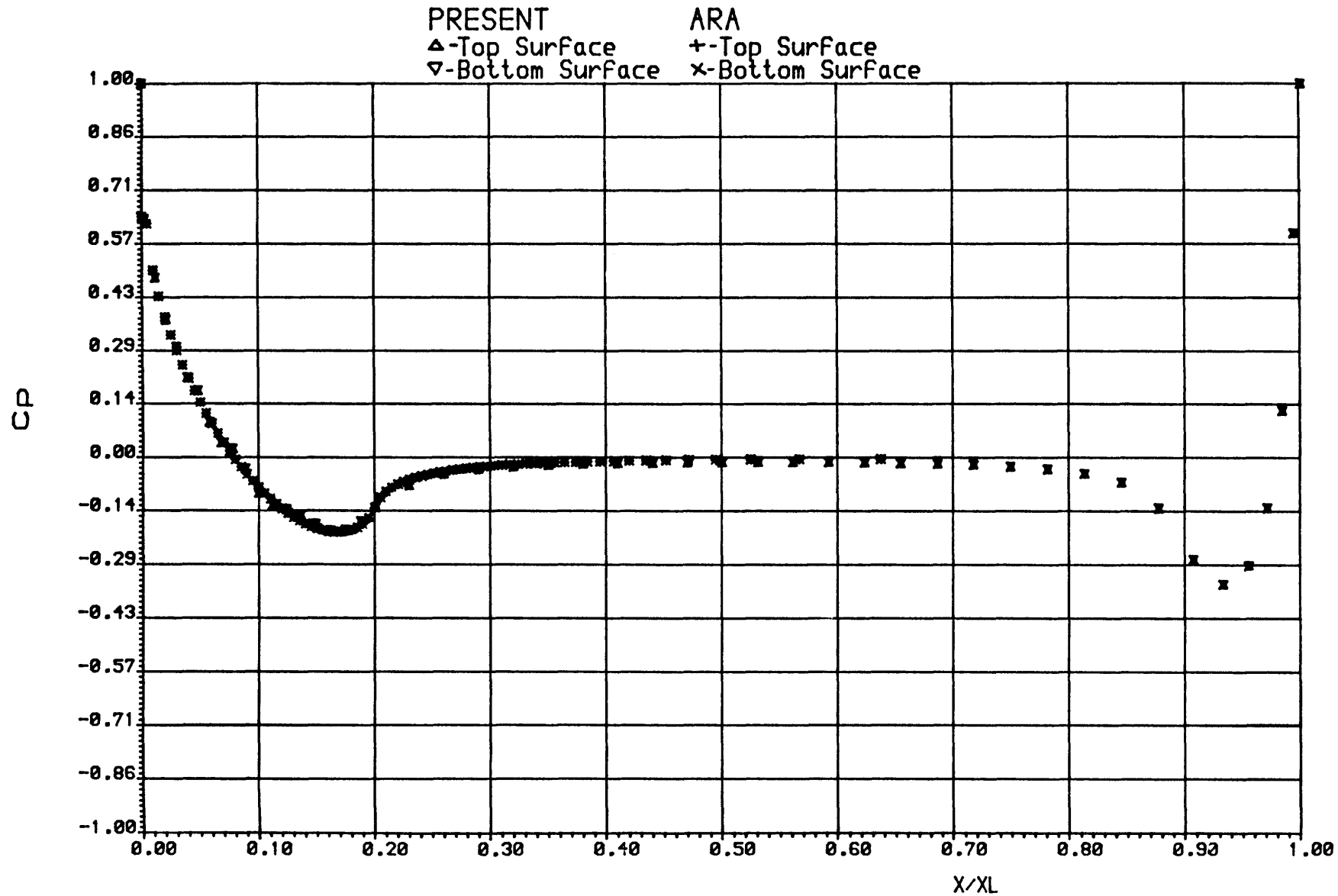


Fig. 49 Pressure distribution comparison for an ogive-cylinder  
 $M=0.5$  Incidence =  $0.0$

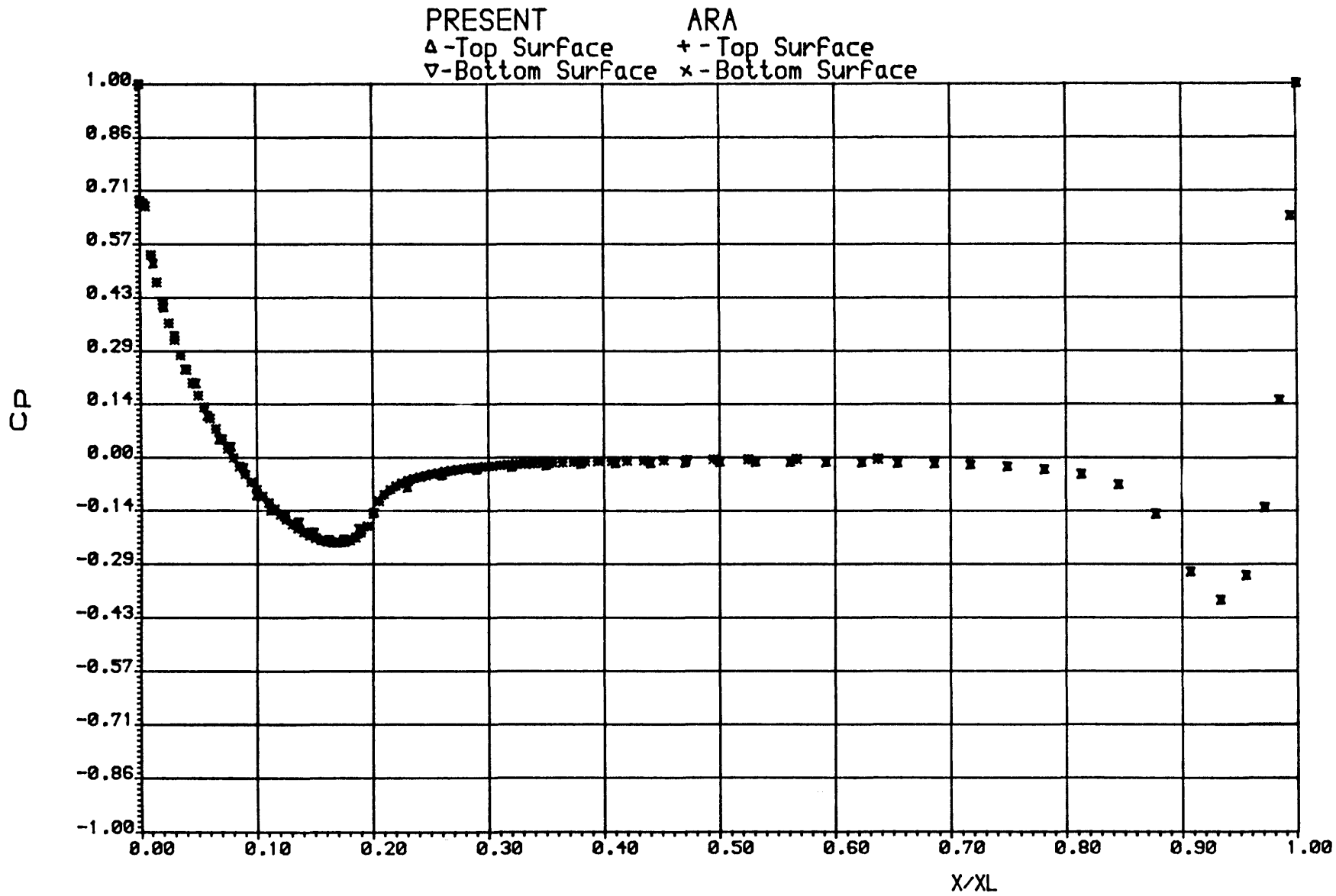


Fig.50 Pressure distribution comparison for an ogive-cylinder  
 $M=0.7$  Incidence=  $0.0$

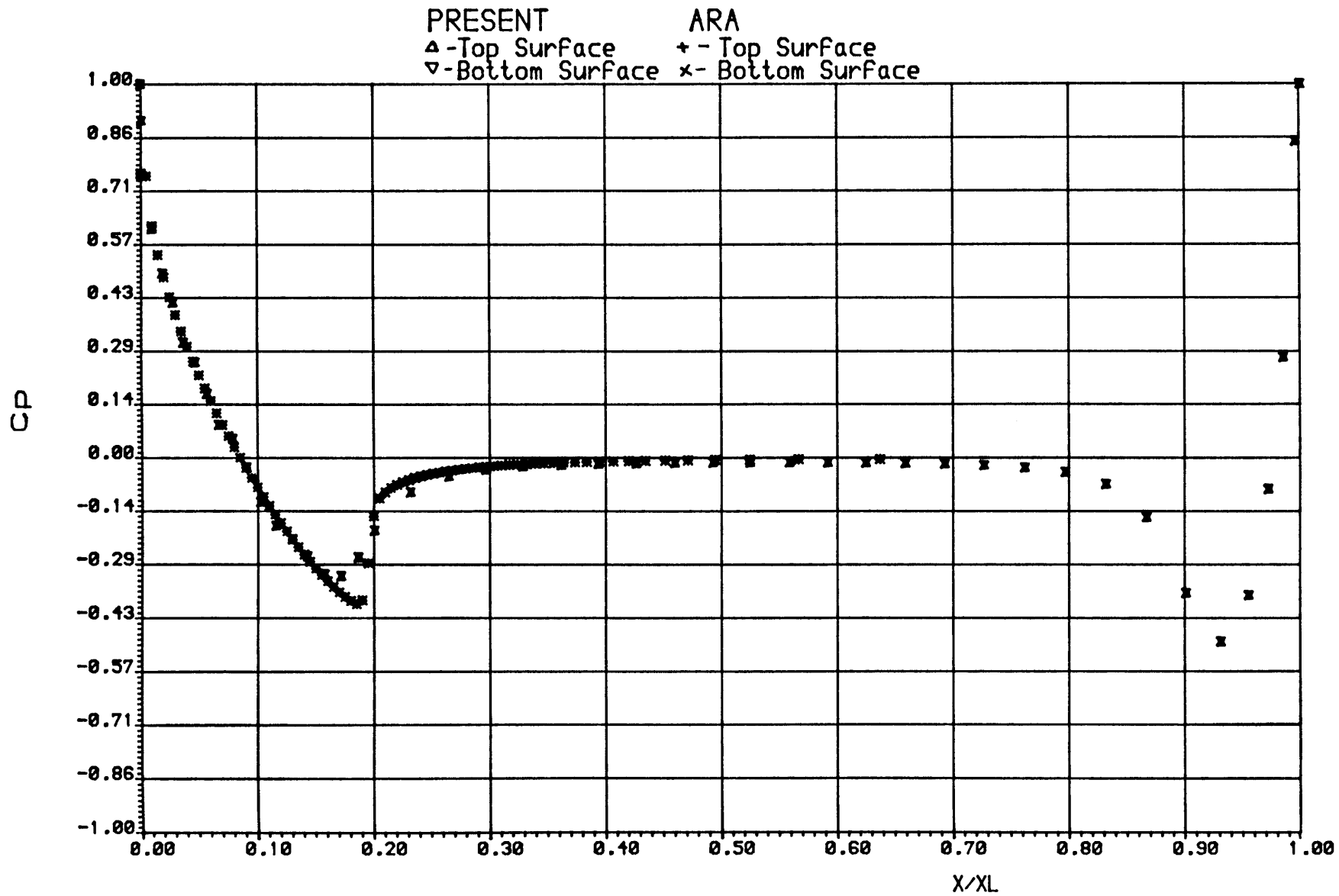


Fig.51 Pressure distribution comparison for an ogive-cylinder  
 M=0.9 Incidence= 0.0

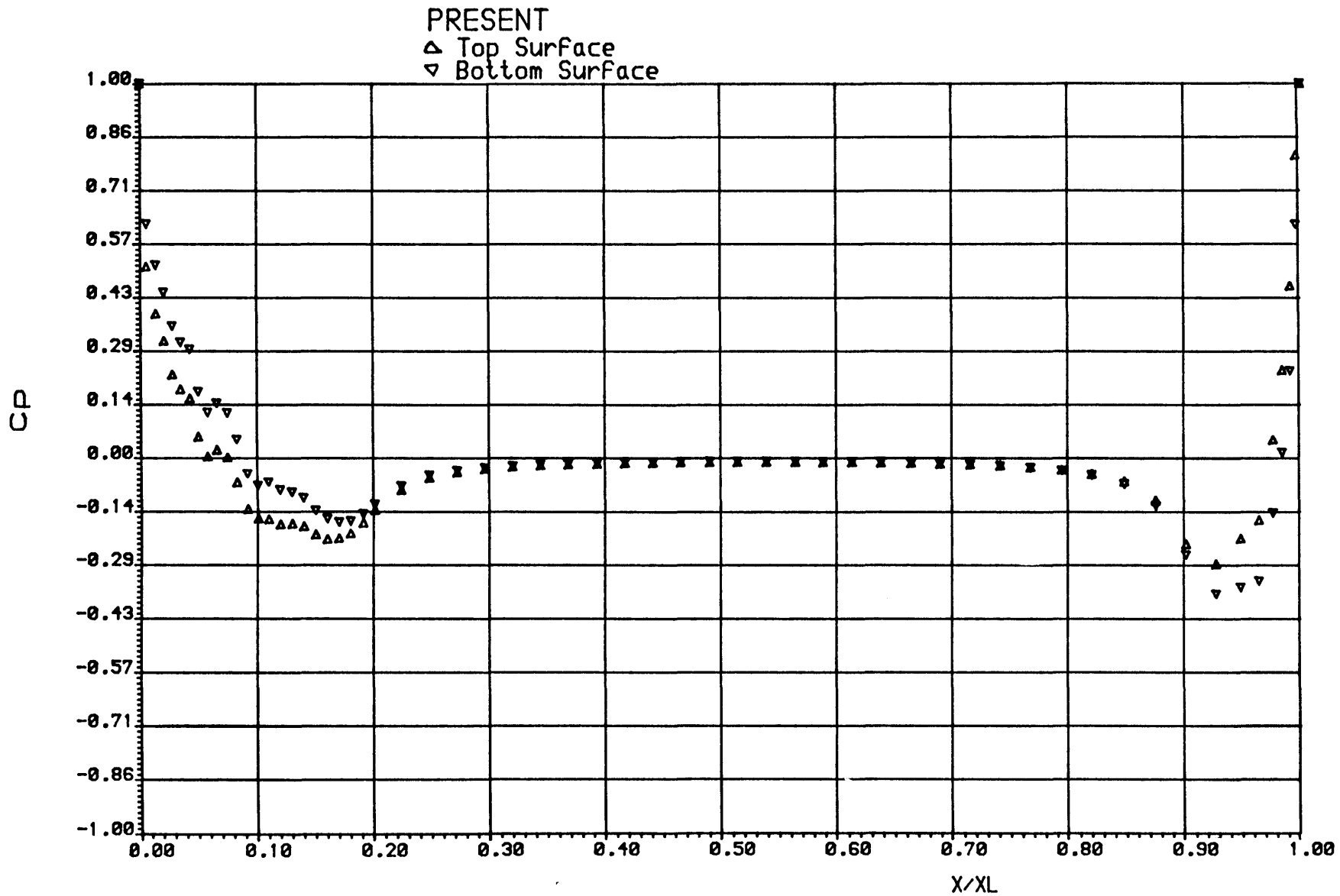


Fig 52a Pressure distribution for a ogive-cylinder  
 M=0.5 Incidence= 3.0

PRESENT  
△ Top Surface  
▽ Bottom Surface

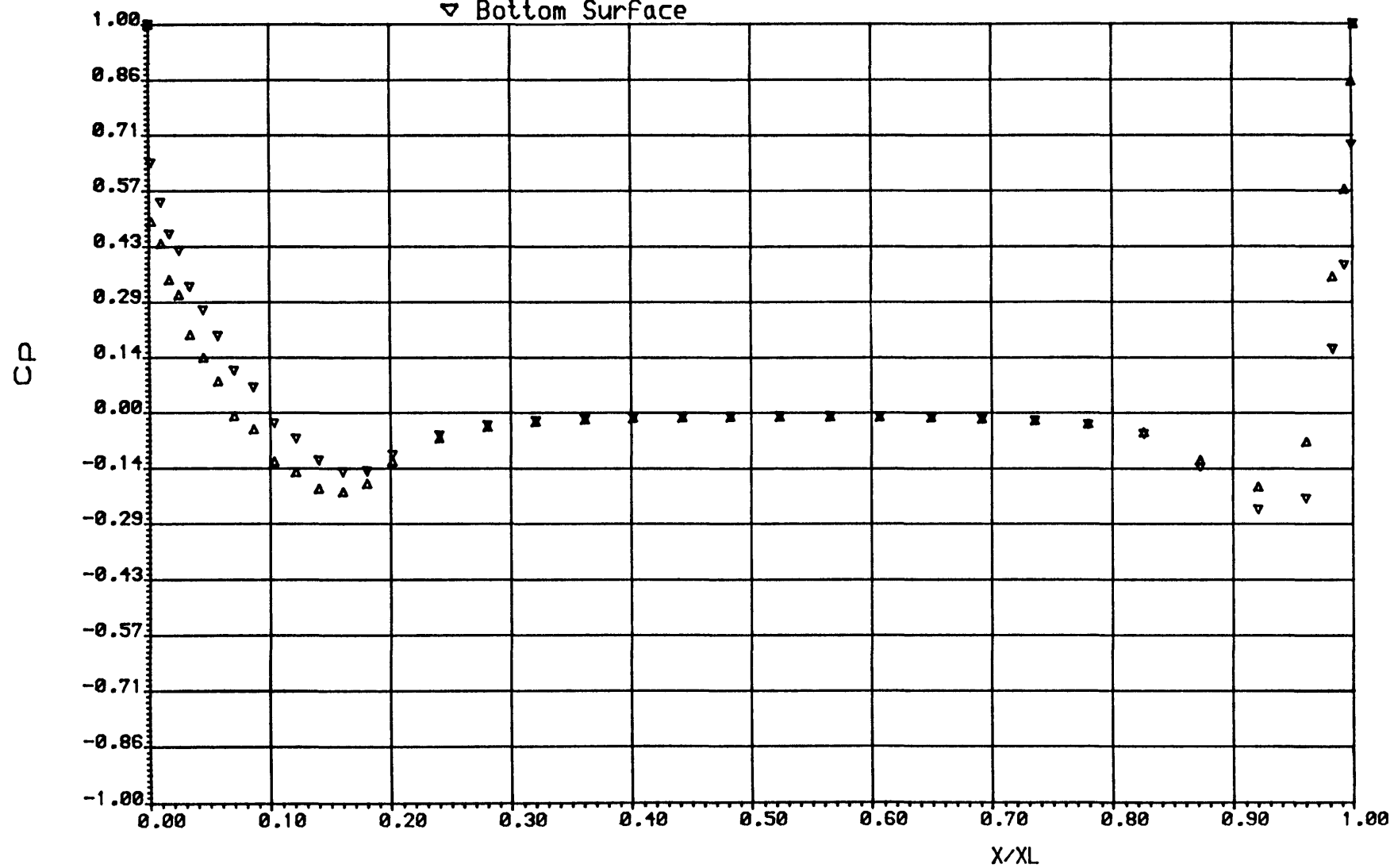
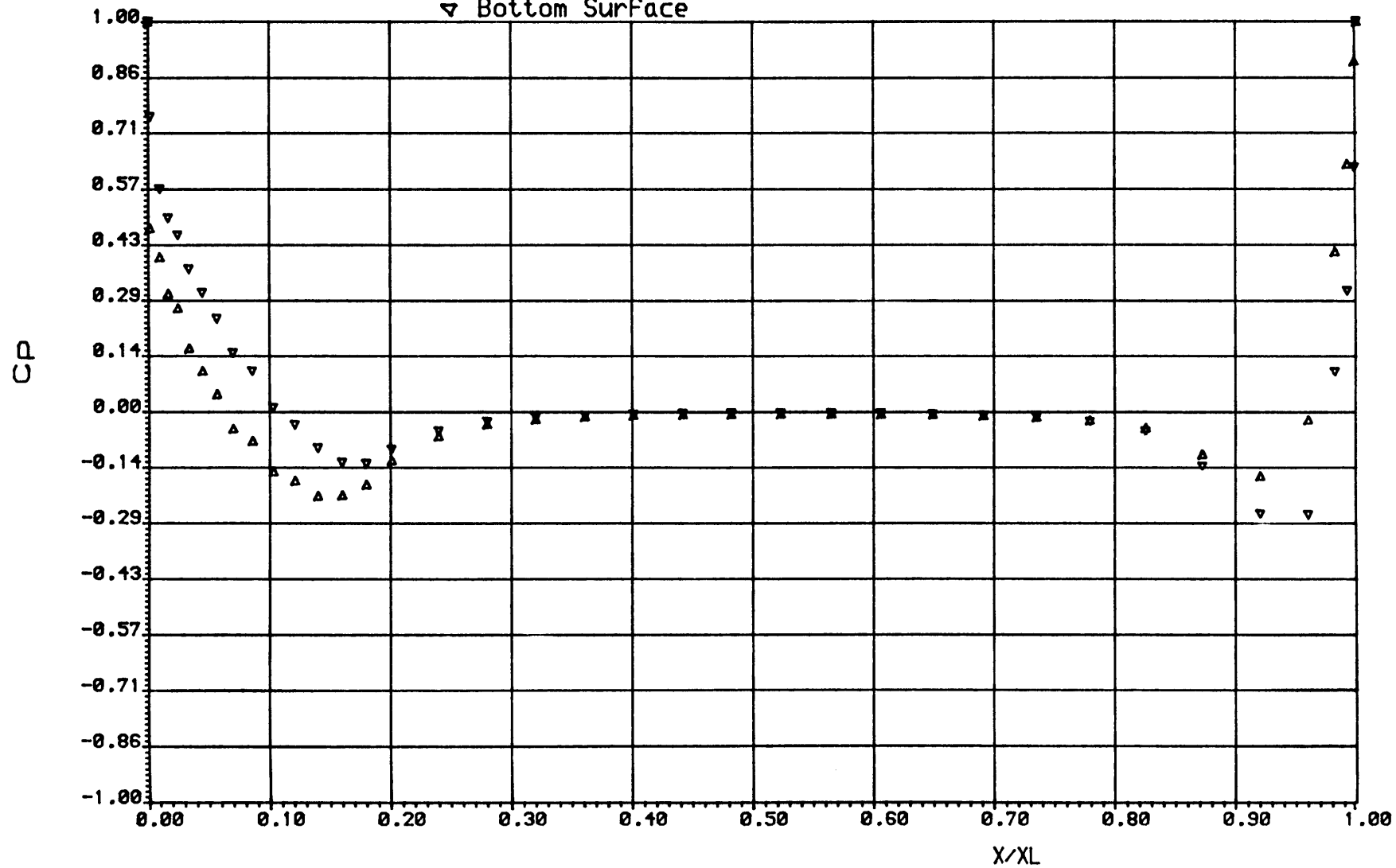


Fig 52b Pressure distribution for an ogive-cylinder at  
M=0.5 Incidence= 3.0



PRESENT  
△ Top Surface  
▽ Bottom Surface



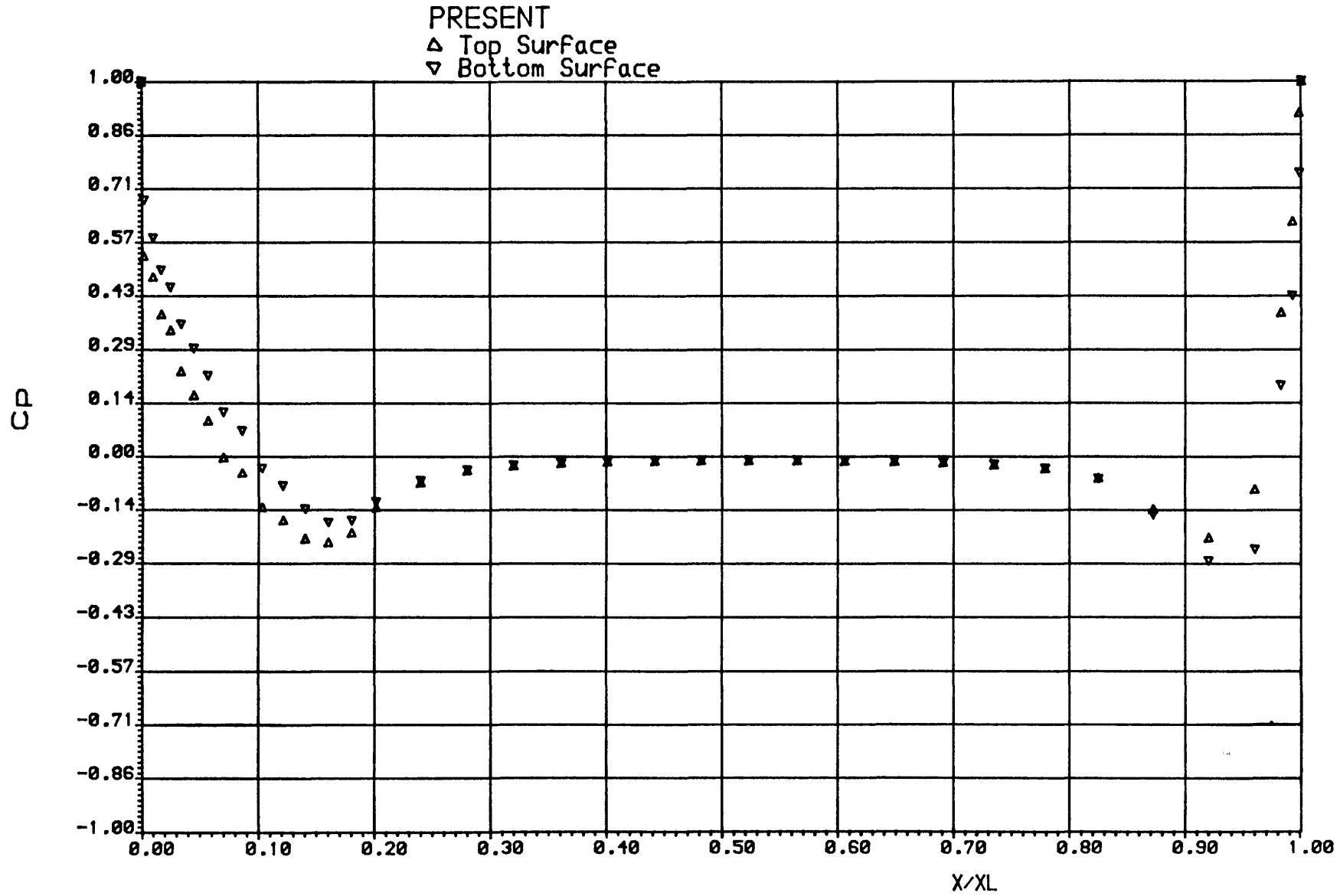


Fig.53 Pressure distribution for an ogive-cylinder  
 $M=0.7$  Incidence=  $3.0$

PRESENT  
△ Top Surface  
▽ Bottom Surface

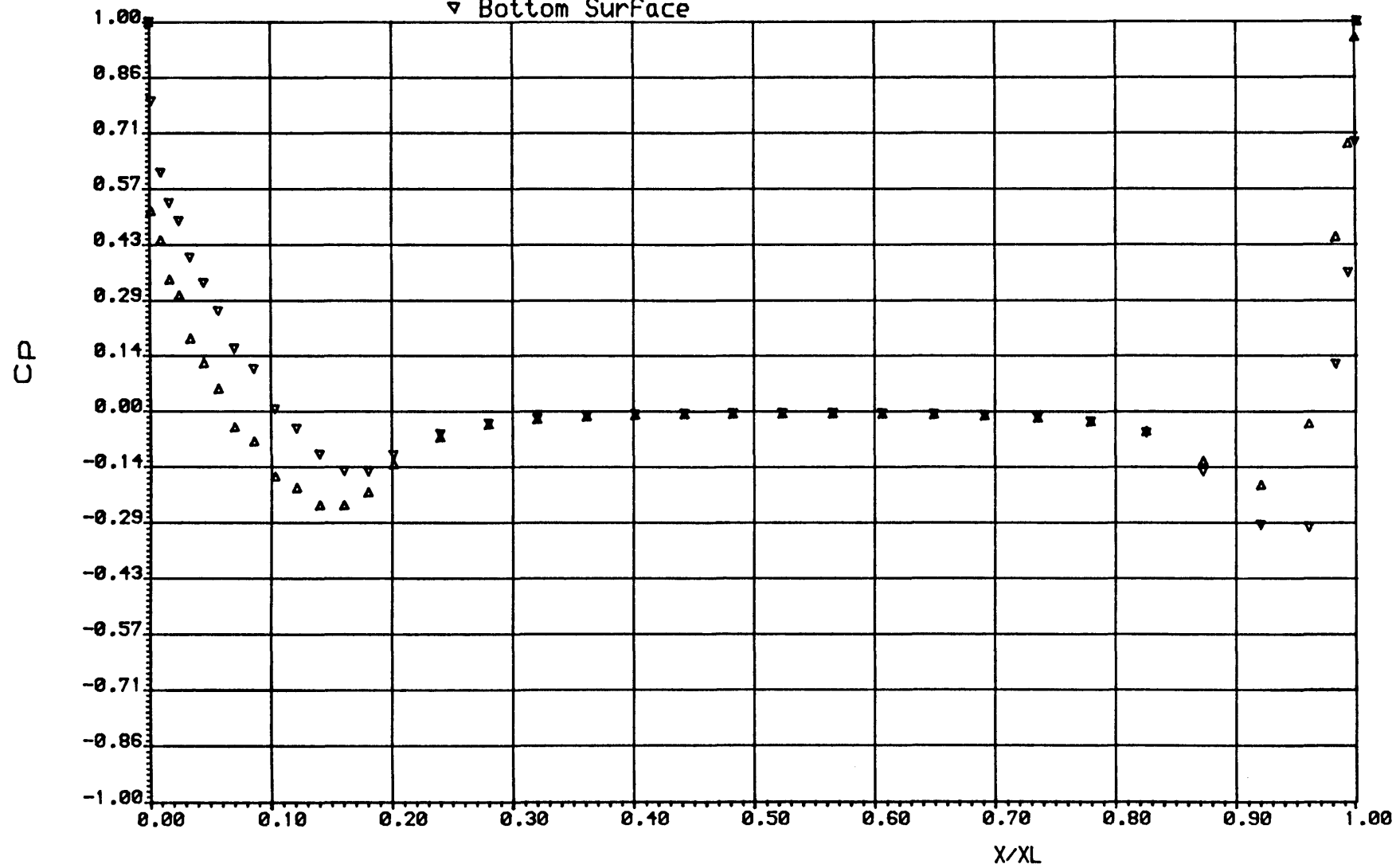


Fig.54 Pressure distribution for an ogive-cylinder  
M=0.7 Incidence= 5.0

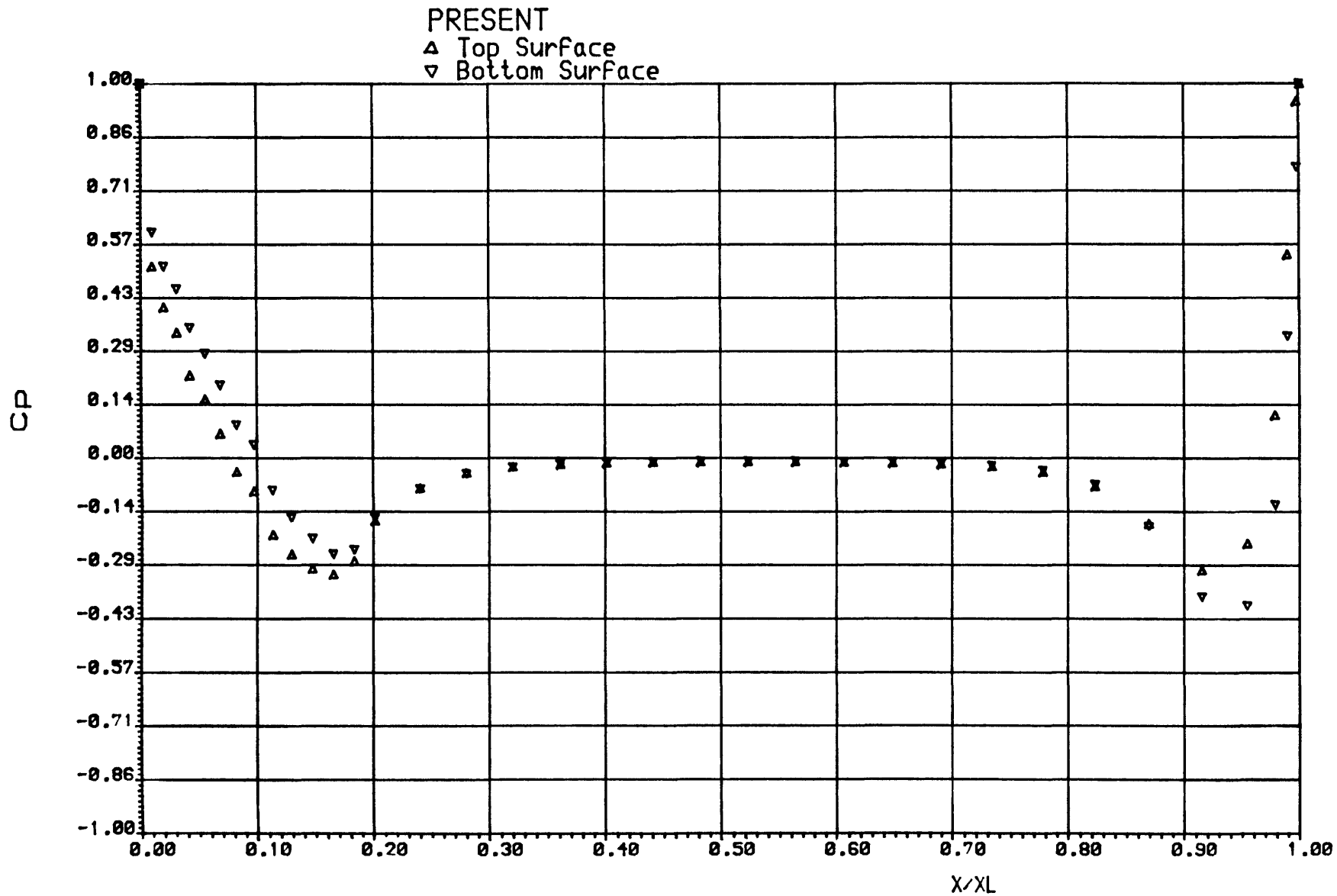


Fig.55 Pressure distribution for an ogive-cylinder  
 M=0.9 Incidence= 3.0

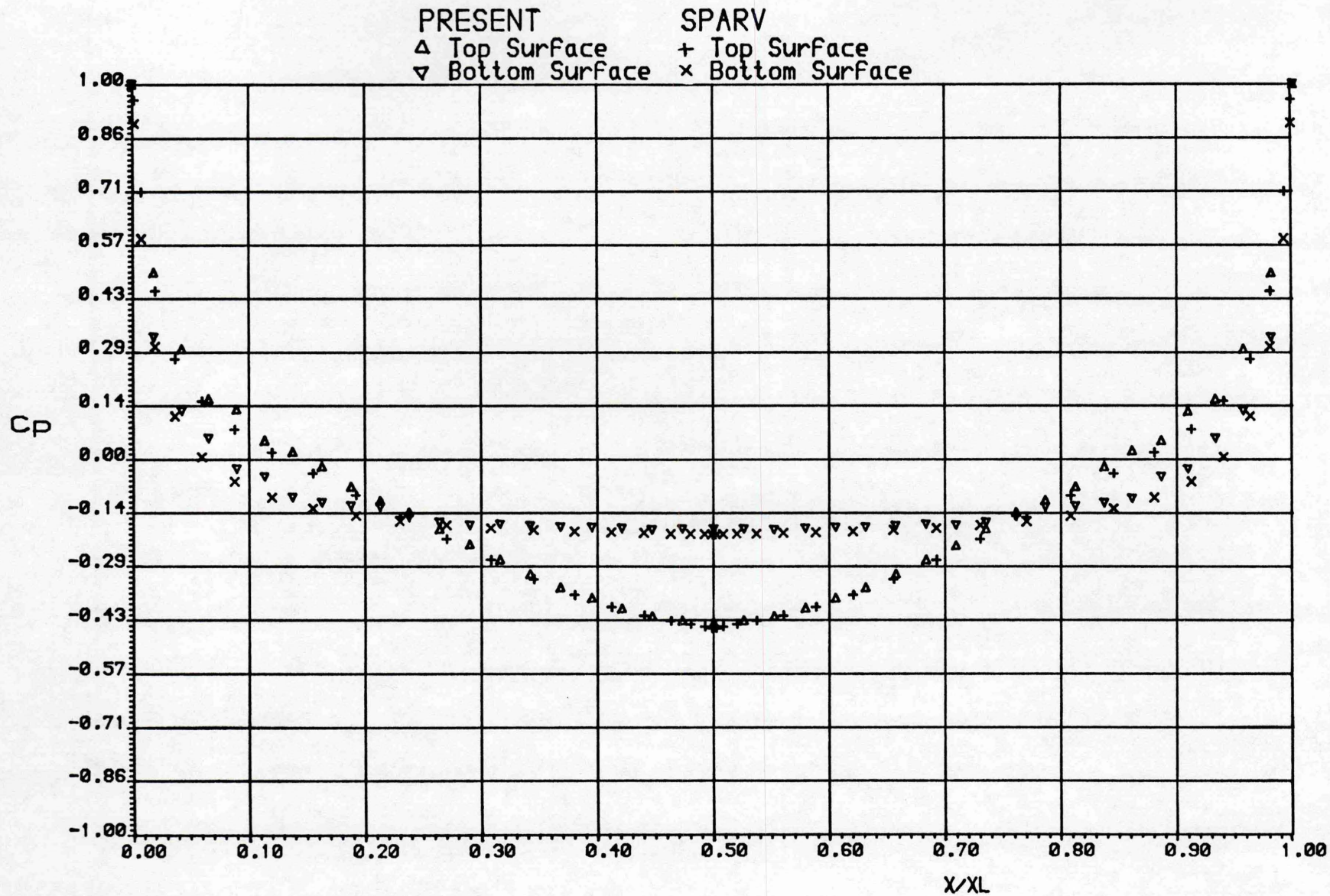


Fig.56. Pressure distribution on bottom ellipsoid of configuration  
 $M=0.0$  Incidence= $0.0$  Spacing= $0.025$

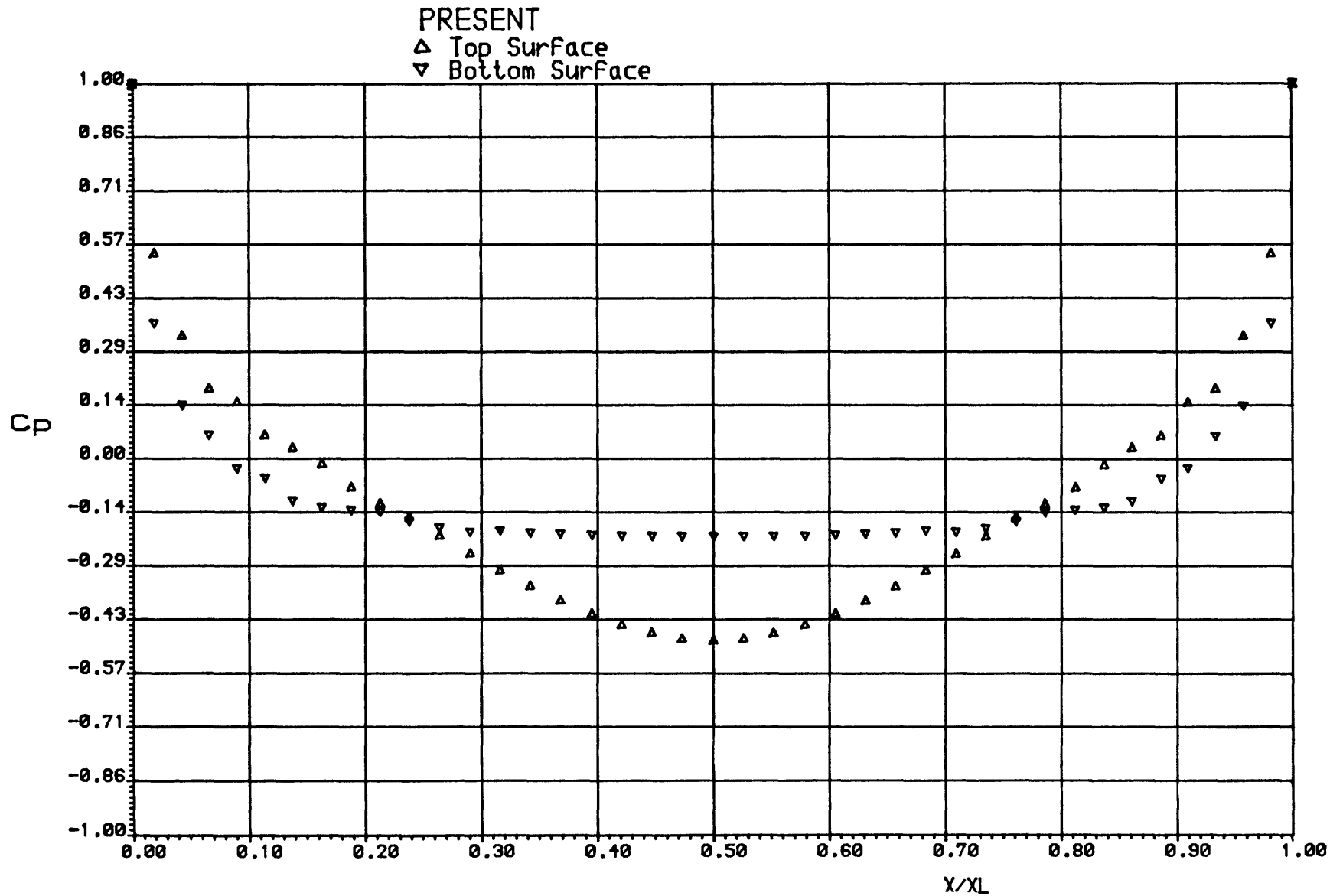


Fig. 57. Pressure distribution on bottom ellipsoid of configuration  
 M=0.5 Incidence=0.0 Spacing=0.025

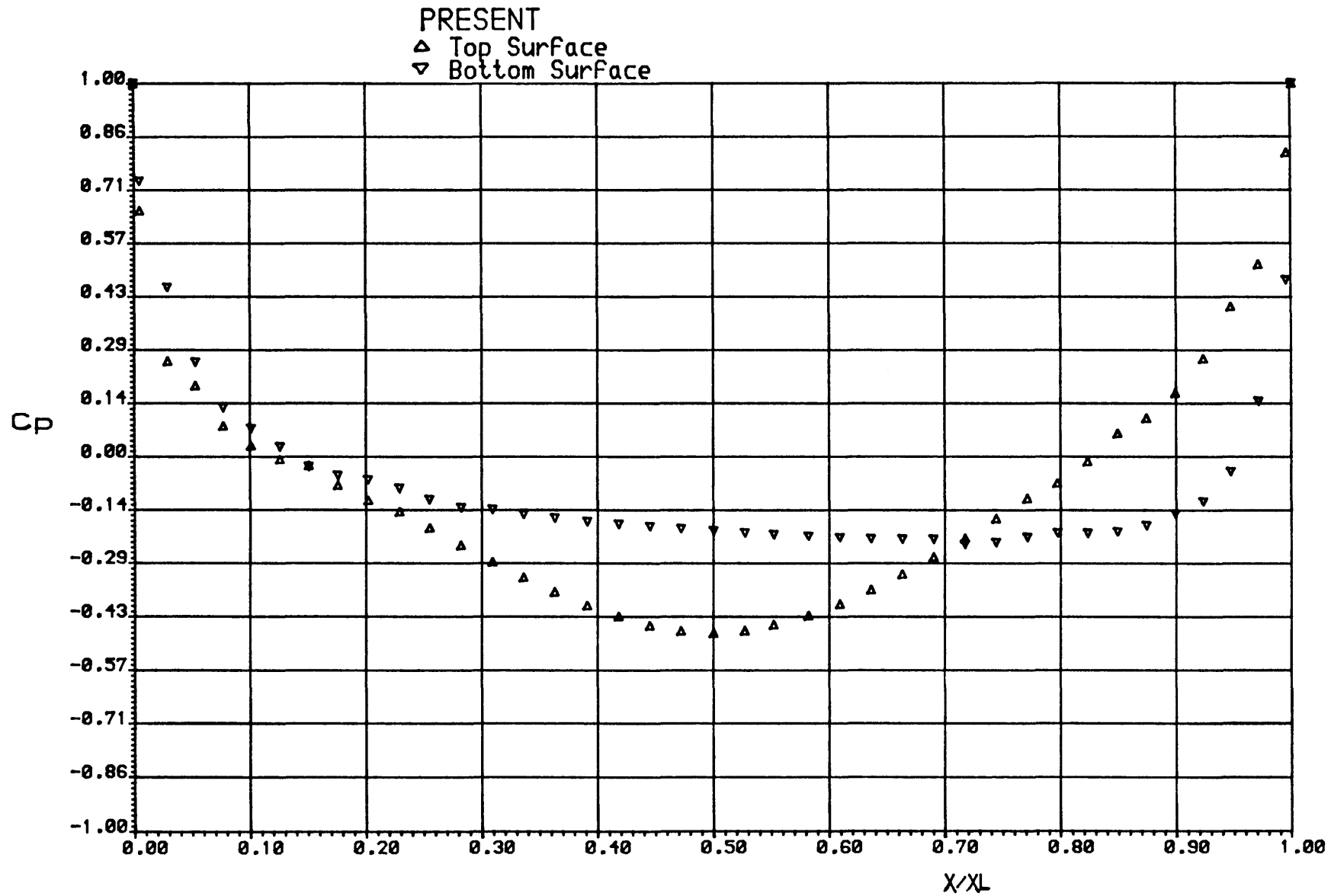


Fig.58. Pressure distribution on bottom ellipsoid of configuration in  $M=0.5$  Incidence= $5.0$  Spacing= $0.025$

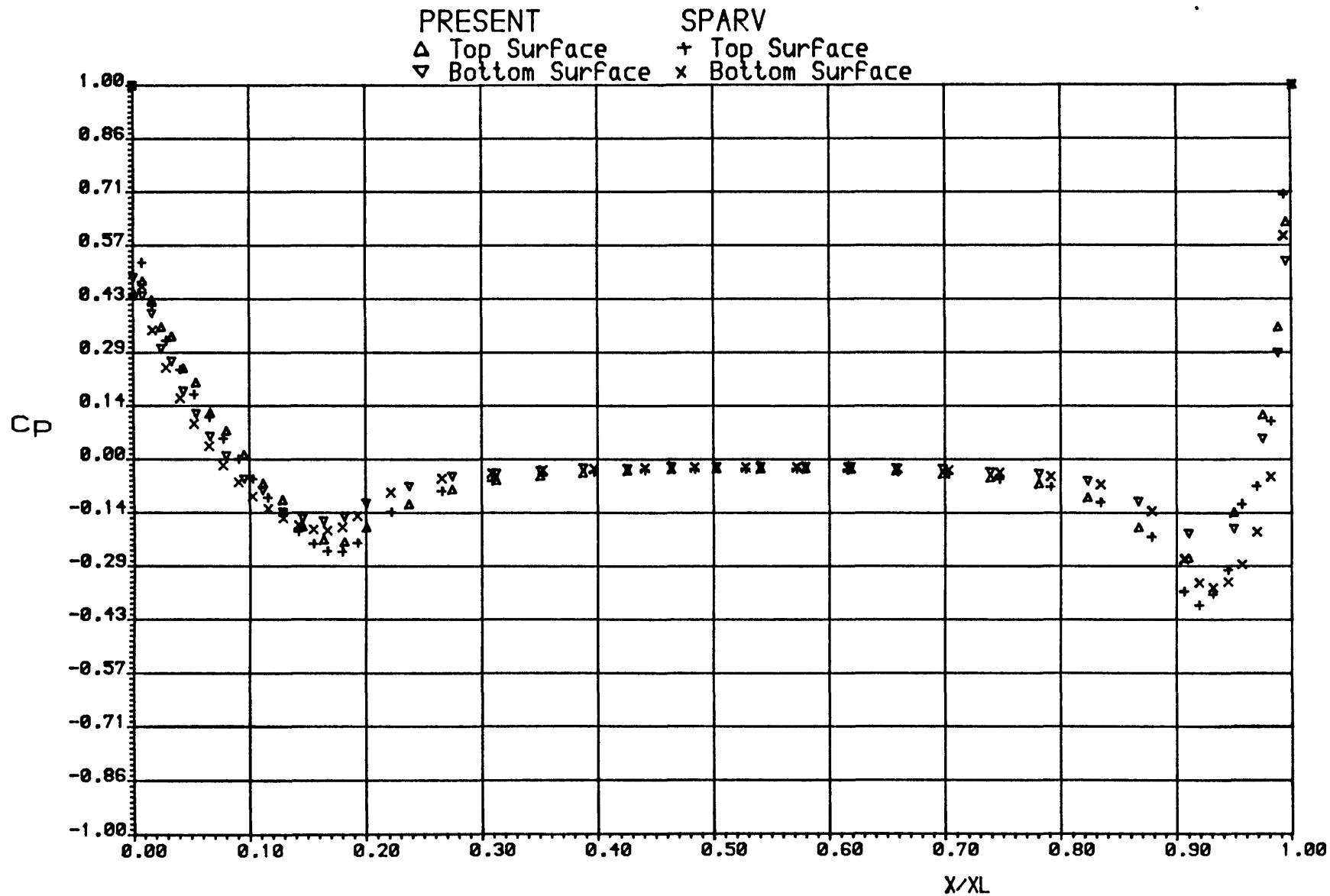


Fig.59 Pressure distribution for double ogive-cylinder configuration  
 $M=0.0$  Incidence= $0.0$  Spacing= $0.025$



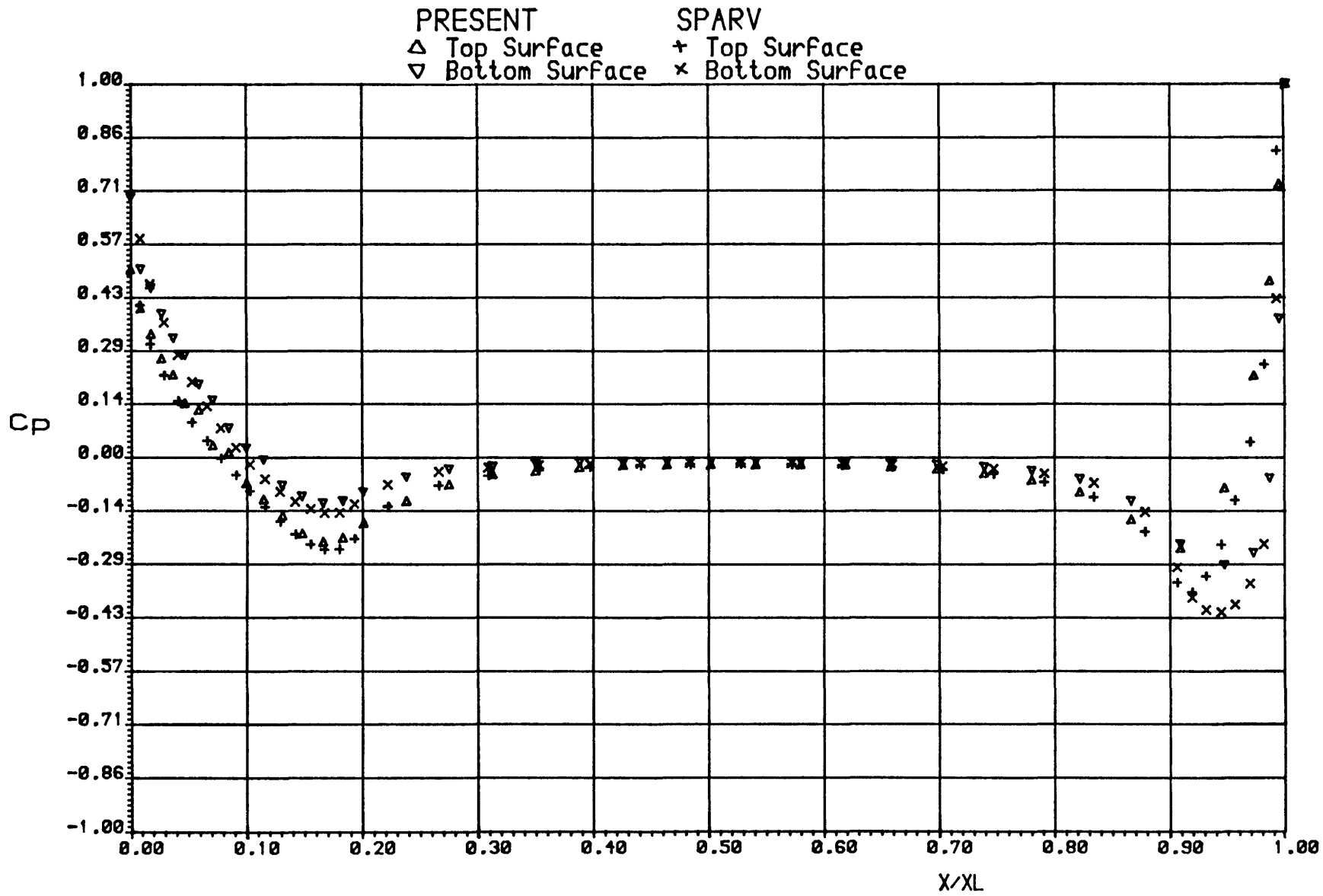


Fig. 60 Pressure distribution for bottom ogive-cylinder of configuration  
 $M=0.0$  Incidence=5.0 Spacing=0.025

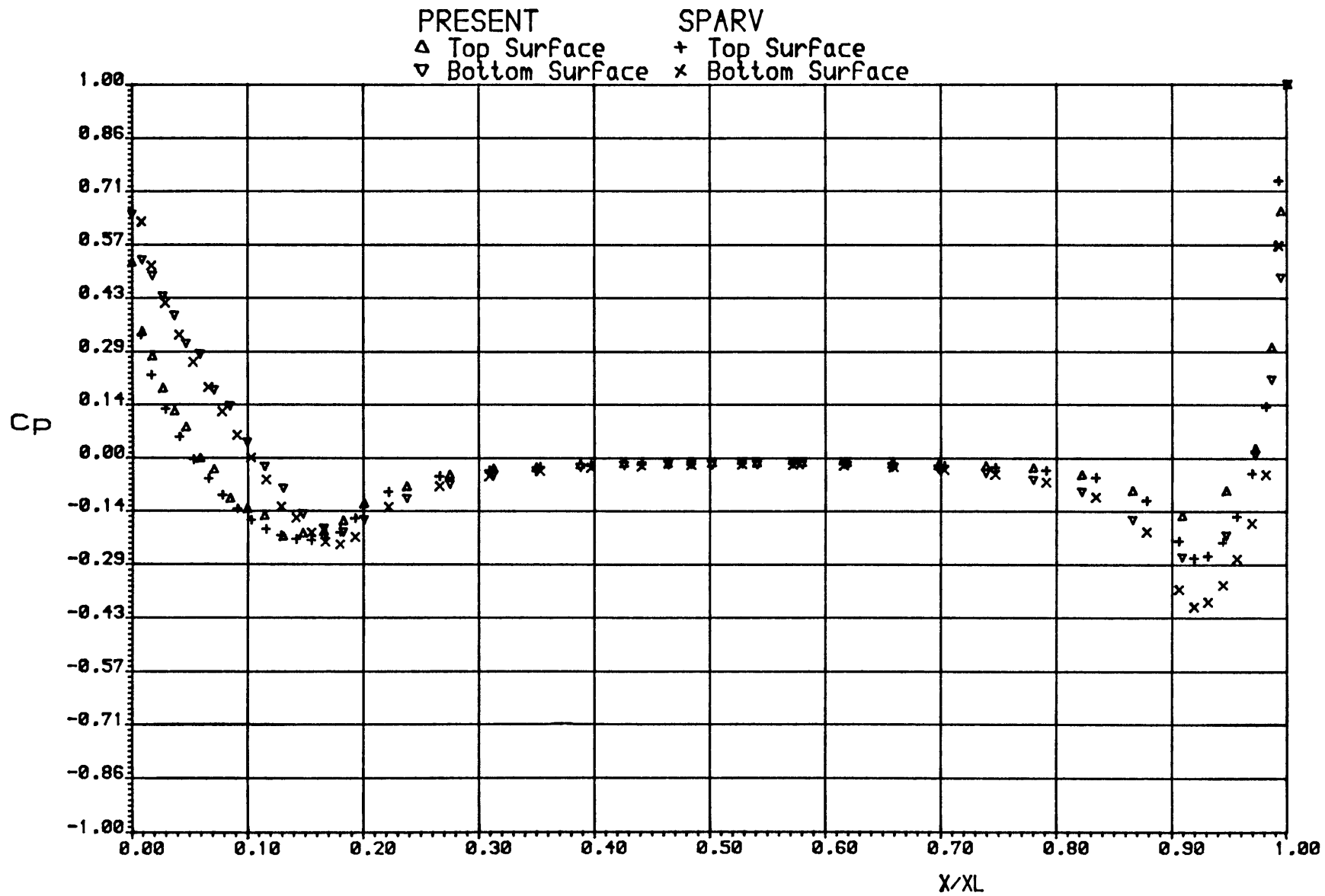


Fig.6.1 Pressure distribution for top ogive-cylinder of configuration  
 $M=0.0$  Incidence=5.0 Spacing=0.025

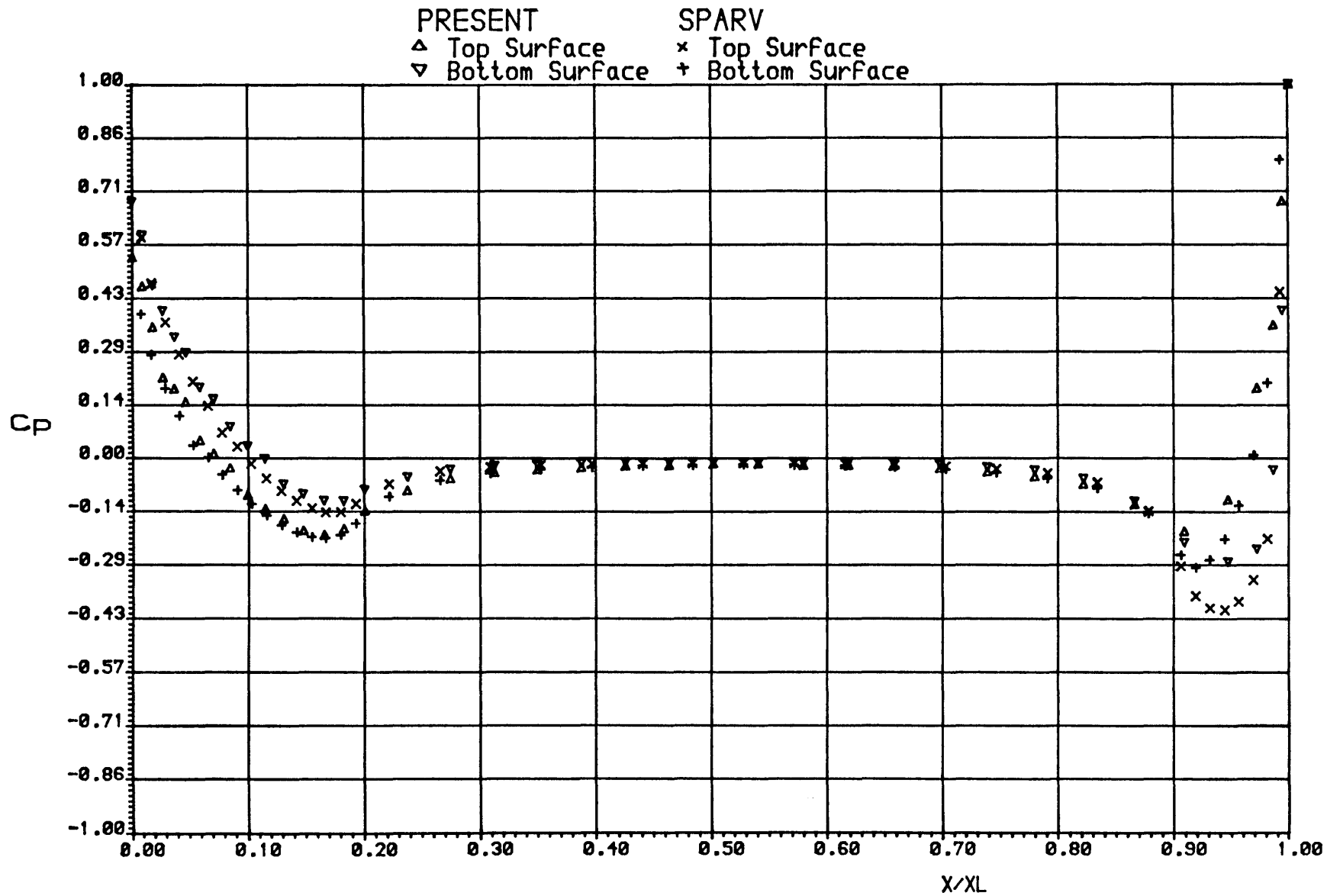


Fig.62 Pressure distribution for bottom ogive-cylinder of configuration  
 $M=0.0$  Incidence=5.0 Spacing=0.05

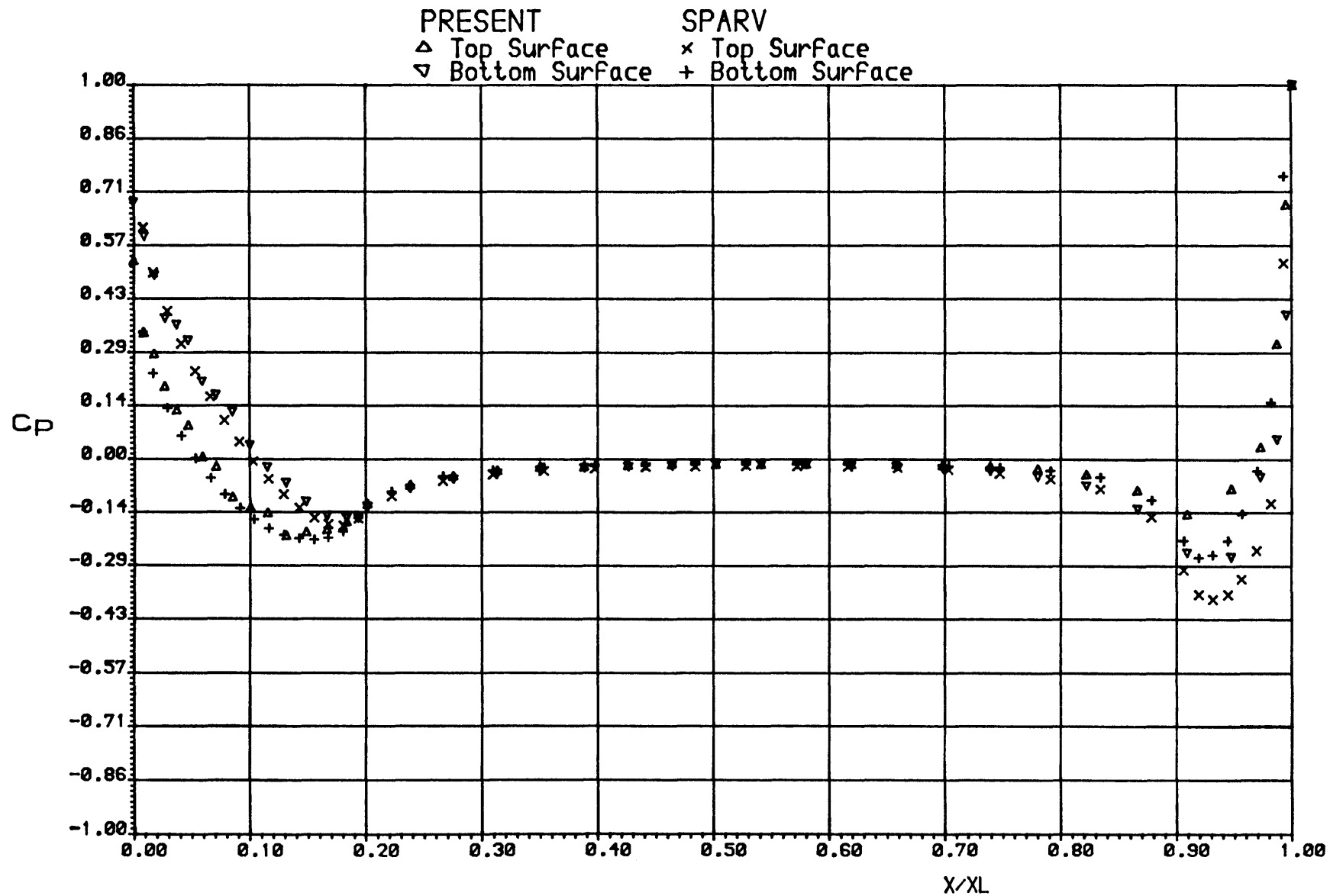


Fig. 63 Pressure distribution for top ogive-cylinder of configuration  
 $M=0.0$  Incidence=5.0 Spacing=0.05

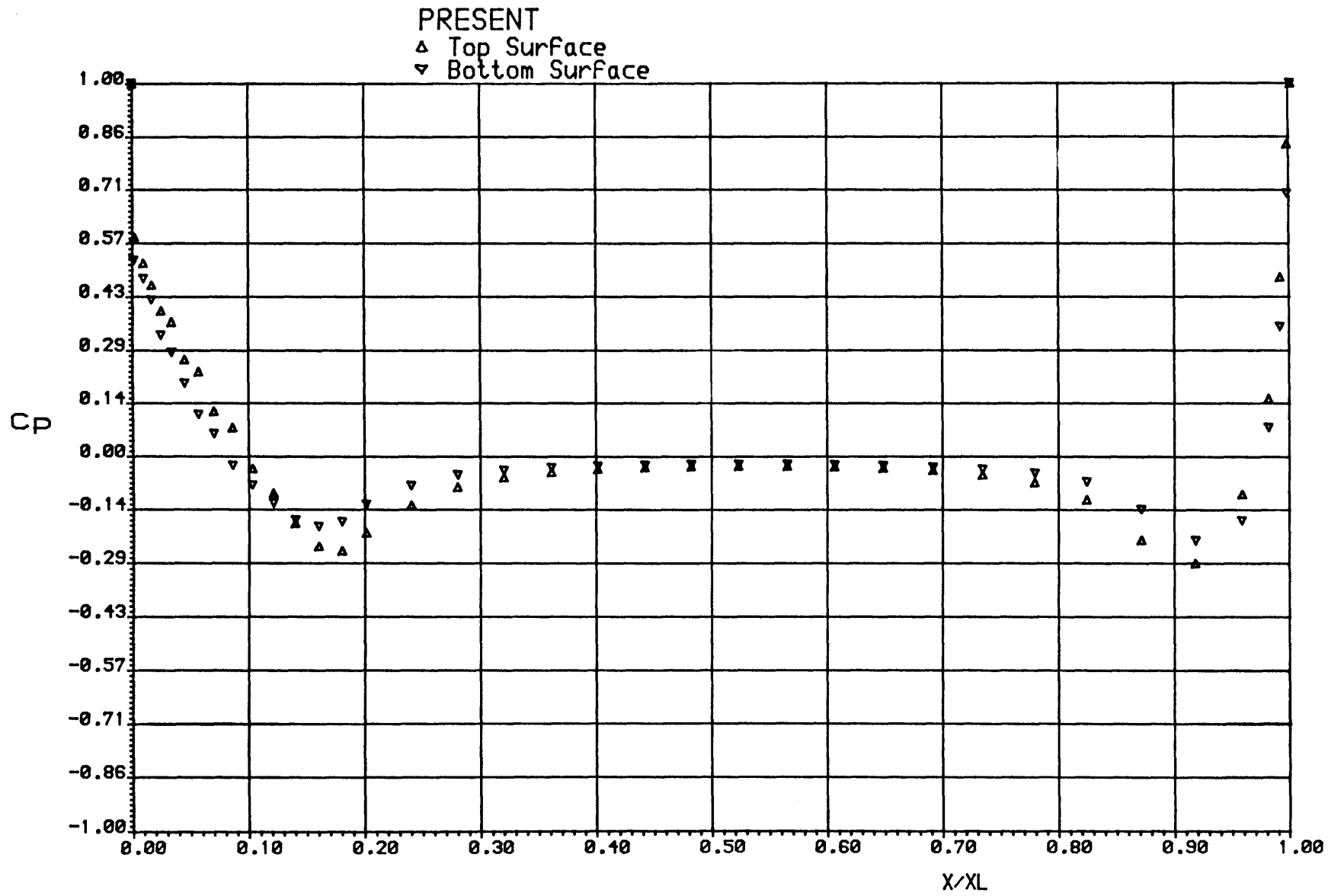


Fig. 64 Pressure distribution for a double ogive-cylinder configuration  
 $M=0.5$  Incidence= $0.0$  Spacing= $0.025$

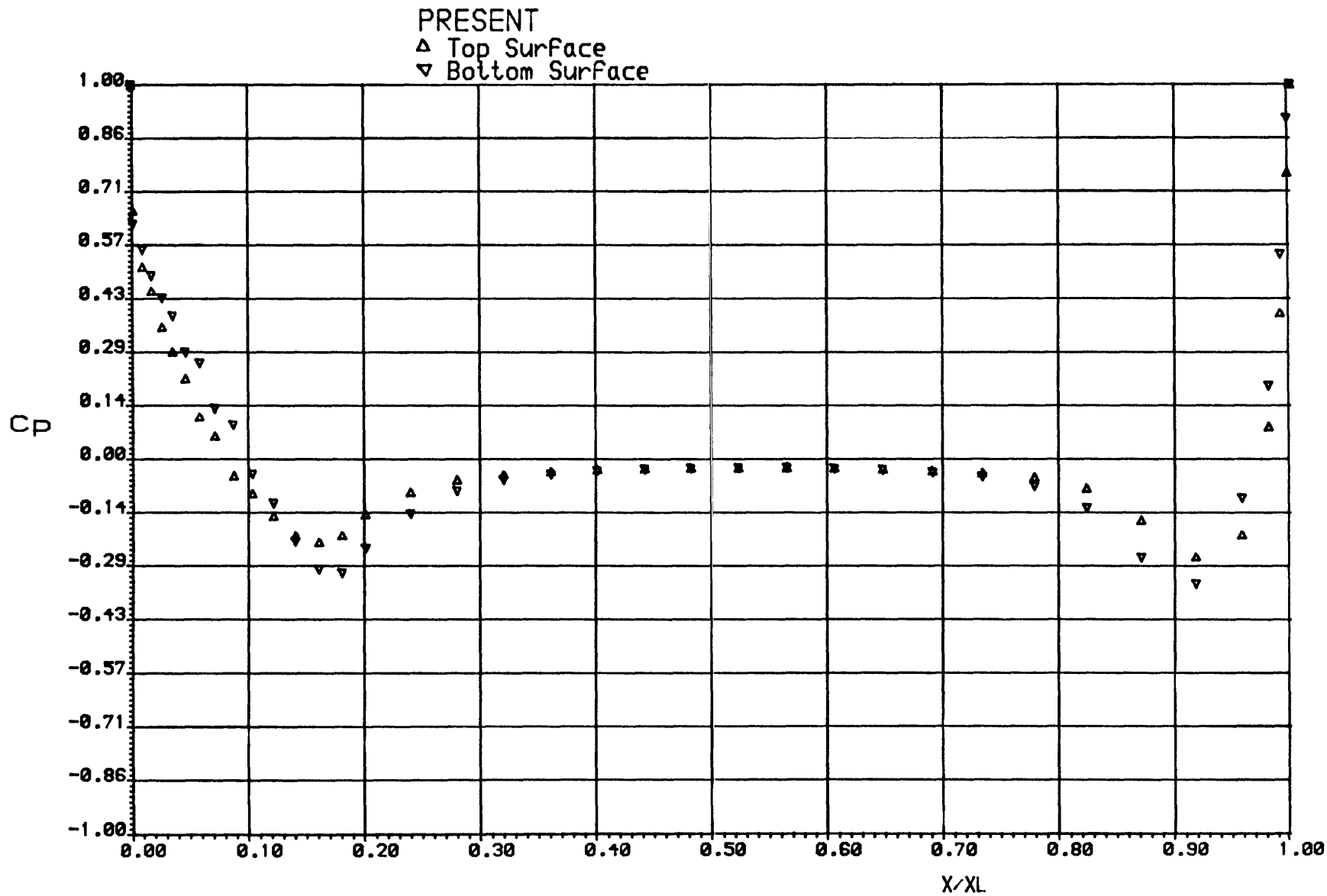


Fig.65 Pressure distribution over a double ogive-cylinder configuration  
 $M=0.7$  Incidence= $0.0$  Spacing= $0.025$

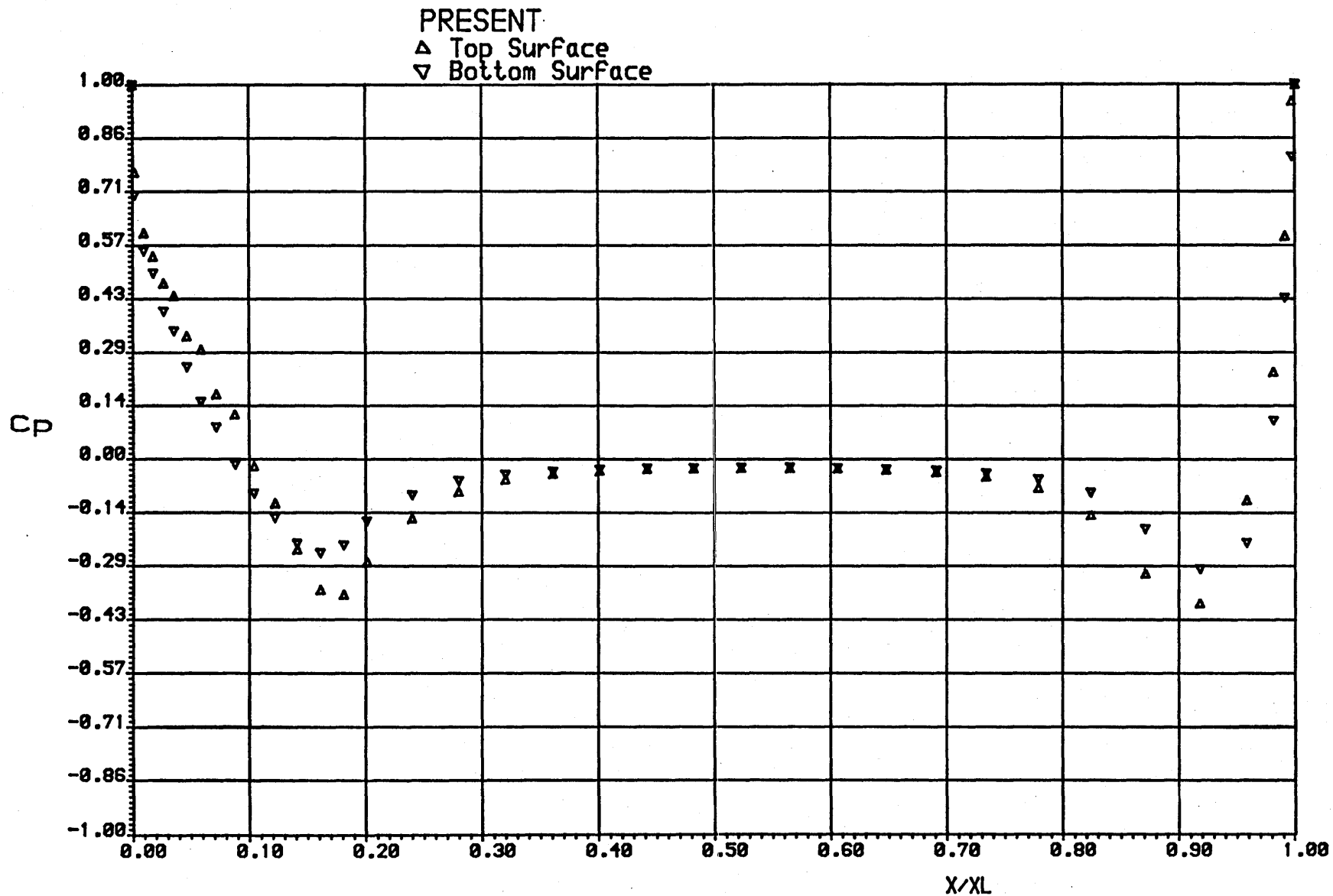


Fig.66 Pressure distribution over a double ogive-cylinder configuration  
 $M=0.8$  Incidence= $0.0$  Spacing= $0.025$

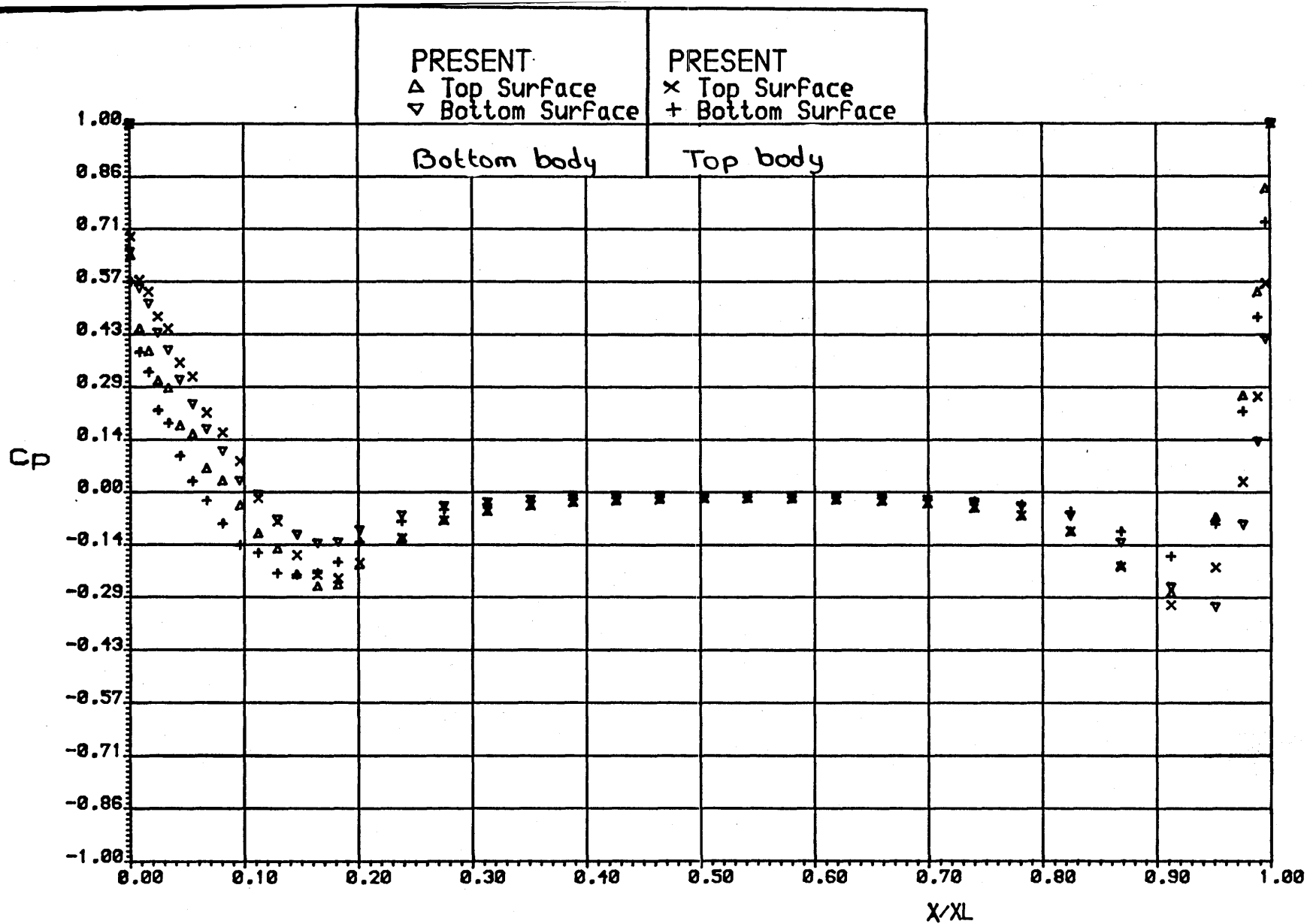


Fig.67 Pressure distribution on both ogive-cylinders of configuration  
 $M=0.5$  Incidence=5.0 Spacing=0.025



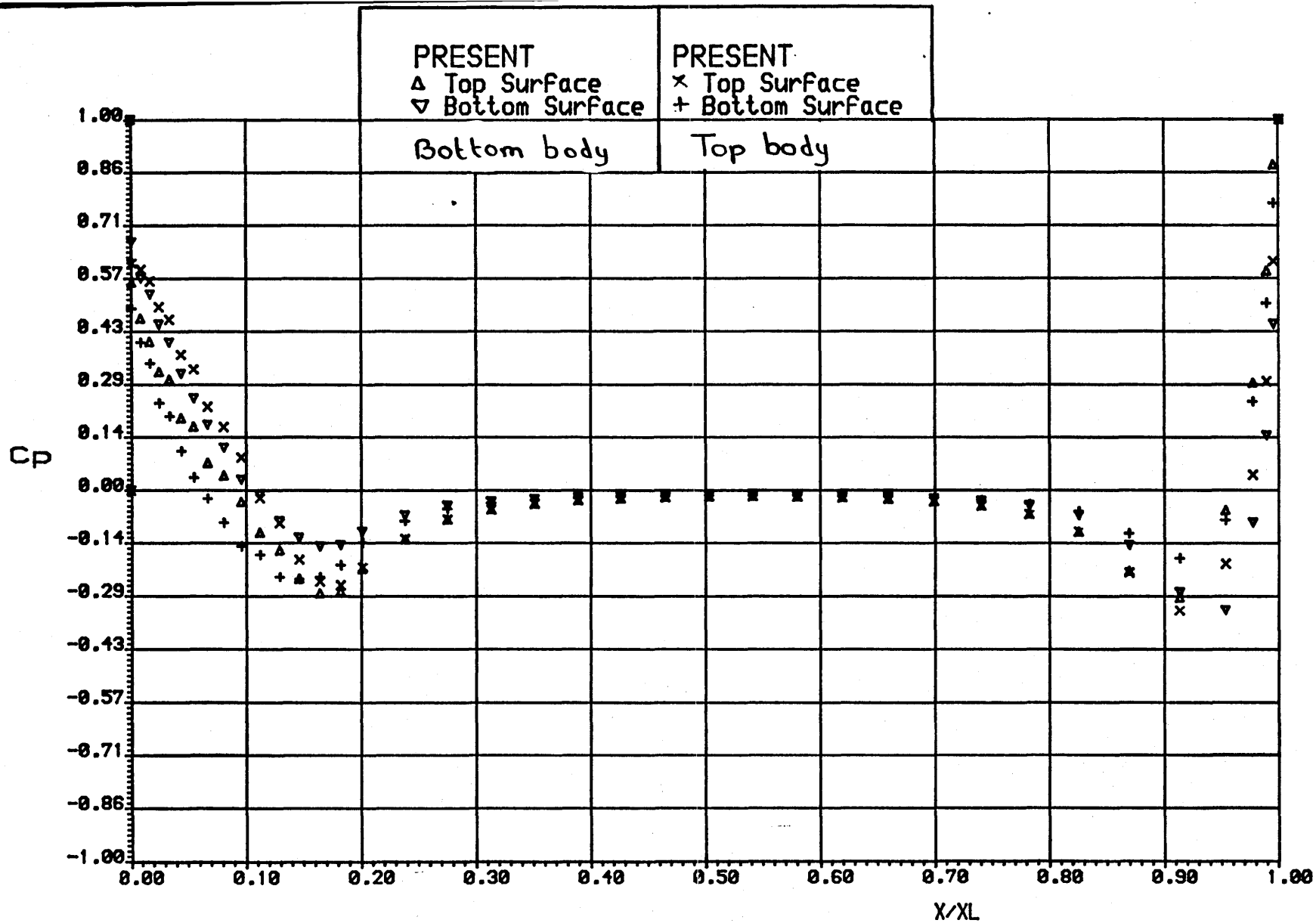


Fig.68 Pressure distribution for both ogive-cylinders of configuration  
 $M=0.6$  Incidence= $5.0$  Spacing= $0.025$

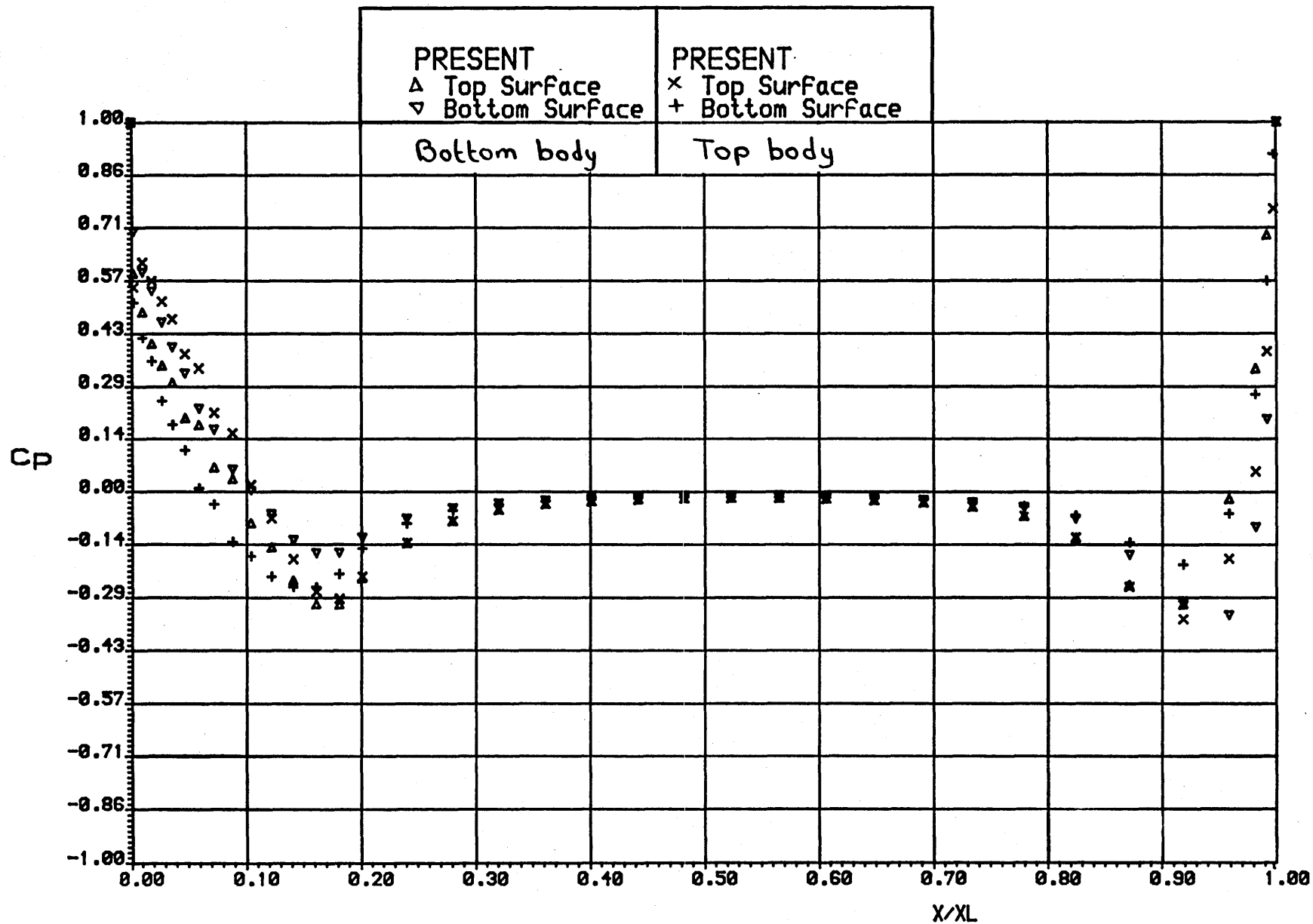


Fig.69. Pressure distribution for both ogive-cylinders of configuration  $M=0.7$  Incidence= $5.0$  Spacing= $0.025$

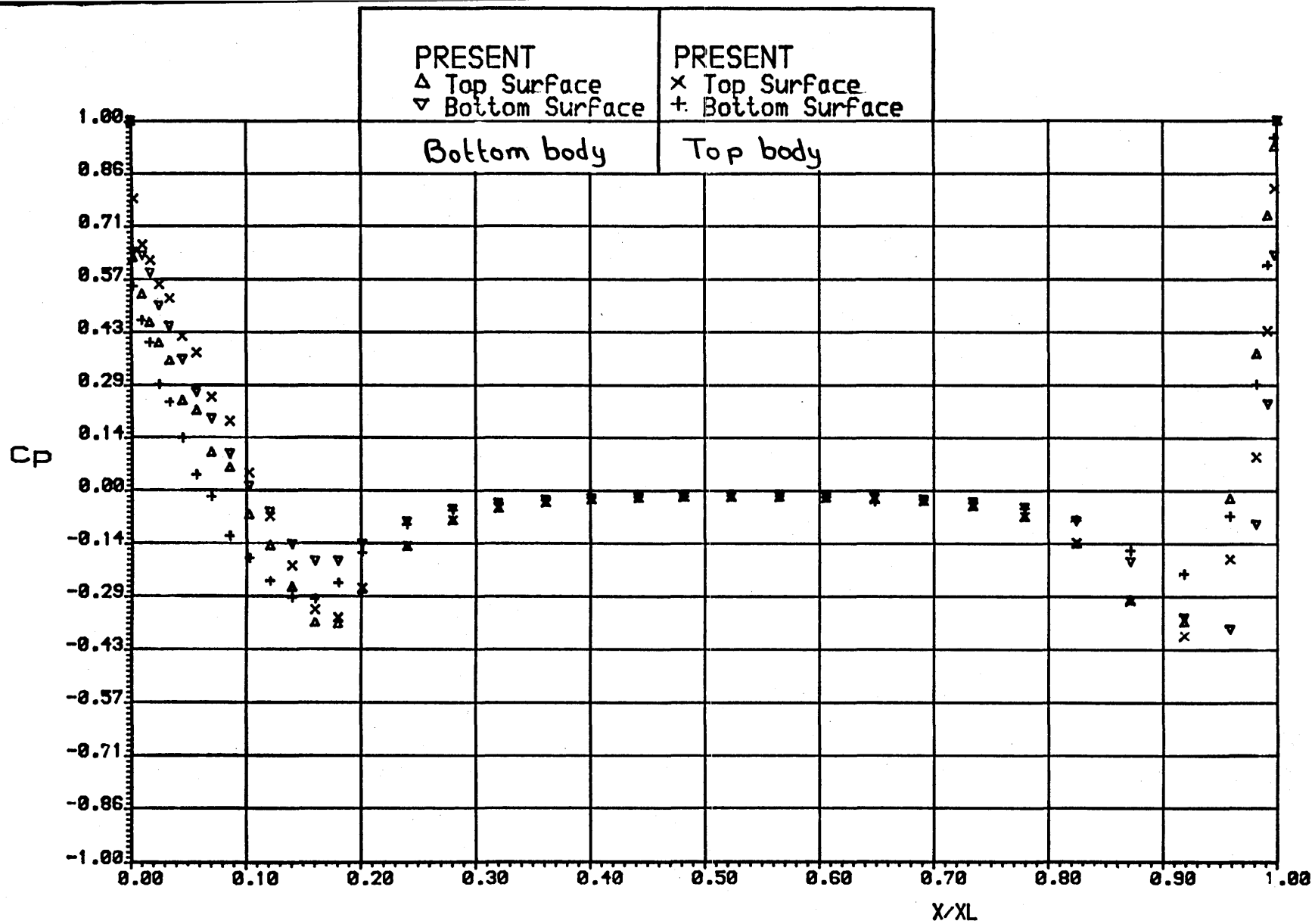


Fig.70 Pressure distribution for both ogive-cylinders of configuration  $M=0.8$  Incidence=5.0 Spacing=0.025

PEAK PRESSURE

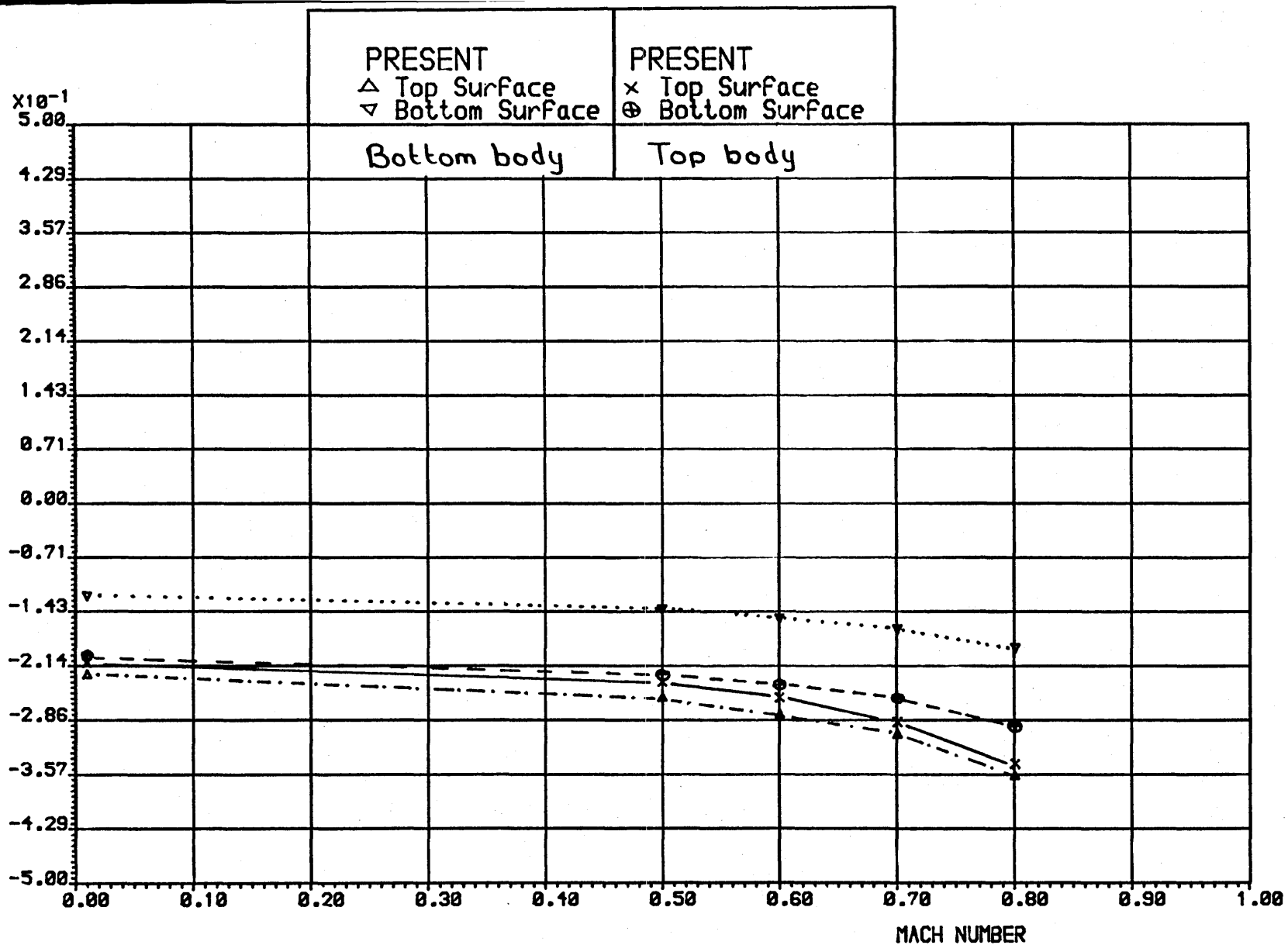


Fig.71. Peak pressure VS mach number for both ogive-cylinders of configuration  
 Incidence=5.0 Spacing=0.025

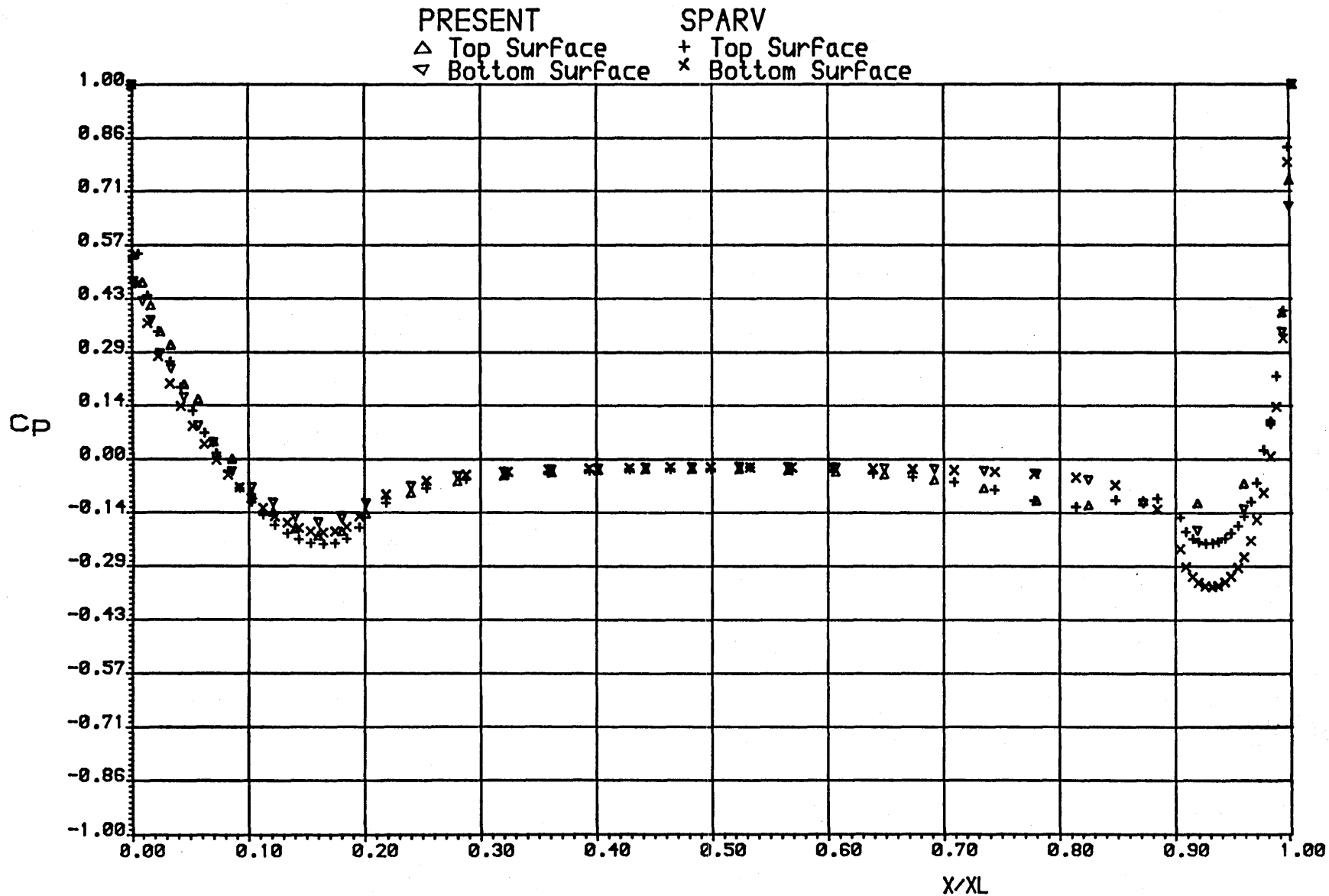


Fig.72 Pressure distribution for bottom ogive-cylinder of configuration  
 $M=0.01$  Incidence= $0.0$  Spacing= $0.025$  Stagger= $0.1$

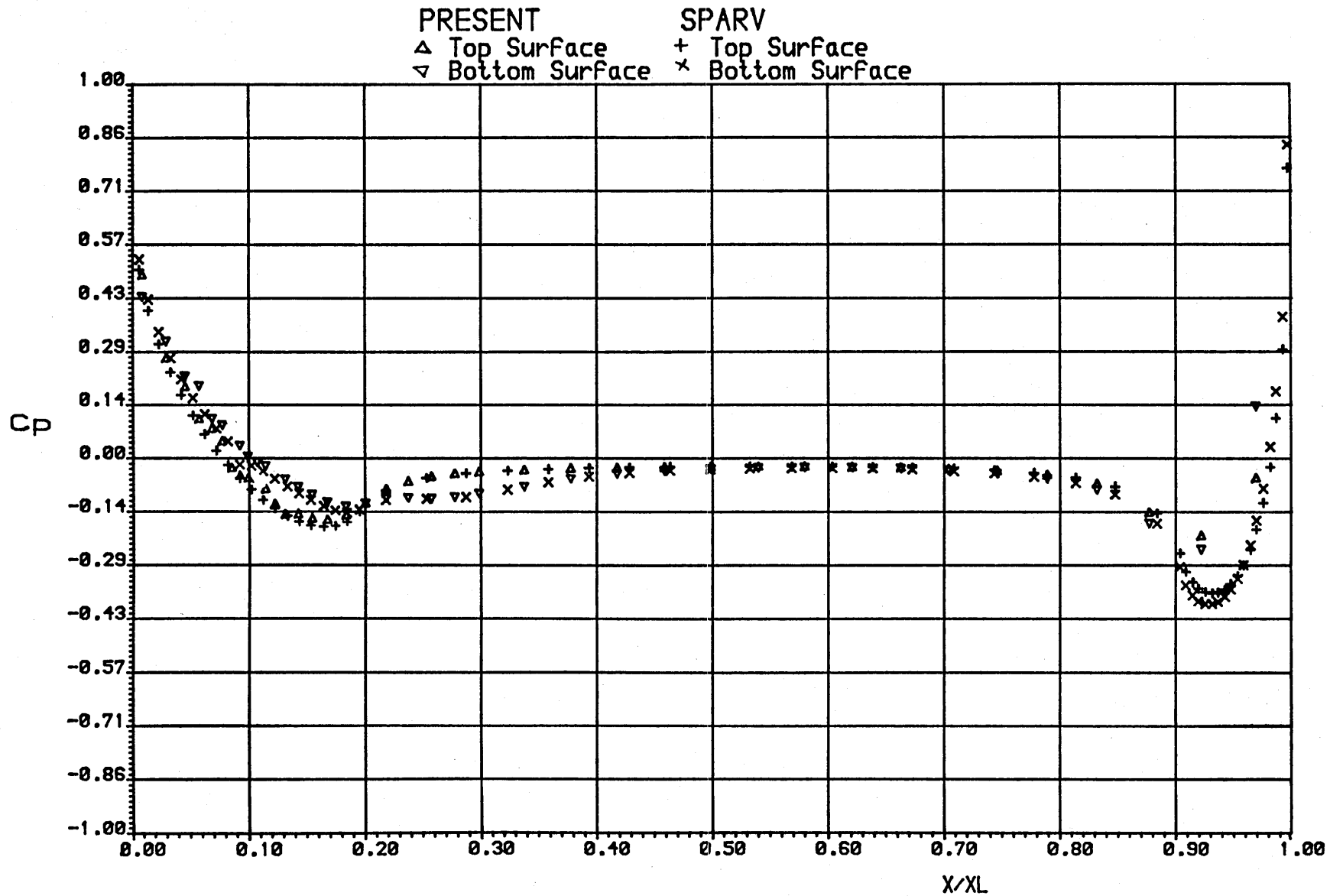


Fig.73 Pressure distribution for top ogive-cylinder of configuration  
 $M=0.01$  Incidence= $0.0$  Spacing= $0.025$  Stagger= $0.1$

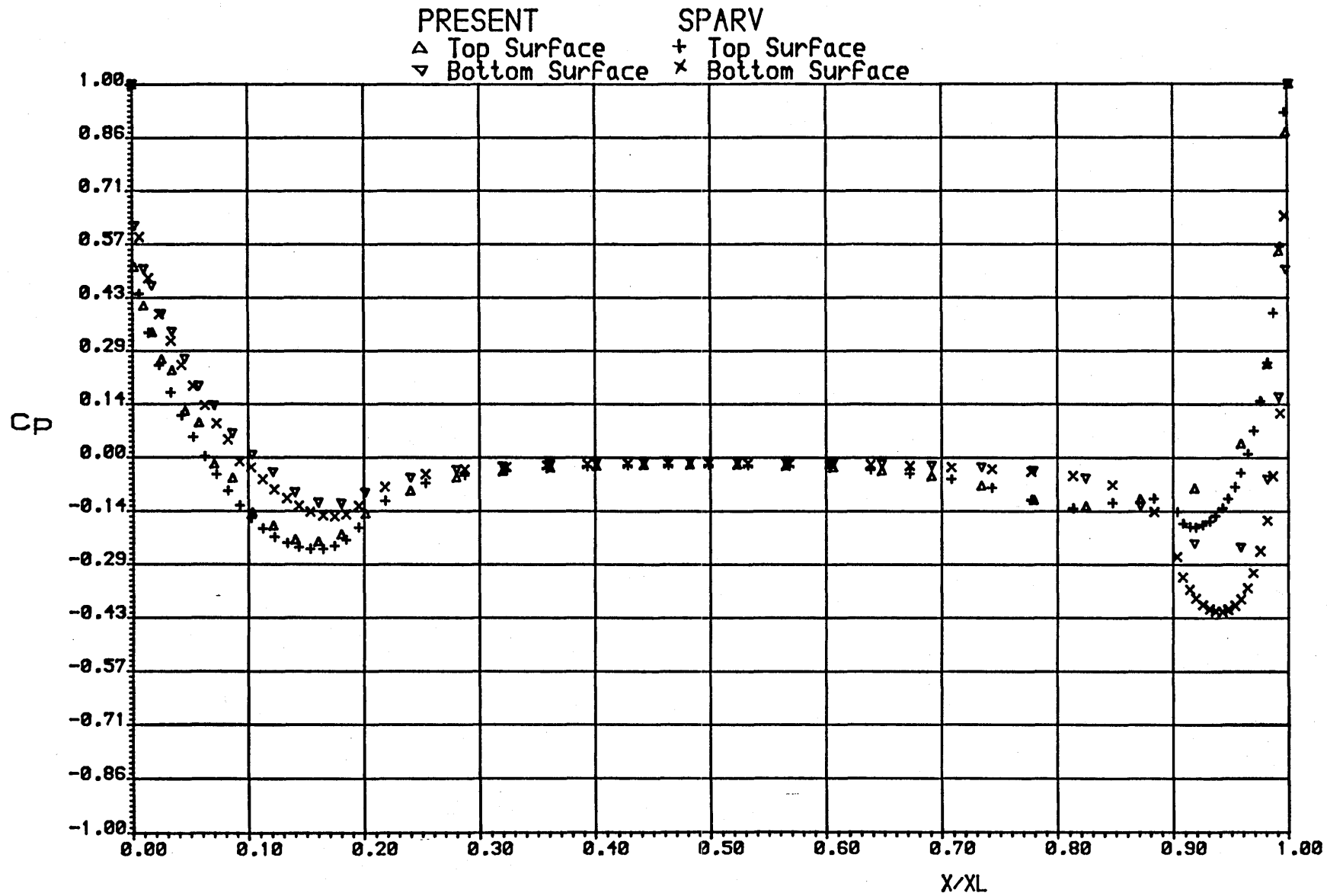


Fig.74 Pressure distribution for bottom ogive-cylinder of configuration  
 $M=0.01$  Incidence= $5.0$  Spacing= $0.025$  Stagger= $0.1$

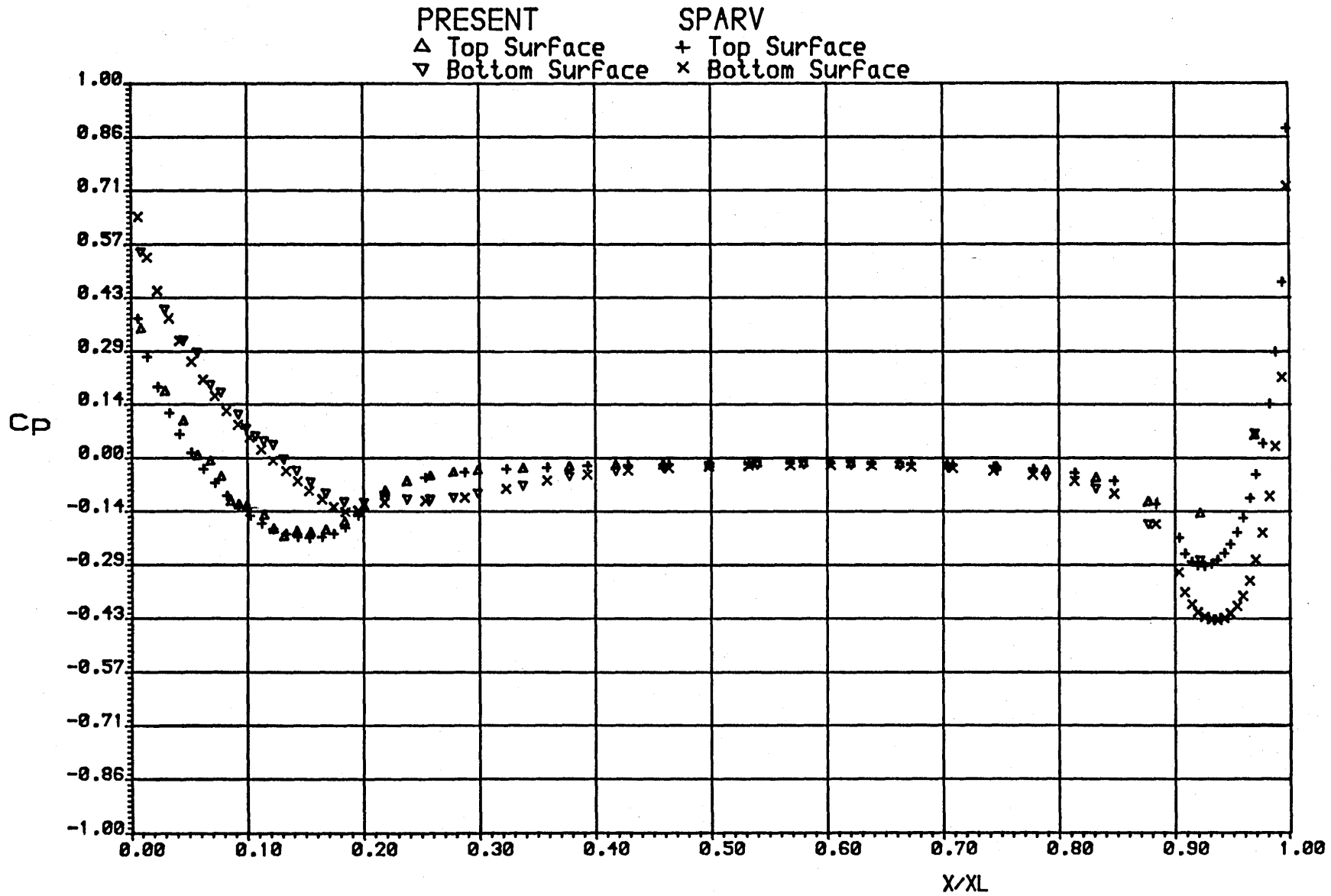


Fig.75 Pressure distribution For top ogive-cylinder of configuration  
 $M=0.01$  Incidence=5.0 Spacing=0.025 Stagger=0.1



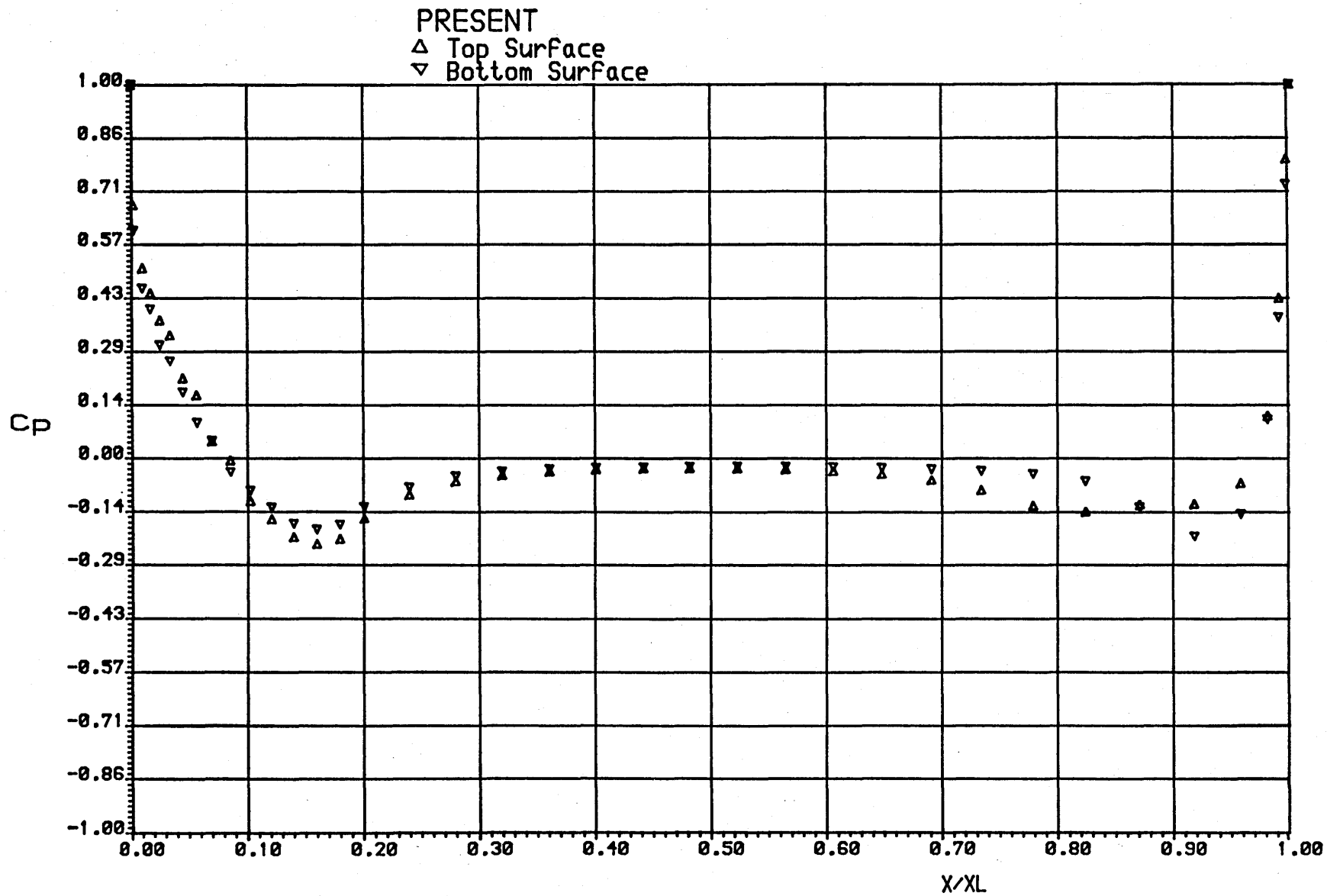


Fig.76 Pressure distribution for bottom ogive-cylinder of configuration  
 M=0.5 Incidence=0.0 Spacing=0.025 Stagger=0.1

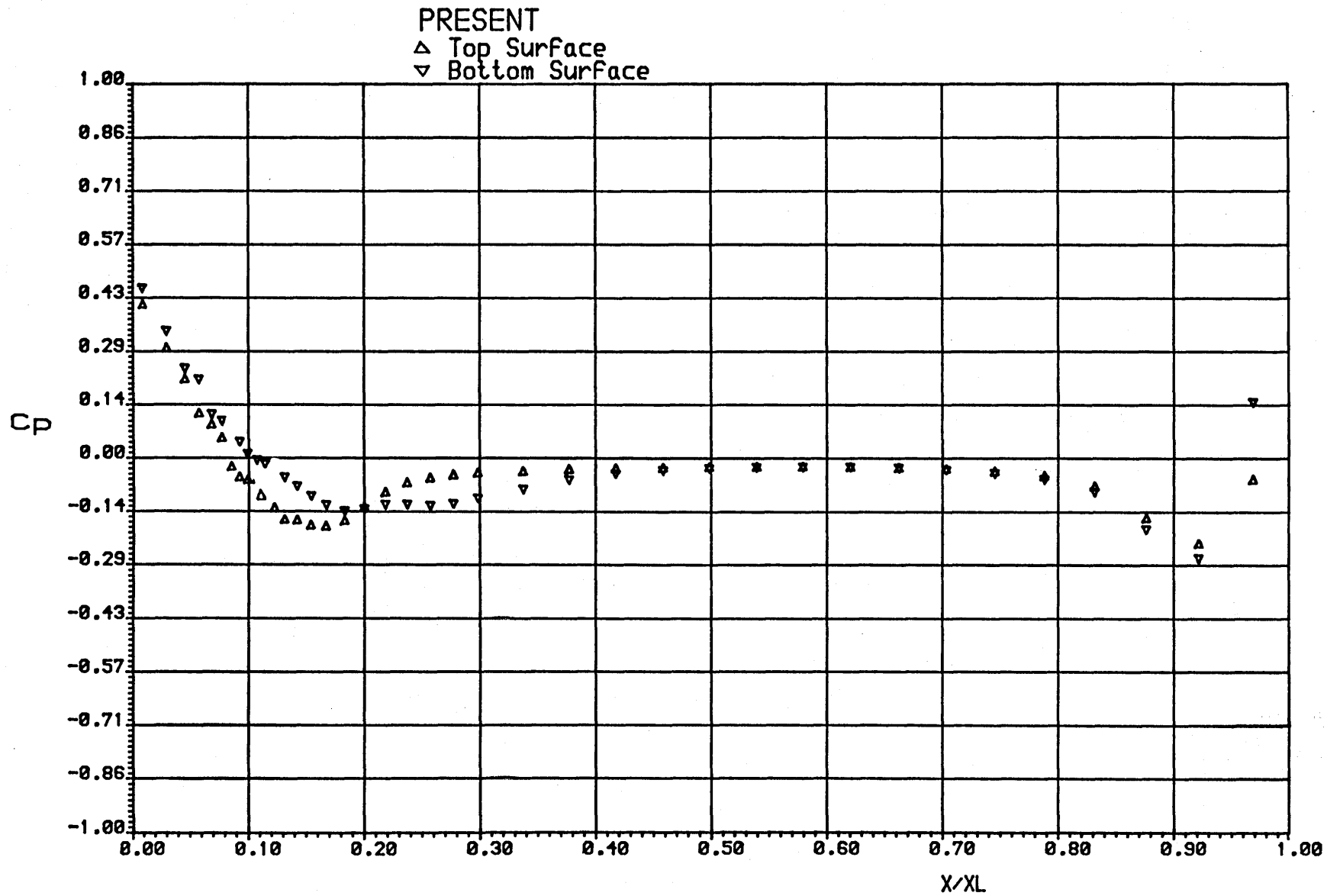


Fig.77 Pressure distribution for top ogive-cylinder of configuration  
 M=0.5 Incidence=0.0 Spacing=0.025 Stagger=0.1

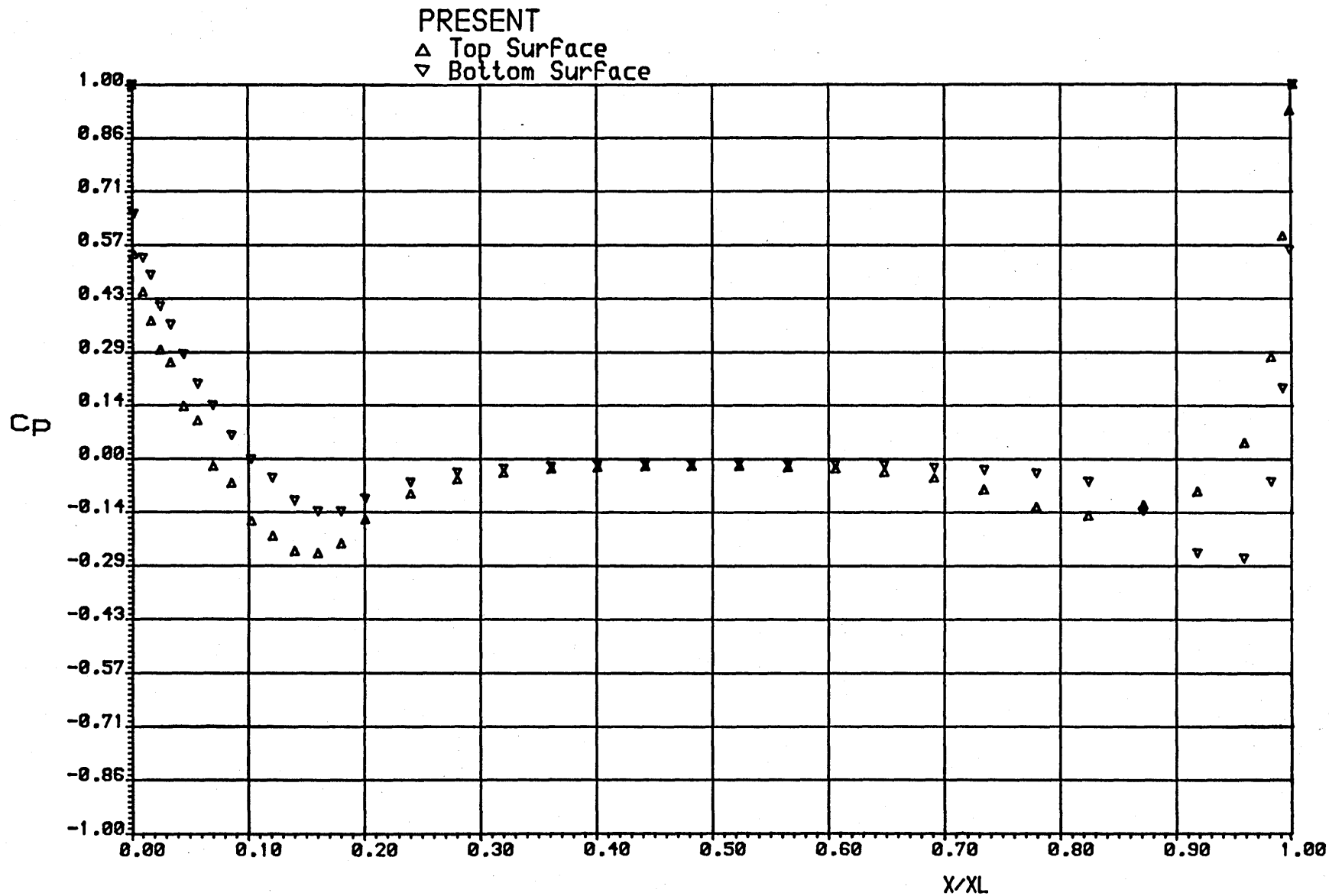


Fig. 78 Pressure distribution for bottom ogive-cylinder of configuration  
 $M=0.5$  Incidence=5.0 Spacing=0.025 Stagger=0.1

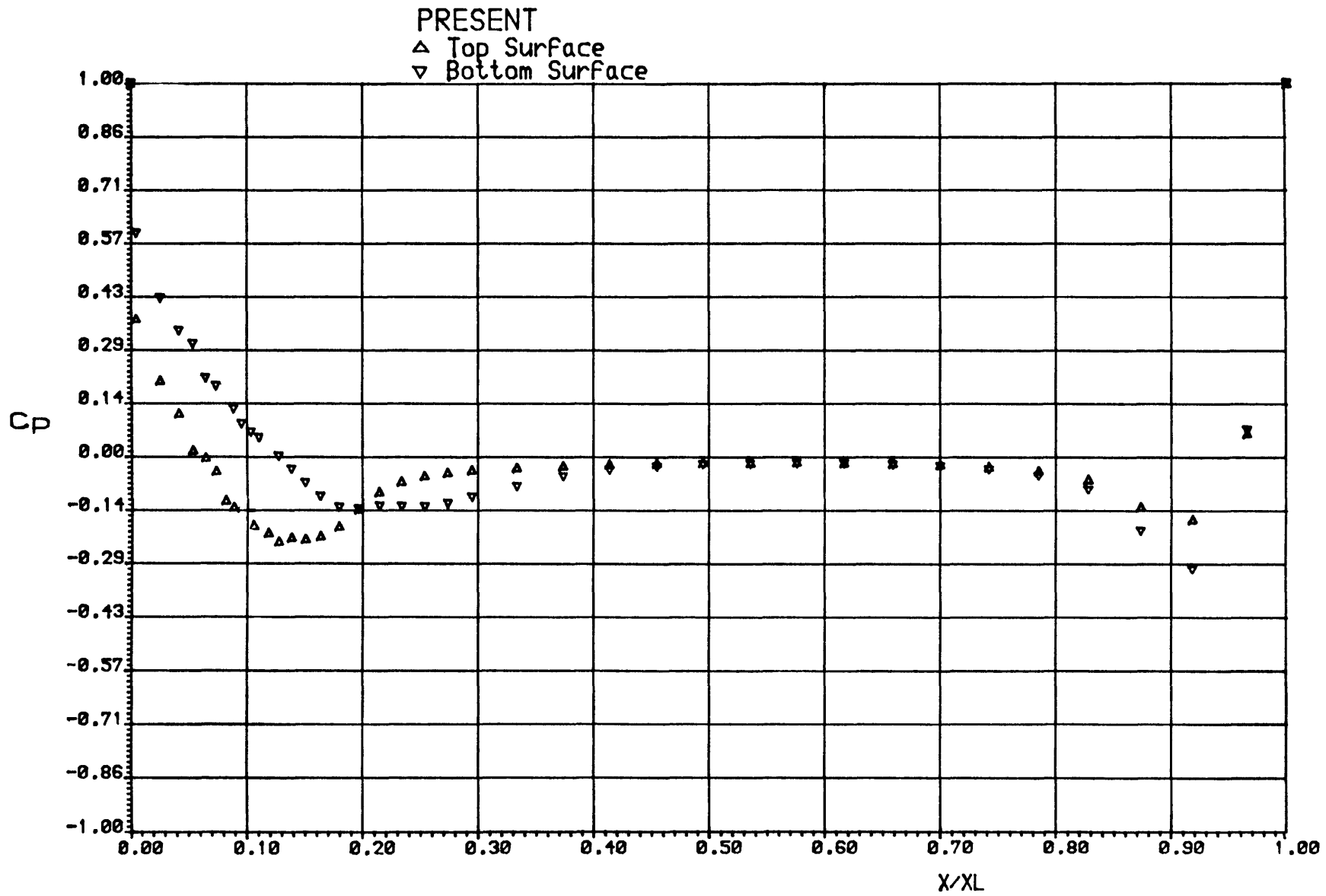


Fig. 79 Pressure distribution for top ogive-cylinder of configuration  
 $M=0.5$  Incidence= $5.0$  Spacing= $0.025$  Stagger= $0.1$

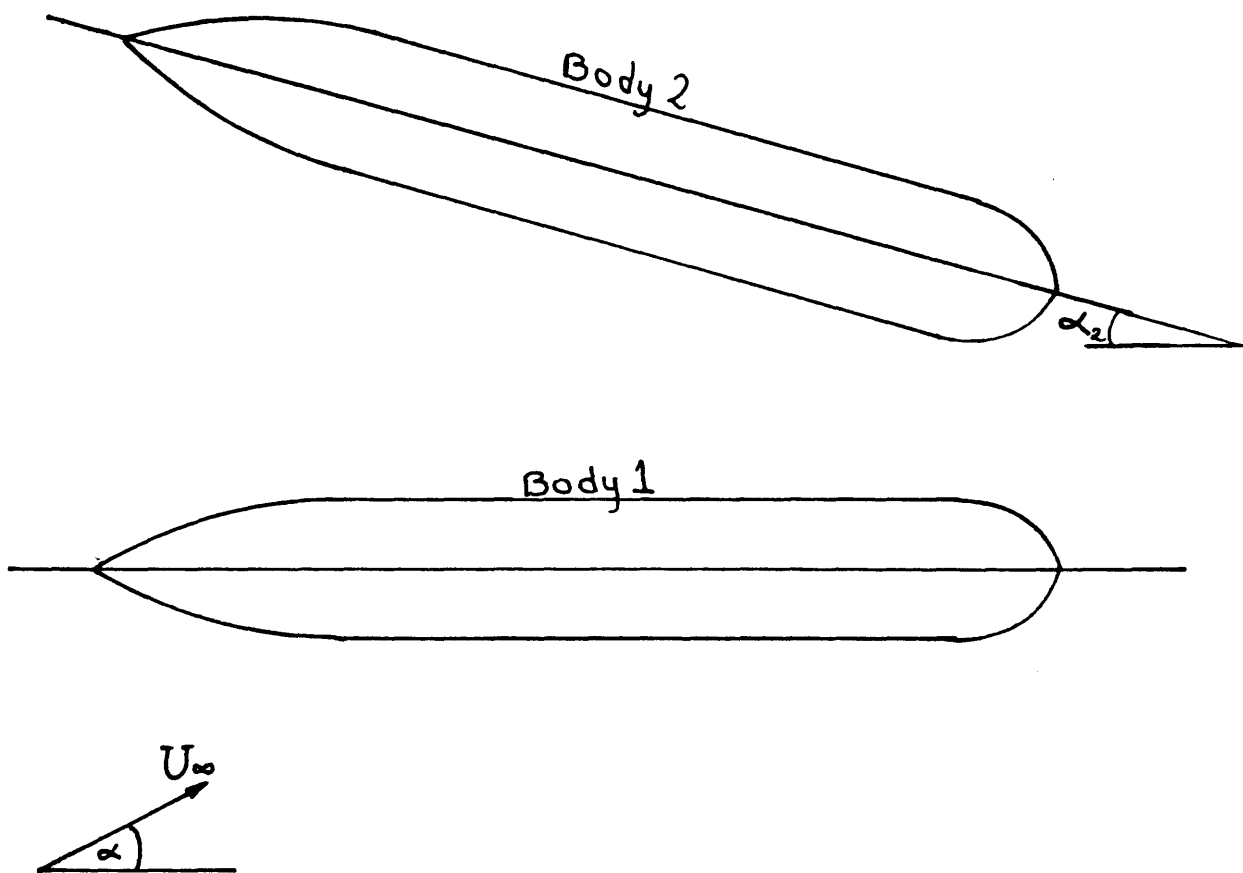


Fig.80 Two bodies in asymmetric configuration

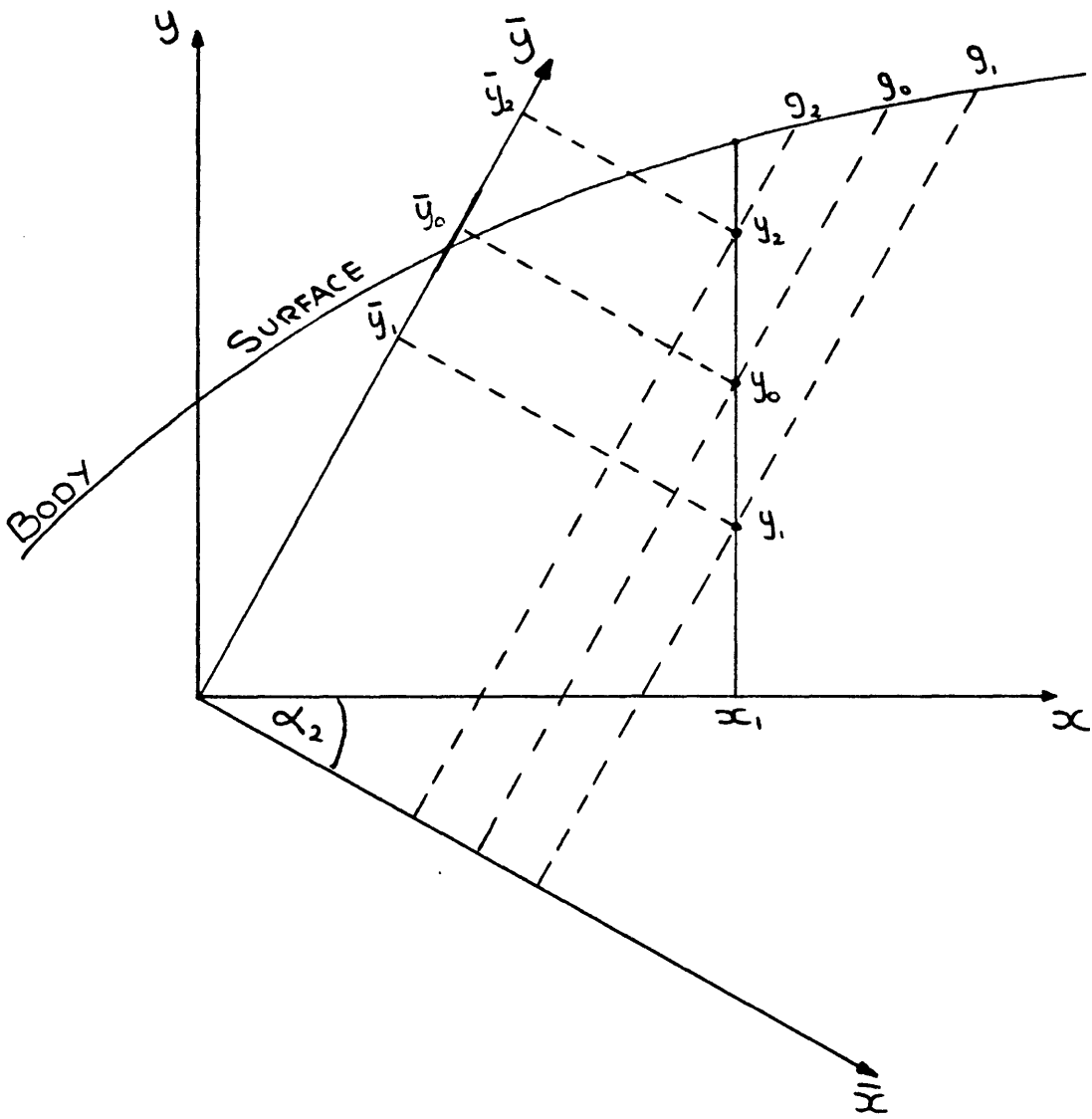


Fig. 81 New coordinate system for a body at incidence

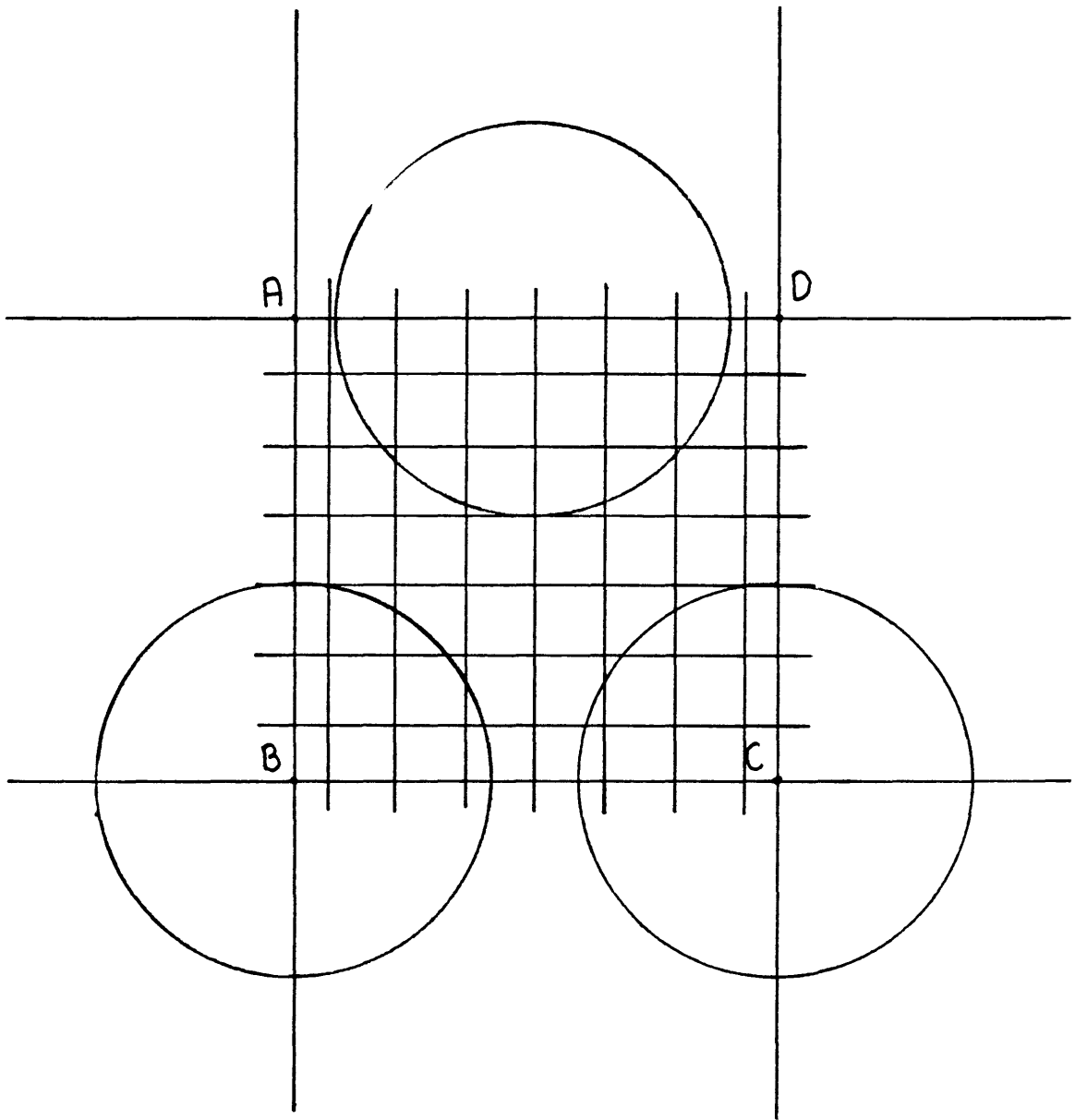


Fig.82 Gridlines between three bodies

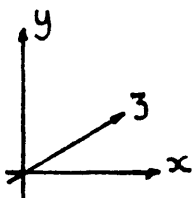
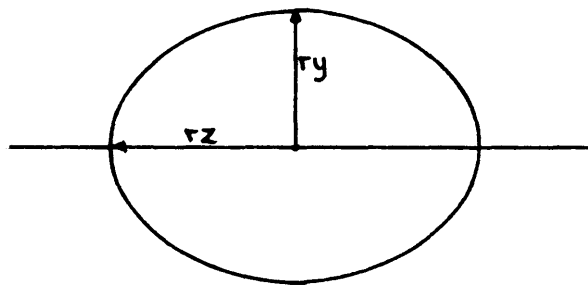
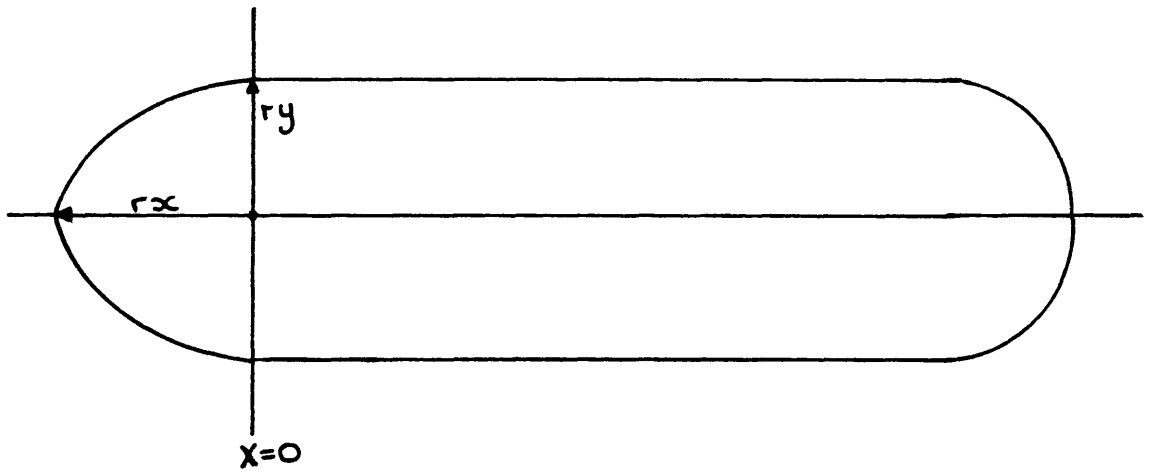


Fig.83 Missile shaped body with non-circular cross-section



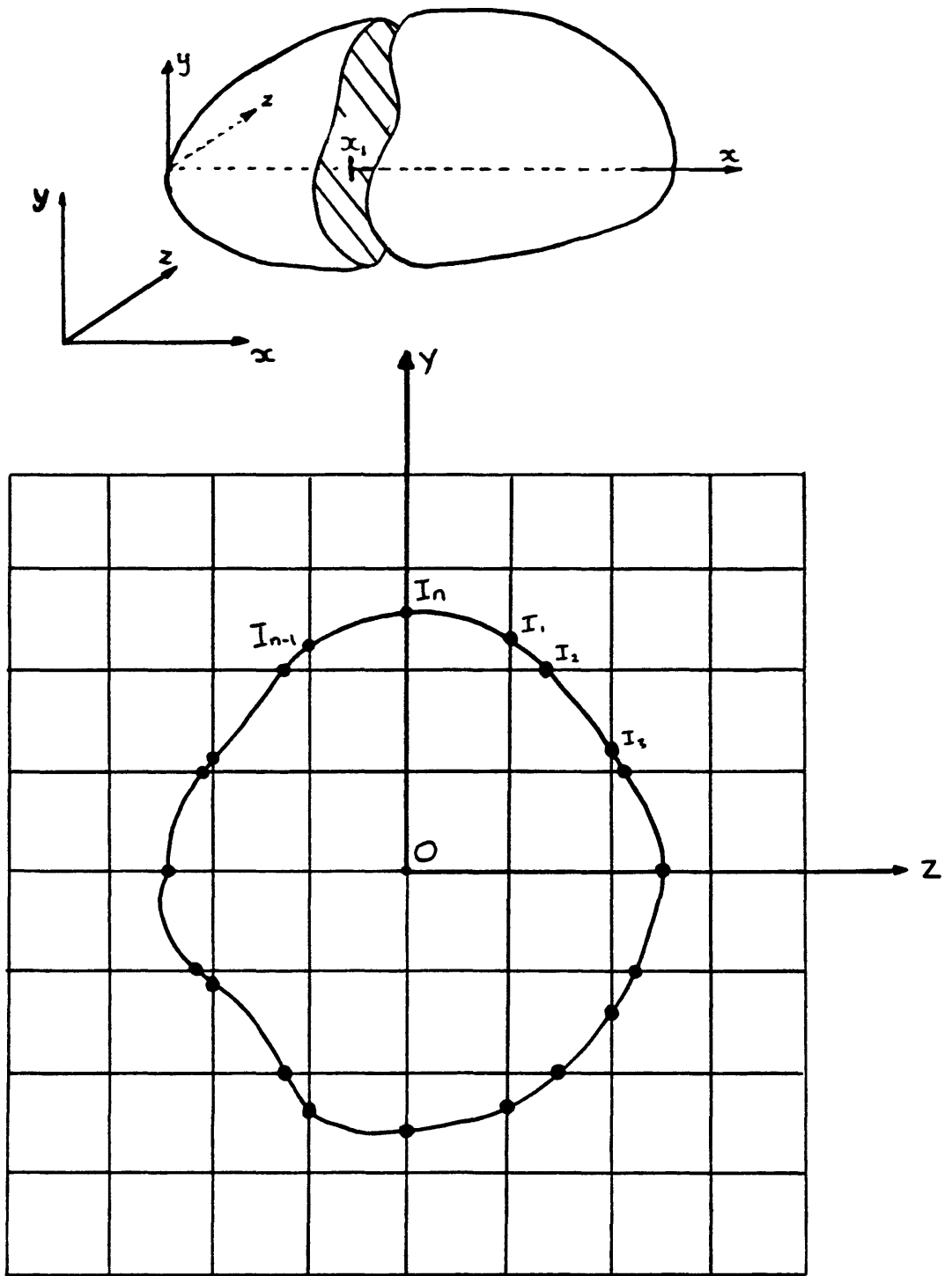


Fig.84 Body section in the x-direction

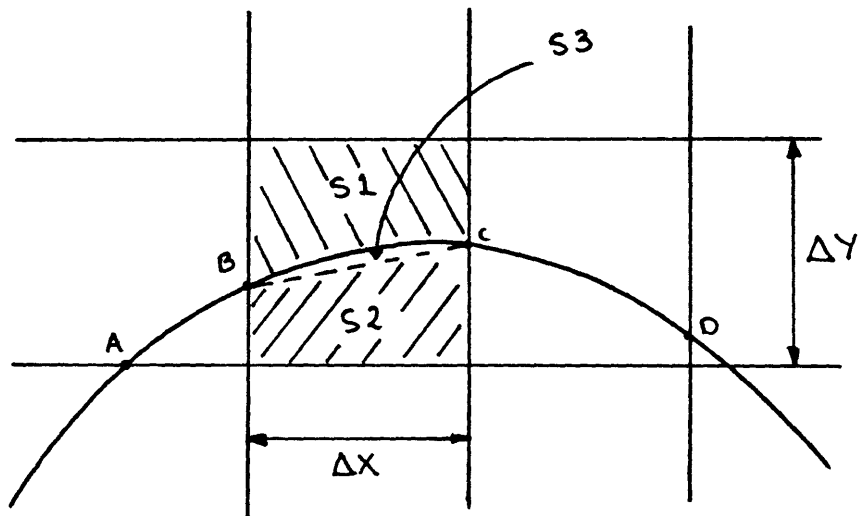
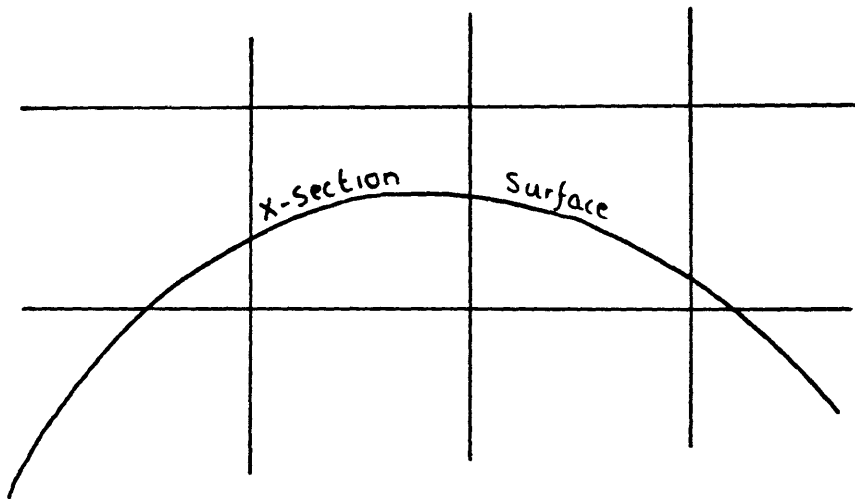


Fig.85 Accurate cell face area calculation using splines

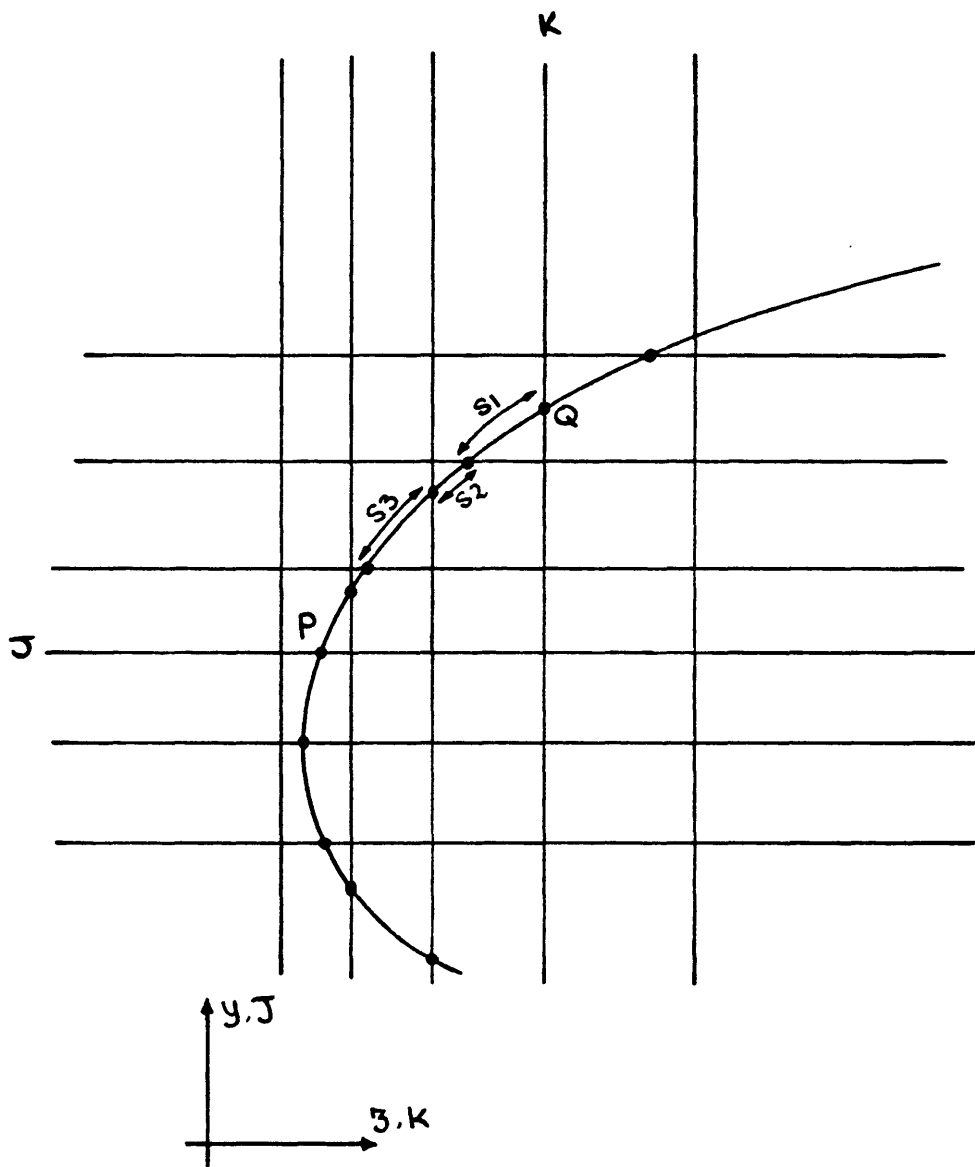


Fig.86 Body points used for calculating the normal force

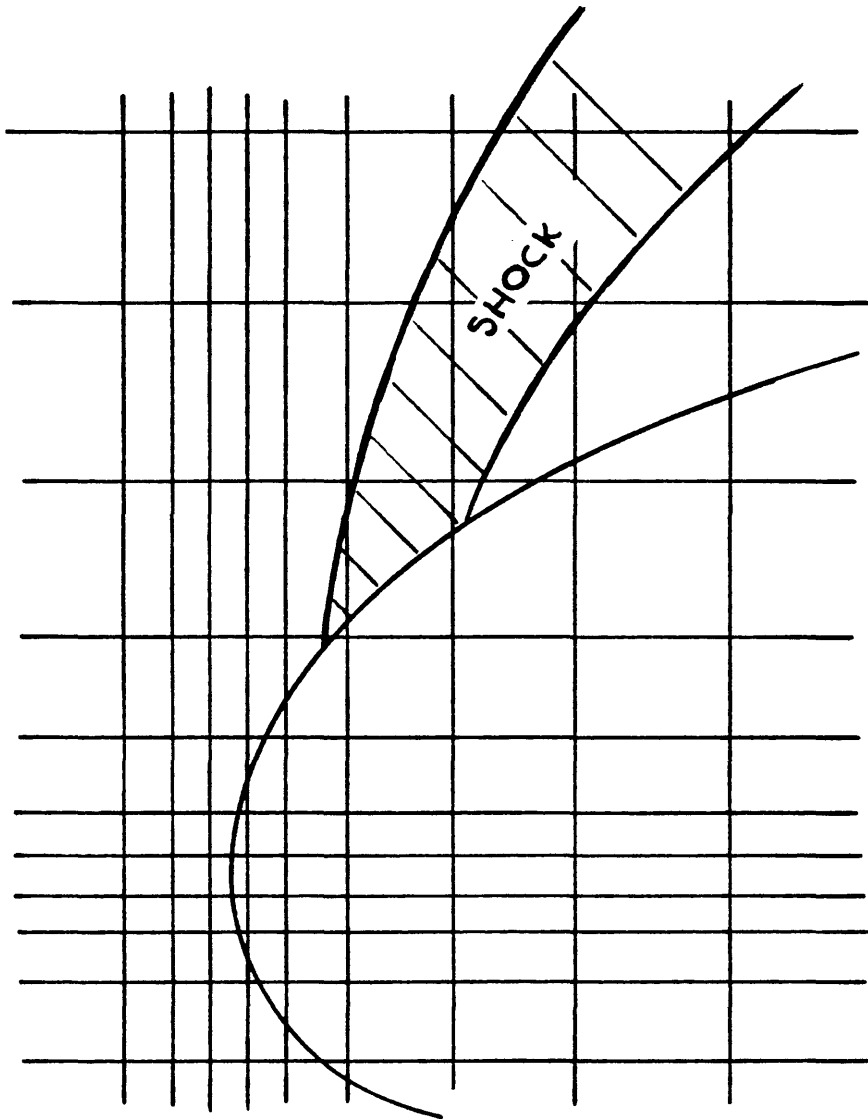
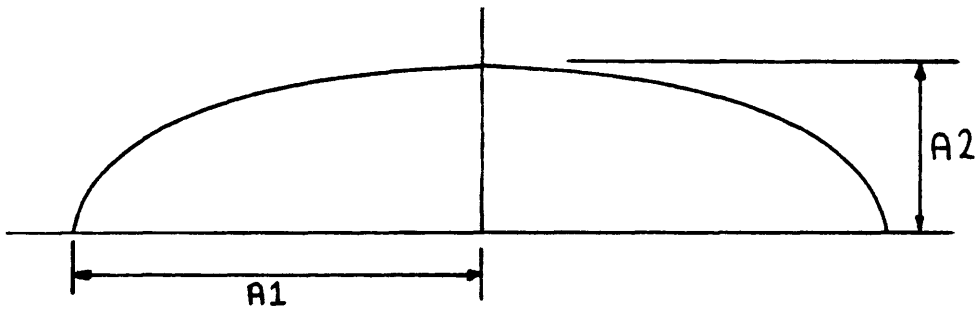


Fig.87 Form of a smeared shock over a few grid points

ellipsoid ratio  $A1:A2$



tangent ogive cylinder

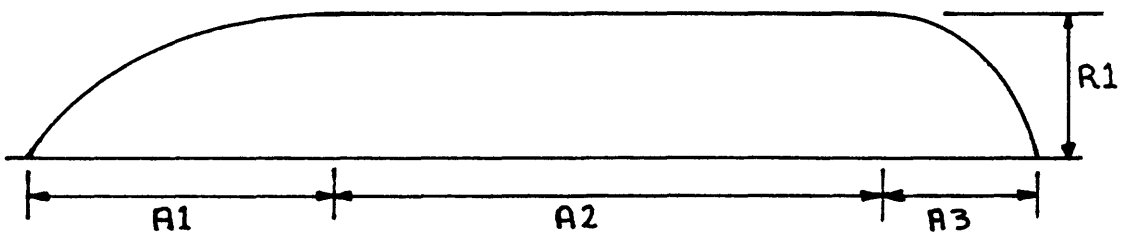


Fig.88 Bodies used as test cases for the CFD work

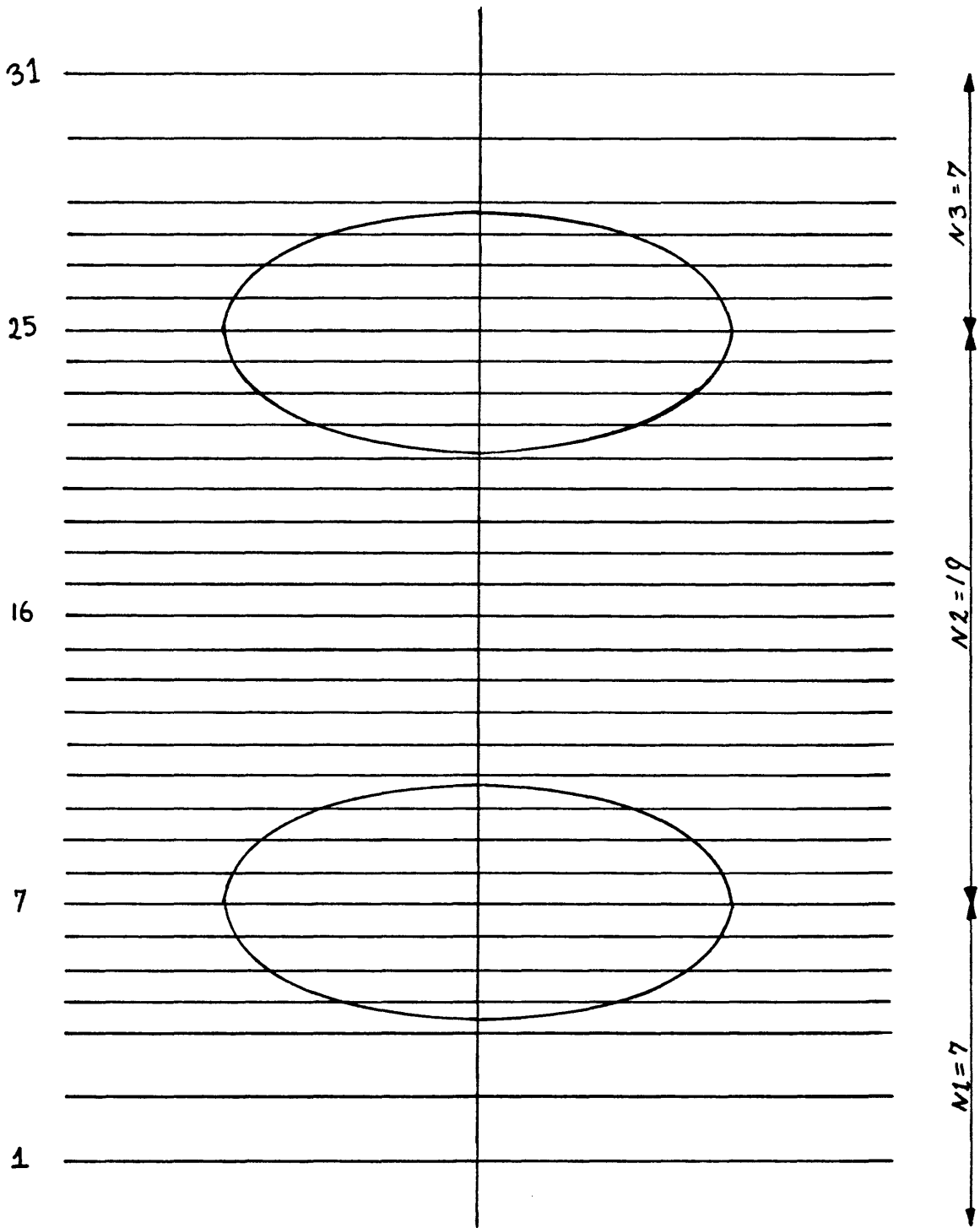


Fig.89 Constant grid line distribution between two bodies

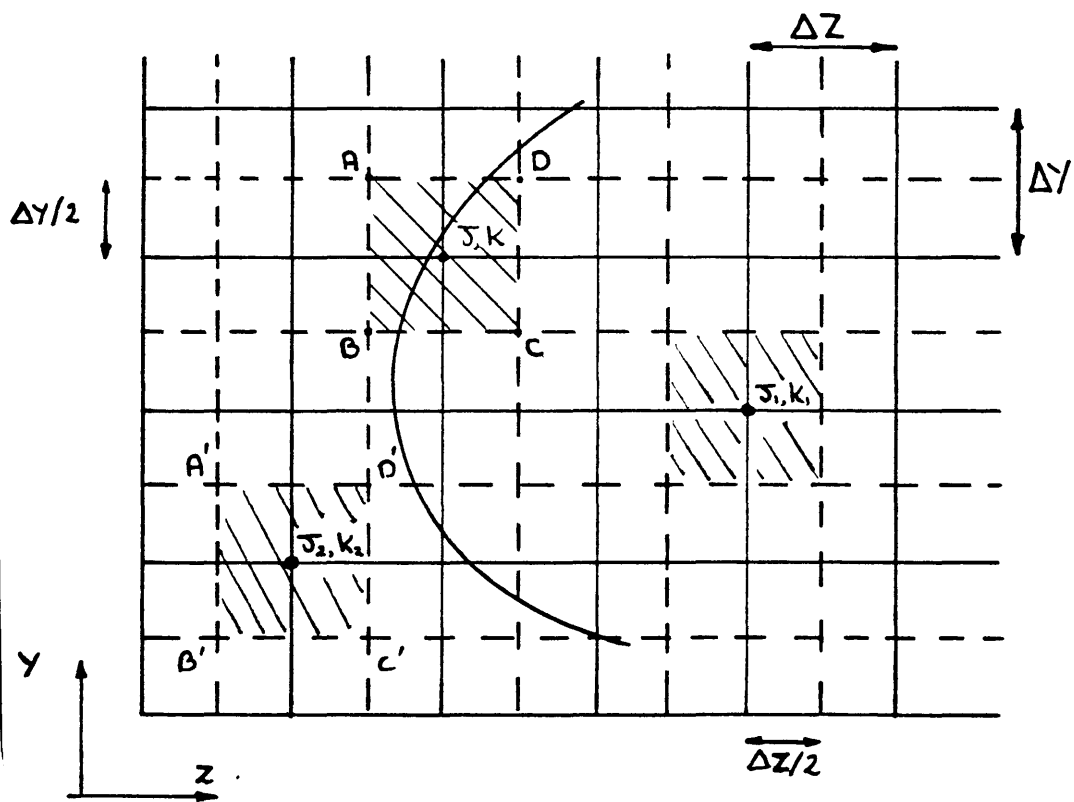
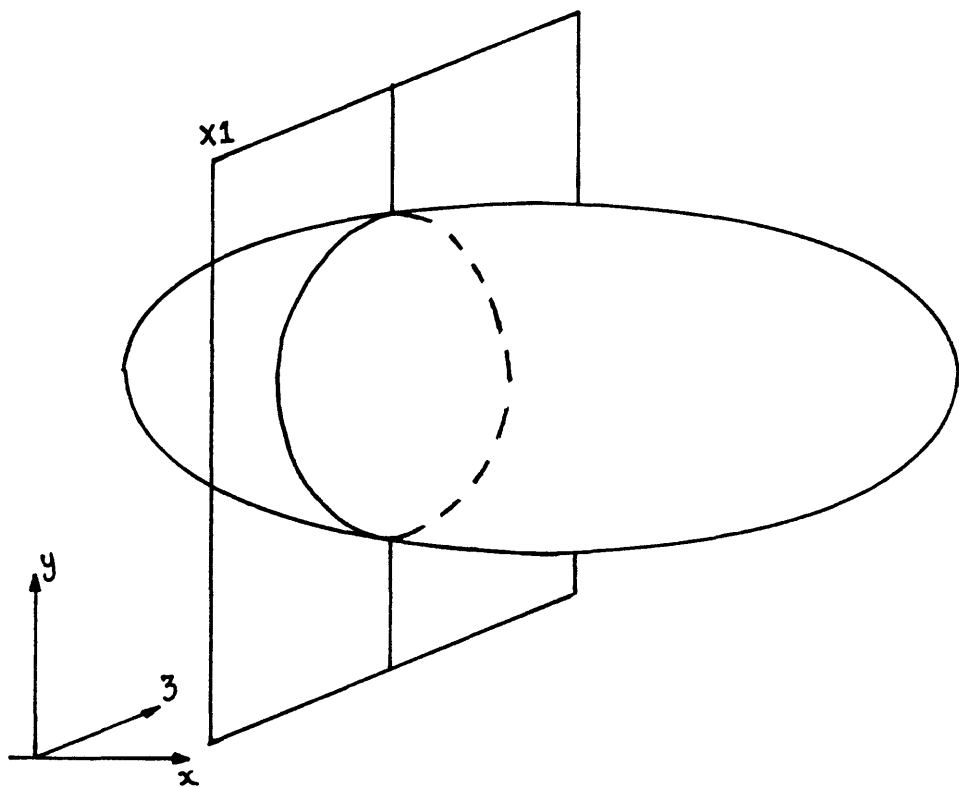
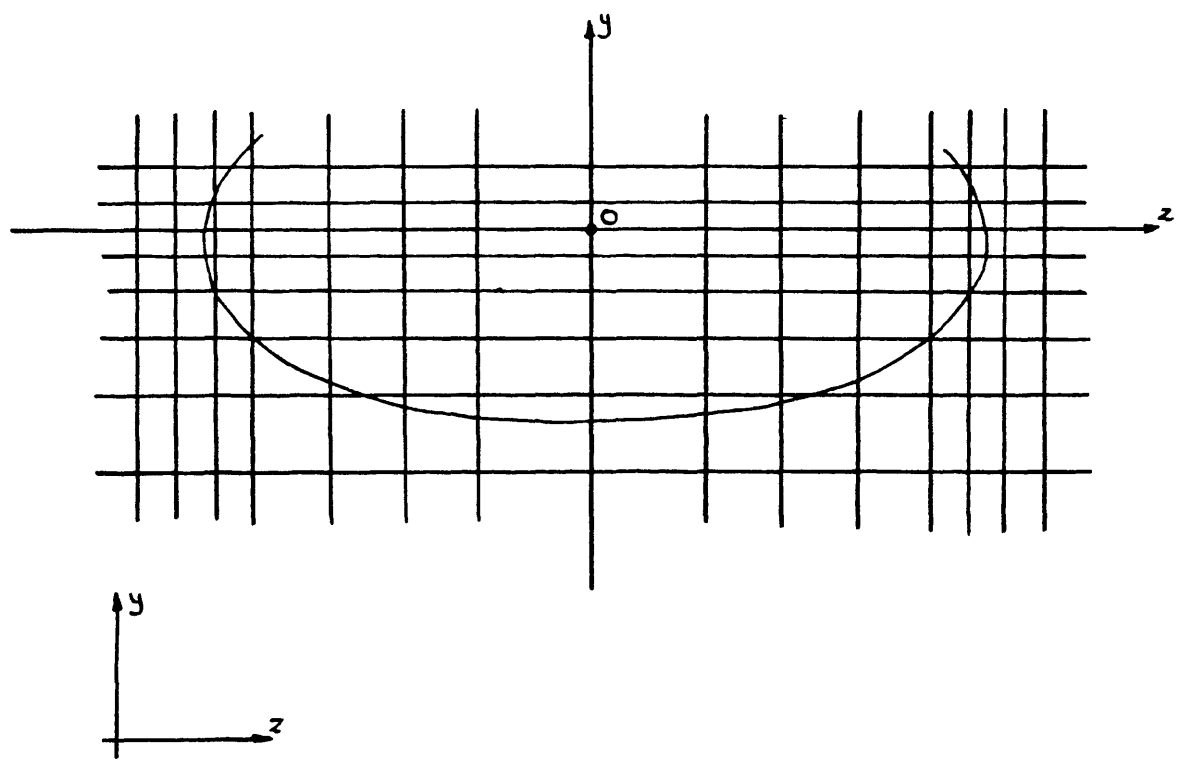


Fig. 90 Cell face area prediction for the  $x$ -flow

Physical Plane



Computational Plane

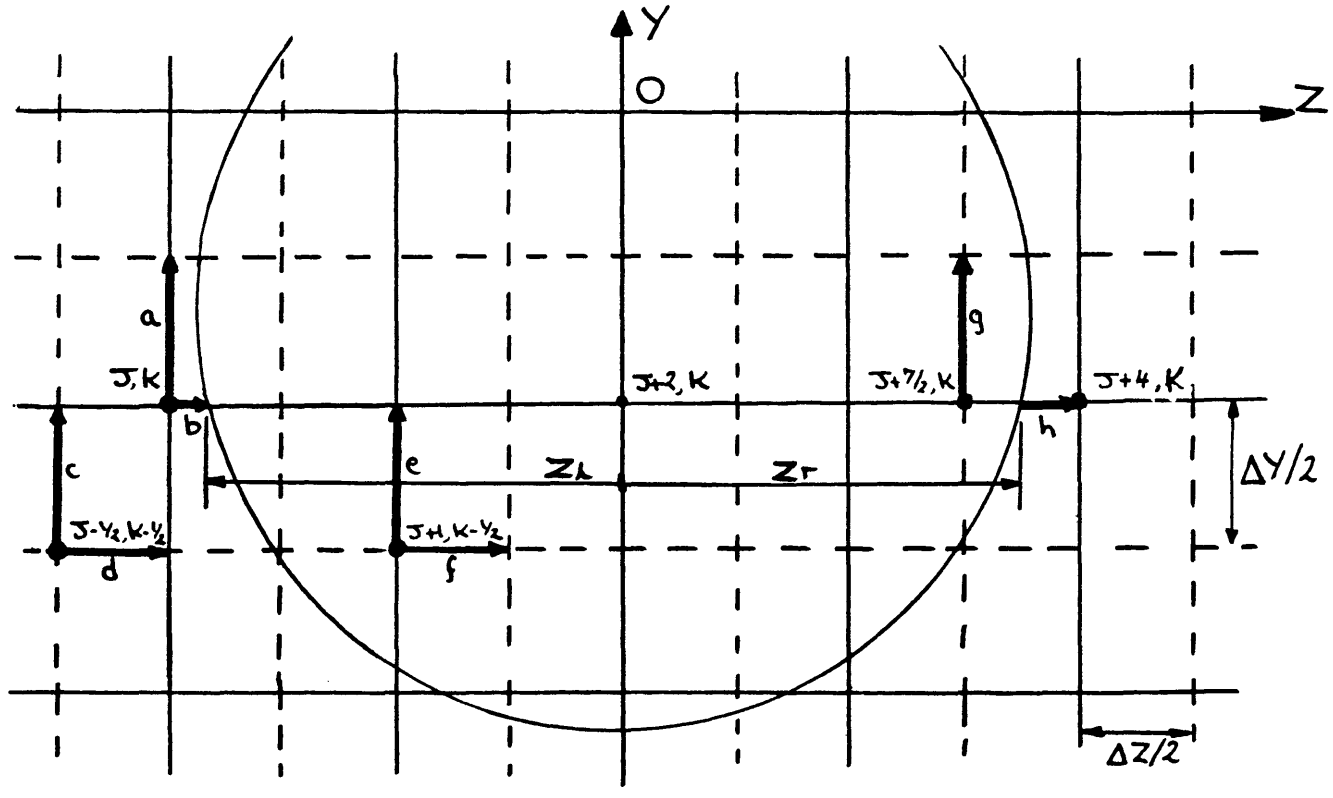


Fig.91a. X-direction cell side calculation



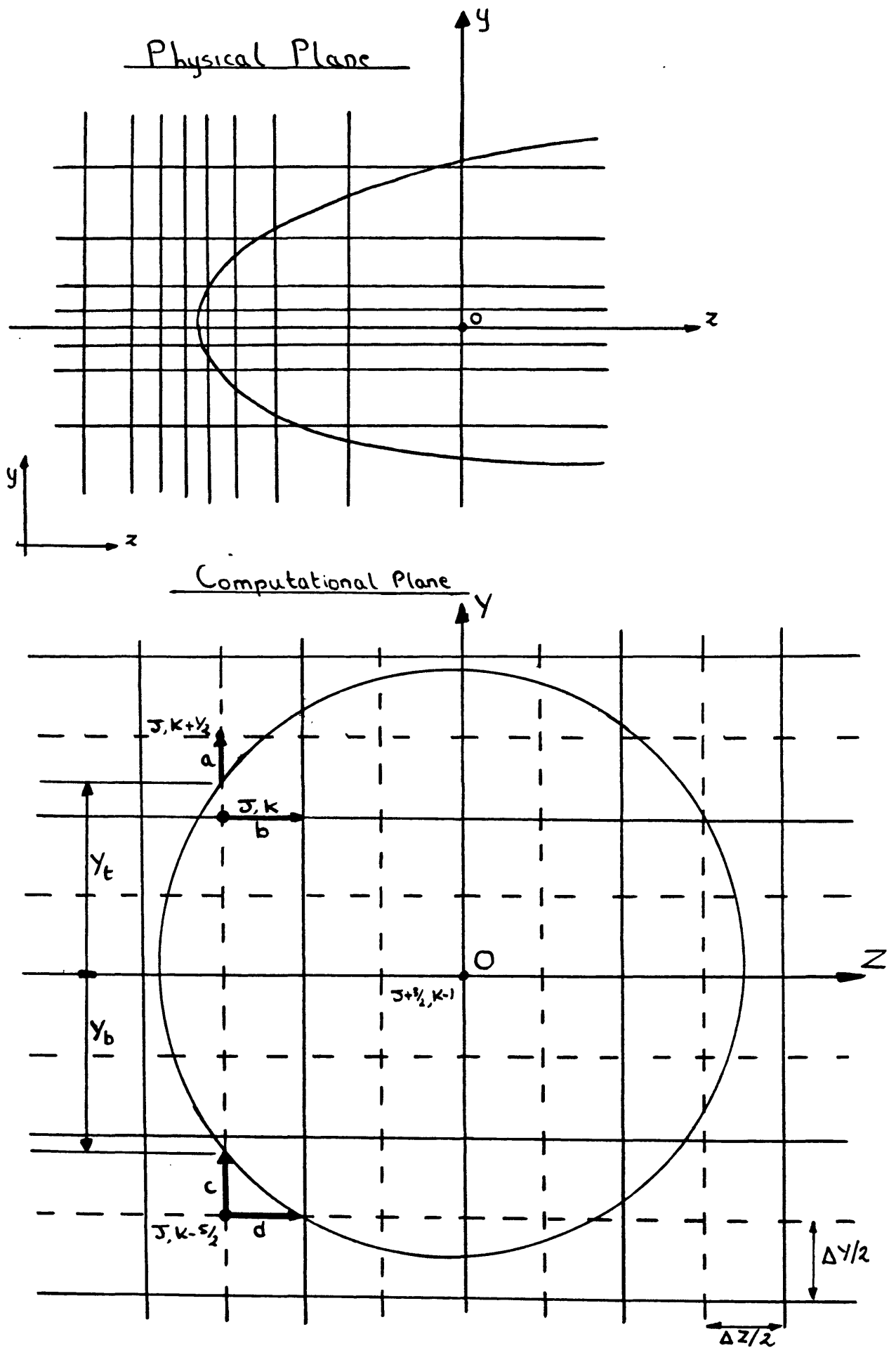


Fig.91b X-direction cell side calculation

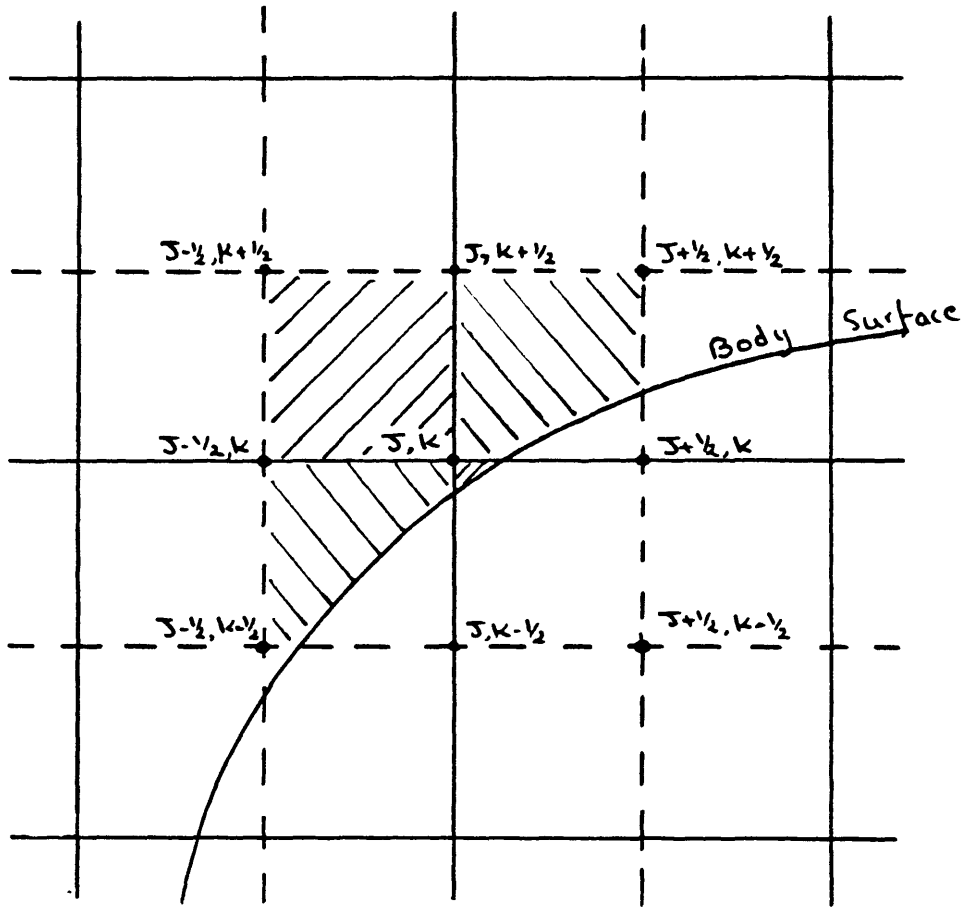


Fig.92. Accurate determination of cell face area

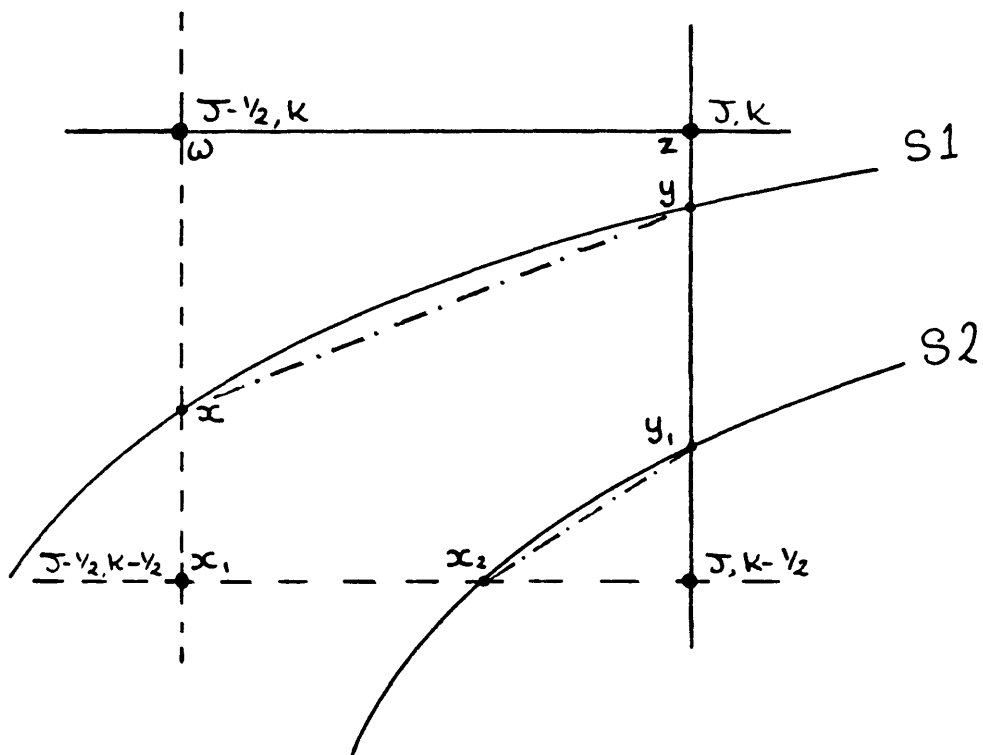


Fig.93 Body surface cutting a cell face

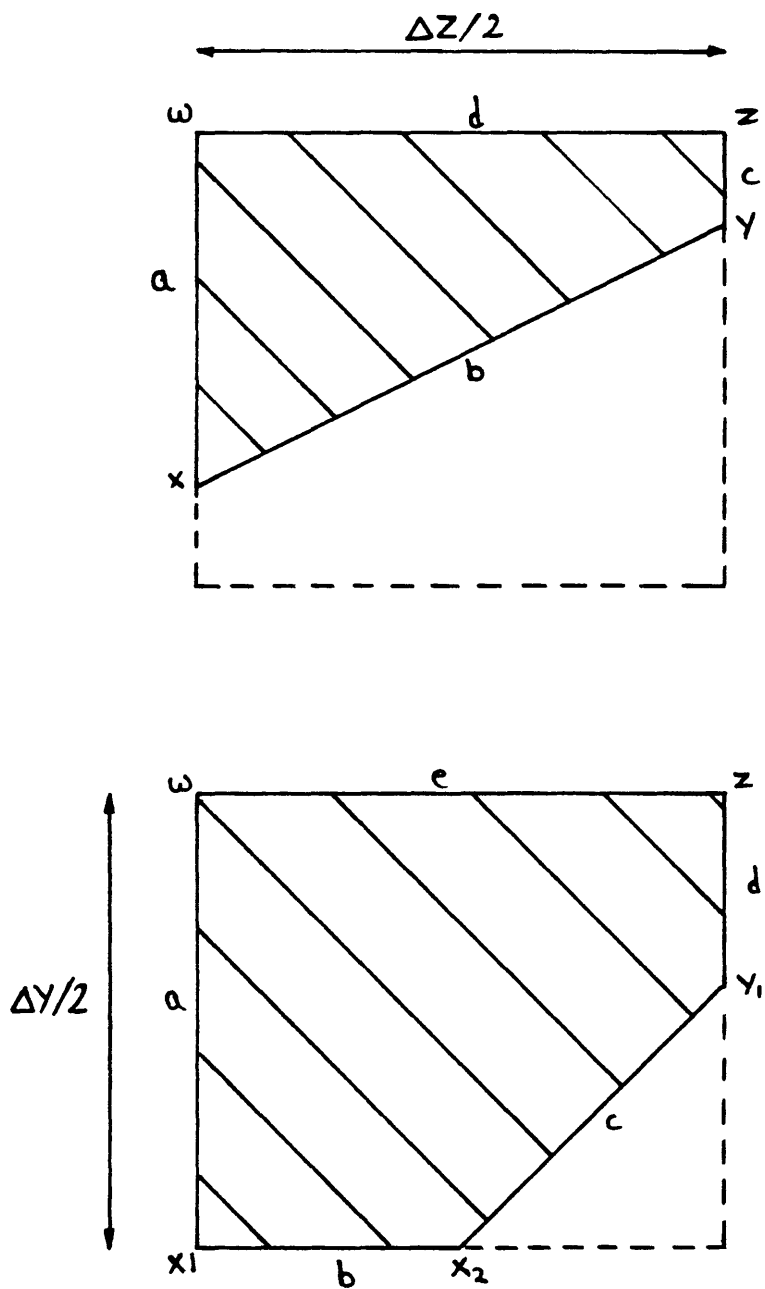


Fig.94 Determination of the area through which fluid flows

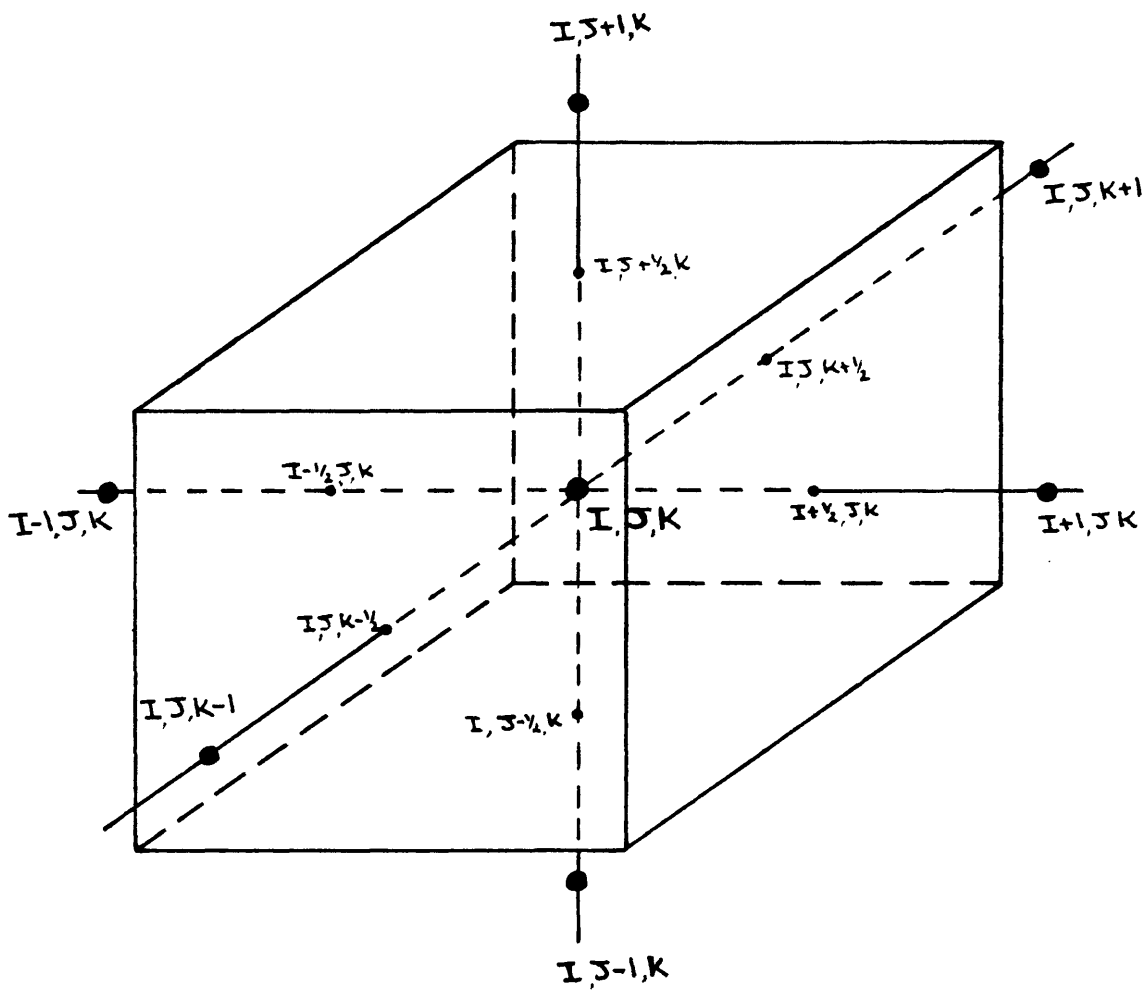


Fig.95 Cell face areas lying midway between control points

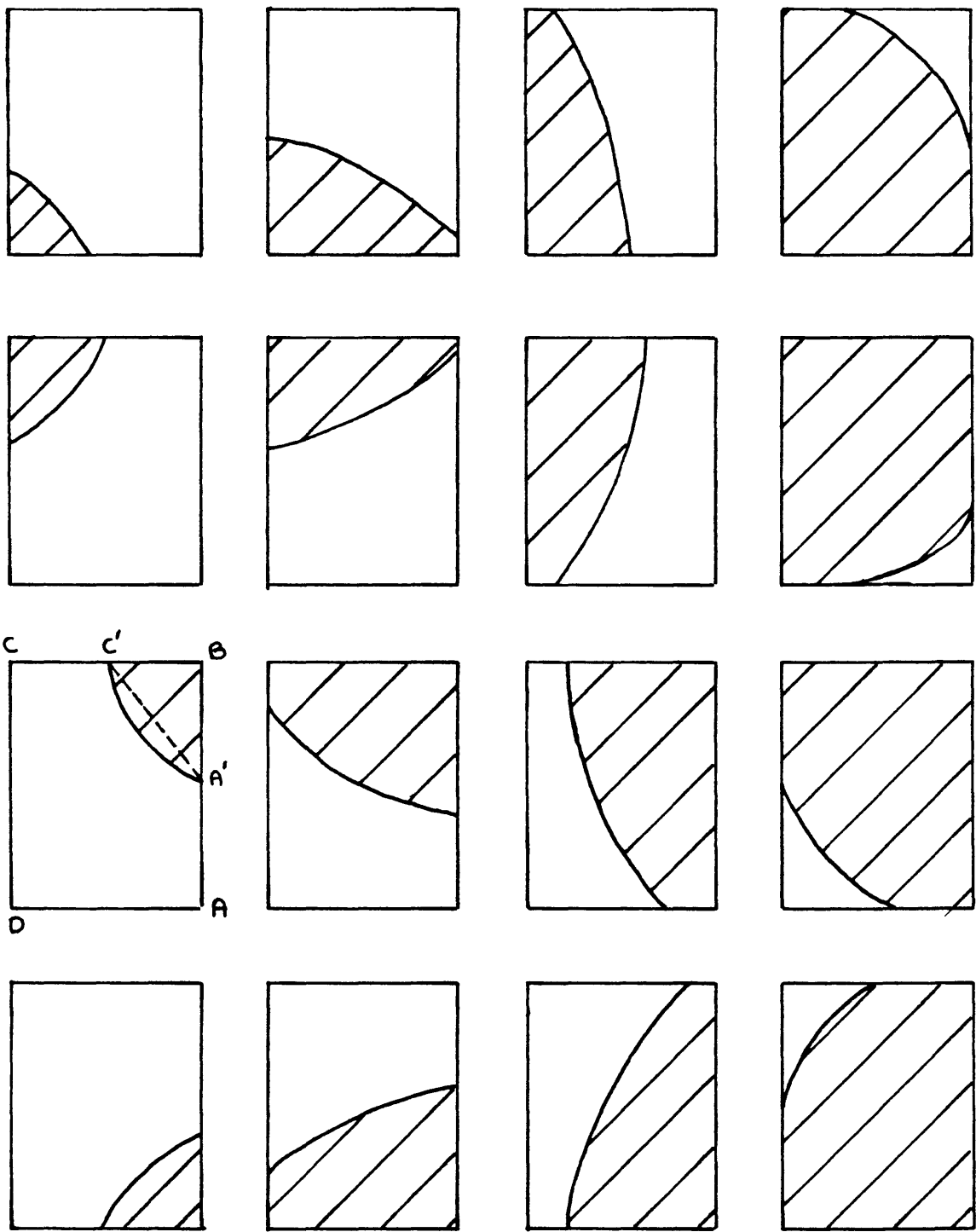


Fig.96 Ways a body surface can cut a cell face